L ANGLEY
GRANT-CR
IN-CAT. 39
74136
p. 239

VIRGINIA TECH

CENTER FOR COMPOSITE MATERIALS AND STRUCTURES

Nonlinear Analysis for the Response
and Failure of Compression-Loaded
Angle-Ply Laminates with a Hole

Steven R. Mathison
Carl T. Herakovich
Marek-Jerzy Pindera
Mark J. Shuart
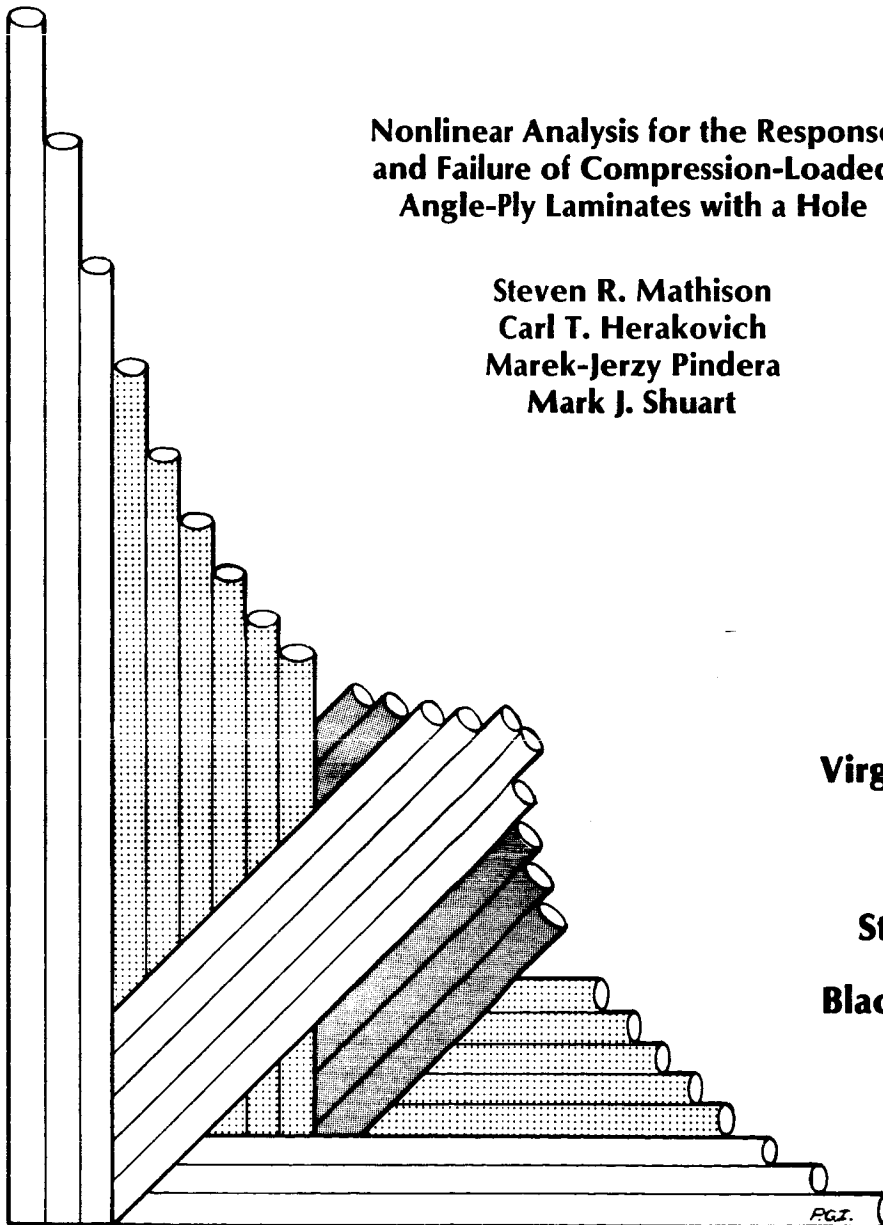
Virginia Polytechnic
Institute
and
State University

Blacksburg, Virginia
24061

College of Engineering
Virginia Polytechnic Institute and State University
Blacksburg, Virginia 24061

July 1987

CCMS-87-12
VPI-E-87-14

Nonlinear Analysis for the Response

and Failure of Compression-Loaded

Angle-Ply Laminates with a Hole

Steven R. Mathison[1]
Carl T. Herakovich[2]
Marek-Jerzy Pindera[3]
Mark J. Shuart[4]

Department of Engineering Science & Mechanics

Prepared for:

Structural Mechanics Branch
National Aeronautics and Space Administration
Langley Research Center
Hampton, VA 23665

---

[1] Graduate Student, Department of Engineering Science & Mechanics

[2] Professor, Department of Engineering Science & Mechanics

[3] Assistant Professor, Department of Engineering Science & Mechanics

[4] NASA Langley Research Center, Structural Mechanics Branch

NONLINEAR ANALYSIS FOR THE RESPONSE
AND FAILURE OF COMPRESSION-LOADED
ANGLE-PLY LAMINATES WITH A HOLE

by

Steven Richard Mathison

Committee Chairman: Carl T. Herakovich
Engineering Science and Mechanics

(ABSTRACT)

The objective of this study was to determine the effect of nonlinear material behavior on the response and failure of unnotched and notched angle-ply laminates under uniaxial compressive loading. The endochronic theory was chosen as the constitutive theory to model the AS4/3502 graphite-epoxy material system.

Three-dimensional finite element analysis incorporating the endochronic theory was used to determine the stresses and strains in the laminates. An incremental/iterative initial strain algorithm was used in the finite element program. To increase computational efficiency, a 180° rotational symmetry relationship was utilized and the finite element program was vectorized to run on a super computer.

Laminate response was compared to experiment revealing excellent agreement for both the unnotched and notched angle-ply laminates. Predicted stresses in the region of the hole were examined and are presented, comparing linear elastic analysis to the inelastic endochronic theory analysis.

A failure analysis of the unnotched and notched laminates was performed using the quadratic tensor polynomial. Predicted fracture loads compared well with experiment for the unnotched laminates, but were very conservative in comparison with experiments for the notched laminates.

Acknowledgements

Table of Contents

Table of Contents   vii

List of Illustrations

List of Tables

1.0 Introduction and Literature Review

1.1 Introduction

Composite materials present increased flexibility to structural designers because laminates from these materials can be tailored to achieve desired stiffness, strength, and dimensional stability properties. A common class of laminates is the angle-ply laminate which consists of $\pm \varphi$ plies. These laminates often exhibit nonlinear material response under in-plane loading. The laminate with a hole is also common in many design applications. When loaded, such notched laminates have an inplane stress concentration at the hole boundary as well as significant interlaminar stresses at all free edges. Few researchers have studied the complex three-dimensional stress distribution in compression-loaded angle-ply laminates with a hole.

The angle-ply laminate is commonly used in advanced aircraft and aerospace designs because its stiffness can be varied over a wide range, dependent on the layup angle φ. Of course, in such design applications, cutouts are often a necessity. Therefore, it is important to know how cutouts affect the stiffness and strength of these laminates. Because composite material strength is lower under compression than in tension, most advanced designs are

compression loading critical. With these considerations, it is easy to see the importance of studying the response of notched angle-ply laminates under uniaxial compression loading.

The objective of the present study is to predict and investigate the three-dimensional stress distribution in compression loaded angle-ply laminates with a central hole. A three-dimensional endochronic constitutive theory for transversely isotropic composite materials is used to model the nonlinear material response. The endochronic theory and incremental/iterative constant stress and constant strain algorithms are incorporated in a finite element program to determine laminate stresses. Inversion symmetry is utilized to significantly reduce the computer storage requirements and execution time. Failure initiation and failure modes are predicted using the tensor polynomial and maximum stress failure criteria. The analytical results from this study are compared with existing experimental results.

1.2 Literature Review

This study involves a broad range of subject areas, among them the endochronic constitutive theory, three-dimensional finite element analysis incorporating the endochronic theory, material nonlinear laminate response, and notched laminate strength prediction. A thorough review of the above areas would be exhausting; therefore, only the most significant subject areas are covered. The following review encompasses material nonlinearity in composites, the endochronic constitutive theory, and finite element analysis with material nonlinearity. For a review on the stress analysis and strength predictions of laminated plates with holes, see Burns, Herakovich, and Williams [1].

1.2.1 Material Nonlinearity in Composites

The literature is rich with papers describing nonlinear constitutive models for isotropic materials. However, for composite materials, the constitutive theory must include anisotropic response. With this additional requirement of anisotropy, the choices of models are more limited. Because composites can be analyzed both on a microscopic scale (as a heterogeneous medium) and on a macroscopic scale (as a homogeneous anisotropic medium), composite material constitutive theories are divided into micro-theories and macro-theories.

1.2.1.1 Microscopic Theories

Microscopic constitutive theories use the elastic and inelastic mechanical properties of the fiber and matrix to formulate the anisotropic constitutive relations on a macroscopic level. Dvorak et al [2] and Aboudi [3] have made significant contributions to the development of microscopic constitutive theories. Many others have contributed as well. Aboudi [3] and Pindera and Herakovich [19] both give thorough reviews of the literature on microscopic constitutive theories for composites.

1.2.1.2 Macroscopic Theories

In contrast to the microscopic approach, macroscopic constitutive theories treat the lamina as a homogeneous anisotropic medium and do not consider the individual constituent properties. Many researchers have contributed to the development of macroscopic constitutive theories for composites. Only a limited number are included in this review. For a thorough review of the literature on macroscopic composite material constitutive theories, see Pindera and Herakovich [19].

One of the earlier works in the area of nonlinear constitutive theories for fibrous composites was that of Hahn and Tsai [4]. They used complementary elastic energy density to develop a material nonlinear stress-strain relationship for a two-dimensional lamina. The stress-strain relationship is linear in uniaxial loading in the longitudinal and transverse directions, but nonlinear in shear. They compared their theory with off-axis coupon tests and obtained satisfactory results for boron/epoxy Narmco 5505 and graphite/epoxy 4612 Morganite II.

Sandhu [5] developed an incremental constitutive theory using the tangential properties of the lamina. The strain-dependent tangential properties were used to express the strain increment in terms of the stress increments. Off-axis unidirectional and multi-directional laminate tests were performed to compare the theory to experiment.

Hashin, Rosen, and Bagchi [6] proposed a theory which modeled the nonlinear behavior of a lamina in shear and transverse directions. The longitudinal (fiber direction) stress is modeled as linear elastic and does not affect the shear and transverse strains. The theory includes interaction between the transverse and shear stresses in the nonlinear range.

An interesting approach was taken by Dvorak et al [7] to develop a continuum theory for the elastic-plastic response of fibrous composites. They used a microscopic scale finite element analysis on materials such as boron-aluminum to develop the theory. The theory agreed well with numerical analysis for a variety of loading programs.

1.2.2 Endochronic Theory

The endochronic theory has most often been applied to isotropic materials. Although the endochronic equations were not originally derived to model anisotropic response, the theory is of a general nature, allowing it to model many material types. Recently, the theory has been extended to anisotropic materials.

1.2.2.1 Isotropic Materials

Although there is some disagreement as to when and with whom the theoretical foundations for the endochronic theory were developed, Valanis [11] [12] is credited with one of the earliest published works of the endochronic theory. He used the concepts of irreversible thermodynamics along with experimentally observed material behavior to develop a mathematical theory of thermo-viscoplasticity. The term "endochronic theory" encompasses all those theories in which "the state of stress at the present time is a function of the history of strain with respect to a time scale, which is not the absolute time scale measured by a clock, but a time scale which in itself is a property of the material at hand" [11].

In a series of papers, Valanis [13] - [18] and Valanis and Lee [17] extended the endochronic theory to model increasingly complex phenomena. They compared various theoretical studies with experimental results and found good agreement in most instances. Through these papers, they brought to light the numerous applications which could be accurately modeled with the endochronic theory.

1.2.2.2 Anisotropic Materials

Only two previous distinct research efforts have directed attention towards the development and application of the endochronic theory to fibrous composites. They are the works of Pindera and Herakovich [19] [20] and Zinov'ev and Sarbaev [21]. Pindera and Herakovich [19] [20] extended Valanis' endochronic theory to anisotropic materials and then used this theory to model the nonlinear response of unidirectional Celion 6000 graphite-polyimide. They derived a set of two-dimensional constitutive equations and used them to model various planar loading cases, including cyclic loading. Their results compared quite well with experimental results.

Zinov'ev and Sarbaev [21] recently used the endochronic theory to model composite laminate behavior. They used classical lamination theory in combination with endochronic equations to develop a material nonlinear laminate analysis code. They found good correlation with experiment for a variety of laminates subjected to in-plane loading.

1.2.3   Finite Element Analysis with Material Nonlinearity

Prior to the finite element method, stress analysis in the presence of inelastic material behavior was a very intractable problem. Many approximate methods were developed to give engineers useful answers; however, the accuracy of these approximate methods left much to be desired. The advent of the finite element method and the digital computer provided engineers with the capability to obtain accurate solutions to complicated, nonlinear material problems.

Inelastic numerical analysis has its roots in the simultaneous development of both the initial strain method [24] and the direct stiffness method [23]. In the initial strain method, the elastic equations of equilibrium are modified to include the inelastic strains which cause no change in stress. The marriage of the initial strain method to the finite element method was initiated by Gallagher and his Co-workers [25][26]. They used the initial strains to calculate an initial force vector (sometimes referred to as a psuedo force vector) which was added to the finite element force vector.

In the direct stiffness method, sometimes called the tangent modulus method, the nonlinear problem is divided into a series of piecewise linear problems by stepping through the solution and modifying the stiffness at each step. The finite element tangent modulus equations were developed by Pope [27], Swedlow and Yang [28], and Marcal and King [29].

Most present day inelastic solution techniques are based on one of these two methods. However, the efficiency, accuracy, and complexity of the present day techniques have all increased substantially. Inelastic analysis, geometric nonlinear analysis, and the combination of the two are now routinely performed using these present day techniques.

1.2.3.1 Endochronic Theory Applications

The first application of the endochronic theory of plasticity in a finite element analysis was that of Valanis and Fan [30]. They used the initial strain method formulation in parallel with an incremental/iterative solution technique to calculate the stress and elastoplastic strain fields in a copper plate containing two symmetrically disposed edge notches. The plate was loaded cyclically in its own plane along its outer edges. Theoretical results were presented, but experimental comparison was not provided.

Watanabe and Atluri [31] used a different form of the endochronic theory, completely analogous to classical plasticity theory, in a finite element analysis to compare and contrast the results of Valanis and Fan [30]. The structure of the new endochronic equations allowed the use of the tangent stiffness method as opposed to the initial strain method used by Valanis and Fan. Again, theoretical results were not compared with experiment.

1.2.3.2 Composite Material Applications

Applications of the finite element method to the analysis of composite material structures exhibiting inelastic behavior have been quite sparce. Adams and Miller [32], Adams [33], and Foye [34] used the finite element method to analyze unidirectional fiber-reinforced composites modelled on the microscale. Their models envisioned arrays of elastic fibers embedded in an elastic-plastic matrix material. Such microscopic analyses can provide an understanding of

the inelastic behavior of unidirectional laminae; however, it cannot be extended efficiently to multidirectional laminates.

Renieri and Herakovich [35] and Nagarkar and Herakovich [36] used a Ramberg-Osgood constitutive model in a quasi-three dimensional finite element analysis of interlaminar stresses in finite width laminates. Cross-ply, angle-ply, and two quasi-isotropic graphite/epoxy laminates were studied. Griffin, Kamat, and Herakovich [37] used a Hill-type yield criterion and an incremental plasticity approach in a fully three-dimensional finite element analysis of notched composite laminates. Material nonlinear isotropic hardening was modelled using the Ramberg-Osgood model and the constitutive equations were assumed temperature dependent. The incremental solution was performed with nonlinearities introduced as psuedo loads computed from initial strains.

Using a previously developed elastic-plastic constitutive theory for composites [38 - 40], Bahei-El-Din, Dvorak, and Utka [41] performed a finite element analysis of Boron/Aluminum plates of various layups with and without cutouts. Their analysis shows good agreement with experiment for uniaxial loading. Several other researchers also have recently applied various constitutive theories to inelastic finite element analysis of fibrous composites [42 - 44].

2.0 The Endochronic Theory

2.1 Introduction

As noted in the literature review, macro-level nonlinear constitutive theories modeling the response of fibrous composite materials are limited in number and validity. The few theories available were considered, and due to its firm thermodynamic foundation and demonstrated correlation with experimental results, the endochronic theory [20] was chosen for this study. Pindera and Herakovich [20] have shown their anisotropic endochronic theory to model lamina response very well for in-plane loading. This study extends the anisotropic equations to three dimensions in order to analyze laminates with three-dimensional stress states.

Valanis [11] [12] originally developed the endochronic theory to explain certain responses exhibited by ductile metals in the nonlinear range. Effects such as cross-hardening in tension due to torsion as well as the formation of hysteresis loops in loading/unloading cycles, not easily or accurately explained by classical plasticity theories, were accurately predicted by Valanis for certain metals. The theory, based on irreversible thermodynamics, was developed using

the concept of internal variables. As previously mentioned, the theory is centered around a deformation scale which is assumed to be a material property.

The deformation scale (also referred to as the time scale) can be either time dependent or time independent. In this study, the deformation scale is assumed to be time independent. Also, the deformation scale may be a function of stress or strain. This study uses a stress based scale (ala Pindera and Herakovich) to make the determination of endochronic constants more direct. This will become more evident later in this chapter. A primary feature of Pindera and Herakovich's development is the use of a multiple set of internal variables, which reduce the strain functions to power law approximations. Whereas metals are linear up to a yield point, facilitating a single internal variable approximation, epoxy resin composites generally show a gradual softening, with no well defined yield point. Multi-internal variables provide such behavior.

Whereas Pindera and Herakovich used a single time scale z which is a function of all the stress components, Zinov'ev and Sarbaev[21] used multiple, separate time scales z_i ($i = 1,2,3$) which were functions of σ_1, σ_2, and τ_{12}, respectively. Valanis[18] similarly used the hypothesis of the existence of two types of intrinsic time for isotropic materials: the "hydrostatic" and the "deviator" types. This made it possible for Valanis to distinguish two deformation mechanisms in the inelastic range: the volumetric and the shear mechanisms, each characterized by its own intrinsic time scale. The use of multiple time scales allows for a more detailed material model and can, theoretically, yield more accurate analysis, at the cost of added complexity. The single time scale used by Pindera and Herakovich yielded good correlation with experiment for laminae, thus the added complexity of multiple time scales was felt to be unnecessary for the present study.

2.2 Development of 3-D Endochronic Equations

The endochronic equations are based on two fundamental laws of thermodynamics governing an irreversible process: 1) Conservation of Energy, and 2) The Dissipation (Clausius-Duhem) Inequality. From this base, Pindera and Herakovich [19] rigorously developed the equations for strain in terms of stress, a deformation scale z, and material constants.

In the equations that follow, all stresses and strains are expressed in reduced notation as is standard in the composites literature,

$$
\begin{bmatrix} \varepsilon_1 \\ \varepsilon_2 \\ \varepsilon_3 \\ \varepsilon_4 \\ \varepsilon_5 \\ \varepsilon_6 \end{bmatrix} = \begin{bmatrix} \varepsilon_{11} \\ \varepsilon_{22} \\ \varepsilon_{33} \\ \gamma_{23} \\ \gamma_{13} \\ \gamma_{12} \end{bmatrix} \quad \text{and} \quad \begin{bmatrix} \sigma_1 \\ \sigma_2 \\ \sigma_3 \\ \sigma_4 \\ \sigma_5 \\ \sigma_6 \end{bmatrix} = \begin{bmatrix} \sigma_{11} \\ \sigma_{22} \\ \sigma_{33} \\ \tau_{23} \\ \tau_{13} \\ \tau_{12} \end{bmatrix} \tag{2.1}
$$

where the 1-2-3 coordinate system corresponds to the material principal coordinates with the 1-direction corresponding to the fiber direction (Figure 1).

The reader is referred to Pindera and Herakovich's work [19] [20] for a detailed thermodynamic derivation of the equations that follow. In the following equation set (2.2), the equations for normal strain $(\varepsilon_i, i=1,2,3)$ are obtained from a small modification of those developed in equation set (2.30) of Pindera and Herakovich's work [19]. The equations for shear strain $(\varepsilon_i, i=4,5,6)$ are identical to those shown in equation set (2.16) of Pindera and Herakovich.

Pindera and Herakovich appropriately modelled the fiber direction response as a stiffening response because σ_1 was always positive in their experiments. Because the laminates ana-
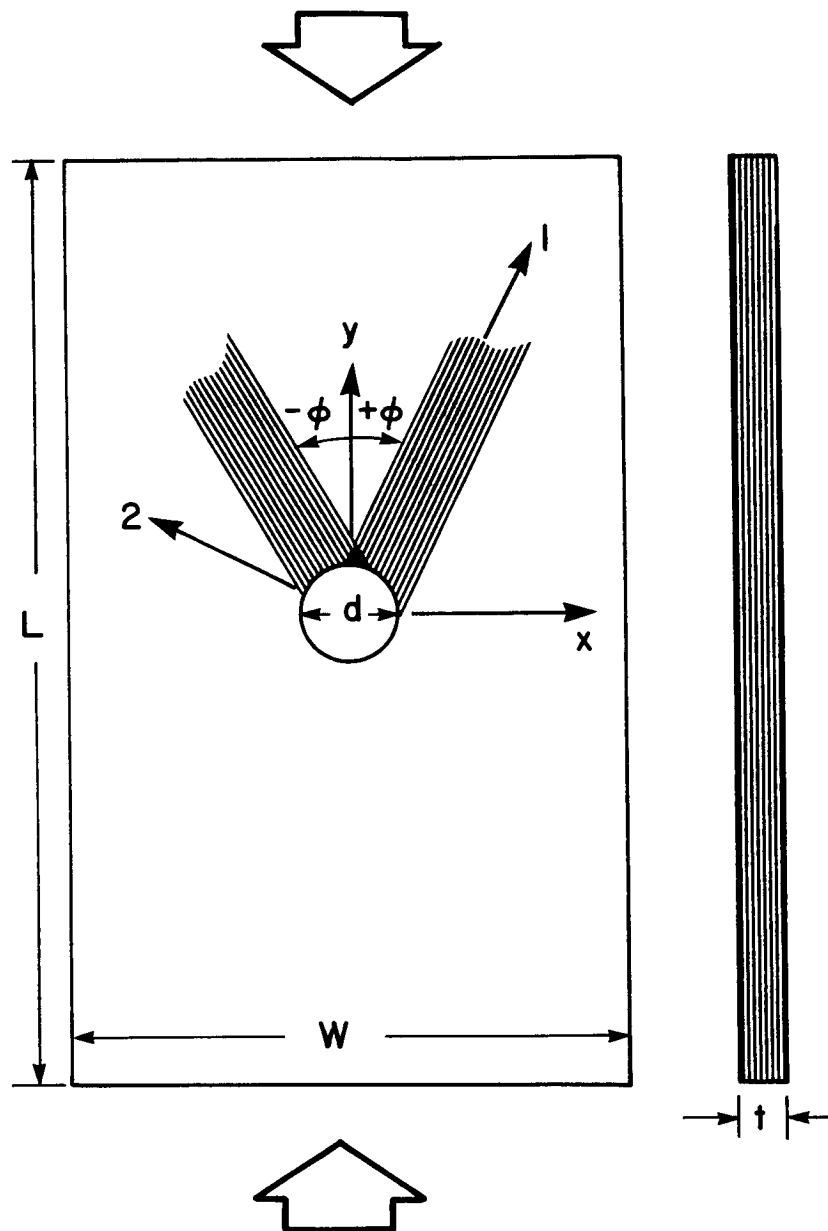
Figure 1. Nomenclature for Compression Loaded Laminate

lyzed in this study are loaded in compression, the normal stress (σ_1) in the fiber direction is generally compressive. Therefore, rather than a stiffening response in the fiber direction, this study uses the softening response which is exhibited by compression $\sigma_1 - \varepsilon_1$ experiments. This softening behavior is assumed to be uncoupled from the other stress components and is accounted for in the expression for ε_1 by a new function $\bar{f}(\sigma_1)$. The form of this function is defined later in this chapter. Notice also that the expressions for the nonlinear portions of ε_2 and ε_3 (the integral quantities) in (2.2) are independent of σ_1. Equation set (2.2) is the complete set of three-dimensional equations needed for this study.

As shown by Pindera and Herakovich, the anisotropic endochronic equations can be expressed in the following form, where the term $\bar{f}(\sigma_1)$ has been added to account for the softening as explained previously. For a single internal variable q_i (see Pindera and Herakovich [19] for details on the internal variables q_i),

$$\varepsilon_1 = \frac{-\partial G_0}{\partial \sigma_1} + \bar{f}(\sigma_1)$$

$$\varepsilon_2 = \frac{-\partial G_0}{\partial \sigma_2} + \int_0^z \bar{B}_{22}(z - z')\sigma_2(z')dz' + \int_0^z \bar{B}_{23}(z - z')\sigma_3(z')dz'$$

$$\varepsilon_3 = \frac{-\partial G_0}{\partial \sigma_3} + \int_0^z \bar{B}_{22}(z - z')\sigma_3(z')dz' + \int_0^z \bar{B}_{23}(z - z')\sigma_2(z')dz'$$

$$\varepsilon_4 = \frac{-\partial G_0}{\partial \sigma_4} + \int_0^z E \cdot \sigma_4(z')e^{-\lambda_4(z - z')}dz' \qquad (2.2)$$

$$\varepsilon_5 = \frac{-\partial G_0}{\partial \sigma_5} + \int_0^z F \cdot \sigma_5(z')e^{-\lambda_5(z - z')}dz'$$

$$\varepsilon_6 = \frac{-\partial G_0}{\partial \sigma_6} + \int_0^z F \cdot \sigma_6(z')e^{-\lambda_6(z - z')}dz'$$

where

$$\overline{B}_{22}(z - z') = E \cdot e^{-\lambda_3(z-z')} + \frac{D^2}{B} \cdot e^{-\lambda_2(z-z')}$$

$$\overline{B}_{23}(z - z') = -E \cdot e^{-\lambda_3(z-z')} + \frac{D^2}{B} \cdot e^{-\lambda_2(z-z')}$$

$$E = \frac{(B_{22} - B_{23})^2}{2(b_{22} - b_{23})}$$

$$F = \frac{B_{66}^2}{b_{66}}$$

$$D = \frac{1}{\gamma}\{[2B_{12}b_{11} - 2B_{11}b_{12}] - [B_{11}(b_{22} + b_{23}) - 2B_{12}b_{12}]\alpha_1\} \cdot [B_{12}\alpha_2 + \frac{1}{2}(B_{22} + B_{23})]$$

$$\gamma = \frac{1}{(1 - \alpha_1\alpha_2)[b_{11}(b_{22} + b_{23}) - 2b_{12}^2]}$$

$$\lambda_4 = \frac{C_{22} - C_{23}}{b_{22} - b_{23}}$$

$$\lambda_5 = \lambda_6 = \frac{C_{66}}{b_{66}}$$

$z' \equiv$ Integration Variable

$\lambda_1, \lambda_2 \equiv$ Eigenvalues of equation (2.23) in [19]

$\alpha_1, \alpha_2 \equiv$ Normalized eigenvalues, equation (2.26) in [19]

In the above, $dz = \sqrt{S_{ij}d\sigma_i d\sigma_j}$ where the terms of the fourth order, positive-definite tensor S_{ij} are material parameters. Likewise, b_{ij}, B_{ij}, and C_{ij} are all positive-definite fourth order tensors whose terms are material parameters. The λ_i terms are referred to as hardening exponents which reflect different dissipation modes. G_o is a potential function defined as a stable equilibrium state, in directly measurable quantities (i.e. no internal variables). Extending

equations (2.2) to multiple internal variables requires a new definition for the $\overline{B}_{ij}(z)$ terms in (2.2) and a new form of the expressions for ε_4, ε_5, and ε_6.

The new expressions for ε_4, ε_5, and ε_6 with multiple internal variables q_i^α ($\alpha = 1$ to M) [19] are:

$$\varepsilon_4 = \frac{-\partial G_0}{\partial \sigma_4} + \int_0^z \overline{B}_{44}(z - z')\sigma_4(z')dz'$$

$$\varepsilon_5 = \frac{-\partial G_0}{\partial \sigma_5} + \int_0^z \overline{B}_{66}(z - z')\sigma_5(z')dz' \qquad (2.3)$$

$$\varepsilon_6 = \frac{-\partial G_0}{\partial \sigma_6} + \int_0^z \overline{B}_{66}(z - z')\sigma_6(z')dz'$$

where all $\overline{B}_{ij}(z)$ in (2.2) and (2.3) are now given as:

$$\overline{B}_{22}(z) = \frac{1}{2} \sum_{\alpha=1}^{M} \left[\frac{(B_{22}^\alpha + B_{23}^\alpha)^2}{(b_{22}^\alpha - b_{23}^\alpha)}e^{-\lambda_2^\alpha(z)} + \frac{(B_{22}^\alpha - B_{23}^\alpha)^2}{(b_{22}^\alpha - b_{23}^\alpha)}e^{-\lambda_3^\alpha(z)} \right]$$

$$\overline{B}_{23}(z) = \frac{1}{2} \sum_{\alpha=1}^{M} \left[\frac{(B_{22}^\alpha + B_{23}^\alpha)^2}{(b_{22}^\alpha - b_{23}^\alpha)}e^{-\lambda_2^\alpha(z)} - \frac{(B_{22}^\alpha - B_{23}^\alpha)^2}{(b_{22}^\alpha - b_{23}^\alpha)}e^{-\lambda_3^\alpha(z)} \right]$$

$$\overline{B}_{44}(z) = \frac{1}{2} \sum_{\alpha=1}^{M} \frac{(B_{22}^\alpha - B_{23}^\alpha)^2}{(b_{22}^\alpha - b_{23}^\alpha)}e^{-\lambda_4^\alpha(z)}$$

$$\overline{B}_{66}(z) = \frac{1}{2} \sum_{\alpha=1}^{M} \frac{B_{66}^\alpha}{b_{66}^\alpha}e^{-\lambda_6^\alpha(z)}$$

$$\lambda_2^\alpha = \frac{C_{22}^\alpha + C_{23}^\alpha}{b_{22}^\alpha + b_{23}^\alpha}$$

$$\lambda_3^\alpha = \lambda_4^\alpha = \frac{C_{22}^\alpha - C_{23}^\alpha}{b_{22}^\alpha - b_{23}^\alpha}$$

$$\lambda_6^\alpha = \frac{C_{66}^\alpha}{b_{66}^\alpha}$$

and

$$M \equiv \text{number of internal variables}$$

The expressions for ε_2 and ε_3 show the response in the direction transverse to the fibers to be governed by two independent sets of hardening exponents, λ_2^g and λ_3^g. Because $\lambda_4^g = \lambda_3^g$, coupling exists between transverse normal and shear response in the plane of isotropy. Assuming the hardening response is similar in shear and transverse tension in the plane of isotropy yields $b_{23}^\alpha = B_{23}^\alpha = C_{23}^\alpha = 0$. This simplifies the expressions for the $\overline{B}_{ij}$ parameters.

$$\lambda_2^\alpha = \lambda_3^\alpha = \lambda_4^\alpha = \frac{C_{22}^\alpha}{b_{22}^\alpha}$$

$$\overline{B}_{22}(z) = \sum_{\alpha=1}^{M} \frac{(B_{22}^\alpha)^2}{b_{22}^\alpha} e^{-\lambda_2^\alpha(z)}$$

$$\overline{B}_{23}(z) = 0 \tag{2.4}$$

$$\overline{B}_{44}(z) = \frac{1}{2}\overline{B}_{22}(z)$$

$$\overline{B}_{66}(z) = \sum_{\alpha=1}^{M} \frac{(B_{66}^\alpha)^2}{b_{66}^\alpha} e^{-\lambda_6^\alpha(z)}$$

This greatly simplifies equation set (2.2) to:

$$\varepsilon_1 = \frac{-\partial G_0}{\partial \sigma_1} + \overline{f}(\sigma_1)$$

$$\varepsilon_2 = \frac{-\partial G_0}{\partial \sigma_2} + \int_0^z \overline{B}_{22}(z - z')\sigma_2(z')dz'$$

$$\varepsilon_3 = \frac{-\partial G_0}{\partial \sigma_3} + \int_0^z \overline{B}_{22}(z - z')\sigma_3(z')dz'$$

$$\varepsilon_4 = \frac{-\partial G_0}{\partial \sigma_4} + \frac{1}{2}\int_0^z \overline{B}_{22}(z - z')\sigma_4(z')dz' \qquad (2.5)$$

$$\varepsilon_5 = \frac{-\partial G_0}{\partial \sigma_5} + \int_0^z \overline{B}_{66}(z - z')\sigma_5(z')dz'$$

$$\varepsilon_6 = \frac{-\partial G_0}{\partial \sigma_6} + \int_0^z \overline{B}_{66}(z - z')\sigma_6(z')dz'$$

To obtain a power-law approximation for equations (2.5) , it is necessary to integrate the equations by parts. This is done for the expression ε_6 below:

$$\varepsilon_6 = \frac{-\partial G_0}{\partial \sigma_6} + \int_0^z \sum_{\alpha=1}^{M} \frac{(B_{66}^\alpha)^2}{b_{66}^\alpha} e^{-\lambda_6^\alpha(z - z')}\sigma_6(z')dz'$$

$$\varepsilon_6 = \frac{-\partial G_0}{\partial \sigma_6} + \int_0^z UdV \qquad (2.6)$$

where

$$U = \sigma_6(z')$$

$$dV = \sum_{\alpha=1}^{M} \frac{(B_{66}^\alpha)^2}{b_{66}^\alpha} e^{-\lambda_6^\alpha(z - z')}dz'$$

$$dU = \frac{\partial \sigma_6(z')}{\partial z'}dz'$$

$$V = \sum_{\alpha=1}^{M} \frac{1}{\lambda_6^\alpha} \frac{(B_{66}^\alpha)^2}{b_{66}^\alpha} e^{-\lambda_6^\alpha(z-z')}$$

Recalling that,

$$\int_0^z U dV = UV\Big|_0^z - \int_0^z V dU$$

we have

$$\varepsilon_6 = \frac{-\partial G_0}{\partial \sigma_6} + \sum_{\alpha=1}^{M} \frac{1}{\lambda_6^\alpha} \frac{(B_{66}^\alpha)^2}{b_{66}^\alpha} e^{-\lambda_6^\alpha(z-z')} \sigma_6(z') \Big|_0^z - \int_0^z \sum_{\alpha=1}^{M} \frac{1}{\lambda_6^\alpha} \frac{(B_{66}^\alpha)^2}{b_{66}^\alpha} e^{-\lambda_6^\alpha(z-z')} \frac{\partial \sigma_6(z')}{\partial z'} dz'$$

$$= \frac{-\partial G_0}{\partial \sigma_6} + \sum_{\alpha=1}^{M} \frac{1}{\lambda_6^\alpha} \frac{(B_{66}^\alpha)^2}{b_{66}^\alpha} \left[\sigma_6(z) - \sigma_6(0) e^{-\lambda_6^\alpha(z)} \right] -$$

$$\int_0^z \sum_{\alpha=1}^{M} \frac{1}{\lambda_6^\alpha} \frac{(B_{66}^\alpha)^2}{b_{66}^\alpha} e^{-\lambda_6^\alpha(z-z')} \frac{\partial \sigma_6(z')}{\partial z'} dz'$$

However,

$$\sum_{\alpha=1}^{M} \frac{1}{\lambda_6^\alpha} \frac{(B_{66}^\alpha)^2}{b_{66}^\alpha} \left[\sigma_6(z) - \sigma_6(0) \right] \equiv \int_0^z \sum_{\alpha=1}^{M} \frac{1}{\lambda_6^\alpha} \frac{(B_{66}^\alpha)^2}{b_{66}^\alpha} \frac{\partial \sigma_6(z')}{\partial z'} dz'$$

therefore,

$$\varepsilon_6 = \frac{-\partial G_0}{\partial \sigma_6} + \sigma_6(0) \sum_{\alpha=1}^{M} \frac{1}{\lambda_6^\alpha} \frac{(B_{66}^\alpha)^2}{b_{66}^\alpha} (1 - e^{-\lambda_6^\alpha(z)}) + \tag{2.7}$$

$$\int_0^z \sum_{\alpha=1}^{M} \frac{1}{\lambda_6^\alpha} \frac{(B_{66}^\alpha)^2}{b_{66}^\alpha} (1 - e^{-\lambda_6^\alpha(z-z')}) \frac{\partial \sigma_6(z')}{\partial z'} dz'$$

Equation (2.7) corresponds to equation (5.17) in Pindera and Herakovich [19].

Similar expressions hold for the remaining principle strains. Assuming a large number of internal variables (M) represent the material response, a power law approximation may be introduced as follows:

$$\sum_{\alpha=1}^{M} \frac{1}{\lambda_6^{\alpha}} \frac{(B_{66}^{\alpha})^2}{b_{66}^{\alpha}} (1 - e^{-\lambda_6^{\alpha} z}) \cong B_{66}^0 \cdot z^{n_6} \qquad \text{for } n_6 > 1 \qquad (2.8)$$

where

B_{66}^0 is an arbitrary constant whose subscripts relate it to $\overline{B}_{66}$

n_6 is a constant whose subscript relates it to $\overline{B}_{66}$

The deformation scale z requires that $\sigma_6(0) = \sigma_5(0) = \sigma_4(0) = \sigma_3(0) = \sigma_2(0) = 0$. Using the power law type expression (2.8) for all the strain components gives the following form of the endochronic equations:

$$\varepsilon_1 = \frac{-\partial G_0}{\partial \sigma_1} + \bar{f}(\sigma_1)$$

$$\varepsilon_2 = \frac{-\partial G_0}{\partial \sigma_2} + \int_0^z B_{22}^0 \cdot (z - z')^{n_2} \frac{\partial \sigma_2}{\partial z'} dz'$$

$$\varepsilon_3 = \frac{-\partial G_0}{\partial \sigma_3} + \int_0^z B_{22}^0 \cdot (z - z')^{n_2} \frac{\partial \sigma_3}{\partial z'} dz'$$

$$\varepsilon_4 = \frac{-\partial G_0}{\partial \sigma_4} + \frac{1}{2} \int_0^z B_{22}^0 \cdot (z - z')^{n_2} \frac{\partial \sigma_4}{\partial z'} dz' \qquad (2.9)$$

$$\varepsilon_5 = \frac{-\partial G_0}{\partial \sigma_5} + \int_0^z B_{66}^0 \cdot (z - z')^{n_6} \frac{\partial \sigma_5}{\partial z'} dz'$$

$$\varepsilon_6 = \frac{-\partial G_0}{\partial \sigma_6} + \int_0^z B_{66}^0 \cdot (z - z')^{n_6} \frac{\partial \sigma_6}{\partial z'} dz'$$

where

B_{22}^0 is an arbitrary constant whose subscripts relate it to $\overline{B}_{22}$

n_2 is a constant > 1 whose subscript relates it to $\overline{B}_{22}$

2.3 Incremental Form of Endochronic Equations

The equations developed in the preceding section are not suitable for use in a finite element program. This is because the strains are functions of complex integrals involving the deformation scale z . Calculation of the parameter z requires knowledge of the load history. For simple cases, such as tensile or compressive loading of a lamina, the stresses are proportional to one another and these proportions do not change with increasing load. This allows z to be expressed as a proportionality constant times the desired component of stress. As an example, consider uniaxial tensile loading of a lamina transverse to the fibers.

$$dz = \sqrt{S_{22}d\sigma_2 d\sigma_2} = \sqrt{S_{22}}\ d\sigma_2 \tag{2.10}$$

$$z = \sqrt{S_{22}}\ \sigma_2$$

Similar expressions may be developed for other lamina orientations under a uniaxial load. In fact, the endochronic constants are calculated using these uniaxial load cases. This is shown later in section 2.4.

In a laminate, the stresses need not be proportional to one another. Since the load history of the stress components is not known a priori, equations (2.8) may not be integrated exactly. However, equations (2.8) may be integrated incrementally by assuming the stress components to be proportional to one another over each load increment. This allows the stress

component load histories to be nonproportional in a piecewise sense. Consider the expression for ε_6:

$$\varepsilon_6 = \frac{-\partial G_0}{\partial \sigma_6} + \int_0^z B_{66}^0 \cdot (z - z')^{n_6} \frac{\partial \sigma_6}{\partial z'} dz'$$

Written incrementally, this becomes

$$\varepsilon_6^N = \frac{-\partial G_0}{\partial \sigma_6} + \int_0^{z_1} B_{66}^0 (z_N - z')^{n_6} S6_1 dz' + \int_0^{z_2} B_{66}^0 (z_N - z')^{n_6} S6_2 dz' +$$

$$\cdots\cdots + \int_0^{z_N} B_{66}^0 (z_N - z')^{n_6} S6_N dz'$$

or

$$\varepsilon_6^N = \frac{-\partial G_0}{\partial \sigma_6} + \frac{B_{66}^0}{(n_6 + 1)} \left\{ S6_1 \left[z_N^{n_6 + 1} - (z_N - z_1)^{n_6 + 1} \right] \right\} +$$

$$\frac{B_{66}^0}{(n_6 + 1)} \left\{ S6_2 \left[(z_N - z_1)^{n_6 + 1} - (z_N - z_2)^{n_6 + 1} \right] + \cdots + S6_N (z_N - z_{N-1})^{n_6 + 1} \right\}$$

$$\varepsilon_6^N = \frac{-\partial G_0}{\partial \sigma_6} + \frac{B_{66}^0}{(n_6 + 1)} \sum_{k=1}^N S6_k \left[(z_N - z_{k-1})^{n_6 + 1} - (z_N - z_k)^{n_6 + 1} \right] \qquad (2.11)$$

where

$$S6_k = \frac{\partial \sigma_6}{\partial z} \bigg|_k \cong \frac{\Delta \sigma_6}{\Delta z_k} \qquad k = 1,2,\ldots,N$$

$$z_N = \sum_{k=1}^N \Delta z_k$$

$$\Delta z_k = \sqrt{S_{ij} \Delta \sigma_i^k \Delta \sigma_j^k}$$

$$N \equiv \text{number of increments}$$

The integration accuracy is a function of the increment size. The smaller the increment, the more accurate the integration. In the limit, as Δz goes to zero, the integration becomes exact. For mildly non-proportional load histories, the error introduced by this process should not be great.

2.4   Determination of Endochronic Parameters

Determination of the endochronic constants requires analyzing many test results. Burns et al [1] performed all the laminate tests as well as the 10° and 45° off-axis tests and the uniaxial [0] and [90] compression tests. All Iosipescu tests as well as the 15° and 30° off-axis tests were performed by Jack Beuth[50] at VPI. Data from at least two and in some cases three tests were used in determining the constants for this study. The final value of a particular endochronic constant is the average of the values determined from all tests. Any exceptions to this procedure are noted. Appendix A shows the least squares method of representing a "best fit" line through the experimental data.

The endochronic equations may be written in terms of reversible strain (ε_i^R) and irreversible strain (ε_i^{IR}). The reversible strains are represented by derivatives of the potential function G_0 in equations (2.9), whereas the irreversible strains are represented by the integral quantities.

$$\varepsilon_i = \varepsilon_i^R + \varepsilon_i^{IR} \tag{2.12}$$

where

$$\varepsilon_i^R = \frac{-\partial G_0}{\partial \sigma_i} \quad i = 1,2,...,6$$

and

$$\varepsilon_1^{IR} = \bar{f}(\sigma_1)$$

$$\varepsilon_2^{IR} = \int_0^z B_{22}^0 \cdot (z - z')^{n_2} \frac{\partial \sigma_2}{\partial z'} dz'$$

$$\varepsilon_3^{IR} = \int_0^z B_{22}^0 \cdot (z - z')^{n_2} \frac{\partial \sigma_3}{\partial z'} dz'$$

$$\varepsilon_4^{IR} = \frac{1}{2} \int_0^z B_{22}^0 \cdot (z - z')^{n_2} \frac{\partial \sigma_4}{\partial z'} dz'$$

$$\varepsilon_5^{IR} = \int_0^z B_{66}^0 \cdot (z - z')^{n_6} \frac{\partial \sigma_5}{\partial z'} dz'$$

$$\varepsilon_6^{IR} = \int_0^z B_{66}^0 \cdot (z - z')^{n_6} \frac{\partial \sigma_6}{\partial z'} dz'$$

2.4.1 Reversible Response

The potential function G_0 has not been discussed in any detail to this point because its form is strongly material dependent and stress sign dependent. As noted earlier, Pindera and Herakovich used a function G_0 which modeled stiffening behavior in the fiber direction of C6000/PMR15 graphite-epoxy under uniaxial tension. AS4/3502 exhibits similar tensile behavior. However, because the laminates in this study are loaded in compression, the fibers are in compression except, possibly, in regions near the hole. A typical uniaxial compression test of AS4/3502 [1] exhibits softening as shown in Figure 2. This softening behavior is modeled in this study as an uncoupled event. Therefore, it is not represented by a function of z nor is it included in the potential function G_0, ala Pindera and Herakovich. Instead, it is expressed as a separate function $\bar{f}(\sigma_1)$ which is determined in the following section.

The function G_0 needs to model only reversible linear response and is defined as

$$-G_0 = \frac{1}{2}A_{ij}\sigma_i\sigma_j \tag{2.13}$$

Therefore,

$$\epsilon_i^R = \frac{-\partial G_0}{\partial \sigma_i} = A_{ij}\sigma_j \qquad i = 1,2,3,4,5,6 \tag{2.14}$$

A thermodynamic constraint on G_0 requires the fourth order tensor A_{ij} to be positive definite [19].

$$\lim_{\sigma_i \to \infty} \delta^2(-G_0) = A_{ij}\delta\sigma_i\delta\sigma_j \geq 0 \tag{2.15}$$

The fourth order tensor A_{ij} is the compliance matrix. It represents the initial compliance of the material and is determined from appropriate tests.

2.4.2 Response Along the Fiber Direction

The function $\bar{f}(\sigma_1)$ originally introduced in equation (2.2) is determined from a uniaxial compressive test (Figure 2) with the fibers aligned along the specimen's axis. A simple power law fits the experimental data very well; therefore, the functional form of $\bar{f}(\sigma_1)$ was chosen to be:

$$\bar{f}(\sigma_1) = \pm B_{11}|\sigma_1|^{n_1} \qquad \text{where} \quad n_1 > 1 \tag{2.16}$$

The absolute value sign is used because σ_1 is usually negative. The function $\bar{f}(\sigma_1)$ is negative if σ_1 is negative and positive if σ_1 is positive.
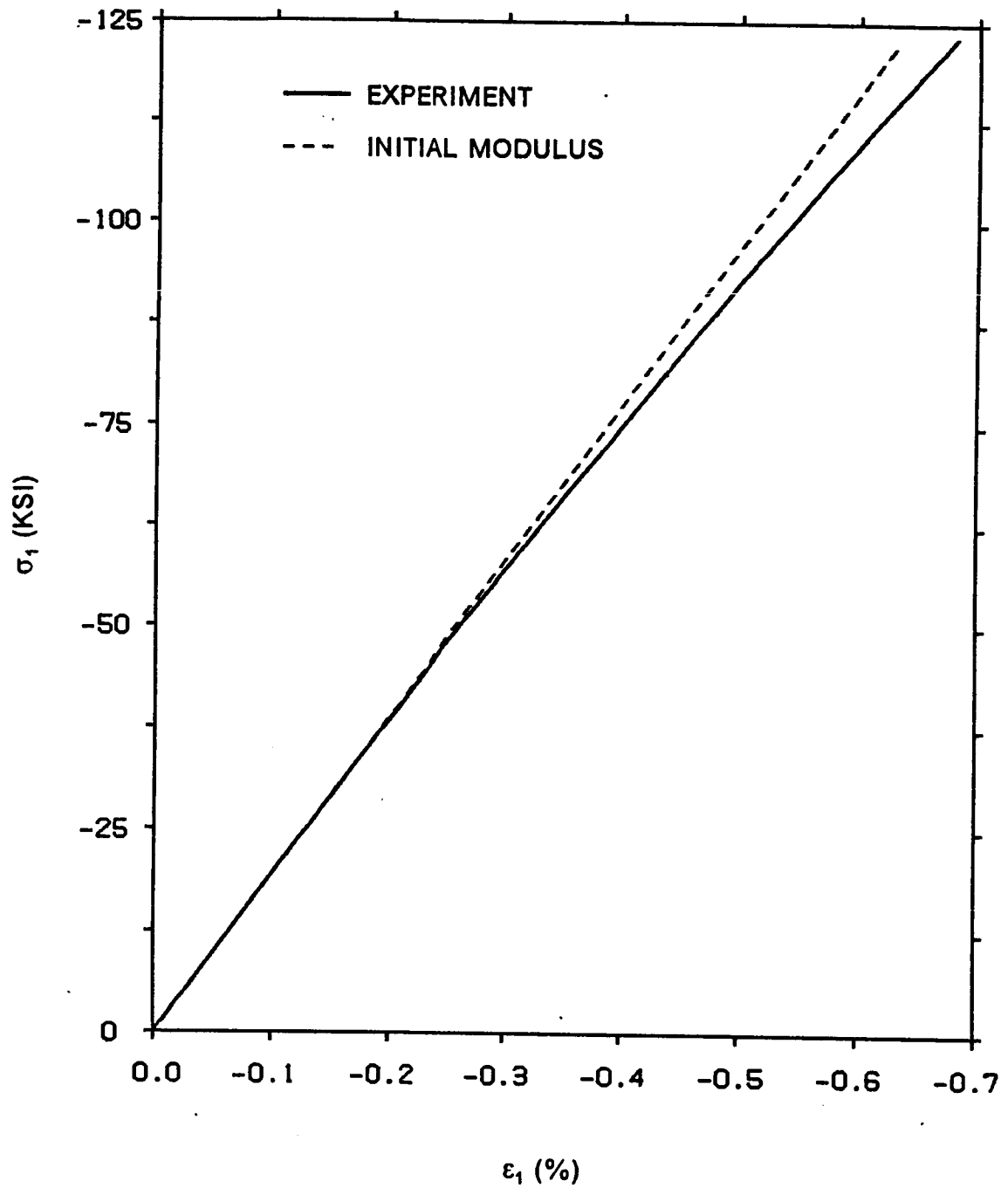
Figure 2. σ_1 Versus ε_1 for a Typical 0° Uniaxial Compression Test for AS4/3502

Substituting equations (2.13) and (2.16) into equation set (2.8), the complete form of the endochronic equations can be written as

$$\varepsilon_1 = A_{1j}\sigma_j \pm B_{11}|\sigma_1|^{n_1}$$

$$\varepsilon_2 = A_{2j}\sigma_j + \int_0^z B_{22}^0 \cdot (z - z')^{n_2}\frac{\partial\sigma_2(z')}{\partial z'}dz'$$

$$\varepsilon_3 = A_{3j}\sigma_j + \int_0^z B_{22}^0 \cdot (z - z')^{n_2}\frac{\partial\sigma_3(z')}{\partial z'}dz'$$

$$\varepsilon_4 = A_{4j}\sigma_j + \frac{1}{2}\int_0^z B_{22}^0 \cdot (z - z')^{n_2}\frac{\partial\sigma_4(z')}{\partial z'}dz' \qquad (2.17)$$

$$\varepsilon_5 = A_{5j}\sigma_j + \int_0^z B_{66}^0 \cdot (z - z')^{n_6}\frac{\partial\sigma_5(z')}{\partial z'}dz'$$

$$\varepsilon_6 = A_{6j}\sigma_j + \int_0^z B_{66}^0 \cdot (z - z')^{n_6}\frac{\partial\sigma_6(z')}{\partial z'}dz'$$

2.4.3 The Compliance Matrix

The reversible strain of the material is expressed in terms of stress and the compliance matrix A_{ij} as

$$\begin{bmatrix} \varepsilon_1^R \\ \varepsilon_2^R \\ \varepsilon_3^R \\ \varepsilon_4^R \\ \varepsilon_5^R \\ \varepsilon_6^R \end{bmatrix} = \begin{bmatrix} A_{11} & A_{12} & A_{13} & 0 & 0 & 0 \\ A_{12} & A_{22} & A_{23} & 0 & 0 & 0 \\ A_{13} & A_{23} & A_{33} & 0 & 0 & 0 \\ 0 & 0 & 0 & A_{44} & 0 & 0 \\ 0 & 0 & 0 & 0 & A_{55} & 0 \\ 0 & 0 & 0 & 0 & 0 & A_{66} \end{bmatrix} \begin{bmatrix} \sigma_1 \\ \sigma_2 \\ \sigma_3 \\ \sigma_4 \\ \sigma_5 \\ \sigma_6 \end{bmatrix} \qquad (2.18)$$

Under the assumption of transverse isotropy in the 2-3 plane, $A_{33} = A_{22}$, $A_{13} = A_{12}$, and $A_{55} = A_{66}$. This simplifies the above expression to

$$
\begin{bmatrix} \varepsilon_1^R \\ \varepsilon_2^R \\ \varepsilon_3^R \\ \varepsilon_4^R \\ \varepsilon_5^R \\ \varepsilon_6^R \end{bmatrix} = \begin{bmatrix} A_{11} & A_{12} & A_{12} & 0 & 0 & 0 \\ A_{12} & A_{22} & A_{23} & 0 & 0 & 0 \\ A_{12} & A_{23} & A_{22} & 0 & 0 & 0 \\ 0 & 0 & 0 & A_{44} & 0 & 0 \\ 0 & 0 & 0 & 0 & A_{66} & 0 \\ 0 & 0 & 0 & 0 & 0 & A_{66} \end{bmatrix} \begin{bmatrix} \sigma_1 \\ \sigma_2 \\ \sigma_3 \\ \sigma_4 \\ \sigma_5 \\ \sigma_6 \end{bmatrix}
\tag{2.19}
$$

Equation (2.19) contains only five independent constants (A_{11}, A_{12}, A_{22}, A_{44}, and A_{66}). The additional A_{23} constant is a function of A_{22} and A_{44} (i.e. $2(A_{22} - A_{23}) = A_{44}$).

2.4.3.1   The A_{11} Constant

The constant A_{11} is determined by considering the compressive loading case of $\sigma_1 \neq 0$ and all $\sigma_i = 0$, (i = 2,3,4,5,6). The reversible strain in the fiber direction is then

$$
\varepsilon_1^R = A_{11}\sigma_1
\tag{2.20}
$$

and

$$
\frac{\partial \varepsilon_1^R}{\partial \sigma_1} = A_{11}
$$

However, from (2.17)

$$
\frac{\partial \varepsilon_1^R}{\partial \sigma_1} = \frac{\partial \varepsilon_1}{\partial \sigma_1}\bigg|_{\sigma_1 = 0}
$$

The Endochronic Theory

Therefore,

$$A_{11} = \left.\frac{\partial \varepsilon_1}{\partial \sigma_1}\right|_{\sigma_1 = 0} \tag{2.21}$$

The data from two compression tests on unidirectional [0] AS4/3502 were essentially linear in the range of $\sigma_1 = 0$ to $\sigma_1 \cong 25$ ksi. A least squares fit through these points gave a straight line with a slope m (or E_1). A_{11} is the inverse of m (or E_1).

Averaging the values for A_{11} from both tests (Table B.1(a)) yields:

$$A_{11} = 5.12687 \times 10^{-8} \ (\text{psi}^{-1}) \tag{2.22}$$

2.4.3.2 The A_{12} Constant

Like A_{11}, the endochronic constant A_{12} is also calculated from a [0] uniaxial compression test. Consider the expression for ε_2^R as shown below:

$$\varepsilon_2^R = A_{12}\sigma_1 \quad \text{for} \quad \sigma_1 \neq 0 \quad \sigma_i = 0 \quad (i = 2,3,4,5,6) \tag{2.23}$$

Now

$$\frac{\partial \varepsilon_2^R}{\partial \varepsilon_1} = A_{12}\frac{\partial \sigma_1}{\partial \varepsilon_1}$$

and

$$\left.\frac{\partial \varepsilon_2^R}{\partial \varepsilon_1}\right|_{\sigma_1 = 0} = A_{12}\left.\frac{\partial \sigma_1}{\partial \varepsilon_1}\right|_{\sigma_1 = 0}$$

From (2.21)

$$\frac{\partial \sigma_1}{\partial \varepsilon_1}\bigg|_{\sigma_1=0} = \frac{1}{A_{11}}$$

and by definition

$$-\frac{\partial \varepsilon_2^R}{\partial \varepsilon_1}\bigg|_{\sigma_1=0} = \nu_{12}$$

Therefore,

$$A_{12} = -A_{11}\nu_{12} \tag{2.24}$$

In order to calculate A_{12}, ν_{12} must first be determined. This is done by fitting a least squares line through a plot of ε_2 versus ε_1 (Figure 3). The least squares fit is used in the range of data points from $\varepsilon_1 = 0$ to $\varepsilon_1 \cong 0.13\%$. The value of ν_{12} is the slope of this line.

Averaging the values of ν_{12} from both tests (Table B.1(b)) yields

$$\nu_{12} = 0.333 \tag{2.25}$$

Combining (2.22), (2.24), and (2.25) gives

$$A_{12} = -1.70722 \times 10^{-8} \ (\text{psi}^{-1}) \tag{2.26}$$

2.4.3.3 The A_{22} Constant

A 90° uniaxial compressive test is used to determine A_{22}. In this test, the fibers are oriented transverse to the loading axis. Because all σ_i (i = 1,3,4,5,6) are zero, the expression for ε_2^R is:

$$\varepsilon_2^R = A_{22}\sigma_2 \tag{2.27}$$
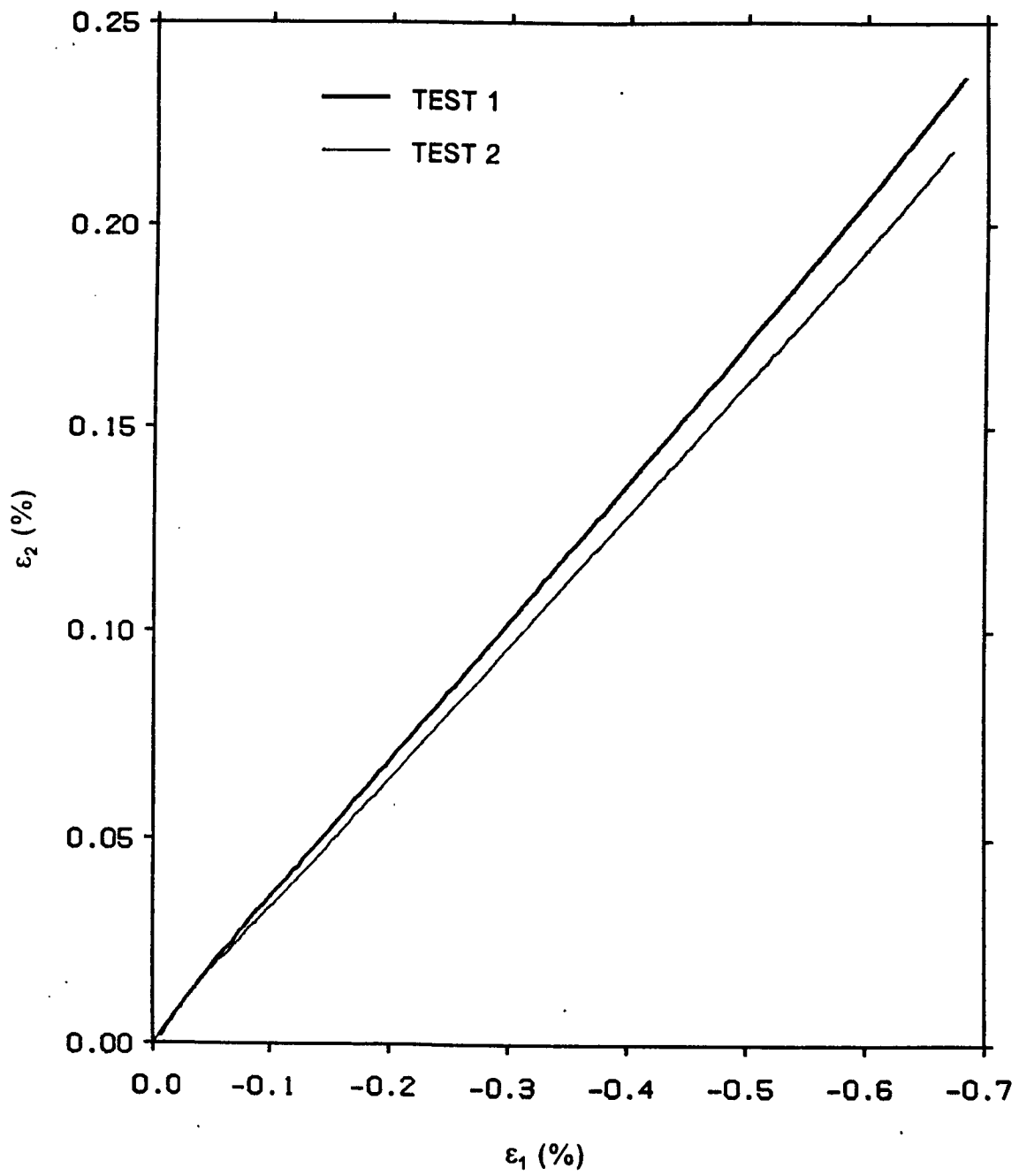
Figure 3. ε_2 Versus ε_1 for 0° Uniaxial Tests of AS4/3502

and

$$\frac{\partial \varepsilon_2^R}{\partial \sigma_2} = A_{22} = \frac{\partial \varepsilon_2}{\partial \sigma_2}\bigg|_{\sigma_2 = 0}$$

Utilizing the plots of σ_2 versus ε_2 shown in Figure 4, a least squares fit is used in the range of data points between $\sigma_2 = 0$ and $\sigma_2 \cong 8$ ksi. The endochronic constant A_{22} is the inverse of the slope of this line (modulus E_2).

Averaging the value of A_{22} from both test runs (Table B.1(c)) yields

$$A_{22} = 6.55133 \times 10^{-7} \ (psi^{-1}) \tag{2.28}$$

2.4.3.4   The A_{44} Constant

The endochronic constant A_{44} is determined from an Iosipescu shear test in the 2-3 plane. This type of test induces an approximately pure 2-3 shear stress σ_4 (τ_{23}) in the central region of the specimen[47]. Figure 5 shows the test specimen and idealized loading conditions used for this test. (The symbol θ in this figure is only valid for 1-2 plane tests. For 2-3 plane tests, the fibers run in the direction of page depth). Figure 6 shows plots of σ_4 (τ_{23}) versus ε_4 (γ_{23}) for two tests. The endochronic constant is determined by fitting a least squares line through the initial portion of the curve for the range of data points between $\sigma_4 = 0$ and $\sigma_4 \cong 6$ ksi. The constant A_{44} is the inverse of the slope of this line (modulus G_{23}).

Averaging the values of A_{44} from tests 1 and 2 (Table B.1(d)) yields

$$A_{44} = 2.18049 \times 10^{-6} \ (psi^{-1}) \tag{2.29}$$
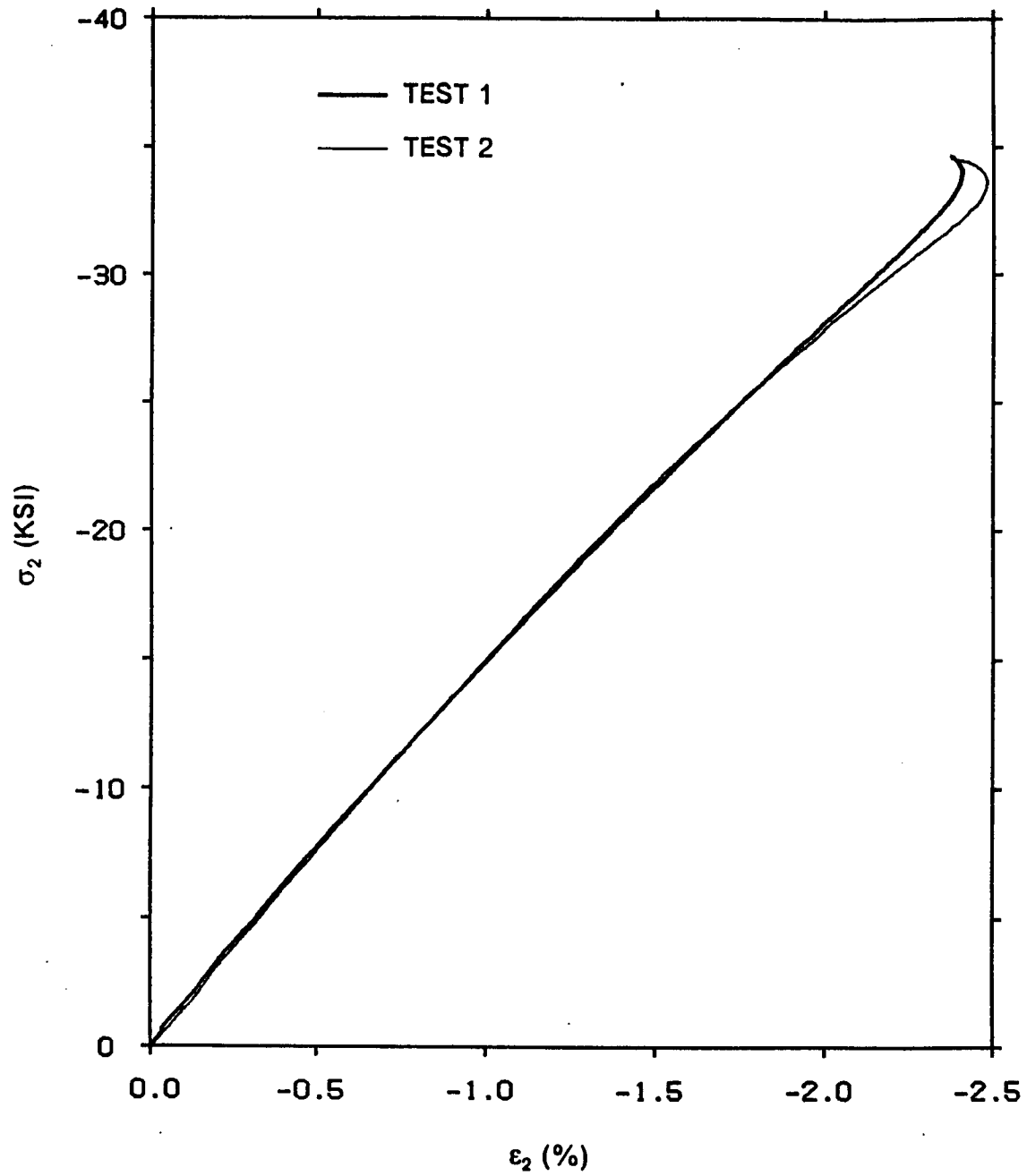
Figure 4. σ_2 Versus ε_2 for 90° Uniaxial Compression Tests of AS4/3502
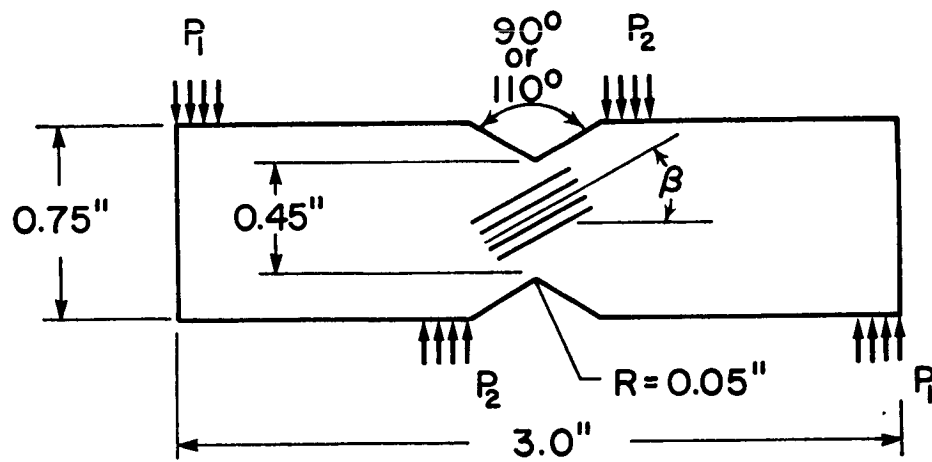
P_1, P_2 ≡ Distributed Forces

β ≡ Fiber Orientation Angle

Figure 5. Test Specimen and Loading Conditions Used for Iosipescu Tests
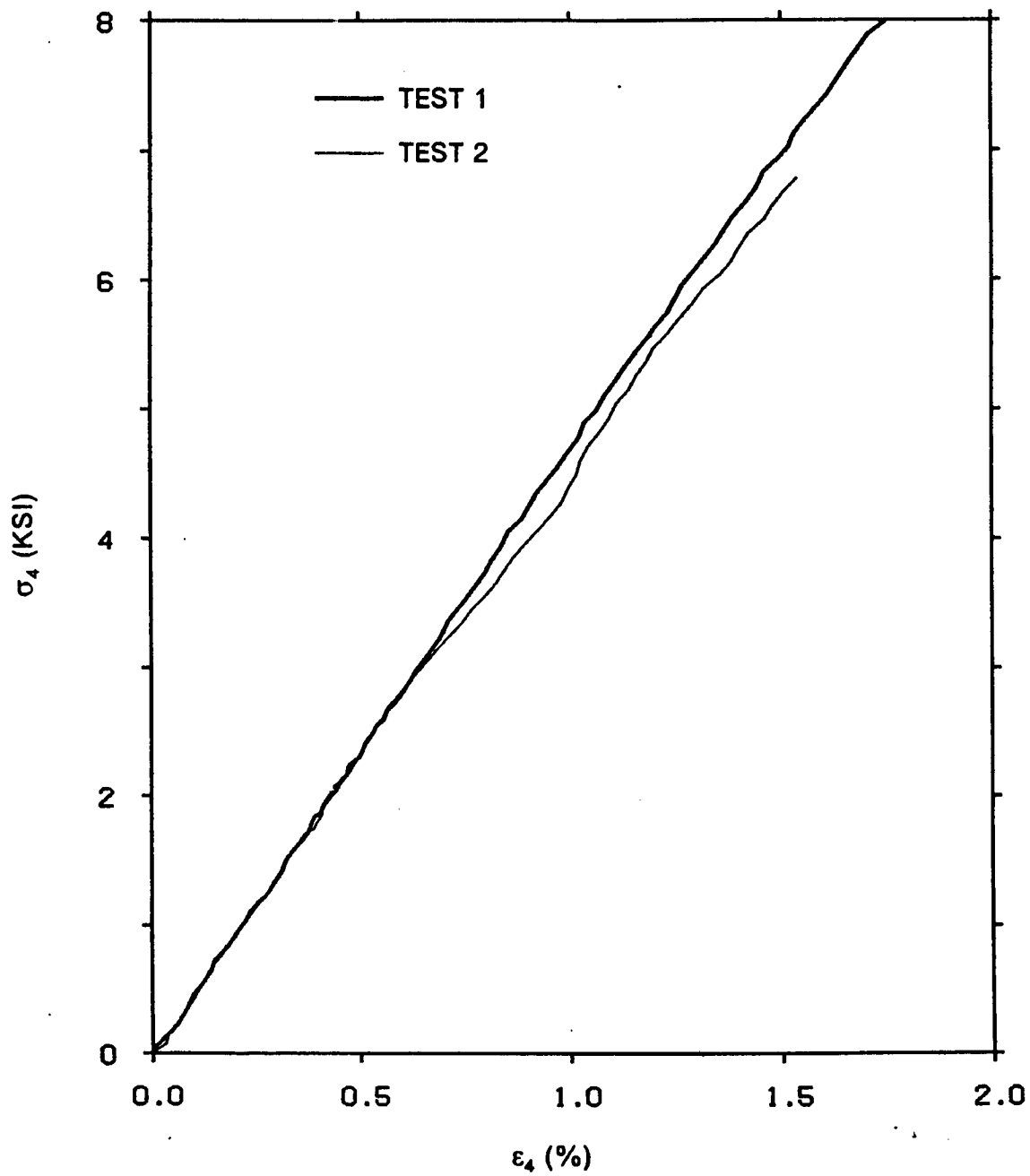
Figure 6. σ_4 Versus ε_4 for Iosipescu Tests in the 2-3 Plane of AS4/3502

2.4.3.5 The A_{23} Constant

Because a transversely isotropic material contains only five independent constants, A_{23} may be determined indirectly. Consider the following expression for the shear modulus G_{ij} (i, j = 1,2,3) in a plane of isotropic symmetry.

$$G_{ij} = \frac{E_i}{2(\nu_{ij} + 1)}$$

(2.30)

$$G_{23} = \frac{E_2}{2(\nu_{23} + 1)}$$

$$\frac{1}{G_{23}} = \frac{2(\nu_{23} + 1)}{E_2} = 2\left(\frac{\nu_{23}}{E_2} + \frac{1}{E_2}\right)$$

However, by definition,

$$A_{44} = \frac{1}{G_{23}}$$

$$A_{22} = \frac{1}{E_2}$$

$$A_{23} = \frac{-\nu_{23}}{E_2}$$

Therefore, as shown earlier,

$$A_{44} = 2(A_{22} - A_{23})$$

$$A_{23} = A_{22} - \frac{A_{44}}{2}$$

From the previously determined values of A_{22} and A_{44}, A_{23} is calculated to be

$$A_{23} = -4.35111 \times 10^{-7} \; (\text{psi}^{-1}) \tag{2.31}$$

2.4.3.6 The A_{66} Constant

The endochronic constant A_{66} is determined in an analogous manner to A_{44}. An Iosipescu shear test in the 1-2 plane yields a region of approximately pure σ_6 (τ_{12}), from which σ_6 versus ε_6 (γ_{12}) may be plotted. Figure 7 shows such a plot for two tests. A least squares fit line through the initial portion of each curve yields a slope m (modulus G_{12}), the inverse of which is A_{66}. The equation for ε_6^R under the condition $\sigma_6 \neq 0$, $\sigma_i = 0$ (i = 1,2,3,4,5) is shown below.

$$\varepsilon_6^R = A_{66}\sigma_6 \tag{2.32}$$

and thus

$$\frac{\partial \varepsilon_6^R}{\partial \sigma_6} = A_{66} = \frac{\partial \varepsilon_6}{\partial \sigma_6}\bigg|_{\sigma_6 = 0}$$

Because the test data was available, off-axis tests of 10°, 15°, 30°, and 45° were also utilized to determine A_{66}. Figure 8 shows σ_6 versus ε_6 for the four off-axis tests.

Averaging the values of A_{66} from the above six tests (Table B.2(a)) yields

$$A_{66} = 1.18373 \times 10^{-6} \; (\text{psi}^{-1}) \tag{2.33}$$

2.4.4 Irreversible Endochronic Constants

The irreversible endochronic constants are determined by plotting $\ln \varepsilon_i^{IR}$ versus $\ln \sigma_i$ for various lamina tests. These plots should be a straight line because when only one stress com-
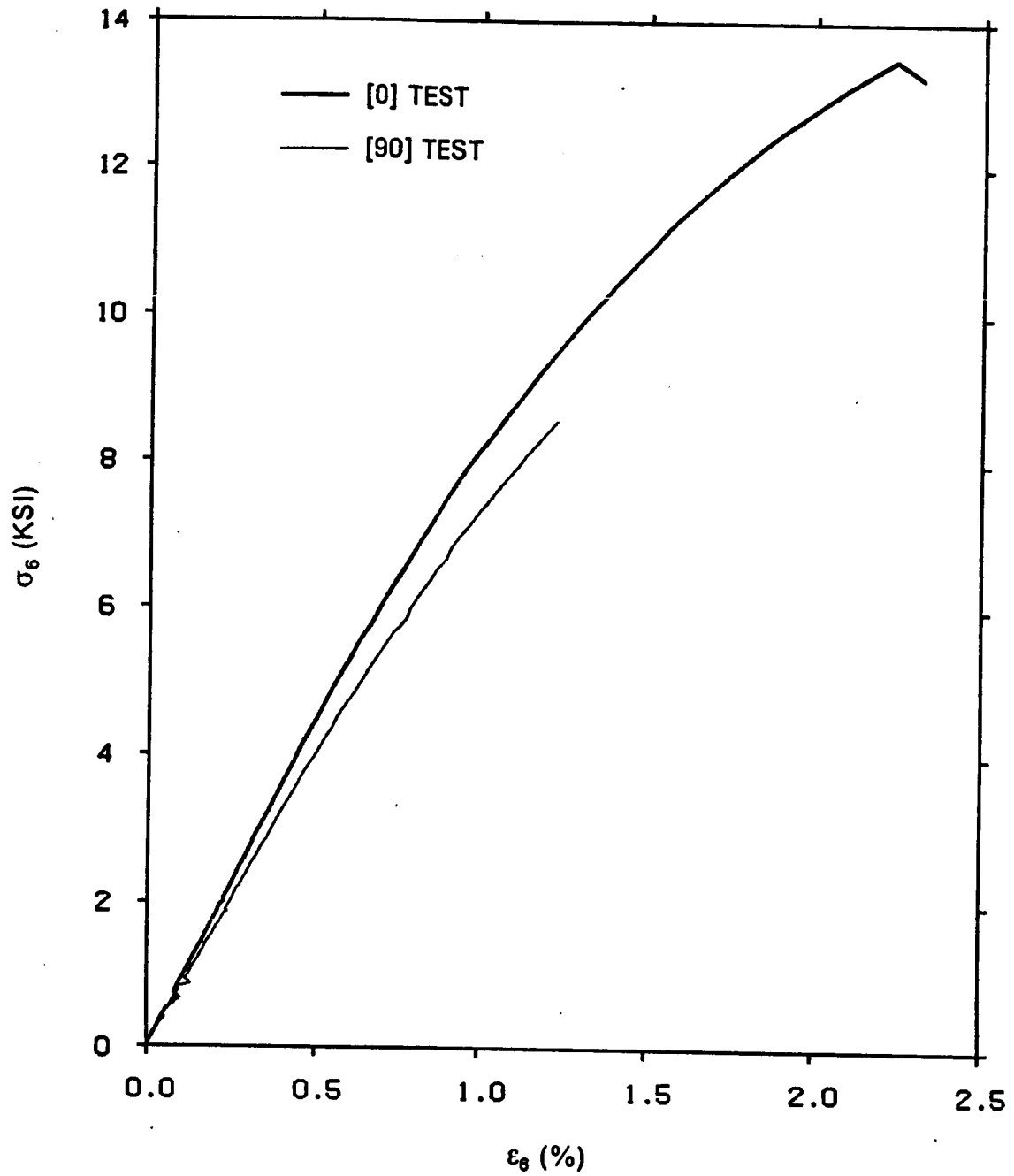
Figure 7. σ_6 Versus ε_6 for Iosipescu Tests in the 1-2 Plane of AS4/3502
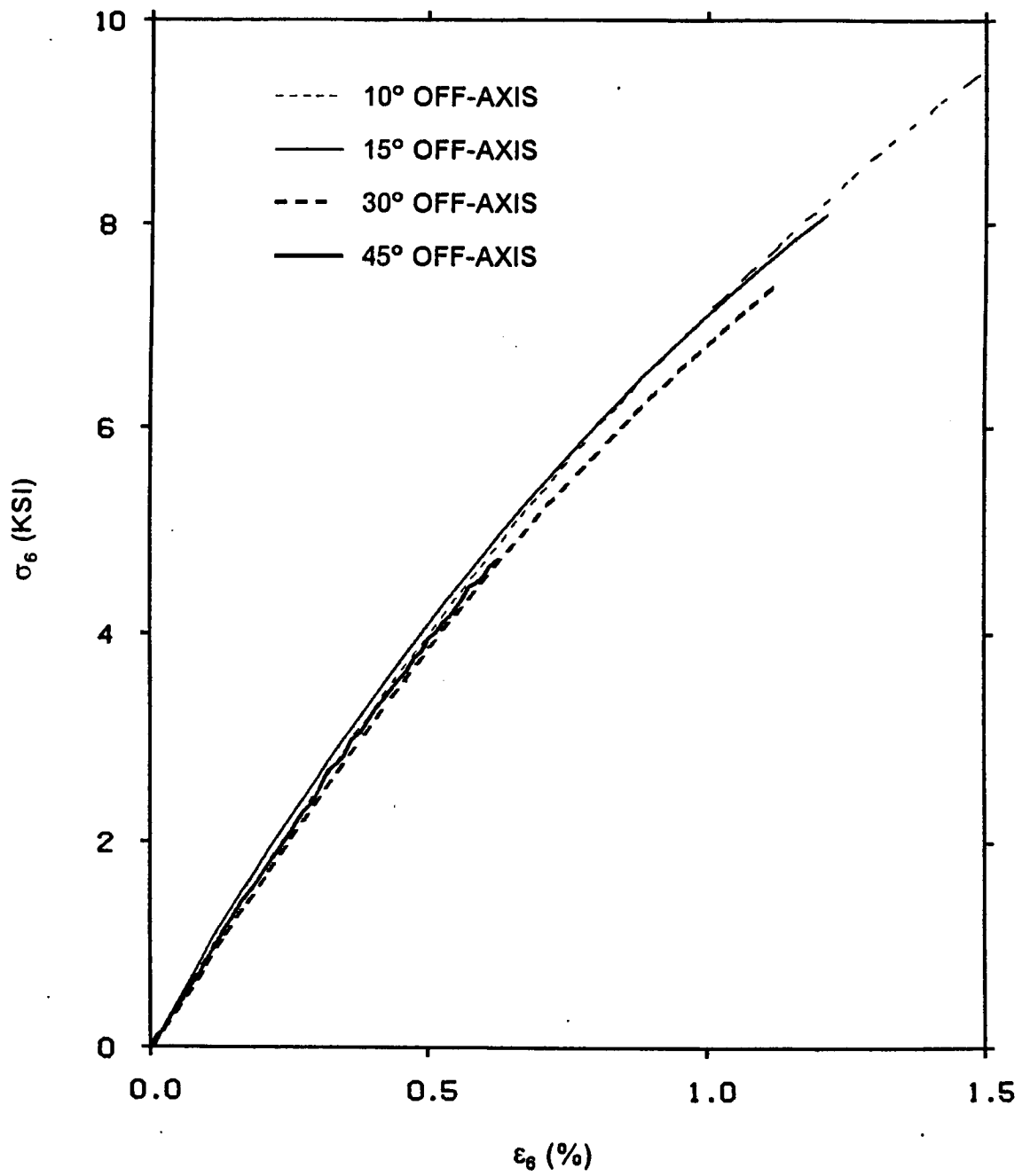
Figure 8. σ_6 Versus ε_6 for 10°, 20°, 30°, and 45° Off-Axis Tests of AS4/3502

ponent (σ_i) is present, the irreversible portion of strain (ε_i^{IR}) is represented by a power law (2.12). Symbolically, we can represent the power law form of ε_i^{IR} as follows:

$$\varepsilon_i^{IR} = C_i \sigma_i^{k_i} \quad (i = 1,2,3,4,5, \text{ or } 6, \text{ no sum on } i) \tag{2.34}$$

where

$$C_i \equiv \text{functions of the irreversible endochronic constants}$$

$$k_1 \equiv n_1$$

$$k_2 \equiv n_2 + 1$$

$$k_3 \equiv n_2 + 1$$

$$k_4 \equiv n_2 + 1$$

$$k_5 \equiv n_6 + 1$$

$$k_6 \equiv n_6 + 1$$

Taking the logarithm of both sides of the above equation gives:

$$\ln \varepsilon_i^{IR} = k_i \ln \sigma_i + \ln C_i \tag{2.35}$$

In the classical x-y coordinate system, the above can be represented as:

$$y = mx + b$$

where

$$y \equiv \ln \varepsilon_i^{IR}$$

$$x \equiv \ln \sigma_i$$

The Endochronic Theory

$$m \equiv k_i$$

$$b \equiv \ln C_i$$

In this coordinate system, m is the slope of the line and b is the y-intercept. The above representation is used in evaluating all of the irreversible endochronic constants.

2.4.4.1 The n and B Parameters

The same tests used to determine the A_{ij} parameters are utilized in calculating the endochronic constants appearing in the irreversible strain expressions. These constants include n_1, B_{11}, n_2, B_{22}^0, n_6, and B_{66}^0 (2.17).

n_1 and B_{11}

The constants n_1 and B_{11} are calculated from the 0° uniaxial compression tests. The expression for ε_1^{IR} is written as follows:

$$\varepsilon_1^{IR} = B_{11}\sigma_{11}^n$$

Using equation (2.34),

$$C_1 = B_{11}$$

$$k_1 = n_1$$

For a power law fit, this plot should yield a straight line with slope k_1 and y-intercept $\ln C_1$. Figure 9 shows the experimental curves to be best represented by a straight line in the range of data points from $\ln \sigma_1 = 11$ to $\ln \sigma_1 = 11.7$.
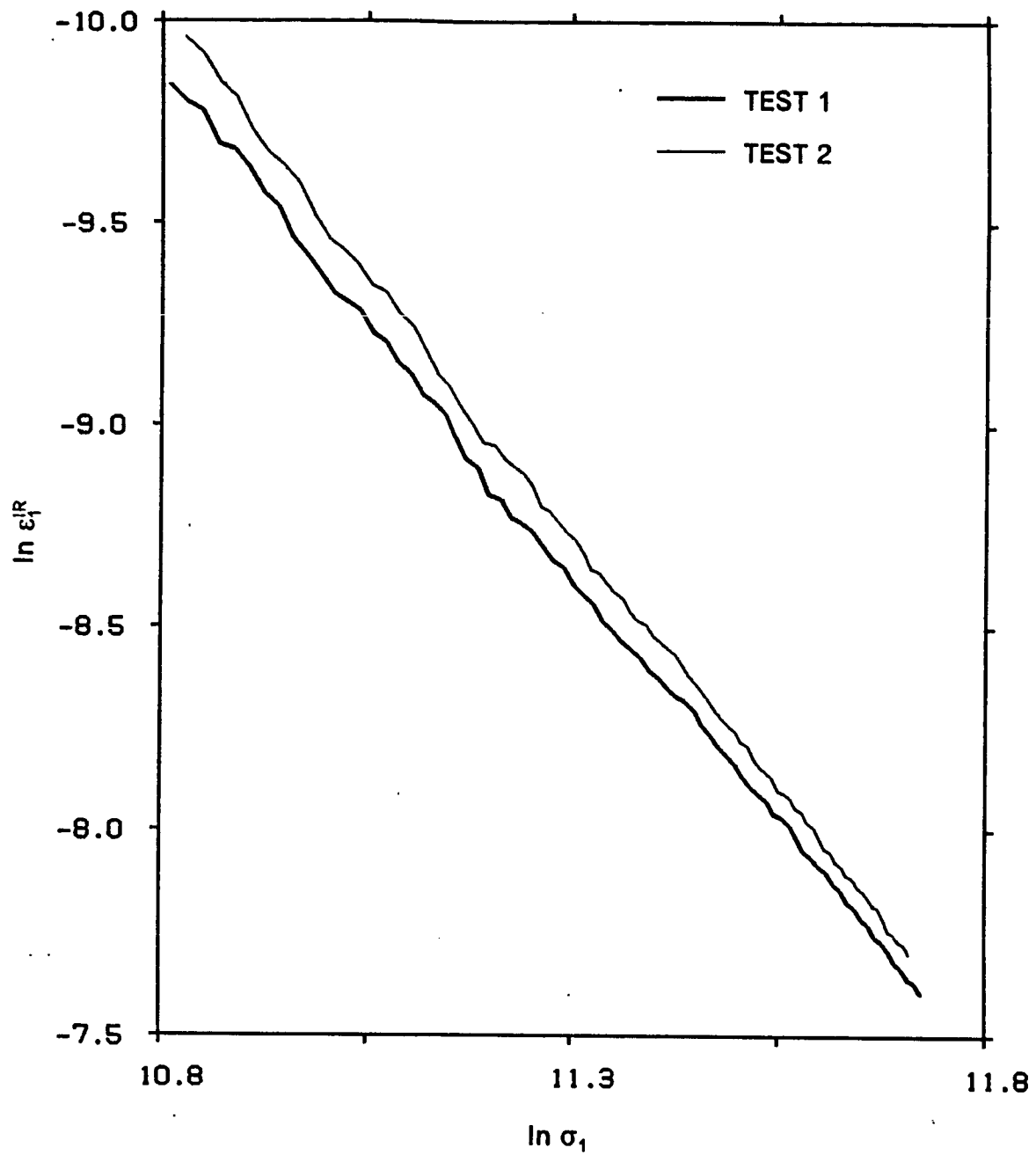
Figure 9. In ε_1^{IR} Versus In σ_1 for 0° Uniaxial Compression Tests of AS4/3502

Averaging the results from tests 1 and 2 (Table B.2(b)) yields

$$n_1 = 2.44791 \tag{2.36}$$

$$B_{11} = 1.90645 \times 10^{-16} \tag{2.37}$$

n_2 and $B^o{}_{22}$

The constants n_2 and B^0_{22} are determined from the 90 ° uniaxial compression tests. The expression for ε^{IR}_2 (2.17) is

$$\varepsilon^{IR}_2 = \int_0^z B^0_{22} \cdot (z - z')^{n_2} \frac{\partial \sigma_2(z')}{\partial z'} dz' \tag{2.38}$$

where

$$dz = \sqrt{S_{ij} d\sigma_i d\sigma_j}$$

Under pure uniaxial loading, $\sigma_2 \neq 0$ and $\sigma_i = 0$ ($i = 1,3,4,5,6$). The expression for dz simplifies to

$$dz = \sqrt{S_{22} d\sigma_2 d\sigma_2} = \sqrt{S_{22}} \, d\sigma_2$$

Therefore,

$$z = \sqrt{S_{22}} \, \sigma_2 \tag{2.39}$$

$$\frac{\partial \sigma_2}{\partial z} = \frac{1}{\sqrt{S_{22}}}$$

and

$$\varepsilon_2^{IR} = \int_0^z B_{22}^0 \cdot (z - z')^{n_2} \frac{1}{\sqrt{S_{22}}} dz'$$

Integrating,

$$\varepsilon_2^{IR} = \frac{B_{22}^0}{\sqrt{S_{22}}} \left[\frac{-(z - z')^{n_2 + 1}}{n_2 + 1} \right] \Bigg|_0^z$$

$$= \frac{B_{22}^0 z^{n_2 + 1}}{\sqrt{S_{22}} (n_2 + 1)}$$

$$\varepsilon_2^{IR} = \frac{B_{22}^0 (S_{22})^{\frac{n_2}{2}}}{n_2 + 1} \sigma_2^{n_2 + 1}$$

Using equation (2.34), the above can be symbolically represented as:

$$\varepsilon_2^{IR} \equiv C_2 \sigma_2^{k_2}$$

where

$$C_2 \equiv B_{22}^0 \frac{(S_{22})^{\frac{n_2}{2}}}{n_2 + 1} \qquad (2.40)$$

$$k_2 \equiv n_2 + 1$$

In the above equations, $\ln C_2$ is the y-intercept and k_2 is the slope of the $\ln \varepsilon_2^{IR}$ versus $\ln \sigma_2$ curve.

The plots of $\ln \varepsilon_2^{IR}$ versus $\ln \sigma_2$ for two tests are shown in Figure 10. A straight line is best represented over the range of $\ln \sigma_2 \cong 9.9$ to $\ln \sigma_2 \cong 10.3$.

Averaging the values of n_2 from both tests (Table B.2(c)) yields
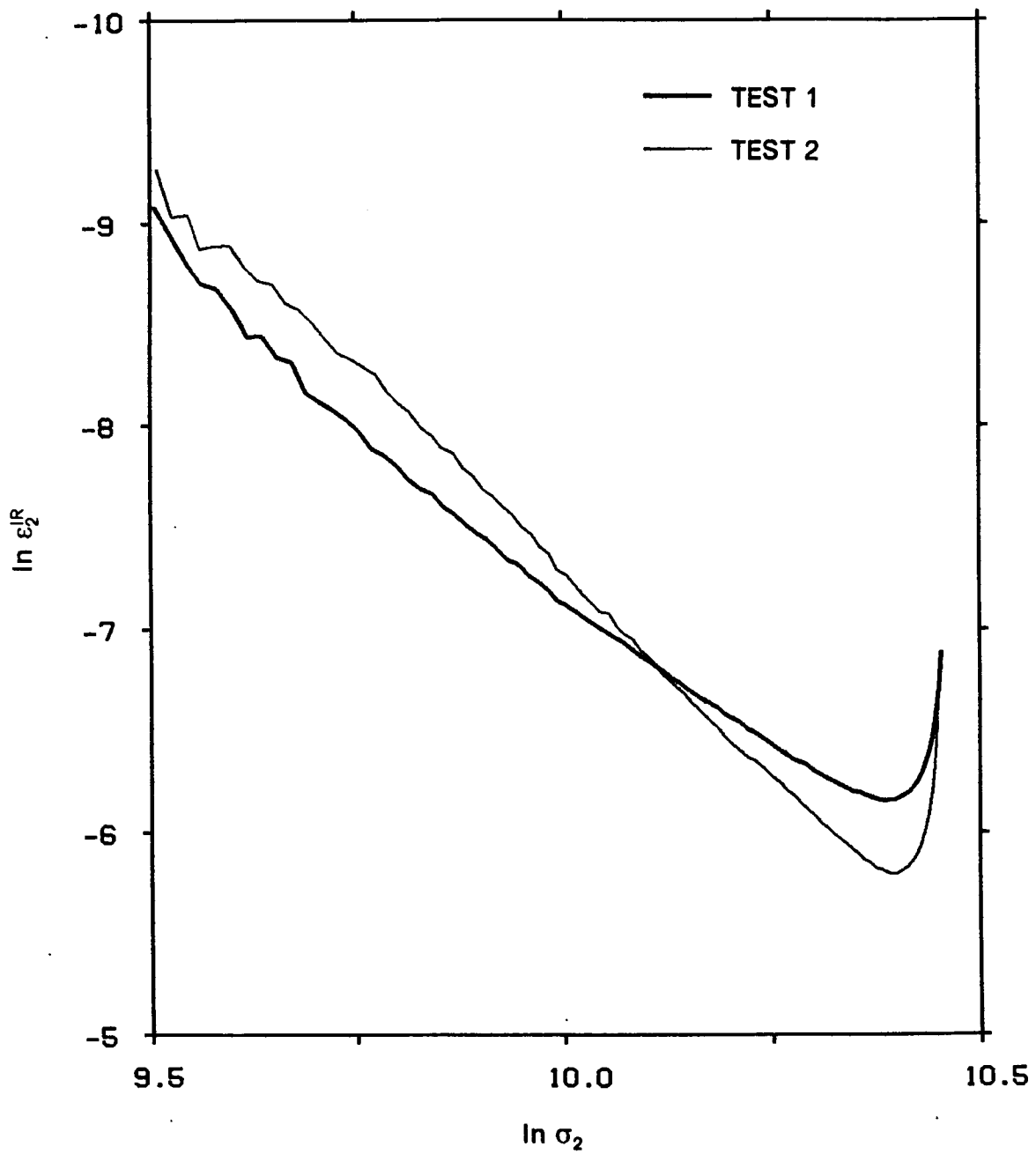
Figure 10. In ε_2^{IR} Versus In σ_2 for 90° Uniaxial Compression Tests of AS4/3502

$$n_2 = 2.45967 \tag{2.41}$$

It was necessary to calculate n_2 before B_{22}^0 because B_{22}^0 is a function of n_2 as well as S_{22} (2.40). Because S_{22} has not yet been determined, B_{22}^0 will be left for now as a function of S_{22}.

Since $\ln C_2$ is the y-intercept, we have

$$\ln \left(\frac{B_{22}^0 (S_{22})^{\frac{n_2}{2}}}{n_2 + 1} \right) = y_{intercept}$$

$$\frac{B_{22}^0 (S_{22})^{\frac{n_2}{2}}}{n_2 + 1} = e^{y_{intercept}}$$

$$B_{22}^0 = (S_{22})^{\frac{-n_2}{2}} (n_2 + 1) e^{y_{intercept}}$$

Averaging the values of B_{22}^0 from both tests (Table B.2(d)) yields

$$B_{22}^0 = S_{22}^{-1.22984} (2.370096 \times 10^{-18}) \tag{2.42}$$

n_6 and $B^0{}_{66}$

The constant n_6 is evaluated in a similar manner to n_2 using the two Iosipescu tests in the 1-2 plane along with the 10°, 15°, 30°, and 45° off-axis tests. The expression for ε_6^{IR} is written as follows:

$$\varepsilon_6^{IR} = \frac{B_{66}^0 (S_{66})^{\frac{n_6}{2}}}{n_6 + 1} \sigma_6^{n_6 + 1} \tag{2.43}$$

Using equation (2.34), the above can be symbolically represented as

$$\varepsilon_6^{IR} = C_6 \sigma_6^{k_6}$$

where

$$C_6 \equiv \frac{B_{66}^0 (S_{66})^{\frac{n_6}{2}}}{n_6 + 1}$$

$$k_6 \equiv n_6 + 1$$

The irreversible strain ε_6^{IR} can be written as:

$$\varepsilon_6^{IR} = \varepsilon_6 - \varepsilon_6^R = \varepsilon_6 - A_{66}\sigma_6$$

The irreversible strain ε_6^{IR} may be calculated in two different ways. The first scheme uses the average value of A_{66} determined in the previous section. The second scheme uses the value of A_{66} determined for each separate test. Since it is not known a priori which scheme will yield the most accurate value of n_6, both schemes are used to determine separate values of n_6. These values are compared with experimental results later to determine a best fit value. Figure 11 shows a least square fit to be best represented in the following ranges: Iosipescu Test 1 (ln $\sigma_6 \cong 8.7$ to 9.5), Iosipescu Test 2 (ln $\sigma_6 \cong 8.62$ to 9.51), 10° Off-Axis Test (ln $\sigma_6 \cong 8.39$ to 9.16), 15° Off-Axis Test (ln $\sigma_6 \cong 8.14$ to 9.0), 30° Off-Axis Test (ln $\sigma_6 \cong 8.62$ to 8.91), and 45° Off-Axis Test (ln $\sigma_6 \cong 8.25$ to 8.46). The following result is based on the average A_{66} value of 1.18373×10^{-6} (psi^{-1}).

Averaging the value of n_6 from the six shear tests (Table B.3(a)) yields

$$n_{6A} = 2.54504 \tag{2.44}$$

where the subscript 6A represents the value of n_6 calculated using the average value of A_{66}.

Averaging the value of n_6 from the six shear tests (Table B.3(b)) yields

$$n_{6B} = 2.53355 \tag{2.45}$$
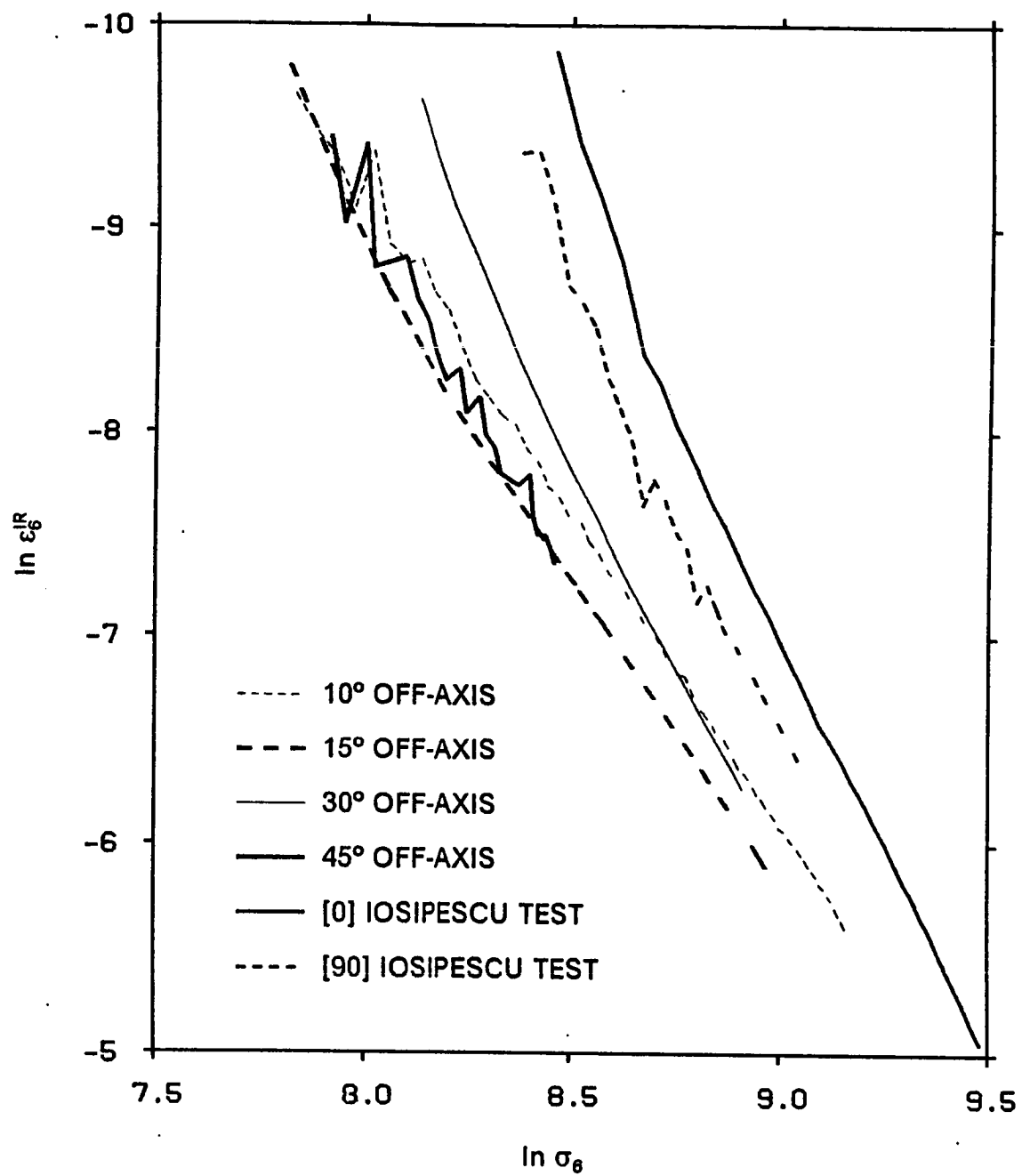
Figure 11. In ε_6^{IR} Versus In σ_6 for Iosipescu Tests and Off-Axis Tests of AS4/3502

where the subscript 6B represents the value of n_6 calculated using the individual test values of A_{66}.

Comparing the plots of $\ln \varepsilon_6^{IR}$ versus $\ln \sigma_6$ in Figure 11 shows that the 0 ° Iosipescu test best represents a straight line. Therefore, the value of n_6 from this test is also considered in the best fit scheme in the following section. Actually, two values of n_6 exist for the 0 ° Iosipescu test; a value based on the average A_{66} compliance and a value based on the A_{66} compliance of the 0° Iosipescu test. These values are represented by the subscripts 6C and 6D respectively and are listed below.

$$n_{6C} = 3.04940 \tag{2.46}$$

$$n_{6D} = 3.1854 \tag{2.47}$$

Because both B_{66}^0 and S_{66} must be calculated from a pure shear test in the 1-2 plane, one of them is redundant (see equation (2.43)). Since B_{66}^0 is simply a multiplicative constant which shifts the curve of $\ln \varepsilon_6^{IR}$ versus $\ln \sigma_6$ to the left or right, it is arbitrarily set equal to the value of 1 in this work.

$$B_{66}^0 = 1 \tag{2.48}$$

2.4.4.2 The S_{ij} Parameters

With the exception of S_{44} and S_{66}, the S_{ij} parameters are calculated from the off-axis coupon tests. S_{44} is calculated from Iosipescu tests in the 2-3 plane and S_{66} is calculated from Iosipescu tests in the 1-2 plane.

The Constant S_{44}

The equation governing the irreversible strain response in a 2-3 plane Iosipescu test is shown below.

$$\varepsilon_4^{IR} = \int_0^z \frac{1}{2} B_{22}^0 \cdot (z - z')^{n_2} \frac{\partial \sigma_4(z')}{\partial z'} dz' \tag{2.49}$$

In the same manner as equations (2.38), (2.39), and (2.34), the above can be symbolically represented as

$$\varepsilon_4^{IR} = C_4 \sigma_4^{k_4}$$

where

$$C_4 \equiv B_{22}^0 \frac{(S_{44})^{\frac{n_2}{2}}}{2(n_2 + 1)} \sigma_4^{n_2 + 1}$$

$$k_4 \equiv n_2 + 1$$

Because n_2 has already been calculated and B_{22}^0 has been calculated as a function of S_{22}, S_{44} may be calculated in terms of B_{22}^0. However, examining the stress-strain behavior of the 2-3 plane Iosipescu tests as shown in Figure 6, the stress-strain response is essentially linear [1]. This observation means the irreversible portion of ε_4 is zero. If ε_4^{IR} is zero and n_2 and B_{22}^0 have been determined (and are used in the irreversible strain expressions of other strain components), then S_{44} must be set equal to zero.

$$S_{44} = 0 \tag{2.50}$$

---

[1] These tests did not fail in a shear mode. Therefore, their ultimate strain values may be significantly larger. It is possible that these specimens would show non-linear behavior at higher strain levels.

The Constant S_{23}

In the same manner as the A_{ij} parameters, the S_{ij} parameters are assumed to obey transversely isotropic conditions. Therefore, S_{4j} (j = 1,2,3,5,6), S_{5j} (j = 1,2,3,4,6), and S_{6j} (j = 1,2,3,4,5) are all set to zero. Likewise, $S_{13} = S_{12}$, $S_{33} = S_{22}$, $S_{55} = S_{66}$, and in general, $S_{ij} = S_{ji}$. The expression for S_{23} in terms of S_{22} and S_{44} must hold as well.

$$S_{23} = S_{22} - \frac{S_{44}}{2} \tag{2.51}$$

However, because $S_{44} = 0$, S_{23} must equal S_{22} .

$$S_{23} = S_{22} \tag{2.52}$$

The Constant S_{66}

As mentioned previously, the S_{66} parameter is determined from Iosipescu tests in the 1-2 plane. The equation governing the irreversible strain state ε_6^{IR} in this test was shown previously to be

$$\varepsilon_6^{IR} = C_6 \sigma_6^{k_6}$$

where

$$C_6 \equiv \frac{B_{66}^0 (S_{66})^{\frac{n_6}{2}}}{n_6 + 1}$$

$$k_6 \equiv n_6 + 1$$

Because $B_{66}^0 = 1$, the expression for S_{66} may be written as

$$\ln\left(\frac{(S_{66})^{\frac{n_6}{2}}}{n_6 + 1}\right) = y_{\text{Intercept}}$$

$$(S_{66})^{\frac{n_6}{2}} = (n_6 + 1)e^{y_{\text{Intercept}}}$$

$$S_{66} = [(n_6 + 1)e^{y_{\text{Intercept}}}]^{\frac{2}{n_6}}$$

Note that S_{66} is a function of n_6. Therefore, there will be four values of S_{66} corresponding to the four values of n_6 ($n_{6A}, n_{6B}, n_{6C}, n_{6D}$). The following value of S_{66} is calculated using n_{6A}.

Averaging the values of S_{66} from tests 1 and 2 (Table B.3(c)) yields a value for S_{66A} of

$$S_{66A} = 1.96639 \times 10^{-13} \tag{2.53}$$

In an analogous manner, S_{66B}, S_{66C}, and S_{66D} are calculated to be

$$S_{66B} = 1.805796 \times 10^{-13} \tag{2.54}$$

$$S_{66C} = 1.26342 \times 10^{-12} \tag{2.55}$$

$$S_{66D} = 1.839071 \times 10^{-12} \tag{2.56}$$

The remaining S_{ij} parameters are calculated from off-axis tests.

The Constants S_{11}, S_{12}, and S_{22}

As mentioned previously, an off-axis test introduces not only the desired shear stress, but normal principle stresses parallel and perpendicular to the fibers. Therefore, an off-axis coupon test will have non-zero stress components σ_1, σ_2, and σ_6 (τ_{12}). The ratio of these stresses depends on the off-axis angle, but throughout the loading, equilibrium requires that

they be proportional. In other words, the ratios of these stress components do not change during loading (i.e. $\frac{\sigma_1}{\sigma_2}$ = const., $\frac{\sigma_2}{\sigma_6}$ = const., etc.). This is a very important result because it allows the three remaining S_{ij} parameters, S_{11}, S_{22}, and S_{12} to be calculated from three separate off-axis tests [2].

The expression for the irreversible strain in the 1-2 plane (ε_6^{IR}) is written

$$\varepsilon_6^{IR} = \int_0^z B_{66}^0 \cdot (z - z')^{n_6} \frac{\partial \sigma_6(z')}{\partial z'} dz' \tag{2.57}$$

where for the combined stress state σ_1, σ_2, σ_6

$$dz = \sqrt{S_{11}d\sigma_1^2 + S_{22}d\sigma_2^2 + 2S_{12}d\sigma_1 d\sigma_2 + S_{66}d\sigma_6^2}$$

Writing $d\sigma_1$ and $d\sigma_2$ in terms of $d\sigma_6$ gives

$$d\sigma_1 = \cot \varphi \, d\sigma_6$$

$$d\sigma_2 = \tan \varphi \, d\sigma_6$$

where

$$\varphi \equiv \text{Angle of Fibers from the Loading Axis}$$

Therefore,

$$dz = \sqrt{S_{11} \cot^2\varphi + 2S_{12} + S_{66} + S_{22} \tan^2\varphi} \; d\sigma_6 \tag{2.58}$$

$$z = \sqrt{S_{11} \cot^2\varphi + 2S_{12} + S_{66} + S_{22} \tan^2\varphi} \; \sigma_6$$

---

[2] It was mentioned earlier in chapter 2 that the endochronic equations were written for strain in terms of stress to facilitate the calculation of the S_{ij} parameters. Note that in the off-axis tests, the strain component ratios are not proportional for nonlinear response. Because of this it would be very difficult to calculate the S_{ij} parameters if stress were expressed in terms of strain.

Substituting the above expression for z into the integral equation (2.57) gives

$$\varepsilon_6^{IR} = \frac{B_{66}^0}{n_6 + 1}\left[S_{11}\cot^2\varphi + 2S_{12} + S_{66} + S_{22}\tan^2\varphi\right]^{\frac{n_6}{2}}\sigma_6^{n_6 + 1} \tag{2.59}$$

Using equation (2.34), equation (2.59) can be symbolically represented as

$$\varepsilon_6^{IR} = C_6\sigma_6^{k_6}$$

where

$$C_6 \equiv \frac{B_{66}^0}{n_6 + 1}\left[S_{11}\cot^2\varphi + 2(S_{12} + S_{66}) + S_{22}\tan^2\varphi\right]^{\frac{n_6}{2}}$$

$$k_6 \equiv n_6 + 1$$

For three off-axis tests of different angles, the above expression yields three equations for the three unknown parameters S_{11}, S_{22}, and S_{12}. To use these equations, the $\ln\varepsilon_6^{IR}$ is plotted against the $\ln\sigma_6$ for each off-axis angle. Figure 11 shows these plots for the angles of 10°, 15°, 30°, and 45° (because four tests were available, four sets of three different off-axis tests were utilized).

Pindera and Herakovich [19] rearranged the above equations to yield simple equations for determining S_{11}, S_{22}, and S_{12}. These equations (eqs. (5.22) and (5.23) in Pindera and Herakovich) are shown below.

$$S_{11} = (n_6 + 1)^{\frac{2}{n_6}} \times \Omega$$

$$S_{22} = (n_6 + 1)^{\frac{2}{n_6}} \times \Psi$$

$$S_{12} = \frac{1}{2}\left\{\left[(n_6 + 1)A_{66}^x(\varphi_i)\right]^{\frac{2}{n_6}} - \left[S_{11}c\varphi_i + S_{22}t\varphi_i\right] - S_{66}\right\} \tag{2.60}$$

where

$$\Omega = \left\{ \frac{\left[A_{66}^{*}(\varphi_1)^{\frac{2}{n_6}} - A_{66}^{*}(\varphi_2)^{\frac{2}{n_6}}\right]\left[t\varphi_1 - t\varphi_3\right] - \left[A_{66}^{*}(\varphi_1)^{\frac{2}{n_6}} - A_{66}^{*}(\varphi_3)^{\frac{2}{n_6}}\right]\left[t\varphi_1 - t\varphi_2\right]}{\left[c\varphi_1 - c\varphi_2\right]\left[t\varphi_1 - t\varphi_3\right] - \left[c\varphi_1 - c\varphi_3\right]\left[t\varphi_1 - t\varphi_2\right]} \right\}$$

$$\Psi = \left\{ \frac{\left[A_{66}^{*}(\varphi_1)^{\frac{2}{n_6}} - A_{66}^{*}(\varphi_2)^{\frac{2}{n_6}}\right]\left[c\varphi_1 - c\varphi_3\right] - \left[A_{66}^{*}(\varphi_1)^{\frac{2}{n_6}} - A_{66}^{*}(\varphi_3)^{\frac{2}{n_6}}\right]\left[c\varphi_1 - c\varphi_2\right]}{\left[t\varphi_1 - t\varphi_2\right]\left[c\varphi_1 - c\varphi_3\right] - \left[t\varphi_1 - t\varphi_3\right]\left[c\varphi_1 - c\varphi_2\right]} \right\}$$

$$A_{66}^{*}(\varphi) = \frac{B_{66}^{0}}{n_6 + 1}\left[S_{11}\cot^2\varphi + S_{22}\tan^2\varphi + (2S_{12} + S_{66})\right]^{\frac{n_6}{2}}$$

where i can be either 1,2, or 3, $t\varphi_i \equiv \tan^2\varphi_i$ and $c\varphi_i \equiv \cot^2\varphi_i$

Using the above equation set along with plots similar to Figure 11 allows S_{11}, S_{22}, and S_{12} to be calculated. Using the four off-axis tests available in conjunction with the four sets of n_6 and S_{66} produces sixteen different sets of parameters. These sets are shown in Table 1.

2.4.5 "Best Fitting" the Parameter Sets to Experiment

It was mentioned earlier that a condition imposed on S_{ij} by thermodynamic constraints is it must be positive definite. Therefore, of the sixteen parameter sets shown in Table 1, only those which are positive definite are possible choices. Appendix C shows the conditions necessary for a tensor to be positive definite. From these conditions, Table 1 lists the parameter sets which are positive definite and those which are not. The parameter sets which are positive definite are numbered in Table 2 for ease of reference.

To determine which of the positive definite parameter sets best fits experimental test results, the parameter sets are used analytically in a comparison with off-axis test results and are then

Table 1. Possible S_{ij} Parameter Sets Marked As Positive Definite or Non-Positive Definite

Angle Set (15 °,30 °,45 °)		Angle Set (10 °,30 °,45 °)		Angle Set (10 °,15 °,45 °)		Angle Set (10 °,15 °,30 °)	
n_{6A}	2.54504E-00	n_{6A}	2.54504E-00	n_{6A}	2.54504E-00	n_{6A}	2.54504E-00
S_{66A}	1.96639E-13	S_{66A}	1.96639E-13	S_{66A}	1.96639E-13	S_{66A}	1.96639E-13
S_{11}	2.34704E-14	S_{11}	3.46034E-15	S_{11}	-8.53148E-15	S_{11}	-1.07261E-14
S_{22}	3.79959E-13	S_{22}	3.19929E-13	S_{22}	-6.57692E-14	S_{22}	-1.04893E-12
S_{12}	-6.36714E-14	S_{12}	-2.36515E-14	S_{12}	1.75194E-13	S_{12}	2.25771E-13
Positive Definite		Non-Positive Definite		Non-Positive Definite		Non-Positive Definite	
n_{6B}	2.53355E-00	n_{6B}	2.53355E-00	n_{6B}	2.53355E-00	n_{6B}	2.53355E-00
S_{66B}	1.80580E-13	S_{66B}	1.80580E-13	S_{66B}	1.80580E-13	S_{66B}	1.80580E-13
S_{11}	1.05681E-14	S_{11}	9.79461E-16	S_{11}	-4.76695E-15	S_{11}	-5.81861E-15
S_{22}	2.63695E-13	S_{22}	2.34929E-13	S_{22}	5.01046E-14	S_{22}	-4.21020E-13
S_{12}	2.26620E-15	S_{12}	2.14432E-14	S_{12}	1.16729E-13	S_{12}	4.40965E-13
Positive Definite		Non-Positive Definite		Non-Positive Definite		Non-Positive Definite	
n_{6C}	3.04940E-00	n_{6C}	3.04940E-00	n_{6C}	3.04940E-00	n_{6C}	3.04940E-00
S_{66C}	1.26342E-12	S_{66C}	1.26342E-12	S_{66C}	1.26342E-12	S_{66C}	1.26342E-12
S_{11}	1.49223E-13	S_{11}	2.26566E-14	S_{11}	-5.31935E-14	S_{11}	-6.70750E-14
S_{22}	2.86855E-12	S_{22}	2.48885E-12	S_{22}	4.92545E-14	S_{22}	-6.16938E-12
S_{12}	-4.38706E-13	S_{12}	-1.85573E-13	S_{12}	1.07215E-12	S_{12}	4.39207E-12
Positive Definite		Non-Positive Definite		Non-Positive Definite		Non-Positive Definite	
n_{6D}	3.18540E-00	n_{6D}	3.18540E-00	n_{6D}	3.18540E-00	n_{6D}	3.18540E-00
S_{66D}	1.83907E-12	S_{66D}	1.83907E-12	S_{66D}	1.83907E-12	S_{66D}	1.83907E-12
S_{11}	1.10652E-13	S_{11}	1.17136E-14	S_{11}	-4.75791E-14	S_{11}	-5.84304E-14
S_{22}	3.57840E-12	S_{22}	3.28159E-12	S_{22}	1.37453E-12	S_{22}	-3.48663E-12
S_{12}	-7.48855E-14	S_{12}	1.22990E-13	S_{12}	1.10616E-12	S_{12}	1.35624E-12
Positive Definite		Positive Definite		Non-Positive Definite		Non-Positive Definite	

Table 2. Positive Definite Parameter Sets

Parameter Set	S_{11}	S_{22}	S_{12}	S_{66}	n_6
1	1.49223E-13	2.86855E-12	-4.38706E-13	1.26342E-13	3.04940
2	1.71360E-14	3.28159E-12	1.22990E-13	1.83907E-12	3.18540
3	2.34704E-14	3.79959E-13	-6.36714E-14	1.96639E-13	2.54504
4	1.10652E-13	3.57840E-12	-7.48855E-14	1.18391E-12	3.18540
5	1.05681E-14	2.63695E-13	2.26620E-15	1.80580E-13	2.53355

used in a laminate analysis to compare with angle-ply laminates. The parameter set which best fits the experimental data is chosen.

2.4.5.1 Off-Axis Test Comparison

The expression for ε_6 in an off-axis specimen (2.56) is

$$\varepsilon_6 = A_{66}\sigma_6 + \frac{B_{66}^0}{n_6 + 1}[S_{11}\cot^2\varphi + (2S_{12} + S_{66}) + S_{22}\tan^2\varphi]^{\frac{n_6}{2}}\sigma_6^{n_6 + 1} \tag{2.61}$$

From this expression, ε_6 may be plotted against σ_6 for any desired off-axis angle φ. A simple program was written for equation (2.58) that uses S_{11}, S_{22}, S_{12}, S_{66}, n_6, and φ as input parameters and produces data for σ_6 versus ε_6. These data were plotted against experimental data and the plots are shown in Figure 12 through Figure 16 for the various parameter sets.

Parameter set 2 (Figure 13) fits the experimental data most accurately in an average sense. Parameter sets 1,3,4, and 5 all seem to match the 15°, 30°, and 45° experimental data very well. However, they do a poor job of modelling the 10° off-axis behavior. This is to be expected because, as Table 1 shows, these parameter sets were all derived from the combination of 15°, 30°, and 45° off-axis tests. Parameter set 2, however, was derived from the combination of 10°, 30°, and 45° off-axis tests. Although it matches these tests well, parameter set 2 also does an adequate job of modelling the 15° off-axis test.

2.4.5.2 Angle-Ply Laminate Comparison

Unlike the off-axis lamina tests, the loading within the layers of a laminate is not proportional. Therefore, no simple expressions exist for strain in terms of stress. Instead, the endochronic equations must be integrated throughout the laminate's load history. This is done in a step-
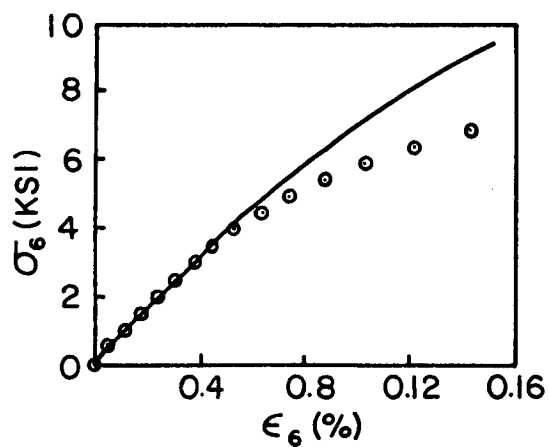
(a) 10° Off-Axis Comparison
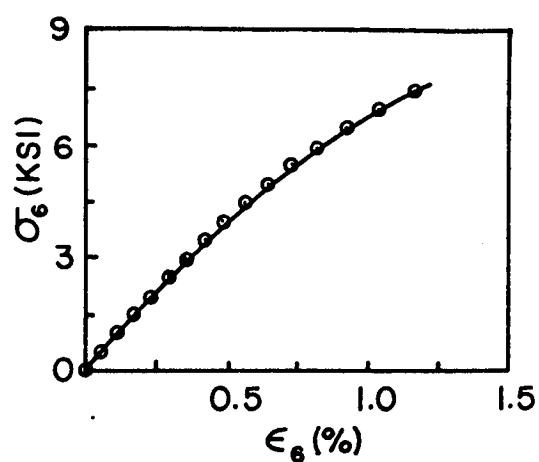
(b) 15° Off-Axis Comparison
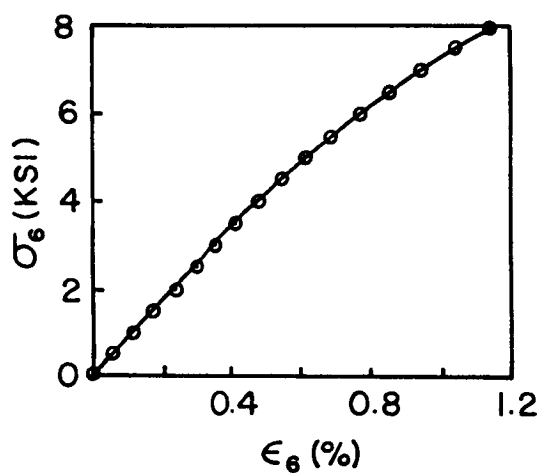
(c) 30° Off-Axis Comparison
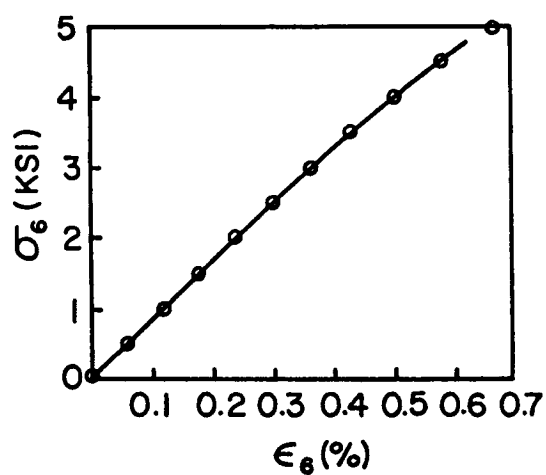
(d) 45° Off-Axis Comparison

⊙ ENDOCHRONIC THEORY　　　　　——— EXPERIMENT

Figure 12.　Analytical/Experimental Comparison of Off-Axis Tests Using Parameter Set 1
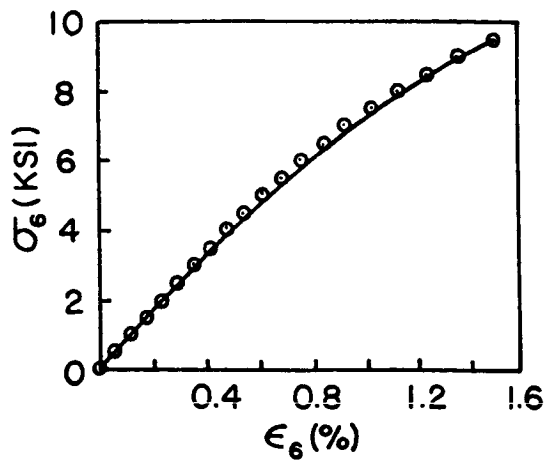
(a) 10° Off-Axis Comparison
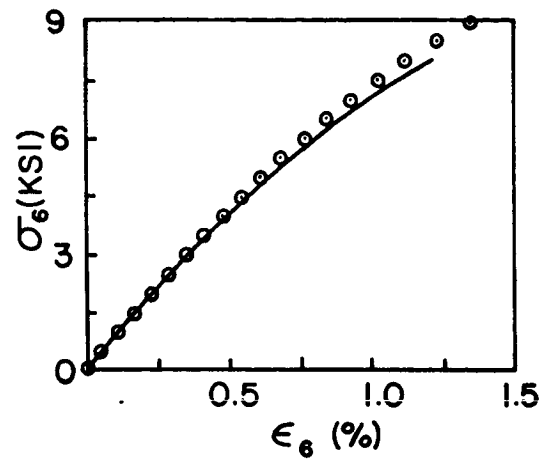
(b) 15° Off-Axis Comparison
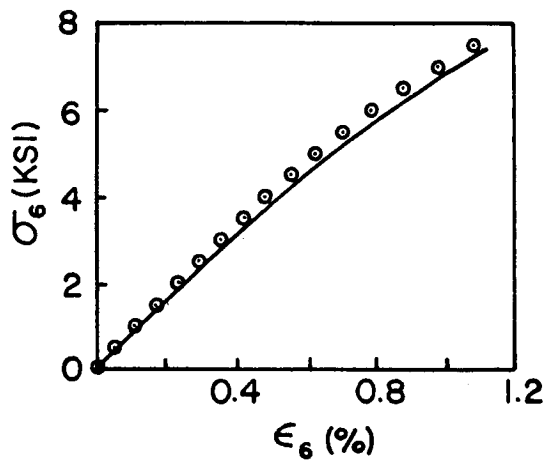
(c) 30° Off-Axis Comparison
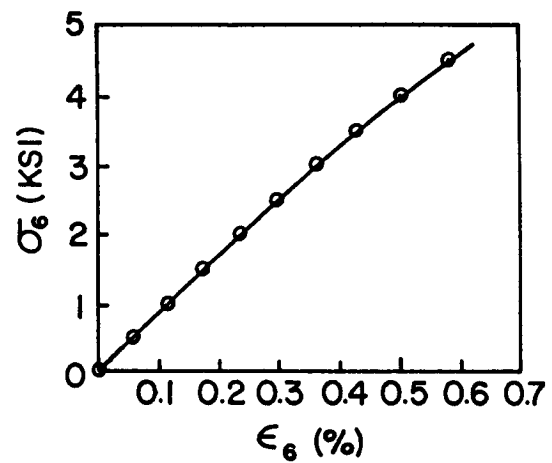
(d) 45° Off-Axis Comparison

⊙ ENDOCHRONIC THEORY — EXPERIMENT

Figure 13. Analytical/Experimental Comparison of Off-Axis Tests Using Parameter Set 2
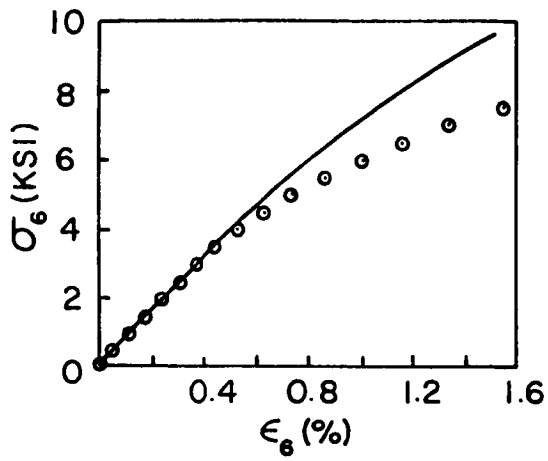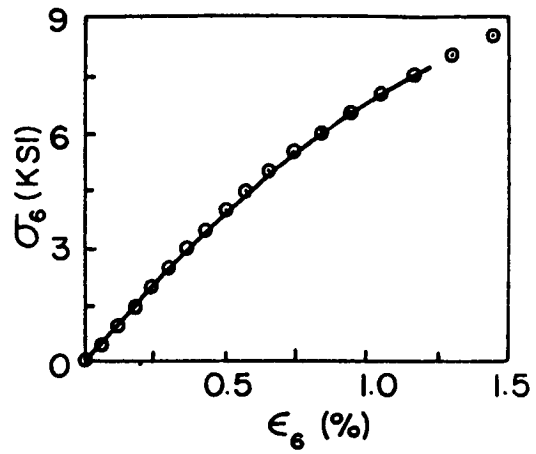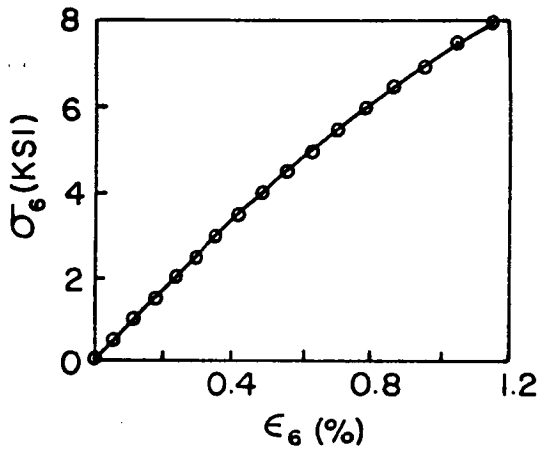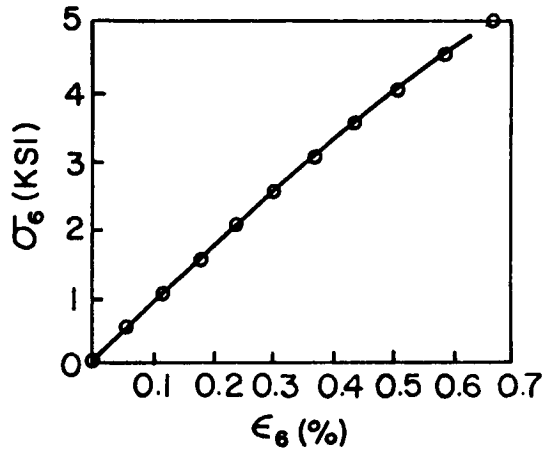
The Endochronic Theory

Figure 14. Analytical/Experimental Comparison of Off-Axis Tests Using Parameter Set 3
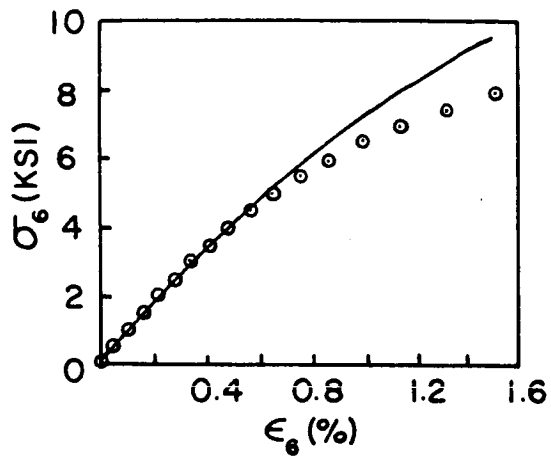
(a) 10° Off-Axis Comparison
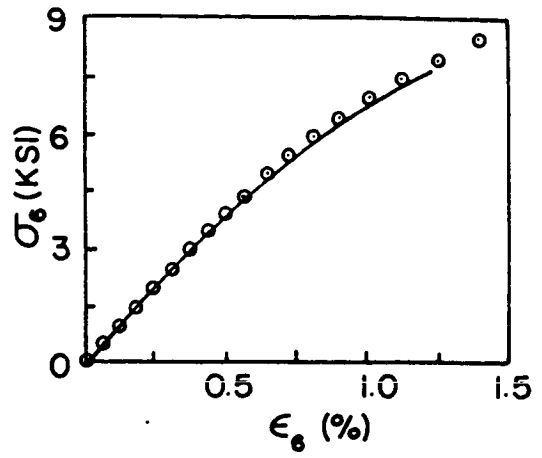
(b) 15° Off-Axis Comparison
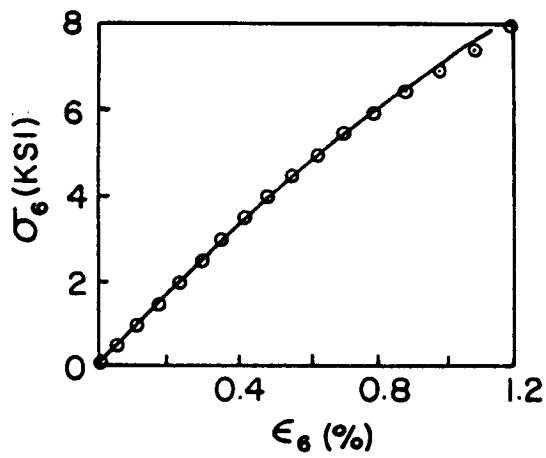
(c) 30° Off-Axis Comparison
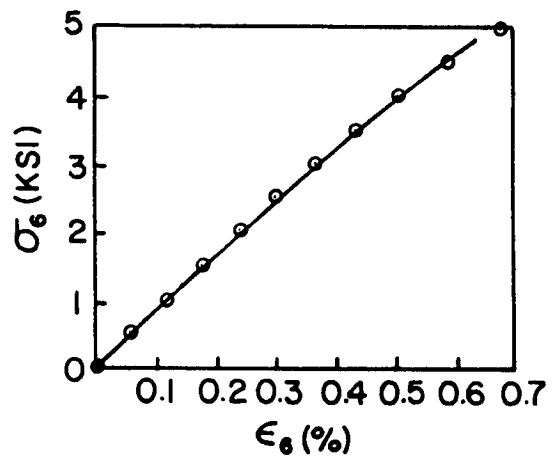
(d) 45° Off-Axis Comparison

⊙ ENDOCHRONIC THEORY   ——— EXPERIMENT

Figure 15.   Analytical/Experimental Comparison of Off-Axis Tests Using Parameter Set 4
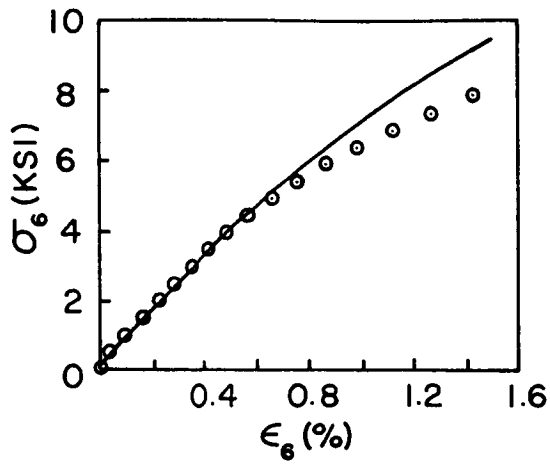
The Endochronic Theory   61

(a) 10° Off-Axis Comparison
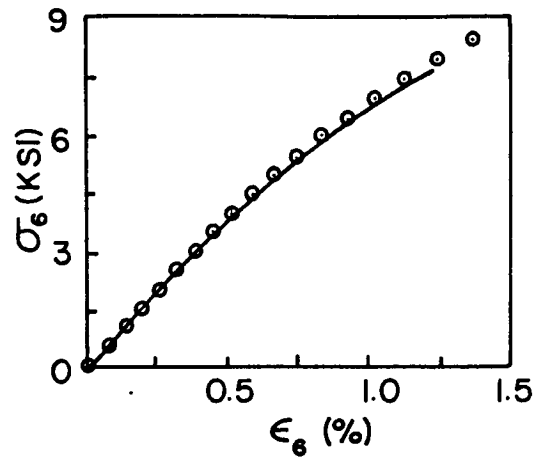
(b) 15° Off-Axis Comparison
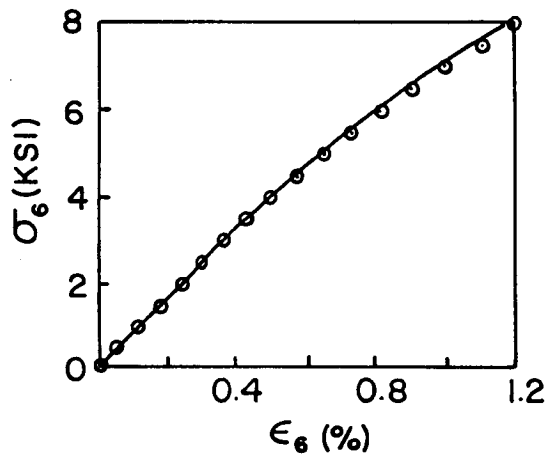
(c) 30° Off-Axis Comparison
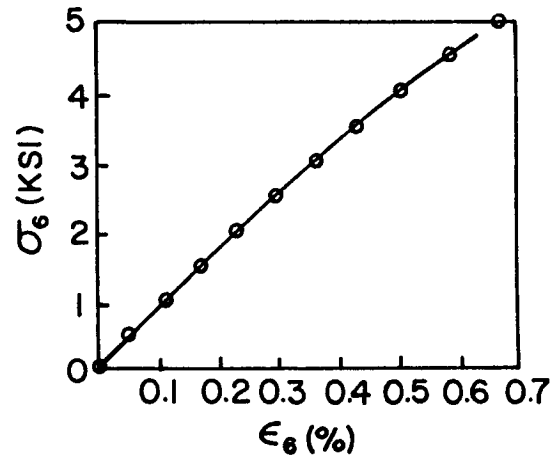
(d) 45° Off-Axis Comparison

⊙ ENDOCHRONIC THEORY   —— EXPERIMENT

Figure 16.   Analytical/Experimental Comparison of Off-Axis Tests Using Parameter Set 5
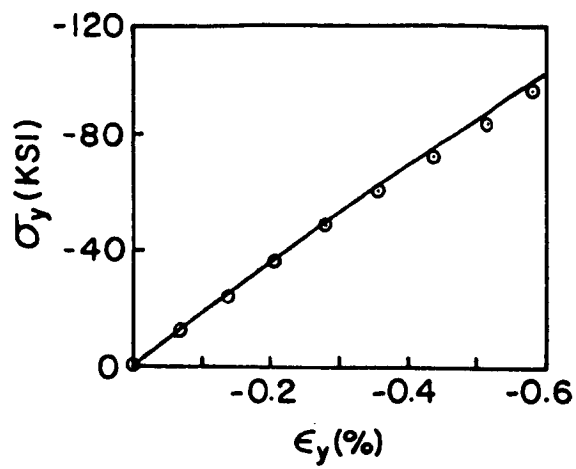
(a) $[(\pm 10)_{12}]_s$ Laminate Comparison
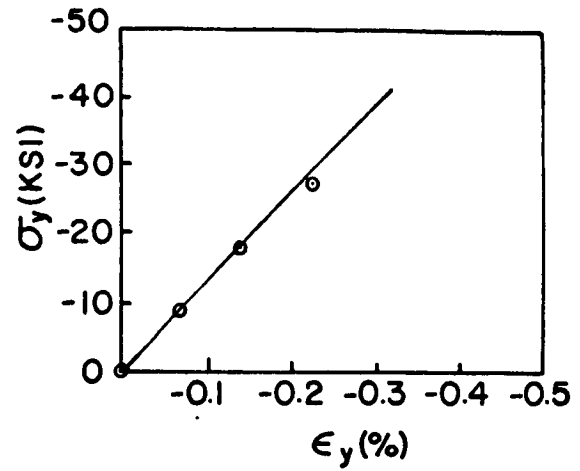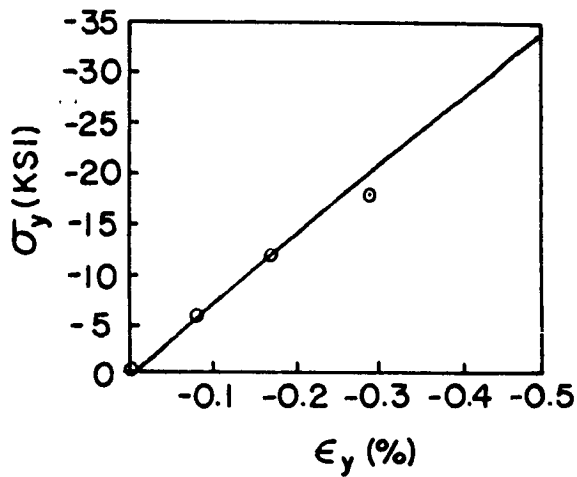
(b) $[(\pm 20)_{12}]_s$ Laminate Comparison

(c) $[(\pm 30)_{12}]_s$ Laminate Comparison
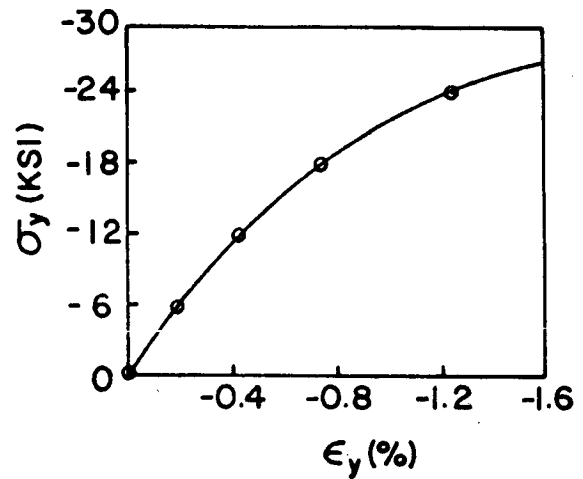
(d) $[(\pm 45)_{12}]_s$ Laminate Comparison

⊙ ENDOCHRONIC THEORY   —— EXPERIMENT

Figure 17. Analytical/Experimental Comparison of Angle-Ply Laminate Tests Using Parameter Set 1
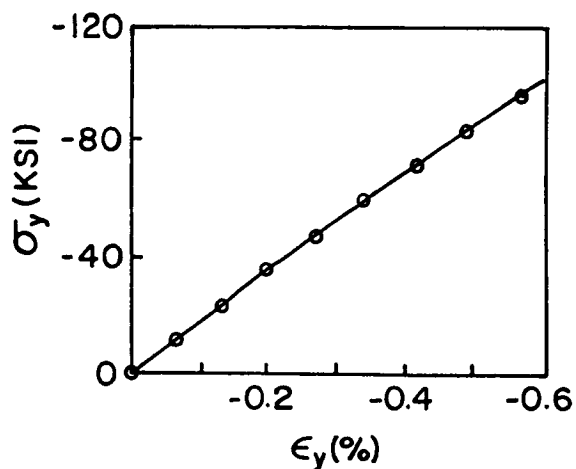
(a) $[(\pm 10)_{12}]_s$ Laminate Comparison
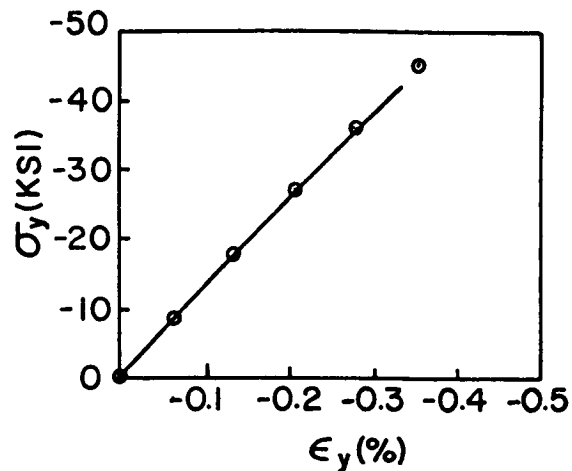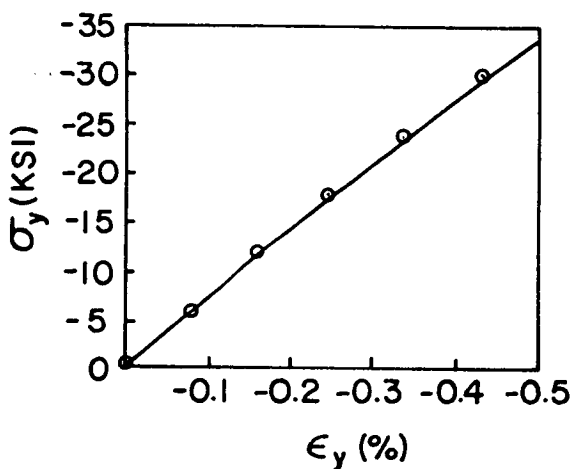
(b) $[(\pm 20)_{12}]_s$ Laminate Comparison

(c) $[(\pm 30)_{12}]_s$ Laminate Comparison
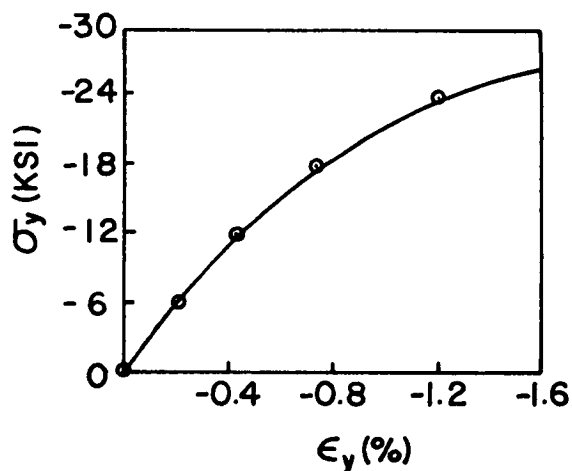
(d) $[(\pm 45)_{12}]_s$ Laminate Comparison

⊙ ENDOCHRONIC THEORY   —— EXPERIMENT

Figure 18. Analytical/Experimental Comparison of Angle-Ply Laminate Tests Using Parameter Set 2
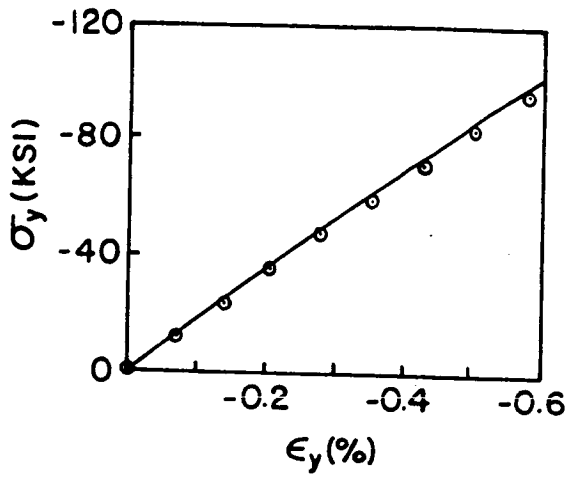
(a) $[(\pm 10)_{12}]_s$ Laminate Comparison
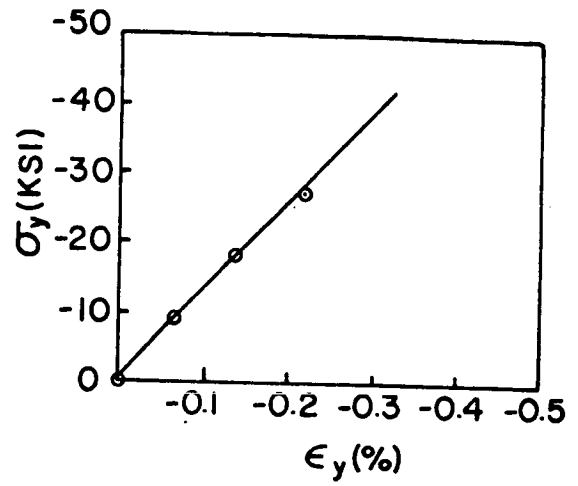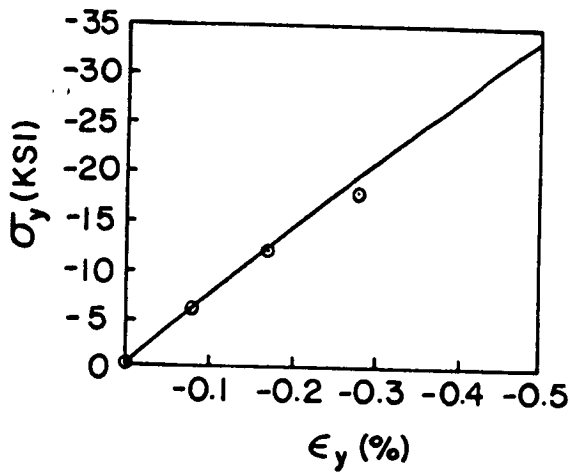
(b) $[(\pm 20)_{12}]_s$ Laminate Comparison

(c) $[(\pm 30)_{12}]_s$ Laminate Comparison
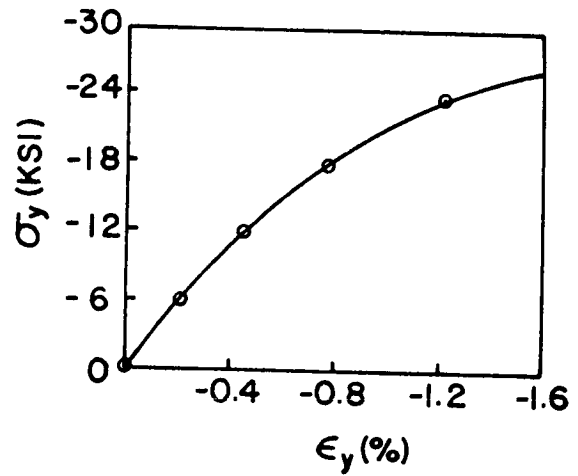
(d) $[(\pm 45)_{12}]_s$ Laminate Comparison

⊙ ENDOCHRONIC THEORY

—— EXPERIMENT

Figure 19. Analytical/Experimental Comparison of Angle-Ply Laminate Tests Using Parameter Set 3
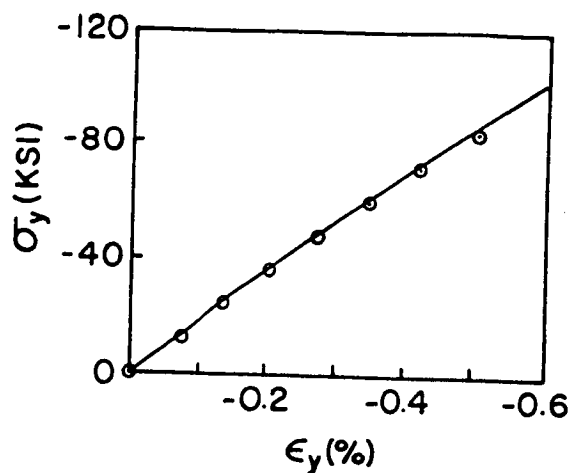
(a) $[(\pm 10)_{12}]_s$ Laminate Comparison
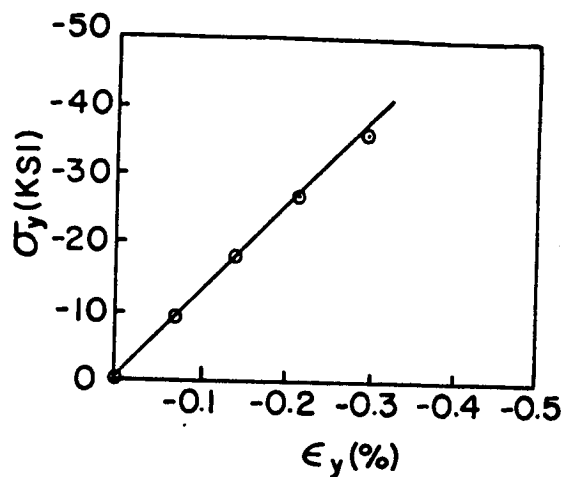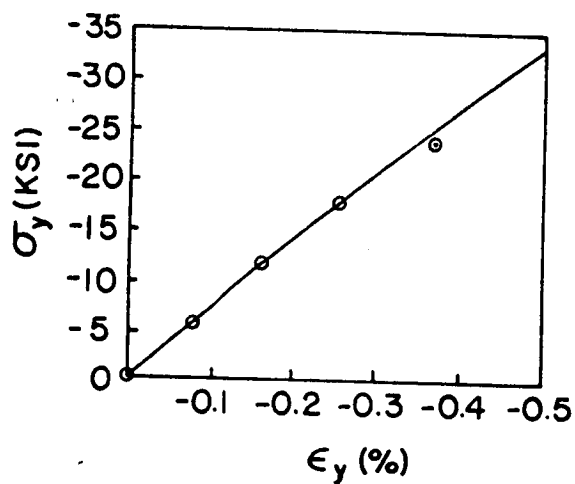
(b) $[(\pm 20)_{12}]_s$ Laminate Comparison

(c) $[(\pm 30)_{12}]_s$ Laminate Comparison
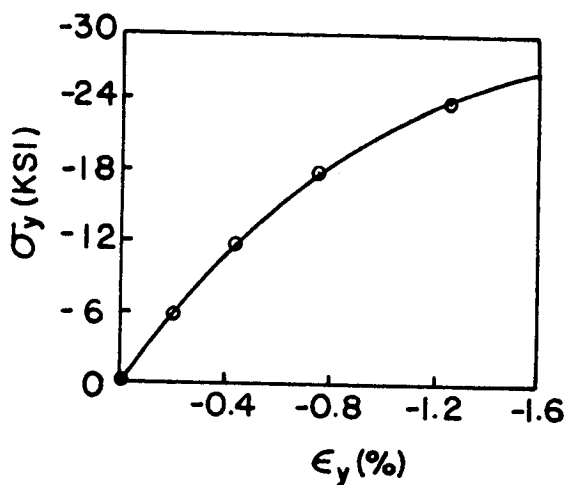
(d) $[(\pm 45)_{12}]_s$ Laminate Comparison

⊙ ENDOCHRONIC THEORY   —— EXPERIMENT

Figure 20. Analytical/Experimental Comparison of Angle-Ply Laminate Tests Using Parameter Set 4
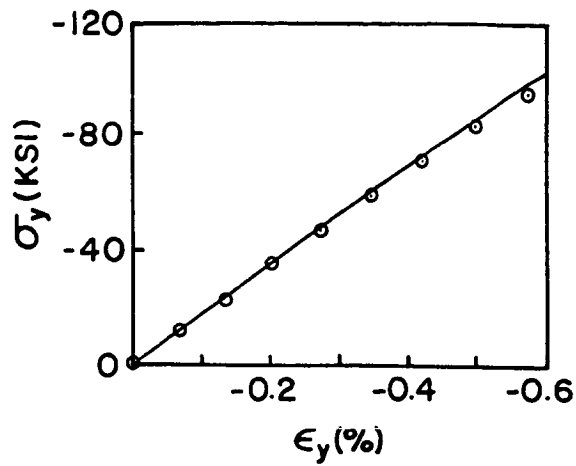
(a) $[(\pm 10)_{12}]_s$ Laminate Comparison
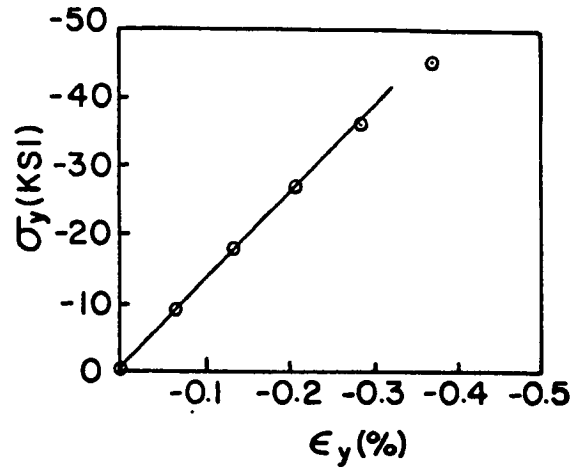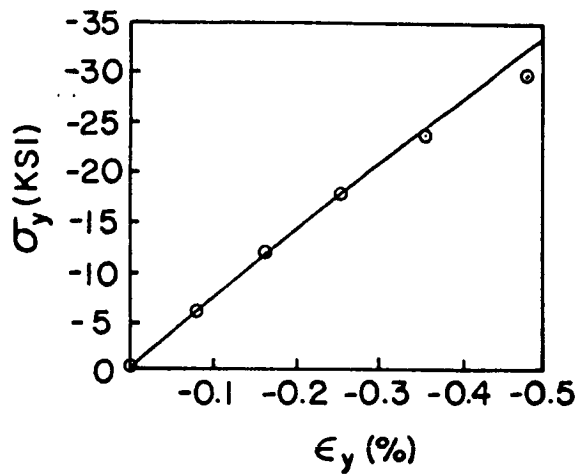
(b) $[(\pm 20)_{12}]_s$ Laminate Comparison

(c) $[(\pm 30)_{12}]_s$ Laminate Comparison
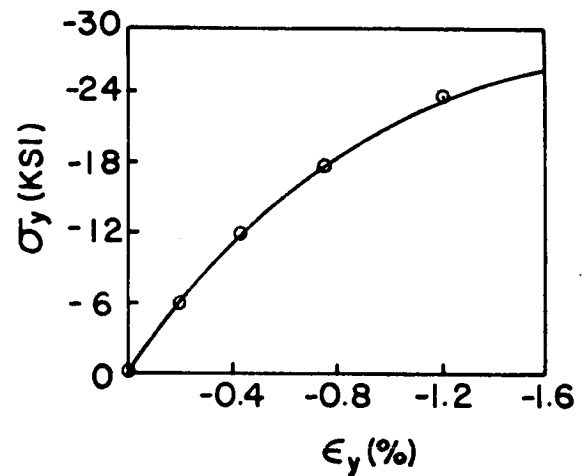
(d) $[(\pm 45)_{12}]_s$ Laminate Comparison

⊙ ENDOCHRONIC THEORY ——— EXPERIMENT

Figure 21. Analytical/Experimental Comparison of Angle-Ply Laminate Tests Using Parameter Set 5

wise fashion and for each step, the loading is assumed to be proportional. The step-iterative constant stress and constant strain algorithms developed in Chapter 3 were used in a finite element program to analyze laminate problems using a four element mesh. The flow charts for this program are analogous to those in Figure 30 and Figure 32 in Chapter 3.

The output from the finite element analysis was plotted against the experimental data [1] for $[\pm 10]_s$, $[\pm 20]_s$, $[\pm 30]_s$, and $[\pm 45]_s$ angle-ply laminates. These plots are shown in Figure 17 through Figure 21. Examining these figures shows that parameter set 2 (Figure 18) also fits the laminate experimental data most accurately. In fact, the correlation may be described as excellent. Many of the other parameter sets match one or two of the laminate tests well, but caused the solution algorithm to diverge for the other tests. This divergence is caused by certain stress components decreasing in magnitude (unloading) and is discussed in more detail in Chapter 4.

From the off-axis and laminate test comparisons, it is obvious that, overall, parameter set 2 correlates best with experimental results. With this parameter set chosen, a complete set of endochronic constants has been derived. The complete set of endochronic parameters are shown in Table 3. From this point on, these are the parameters used in all analyses.

2.5 Summary

This chapter has shown the development of a full set of three-dimensional endochronic equations, the development of the incremental form of these equations, and the experimental determination of a complete set of endochronic constants. The endochronic equations, based on the Conservation of Energy and the Dissipation Inequality, are slightly different in form

Table 3. "Best Fit" Set of Endochronic Parameters for AS4/3502 Graphite-Epoxy

A_{11} = 5.12687E-08	A_{12} = -1.70722E-08	A_{23} = -4.35111E-07
A_{22} = 6.55133E-07	A_{44} = 2.17931E-06	A_{66} = 1.18373E-06
S_{11} = 1.17136E-14	S_{12} = 1.22990E-13	S_{23} = 3.28159E-12
S_{22} = 3.28159E-12	S_{44} = 0.00000E-00	S_{66} = 3.28159E-12
B_{11} = 1.90645E-16	B^0_{22} = 3.14838E-04	B^0_{66} = 1.00000
n_1 = 2.44791E-00	n_2 = 2.45967E-00	n_6 = 3.18540E-00

where

A_{ij} units are 1/psi

All other parameters are dimensionless

from Pindera and Herakovich's[19] equations, due to a softening rather than stiffening behavior for compression loading in the fiber direction.

The incremental form of the endochronic equations allows them to be used in a finite element program. During each increment of loading, stress components are assumed to be proportional to one another and to the loading increment. This allows explicit integration of the equations. The final incremental form of the equations is a summation expression which may be implemented into a finite element or laminate analysis program.

Determination of the endochronic constants required analyzing uniaxial compression tests, off-axis tension tests, and Iosipescu shear tests. The final set of eighteen endochronic parameters obtained is unique to AS4/3502 graphite-epoxy. These constants are further unique in that they were derived assuming compression loading in the fiber direction.

3.0 Finite Element Program AMNISAP

3.1 Introduction

Out-of-plane interlaminar stresses are present in boundary layer regions near all free edges of notched angle-ply laminates subjected to in-plane loading. In order to account for this in a finite element analysis, three-dimensional elements are required. This study uses a three-dimensional, material nonlinear finite element program which is a modification of an existing linear elastic three-dimensional program [1]. The present program is called AMNISAP, which is an acronym for Anisotropic Material Nonlinear Inversion Symmetric Analysis Program.

Because of the extreme stress gradients present in the immediate region of the hole, a fine mesh was used in this region. In order to handle the large storage requirements produced by the fine mesh, a large capacity computer was necessary. Storage and run time efficiency were increased by utilizing an inversion symmetry condition and by running the program on a computer with vector processing capabilities.

Incorporation of the endochronic constitutive equations into a finite element program requires solving a set of nonlinear equations. There are many algorithms which may be used to solve such equations; each has its own advantages and disadvantages. This chapter examines some of the commonly used algorithms. The two algorithms used in the finite element program AMNISAP are developed and described in detail in this chapter.

3.2 Inversion Symmetry

Inversion symmetry is a symmetry condition present in all anisotropic shells and plates whose geometry, elastic coefficients, boundary conditions and loading are 180 degrees rotationally symmetric about some axis [45]. This axis of symmetry, commonly referred to as the center of symmetry, is normal to the body and intersects the origin of the in-plane coordinate axes. The two-dimensional inversion symmetry transformation consists of rotating the shell or plate through 180 degrees about the axis of symmetry. Defining an x_i coordinate system ($i = 1,2,3$), with the x_3 coordinate the axis of symmetry, a symmetry transformation changes the coordinates x_α ($\alpha = 1,2$) of each material point of the shell or plate into $-x_\alpha$. Figure 22 shows an anisotropic shell exhibiting the required conditions for inversion symmetry.

A plate's requirements are less stringent than a shell's requirements and are listed below.

INVERSION SYMMETRY PLATE REQUIREMENTS:

GEOMETRY

$$d(x_1, x_2) = d(-x_1, -x_2)$$

ELASTIC COEFFICIENTS
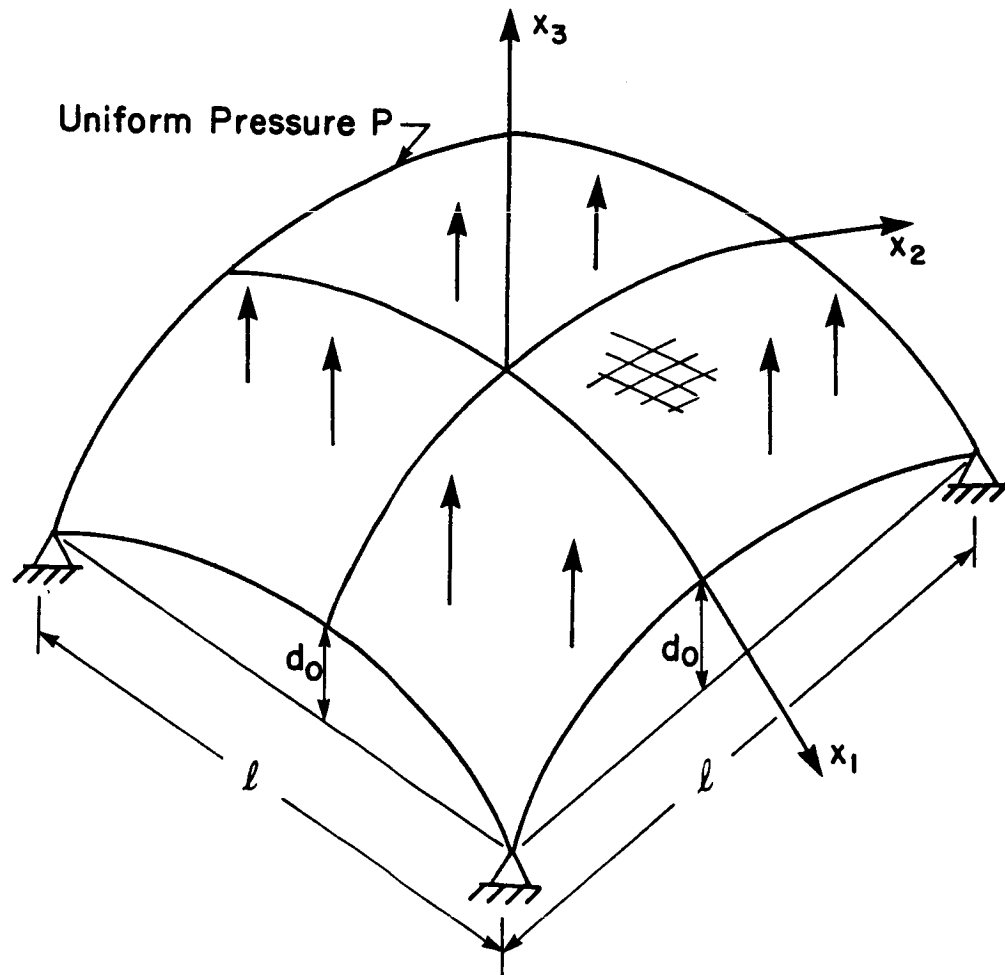
Figure 22.   Anisotropic Laminated Shell Exhibiting Inversion Symmetry Requirements

$$C_{\alpha\beta\gamma\rho}(x_1, x_2) = C_{\alpha\beta\gamma\rho}(-x_1, -x_2)$$

$$F_{\alpha\beta\gamma\rho}(x_1, x_2) = F_{\alpha\beta\gamma\rho}(-x_1, -x_2)$$

$$D_{\alpha\beta\gamma\rho}(x_1, x_2) = D_{\alpha\beta\gamma\rho}(-x_1, -x_2)$$

BOUNDARY CONDITIONS

$$B(x_1, x_2) = B(-x_1, -x_2)$$

LOADING

$$P(x_1, x_2) = P(-x_1, -x_2)$$

$$M(x_1, x_2) = M(-x_1, -x_2)$$

In the above, d is the distance from the center of symmetry to the plate boundary, $C_{\alpha\beta\gamma\rho}$ are the extensional stiffness coefficients, $F_{\alpha\beta\gamma\rho}$ are the bending-extension interaction coefficients, and $D_{\alpha\beta\gamma\rho}$ are the bending stiffness coefficients. B represents the boundary conditions, P represents the in-plane loads, and M represents moment (bending) loads. The response of an inversion symmetric plate to this loading will follow the relationships below.

INVERSION SYMMETRIC PLATE RESPONSE:

DISPLACEMENTS

$$U_1(x_1, x_2) = U_1(-x_1, -x_2)$$

$$U_2(x_1, x_2) = U_2(-x_1, -x_2)$$

$$W(x_1, x_2) = W(-x_1, -x_2)$$

STRESS RESULTANTS

$$\sigma_{\alpha\beta}(x_1, x_2) = \sigma_{\alpha\beta}(-x_1, -x_2)$$

$$\sigma_{\alpha 3}(x_1, x_2) = -\sigma_{\alpha 3}(-x_1, -x_2)$$

$$\sigma_{33}(x_1, x_2) = \sigma_{33}(-x_1, -x_2)$$

where $\alpha, \beta = 1, 2$

In the above, U_1 and U_2 represent the in-plane displacements in the x_1 and x_2 directions, and W represents the out-of-plane displacements. The stresses $\sigma_{\alpha\beta}$ are the in-plane components, $\sigma_{\alpha 3}$ are the out-of-plane shear stress components, and σ_{33} is the out-of-plane normal stress.

From these requirements, it is apparent that an angle-ply laminated plate with a central hole under uniaxial loading (Figure 23) exhibits inversion symmetry. The center of symmetry coincides with the center of the hole.

By combining the inversion symmetry condition with the mid-plane symmetry condition which is present in all symmetric laminates, only one quarter of the plate need be analyzed (Figure 23). The mid-plane symmetry condition is invoked simply by fixing the mid-plane nodal points' out-of-plane displacements W. Exploitation of the inversion symmetry condition requires modification of the finite element program. Appendix D gives a detailed description of the modifications required. It is desireable to add a flag variable for each nodal point of a finite element grid identifying those nodes which are independent and those which are dependent. Once these modifications are made, both inversion symmetric and non-inversion symmetric analysis may be performed with the same program.
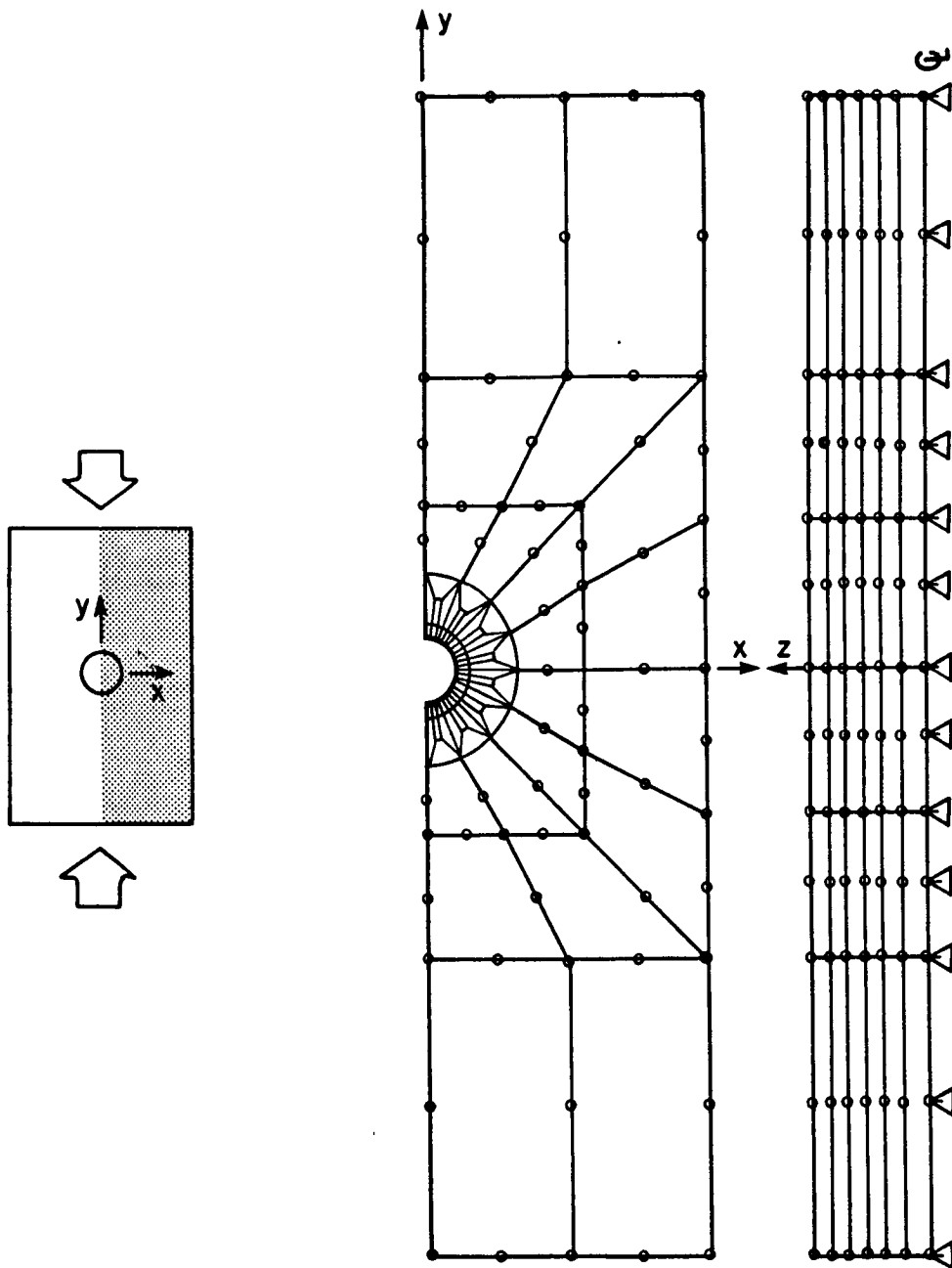
Figure 23. Inversion Symmetric Quarter Plate Analysis Using 124 Element Mesh

3.3 Vectorization

Even with the inversion symmetry condition fully utilized, the storage requirements for many of the analyses performed in this study (dependent upon mesh refinement) were excessive for the IBM 3090 or 3084 main frame computers at Virginia Tech. Therefore, the Cyber 205 super computer at the NASA Langley Research Center was used. This machine easily handled the storage requirements. An added bonus of the Cyber 205 is its parallel and vector processing capabilities. Using vector instructions, one instruction performs many operations, thus reducing CPU time significantly. The measure used to define this performance feature is MEGAFLOPS (Millions of Floating Point Operations Per Second). The Cyber 205 operates in the range of 50 to 200 MEGAFLOPS, depending upon the vector length. Appendix E shows an example subroutine comparing scalar operations to vector operations.

Because many do-loops in a program are not candidates for vectorization and because there are usually only a few do-loops which use the majority of CPU time, it is necessary to be selective when vectorizing a program. To determine which scalar code subroutines were the most time consuming, a timing option was run which output the total time and time per call for each subroutine. Table 4 shows these results. It is noted that these results vary depending upon job size. Table 4 shows that subroutines COLSOL (the global equation solver) and ELKAY (calculates the element stiffness matrices) used 85% of the total CPU time for the example considered. It is in these subroutines that the largest gains were realized through vectorization.

Subroutines COLSOL, ELKAY, and STRESS were vectorized by an automatic vectorizing utility named VAST. The FORTRAN program was run through this utility before it was compiled. VAST replaces scalar do loops with vector syntax wherever possible. It also returns a listing file which shows those do loops that were vectorized, lists those do-loops that weren't

Table 4. Timing Results for Scalar Linear Code Using a 20 Element Mesh

Subroutine	Call Freq. Counts	% Call Freq.	Total CPU Time (secs)	CPU Time Per Call	% Total CPU Time
ADDBAN	20	6	0.052793	0.002563	1
ADDRES	1	0	0.000767	0.000488	0
AMNISAP	0	0	0.015310	0.000000	0
ASSEM	1	0	0.045322	0.031250	1
BCIMP	1	0	0.017408	0.015625	0
BEDGE	20	6	0.000020	0.95E-06	0
BSTRS	1	0	0.040216	0.031250	1
CLEAR	1	0	0.009775	0.007813	0
COLHT	20	6	0.002568	0.000122	0
COLSOL	2	0	1.73258	0.750000	27
DMAT	2	0	0.001442	0.000488	0
DN16	2	0	0.000342	0.000122	0
DN20	2	0	0.000002	0.95E-06	0
DN24	2	0	0.000002	0.95e-06	0
ELKAY	20	6	3.78203	0.187500	58
ELSUM	2	0	0.042023	0.015625	1
ERROR	3	1	0.000006	0.000002	0
GCOORD	4	1	0.000060	0.000013	0
GPN16	2	0	0.000159	0.000061	0
GPN20	2	0	0.000002	0.95e-06	0
GPN24	2	0	0.000004	0.000002	0
INPUT	1	0	0.174491	0.125000	3
INVERT	180	53	0.004861	0.000027	0
LOADS	1	0	0.000744	0.000488	0
LOADV	1	0	0.002422	0.001953	0
STRESS	1	0	0.48726	0.250000	7
SYMDUMP	1	0	0.043696	0.031250	1
T	44	13	0.001848	0.000042	0
WRITE	1	0	0.046071	0.031250	1
TOTAL CALLS = 340			TOTAL CPU TIME = 6.499723 secs		

vectorized, and explains why certain do-loops were not vectorized. In many instances, simply rearranging a do-loop will allow VAST to vectorize it. In other cases, the algorithm must be rethought and changed. Besides using VAST on the above subroutines, a few do-loops throughout the program were vectorized explicitly using vector syntax. The major gains, however, were obtained through using VAST.

3.4 Program Efficiency Comparison

Table 5 shows vectorized timing results for a 20 element mesh (very coarse) model of a compression loaded angle-ply plate with a central hole. The comparison is for linear elastic analysis with no inversion symmetry. It must be noted that significantly larger speed factors are possible using a more refined mesh due to larger array sizes. Table 5 shows an overall speed factor of almost 4 with very little effort. Most of these gains were realized by rearranging do-loops within the subroutines.

Table 6 compares inversion symmetry analysis (which requires a quarter plate) with half plate and fixed node quarter plate analysis for a compression loaded $[\pm 30]_s$ laminate with a central hole. The fixed node quarter plate analysis is performed with the nodes along the y-axis fixed in the x-direction. These are approximate boundary conditions which give erroneous results in regions close to the y-axis but give acceptable results elsewhere [1]. Inversion symmetry results agree with half plate results everywhere. Note that the half plate storage requirements are more than 2.5 times the inversion symmetry requirements, while the inversion symmetry requirements are only 1.2 times greater than the fixed node quarter plate requirements. Half plate CPU time is more than 3.0 times that of inversion symmetry, yet inversion symmetry CPU time is only 1.3 times greater than that of the fixed node quarter plate analysis. Half plate total run cost is 2.9 times that of inversion symmetry, while inversion

Table 5. Vectorizing Timing Results for Non-Inversion Symmetric Linear Elastic Analysis Using a 20 Element Mesh

Vectorization Modifications	Total Run Time (CPU'S)	Overall Speed Factor	COLSOL Speed Factor	ELKAY Speed Factor	STRESS Speed Factor
AMNISAP in original form - no vectorization	6.50	1.00	1.00	1.00	1.00
VAST applied to AMNISAP (only subroutines ELKAY, COLSOL, STRESS)	3.49	1.86	5.44	1.65	1.22
VAST applied to AMNISAP - 2 do-loops in ELKAY modified (80 & 85)	3.18	2.04	5.42	1.91	1.22
VAST applied to AMNISAP - 2 more do-loops in ELKAY modified (60 & 70)	3.02	2.15	5.39	2.09	1.22
VAST applied to AMNISAP - 2 more do-loops in ELKAY modified (90 & 91)	1.75	3.72	5.41	6.97	1.22
VAST applied to AMNISAP - do-loop 100 modified in COLSOL	1.66	3.93	7.61	6.97	1.22

$$\text{Speed Factor} = \frac{\text{Original Run Time}}{\text{Vectorized Run Time}}$$

Table 6. Inversion Symmetry Results for $[\pm 30]_2$ Laminate with a Central Hole Run on Scalar Code

Parameters	Half Plate	Inversion Symmetry	Fixed Node 1/4 Plate
# of Elements	200	100	100
# of Nodes	2004	1041	1041
# of Equations	5338	2669	2698
# of Global Stiffness Terms	1,809,178	630,897	406,513
Total Storage (words)*	2,886,800	1,163,400	943,400
Maximum Half Bandwidth	5320	2606	366
Mean Half Bandwidth	338	236	150
CPU Time*	324.1	104.8	71.4
Run Costs (CRUs)*	356.4	124.3	99.2

* NASA Langley's Cyber 205

symmetry analysis' total run cost is only 1.3 times that of fixed node quarter plate analysis. In conclusion, for a fraction more of the fixed node quarter plate computer resources, half plate results are realized by using inversion symmetry at a significant reduction in computer resources.

If the results from Table 5 and Table 6 are combined, a total speed factor of 12 is realized when comparing half plate non-vectorized analysis to inversion symmetric vectorized analysis. Note also that this result is conservative being based on the speed factor for the 20 element mesh.

3.5 Numerical Solution of Nonlinear Algebraic Equations

Nonlinearities in structural mechanics exist in two forms -- material nonlinearities and geometric nonlinearities. Material nonlinearities arise from nonlinear constitutive laws. Geometric nonlinearities are the result of finite changes in the geometry of the body. Many numerical solution techniques are currently available for solving the set of nonlinear algebraic equations arising from both causes. However, all of these techniques have limitations. Some methods work well for geometric nonlinearities while others work best for material nonlinearities. The accuracy and efficiency of each method varies widely as well. All of these factors and features must be accounted for when choosing a method for a particular application.

This study focuses on material nonlinear finite element analysis. The solution techniques most commonly used for material nonlinearities are: (1) Incremental or stepwise procedures, (2) Iterative procedures, and (3) Step-iterative or mixed procedures. Each of these methods has its own distinct advantages and disadvantages and each one was considered as a sol-

ution technique in this study. Common to all of these techniques is the set of equations they must solve. This set is typically written for a single element as

$$[\bar{K}]\{U\} = \{F\} \qquad (3.1)$$

where

$$[\bar{K}] = [K] + [K^{NL}]$$

$$[K^{NL}] = [K^{NL}(\{U\}, \{F\})]$$

$$\{U\} \equiv \text{nodal displacements}$$

$$\{F\} \equiv \text{nodal forces}$$

$$[\bar{K}] \equiv \text{stiffness matrix}$$

$$[K] \equiv \text{linear portion of stiffness matrix}$$

$$[K^{NL}] \equiv \text{nonlinear portion of stiffness matrix}$$

Figure 24 shows a typical force/displacement curve for a given element and a typical nonlinear stress/strain curve. Following is a discussion of the solution techniques.

3.5.1 Incremental Procedures

Incremental procedures involve dividing the load into a series of increments. A solution is generated for each load increment until the final load is reached. Normally, the load increments are equal in magnitude but this is not a requirement. The stiffness matrix $[\bar{K}]$ is a constant for a given load step, but may change for each load increment. This matrix is re-
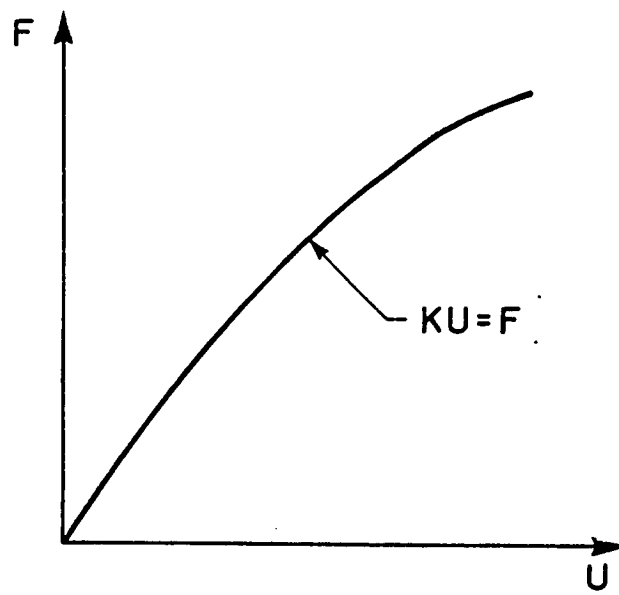
(a) Force-Displacement Curve
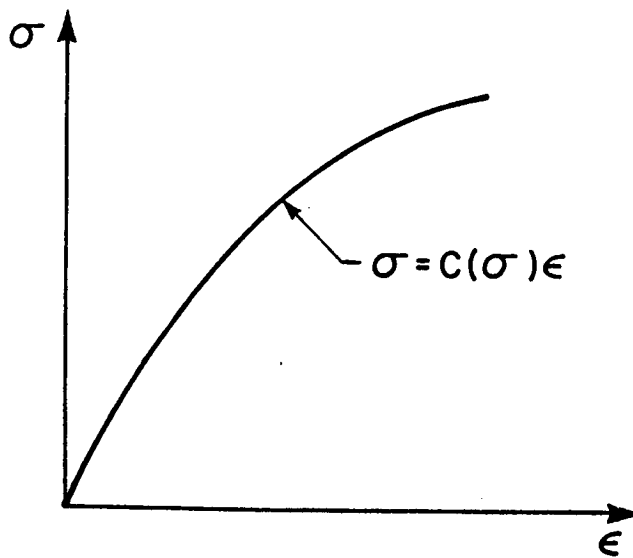
(b) Stress-Strain Curve

Figure 24. Typical Nonlinear Curves

ferred to as the tangent stiffness matrix in this procedure. For each incremental set of loads, a set of incremental displacements are generated. The final set of loads and displacements is the sum of the incremental loads and displacements. This is written symbolically as

$$\{F\} = \{F_0\} + \sum_{i=1}^{M} \{\Delta F_i\}$$

(3.2)

$$\{U\} = \{U_0\} + \sum_{i=1}^{M} \{\Delta U_i\}$$

where the Δ symbol represents an increment, M is the total number of increments, and subscripts 0 refer to the initial state. At a given load step,

$$\{F_j\} = \{F_0\} + \sum_{i=1}^{j} \{\Delta F_i\}$$

(3.3)

$$\{U_j\} = \{U_0\} + \sum_{i=1}^{j} \{\Delta U_i\}$$

The incremental element equations are then written as

$$[\overline{K}_{i-1}]\{\Delta U_i\} = \{\Delta F_i\} \quad \text{for } i = 1,2,3,.....,M$$

(3.4)

where

$$[\overline{K}_{i-1}] = [\overline{K}_{i-1}(\{U_{i-1}\}, \{F_{i-1}\})]$$

Figure 25 depicts this incremental procedure.

The accuracy of the incremental method is very dependent upon the load step size. The accuracy can be improved by taking smaller load steps. However, as load step size decreases and the number of load steps increases, the efficiency of the procedure decreases because $[\overline{K}_{i-1}]$ must be computed for each load step.

C - 2
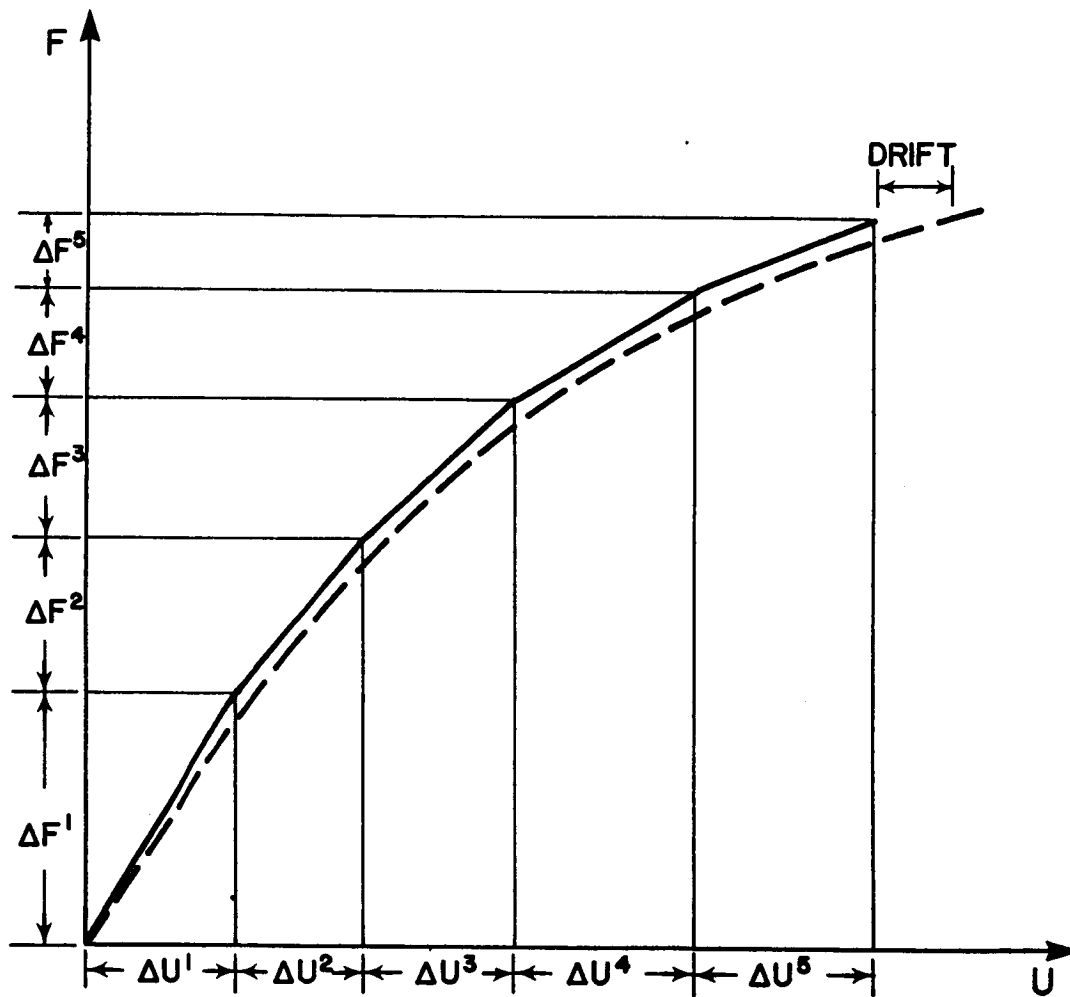
Figure 25. Force/Displacement Curve for a Typical Incremental Procedure

3.5.2 Iterative Procedures

Iterative procedures consist of a sequence of calculations in which force equilibrium is more exactly satisfied with each new iteration. The sequence of calculations (or iterations) is continued until the force imbalance (or residual) falls below an acceptable magnitude. The full force is applied at each iteration of this method. After each iteration, the force residual is calculated and used in the next iteration to compute the displacement.

The two most common iterative techniques used in finite element analysis are [46]: (1) Functional iterations (or successive substitutions) and (2) the Newton Raphson method. In both of these methods, the finite element equations are written

$$[K]\{U\} = \{F\} - \{F^{NL}\} \tag{3.5}$$

where

$$[K] \equiv \text{linear portion of stiffness matrix}$$

$$\{F\} \equiv \text{applied load vector}$$

$$\{F^{NL}\} \equiv \text{psuedo load vector resulting from } [K^{NL}]\{U\}$$

3.5.2.1 Method of Functional Iterations

This method seeks to find $\{U\}$ for a given $\{F\}$. It starts with an initial estimate of the displacements $\{U\}$ (solving the linear part of the finite element equations yields a reasonable estimate) and performs the following iteration sequence

$$[K]\{U^{(r)}\} = \{F\} - \{F^{NL}(\{U^{(r-1)}\})\} \tag{3.6}$$

where r, r − 1 refer to the iteration cycle. The sequence of iterations is continued until the difference in displacements between successive iterations falls below a preset value. The linear stiffness matrix [K] is decomposed only once and remains constant throughout the iterative process -- the changing nonlinear terms are contained in the psuedo load vector $\{F^{NL}\}$. Figure 26 shows a schematic representation of this iterative procedure for a one degree of freedom system.

3.5.2.2 Newton Raphson Method

In the Newton Raphson method, a force residual represents the initial unbalance between the two sides of equation (3.5). This force residual is written

$$\{f(U)\} = [K]\{U\} - \{F\} + \{F^{NL}\} \tag{3.7}$$

This method expands the force residual $\{f(U)\}$ in a Taylor Series about the initial estimate.

$$\{f(U + \Delta U)\} = \{f(U)\} + [\frac{\partial\{f(U)\}}{\partial\{U\}}]\{\Delta U\} + \text{Error}\left(\{\Delta U\}\right)^2 \tag{3.8}$$

An approximation used in the Newton Raphson Method is to truncate the series after two terms which yields the error term in the above expansion. A requirement of the method is to set the expanded force residual to zero, $\{f(U + \Delta U)\} = \{0\}$. These approximations yield

$$[\frac{\partial\{f(U)\}}{\partial\{U\}}]\{\Delta U\} = -\{f(U)\} \tag{3.9}$$

Now from equation (3.7), with $\{F\}$ independent of $\{U\}$

$$[\frac{\partial\{f(U)\}}{\partial\{U\}}] = [K] + [\frac{\partial\{F^{NL}\}}{\partial\{U\}}] = [K] + [\hat{K}(U)] \tag{3.10}$$
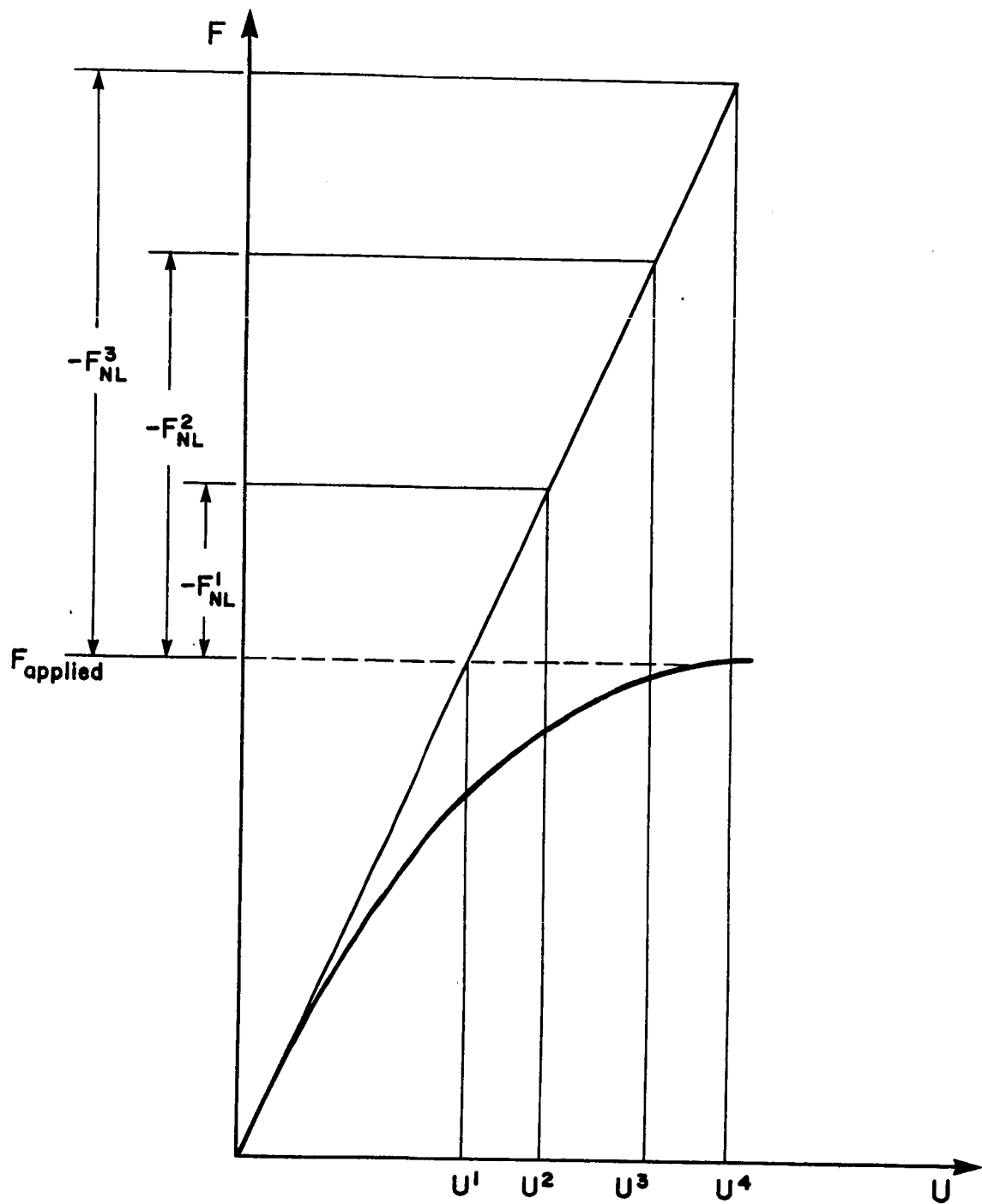
Figure 26.   Force/Displacement Curve for Functional Iteration Procedure

Combining (3.9) and (3.10) gives

$$[K + \hat{K}(U)] \{\Delta U\} = - \{f(U)\}$$

In terms of the iterative cycle, this is written

$$\left[[K] + [\hat{K}(u^{(r-1)})] \right] \{\Delta u^{(r)}\} = - \left\{ f(u^{(r-1)}) \right\} \qquad (3.11)$$

Note that each iterative cycle of the Newton Raphson Method requires computation of $\{f(U)\}$, computation of $[\hat{K}(U)]$, and decomposition, forward reduction, and back substitution to compute $\{\Delta U\}$. Figure 27 shows a schematic representation of this iteration procedure, where $\{K^r\}$ is the tangent stiffness matrix and the superscript r represents the iteration number.

3.5.3 Step-Iterative Procedures

Step-iterative procedures are simply a combination of incremental procedures and iterative procedures. These method yields higher accuracy but may require more computational effort. A typical step-iterative method is depicted in Figure 28. More details on this method are presented in a later section.

3.5.4 Procedure Comparison

The advantages of the incremental procedures are many fold, not the least being simplicity. They are easy to program, they admit a simple physical interpretation, they are applicable to nearly all types of nonlinear behavior, and they provide a relatively complete description of
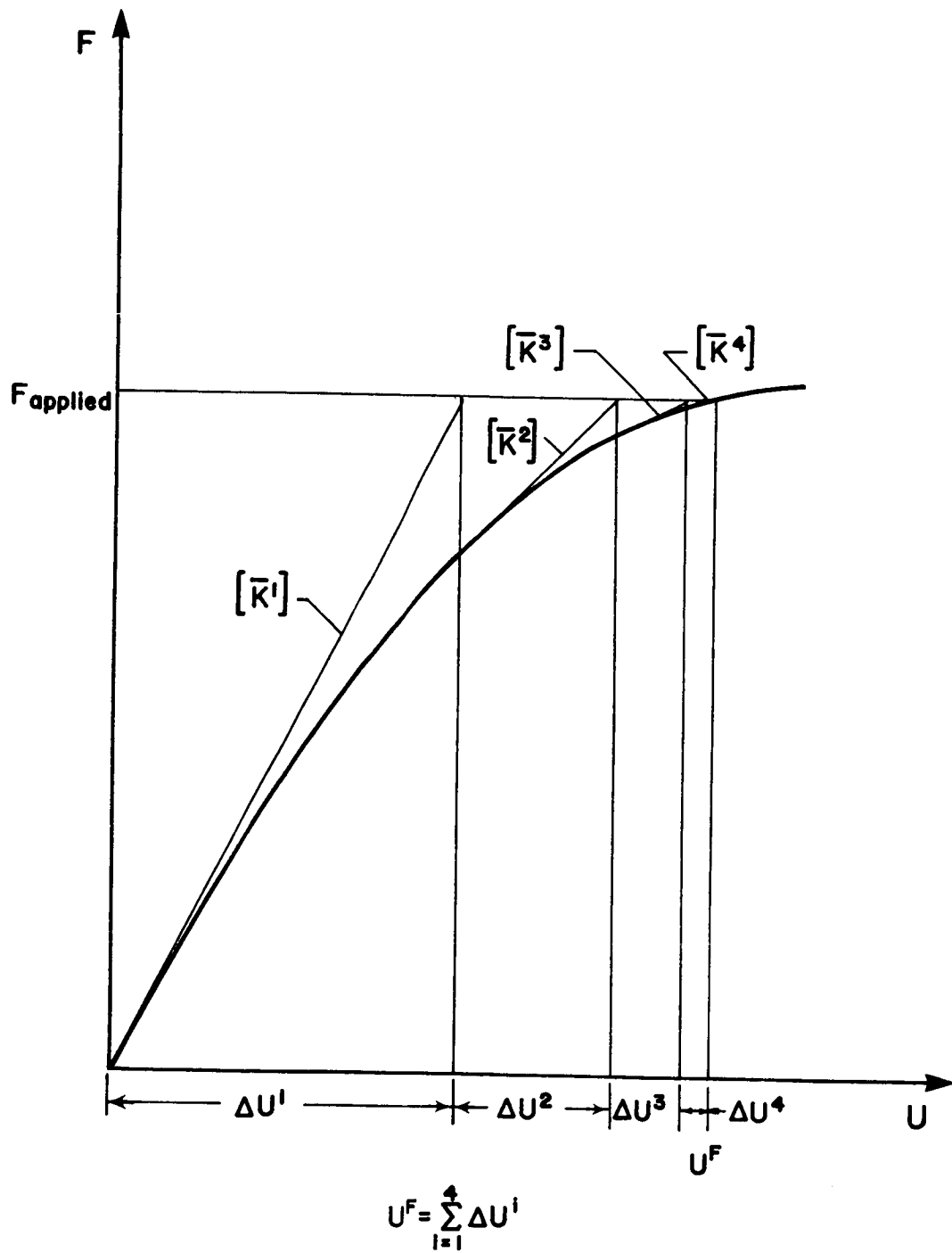
Figure 27. Force/Displacement Curve for Newton Raphson Procedure

$$U^F = \sum_{i=1}^{4} \Delta U^i$$

Finite Element Program AMNISAP
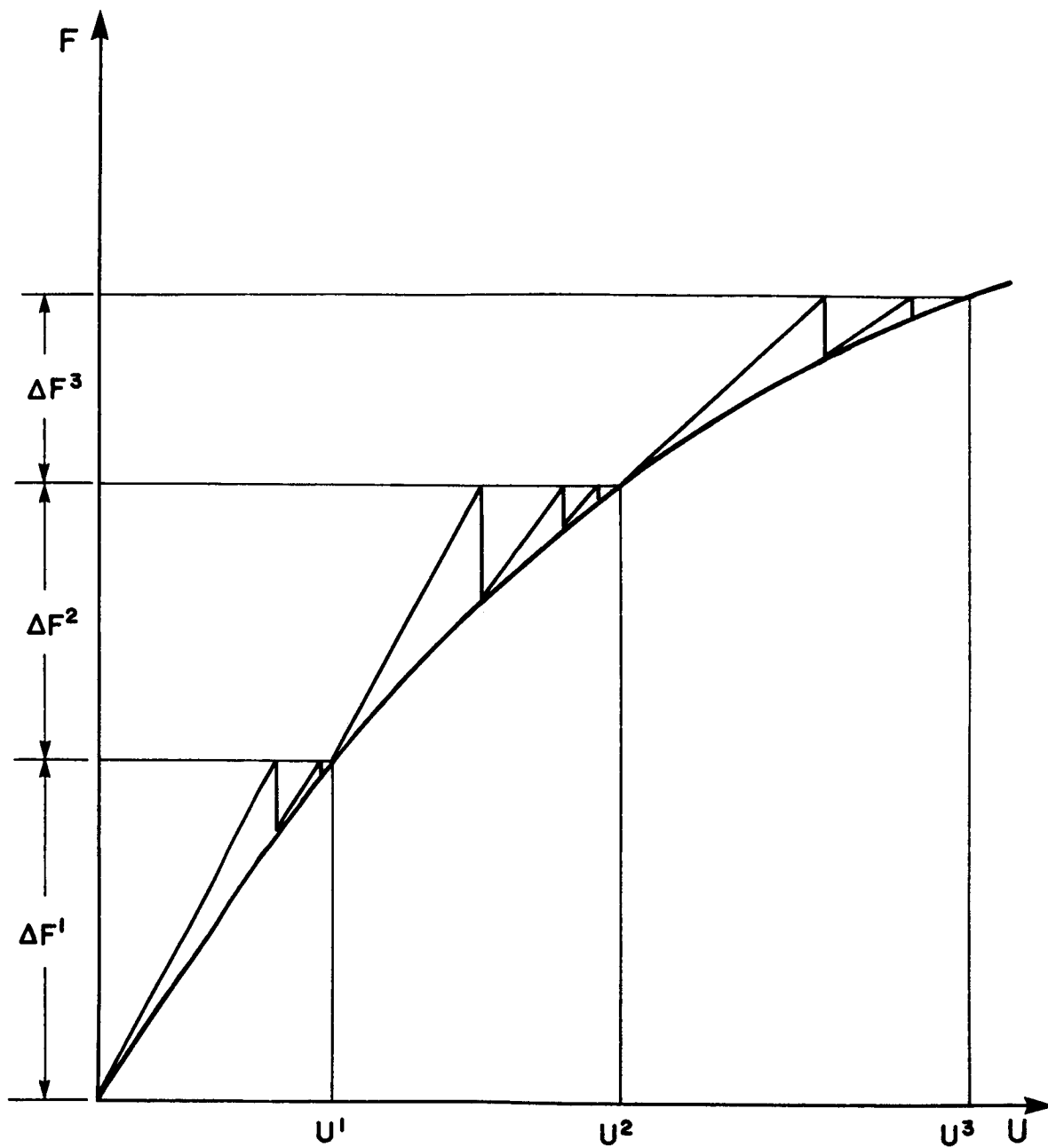
Figure 28. Force/Displacement Curve for a Typical Step-Iterative Procedure

the load-deformation behavior. However, their disadvantages are just as numerous. Incremental procedures require solving a linear system of algebraic equations at each step which necessitates formation of $[\bar{K}]$, and requires decomposition, forward reduction, and back substitution to compute $\{\Delta U\}$. Also, there is no rational way of selecting step size or checking convergence of the solution; hence the accuracy of the solution tends to drift.

The advantages and disadvantages of the iterative methods must be separated to include those of the functional iterative method and those of the Newton Raphson method. The advantages of the functional iterative method are its simplicity of application -- the stiffness matrix $[K]$ is decomposed only once -- and the solution's accuracy may be specified through the convergence criterion. However, the functional iterative method is not suitable for highly nonlinear problems. It displays slow convergence (and sometimes divergence) for elasto-plastic or near elasto-plastic problems, and the solution converges in a linear fashion requiring many iterations.

The Newton Raphson method's advantages are that it works well for highly nonlinear problems, and that it converges quadratically requiring fewer iterations (not necessarily faster CPU time). Its disadvantages include slow convergence for highly nonlinear problems, convergence problems due to oscillation about a local maximum or minimum point, and a high computational expense because $[K + \hat{K}]$ is decomposed many times.

The step iterative procedures combine the advantages of the incremental and iterative methods and tend to minimize the disadvantages. Because of this, step iterative methods have become increasingly prevalent in modern nonlinear finite element analysis.

Many factors were considered when choosing a nonlinear solution technique for the finite element program of this study. The first of these factors was the complexity of the endochronic equations. Explicit differentiation with respect to the displacements, as required in the Newton Raphson method, is very difficult if not impossible with the form of the endochronic equations.

Numerical differentiation requires still more complexity and computational time as well as an additional approximation in the solution. The form of the endochronic equations was also considered -- strain is written in terms of stress. Although a rederivation of the equations could yield stress in terms of strain, the endochronic parameters are much more difficult to determine with the equations in this form. Also, as shown in Chapter 2, the equations can only be integrated incrementally, with proportional loading assumed over each increment. Therefore, the form of the endochronic equations limited the choice of solution techniques. The final factor considered was the size of the finite element analysis. A method requiring many decompositions, forward reductions, and back substitution of the stiffness matrix would considerably increase CPU time.

With all these factors considered, two step-iterative procedures were chosen -- the constant stress method and the constant strain method. These methods are discussed and developed below.

3.5.5 Constant Stress Method

The constant stress method is an initial strain method in that the total strain is separated into a conservative portion and a non-conservative portion. The non-conservative strain (also called the irreversible strain) is integrated separately as a psuedo force array which is added to the applied force array to yield the total force array. Therefore, all the nonlinearities in the equations are represented by this psuedo force array. Because of this, the stiffness matrix [K] is decomposed only once in the solution process. This reduces CPU time and increases computational efficiency. The initial strain formulation of the finite element equations is shown below.

$$\{\varepsilon\} = \{\varepsilon^R\} + \{\varepsilon^{IR}\} \tag{3.12}$$

$$\{\varepsilon^R\} = [A]\{\sigma\}$$

$$\{\varepsilon^{IR}\} = \{\varepsilon^{IR}(z)\}$$

where

$$\{\varepsilon^R\} \equiv \text{ reversible portion of strain}$$

$$\{\varepsilon^{IR}\} \equiv \text{ irreversible portion of strain}$$

$$z \equiv \text{ intrinsic time scale}$$

Therefore,

$$\{\sigma\} = [A]^{-1}\{\varepsilon^R\} = [A]^{-1}\{\varepsilon - \varepsilon^{IR}\} \qquad (3.13)$$

The strain energy of an element ($\Lambda^\bullet$) is expressed as

$$\Lambda^e = \int_{V^\bullet} \frac{1}{2}\{\varepsilon^R\}^T\{\sigma\}dV = \int_{V^\bullet} \frac{1}{2}(\{\varepsilon\}^T\{\sigma\} - \{\varepsilon^{IR}\}^T\{\sigma\})dV \qquad (3.14)$$

where

$$V^e \equiv \text{ volume of an element}$$

Combining (3.13) and (3.14) gives the strain energy in the form

$$\Lambda^e = \int_{V^\bullet} \left(\frac{1}{2}\{\varepsilon\}^T[A]^{-1}\{\varepsilon\} - \frac{1}{2}\{\varepsilon\}^T[A]^{-1}\{\varepsilon^{IR}\} - \frac{1}{2}\{\varepsilon^{IR}\}^T[A]^{-1}\{\varepsilon\} + \frac{1}{2}\{\varepsilon^{IR}\}[A]^{-1}\{\varepsilon^{IR}\} \right) dV$$

$$\Lambda^e = \int_{V^\bullet} \frac{1}{2}(\{\varepsilon\}^T[A]^{-1}\{\varepsilon\} - 2\{\varepsilon\}^T[A]^{-1}\{\varepsilon^{IR}\} + \{\varepsilon^{IR}\}^T[A]^{-1}\{\varepsilon^{IR}\}) dV \qquad (3.15)$$

The strain-displacement equations can be written

Finite Element Program AMNISAP

$$\{\epsilon\} = [B]\{U\} \tag{3.16}$$

where [B] is a matrix containing the derivatives of the finite element interpolation functions. The transpose of the strain vector is

$$\{\epsilon\}^T = \{U\}^T[B]^T$$

Therefore,

$$\Lambda^e = \int_{V^e} \frac{1}{2} \left(\{U\}^T[B]^T[A]^{-1}[B]\{U\} - 2\{U\}^T[B]^T[A]^{-1}\{\epsilon^{IR}\} + \{\epsilon^{IR}\}^T[A]^{-1}\{\epsilon^{IR}\} \right) dV \tag{3.17}$$

The potential energy of an element due to externally applied forces is given by

$$\Gamma^e = -\{U\}^T\{P^e\} \tag{3.18}$$

where

$$\{P^e\} \equiv \text{ applied load vector for a given element}$$

The total potential energy of an element (Π^e) is the sum of the strain energy (Λ^e) and potential energy (Γ^e).

$$\Pi^e = \Lambda^e + \Gamma^e \tag{3.19}$$

The total potential energy of the finite element model is the sum of the elemental potential energy over the elements.

$$\Pi = \sum_{e=1}^{N} \Pi^e \tag{3.20}$$

Therefore, the total potential energy is

$$\Pi = \sum_{e=1}^{N}\left[\int_{V^e}\frac{1}{2}\{U\}^T[B]^T[A]^{-1}[B]\{U\}\,dV - \int_{V^e}\{U\}^T[B]^T[A]^{-1}\{\varepsilon^{IR}\}\,dV \right] + \qquad (3.21)$$

$$\sum_{e=1}^{N}\left[\int_{V^e}\{\varepsilon^{IR}\}^T[A]^{-1}\{\varepsilon^{IR}\}\,dV - \{U\}^T\{P^e\} \right]$$

where

$$N \equiv \text{number of elements}$$

In order to obtain the correct displacement solution solution from (3.21), the total potential energy Π must be minimized. This is done by taking the partial derivative of the total potential energy with respect to the displacements as follows

$$\frac{\partial\Pi}{\partial\{U\}} = \{0\} = \sum_{e=1}^{N}\left[\int_{V^e}[B]^T[A]^{-1}[B]\,dV\,\{U\} - \int_{V^e}[B]^T[A]^{-1}\{\varepsilon^{IR}\}\,dV - \{P^e\} \right] \qquad (3.22)$$

Defining:

$$[K^e] = \int_{V^e}[B]^T[A]^{-1}[B]\,dV$$

and

$$\{f^{NL}\} = \int_{V^e}[B]^T[A]^{-1}\{\varepsilon^{IR}\}\,dV$$

$$\{f^e\} = \{f^{NL}\} + \{P^e\}$$

where

$$[K^e] \equiv \text{element stiffness matrix}$$

$$\{f^{NL}\} \equiv \text{element psuedo load vector}$$

$$\{P^e\} \equiv \text{element force vector}$$

$$\{f^e\} \equiv \text{element total load vector}$$

gives

$$\sum_{e=1}^{N} \left\{ [K^e]\{U\} - \{f^e\} \right\} = \{0\}$$

where

$$N \equiv \text{number of elements}$$

Writing the above in global matrix form yields

$$[K]\{U\} = \{F\} \tag{3.23}$$

where

$$\{F\} = \left\{ F^{NL} \right\} + \{P\}$$

$$\left\{ F^{NL} \right\} = \sum_{e=1}^{N} \int_{V^e} [B]^T [A]^{-1} \left\{ \varepsilon^{IR} \right\} dV \equiv \text{global psuedo force array}$$

$$\{P\} = \sum_{e=1}^{N} \{P^e\} \equiv \text{global applied force array}$$

The iterative form of equation (3.23) is written as

$$[K] \left\{ U_i^{(r)} \right\} = \left\{ F^{NL}\left(\left\{ \Delta U_i^{(r-1)} \right\} \right) \right\} + \{P_i\} \tag{3.24}$$

where

$$r \equiv \text{iteration cycle}$$

$$i \equiv \text{load step number}$$

Note that the full load is applied at each step resulting in total (as opposed to incremental) displacements. This differs somewhat from true incremental procedures in which only an incremental load is applied at each step. Although the full load and full displacements are represented in the equations, the psuedo force array $\{F^{NL}\}$ is a function of the incremental stresses $\{\Delta\sigma\}$ at the previous iteration.

With the equations written in the above form, the constant stress method simply defines the order of calculations. This order of calculations is outlined below:

1) For a given load step i and iteration r, convergence is checked comparing the total displacements at the present iteration $\{U_i^{(r)}\}$ with the total displacements at the previous iteration $\{U_i^{(r-1)}\}$.

2) The element strains are computed from the element displacements

$$\{\varepsilon_i^{(r)}\} = [B]\{U_i^{(r)}\} \tag{3.25}$$

3) The stresses in the element are found from the strains at the current iteration $\{\varepsilon_i^{(r)}\}$ and the irreversible strains at the previous iteration $\{\varepsilon_i^{IR(r-1)}\}$

$$\{\sigma_i^{(r)}\} = [A]^{-1}\{\{\varepsilon_i^{(r)}\} - \{\varepsilon_i^{IR\,(r-1)}\}\} \tag{3.26}$$

4) The incremental stresses in the element are calculated by subtracting the stresses from the previous load step from the stresses at the present load step i

$$\{\Delta\sigma_i^{(r)}\} = \{\sigma_i^{(r)}\} - \{\sigma_{i-1}^{(r)}\} \tag{3.27}$$

Finite Element Program AMNISAP 99

5) The irreversible strains from the present iteration r are computed using the incremental stresses $\{\Delta\sigma_i^{(r)}\}$

$$\left\{\varepsilon_i^{IR\ (r)}\right\} = \left\{\varepsilon^{IR}\!\left(\left\{\Delta\sigma_i^{(r)}\right\}\right)\right\} \tag{3.28}$$

6) Finally, the psuedo forces for the r + 1 iteration are calculated from the irreversible strains at the present iteration r

$$\left\{F_i^{NL\ (r+1)}\right\} = \left\{F^{NL}\!\left(\left\{\varepsilon_i^{IR\ (r)}\right\}\right)\right\} \tag{3.29}$$

If displacement convergence is satisfied, the load is incremented and the process is repeated. If displacement convergence is not satisfied, the above sequence is repeated in a do-loop until a convergence criterion on the displacements is satisfied. The constant stress method gets its name because the sequence of calculations are performed at essentially a constant stress level. The displacements and thus the strains change during the iteration process until convergence is satisfied. Figure 29 gives a schematic representation of the constant stress method and Figure 30 shows a flow chart for the method.

3.5.6   The Constant Strain Method

The constant strain method is also an initial strain method and uses the same form of the finite element equations as the constant stress method. It differs only in the sequence of calculations required to solve the finite element equations. Whereas the constant stress method iterations were performed at essentially a constant stress level, the constant strain method iterations are performed at essentially a constant strain level. The stresses and thus the applied loads change during the iteration process until a convergence criterion is satisfied. Whereas the constant stress method consists of one do-loop, the constant strain method contains two do-loops -- an inner loop and an outer loop. The inner loop iterates at a given
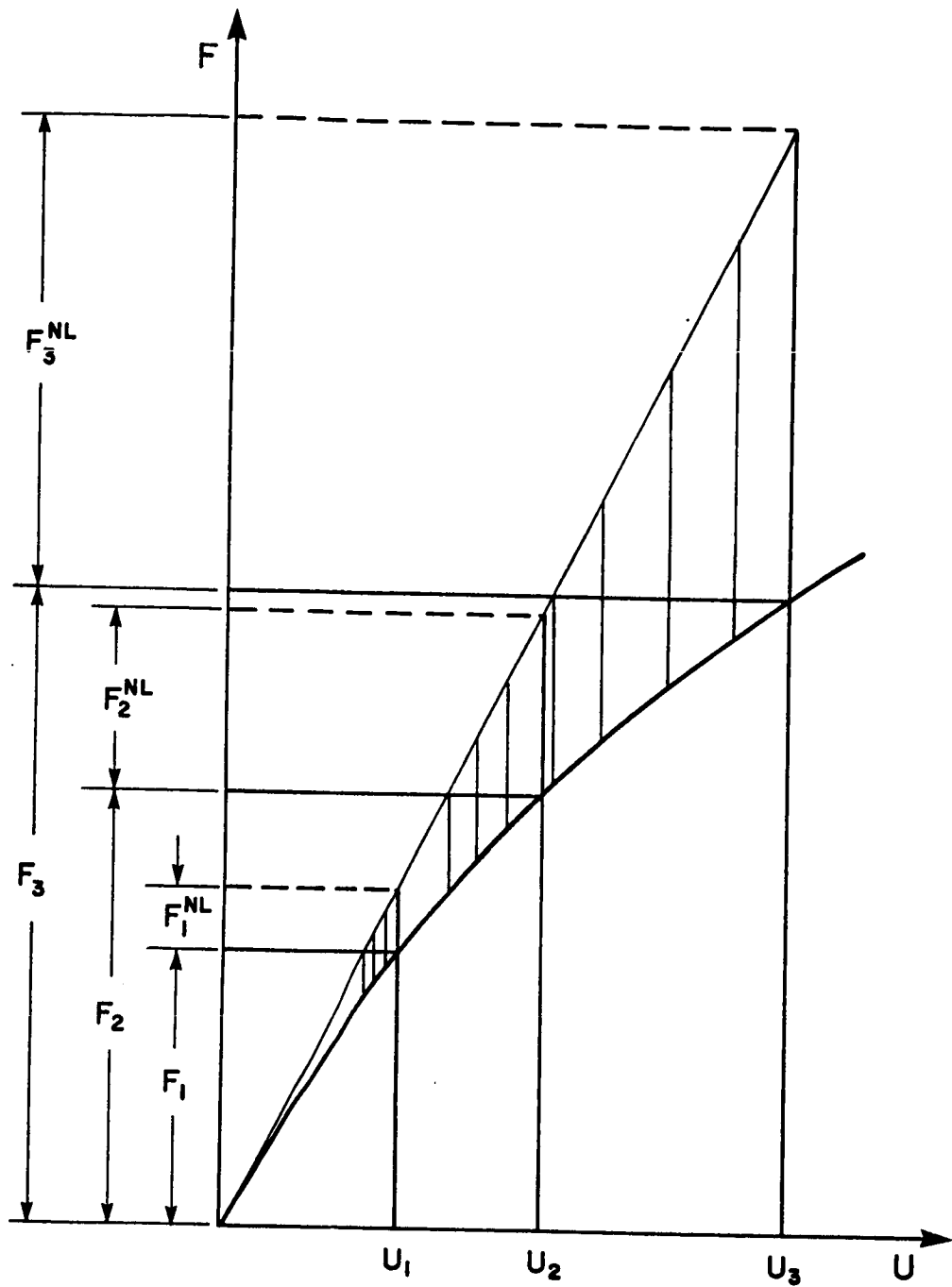
Figure 29.   Force/Displacement Curve for Constant Stress Method

```
┌─────────────────────────────────────┐
│   Calculate and assemble element stiffness │
│        matrices and nodal forces     │
└─────────────────────────────────────┘
                    │
                    ▼
┌─────────────────────────────────────┐
│          Solve for displacements     │
└─────────────────────────────────────┘
                    │
                    ▼
┌─────────────────────────────────────┐
│          Check for convergence       │
└─────────────────────────────────────┘
                    │
                    ▼
┌─────────────────────────────────────┐
│   Calculate strains from displacements │
└─────────────────────────────────────┘
                    │
                    ▼
┌─────────────────────────────────────┐
│       Calculate stresses from strains │
│        and previous plastic strains  │
└─────────────────────────────────────┘
                    │
                    ▼
┌─────────────────────────────────────┐
│       Calculate incremental stresses │
└─────────────────────────────────────┘
                    │
                    ▼
┌─────────────────────────────────────┐
│       Calculate plastic strains from │
│            incremental stresses      │
└─────────────────────────────────────┘
                    │
                    ▼
┌─────────────────────────────────────┐
│      Calculate psuedo force array    │
│          from plastic strains        │
└─────────────────────────────────────┘
                    │
          No        ▼
      ◄─────────┤  Convergence?          │
                    │
                    │ Yes
                    ▼
┌─────────────────────────────────────┐
│      Increment applied force array   │
└─────────────────────────────────────┘
                    │
          No        ▼
      ◄─────────┤ Check if force array is greater │
                 │ than final specified force array │
                    │
                    │ Yes
                    ▼
┌─────────────────────────────────────┐
│                Stop                  │
└─────────────────────────────────────┘
                    │
                    ▼
┌─────────────────────────────────────┐
│                End                   │
└─────────────────────────────────────┘
```

Iteration Limit Exceeded

Figure 30.   Flow Chart Showing Constant Stress Method

strain level until a stress convergence criterion is satisfied. The outer loop iterates until a displacement convergence criterion is satisfied. Once the the outer loop has converged, the procedure is incremented. The constant strain method is outlined below:

1) For a given load step i and iteration r, convergence is checked comparing the total displacements at the present iteration $\{U_i^{(r)}\}$ with the total displacements at the previous iteration $\{U_i^{(r-1)}\}$.

2) The element strains are computed from the element displacements

$$\left\{\varepsilon_i^{(r)}\right\} = [B]\left\{U_i^{(r)}\right\} \tag{3.30}$$

3) The stresses in the element are calculated from the strains of the current iteration $\{\varepsilon_i^{(r)}\}$ and the irreversible strains at the previous iteration $\{\varepsilon_i^{IR\,(r-1)}\}$.

$$\left\{\sigma_i^{(r)}\right\} = [A]^{-1}\left\{\left\{\varepsilon_i^{(r)}\right\} - \left\{\varepsilon_i^{IR\,(r-1)}\right\}\right\} \tag{3.31}$$

4) Convergence is checked comparing the total stresses at the present iteration $\{\sigma_i^{(r)}\}$ with the stresses at the previous iteration $\{\sigma_i^{(r-1)}\}$.

5) The incremental stresses in the element are calculated by subtracting the stresses from the previous load step from the stresses at the present load step i

$$\{\Delta\sigma_i^{(r)}\} = \{\sigma_i^{(r)}\} - \{\sigma_{i-1}^{(r)}\} \tag{3.32}$$

6) The irreversible strains for the present iteration r are computed using the incremental stresses $\{\Delta\sigma_i^{(r)}\}$

$$\left\{\varepsilon_i^{IR\,(r)}\right\} = \left\{\varepsilon^{IR}\left(\{\Delta\sigma_i^{(r)}\}\right)\right\} \tag{3.33}$$

7) If stress convergence is satisfied, then the solution proceeds. If it is not satisfied, the solution returns to step 3.

8) The psuedo force array for the r + 1 iteration is calculated from the irreversible strains at the present iteration r

$$\left\{ F_i^{NL\,(r+1)} \right\} = \left\{ F^{NL}\!\left(\left\{ \varepsilon_i^{IR\,(r)} \right\} \right) \right\} \tag{3.34}$$

If displacement convergence is satisfied, the load is incremented and the process is repeated. If displacement convergence is not satisfied, the equations are solved for the r + 1 iteration and the process is repeated. Figure 31 illustrates a schematic representation of the constant strain method and Figure 32 shows a flow chart.

3.6 Summary

The three-dimensional material nonlinear finite element program AMNISAP contains both the constant stress and the constant strain methods of solution. The user may choose the desired method. The reason for incorporating both methods into the program is that the constant stress method works better for some problems while the constant strain method works better for others.

The constant stress method has been previously shown to be inherently unstable under certain circumstances [46]; it may suddenly and catastrophically diverge. However, under stable conditions, it converges rapidly. On the other hand, the constant strain method is inherently stable, but converges much slower than the constant stress method. It too may diverge, but does so in a progressive, not catastrophic, manner.
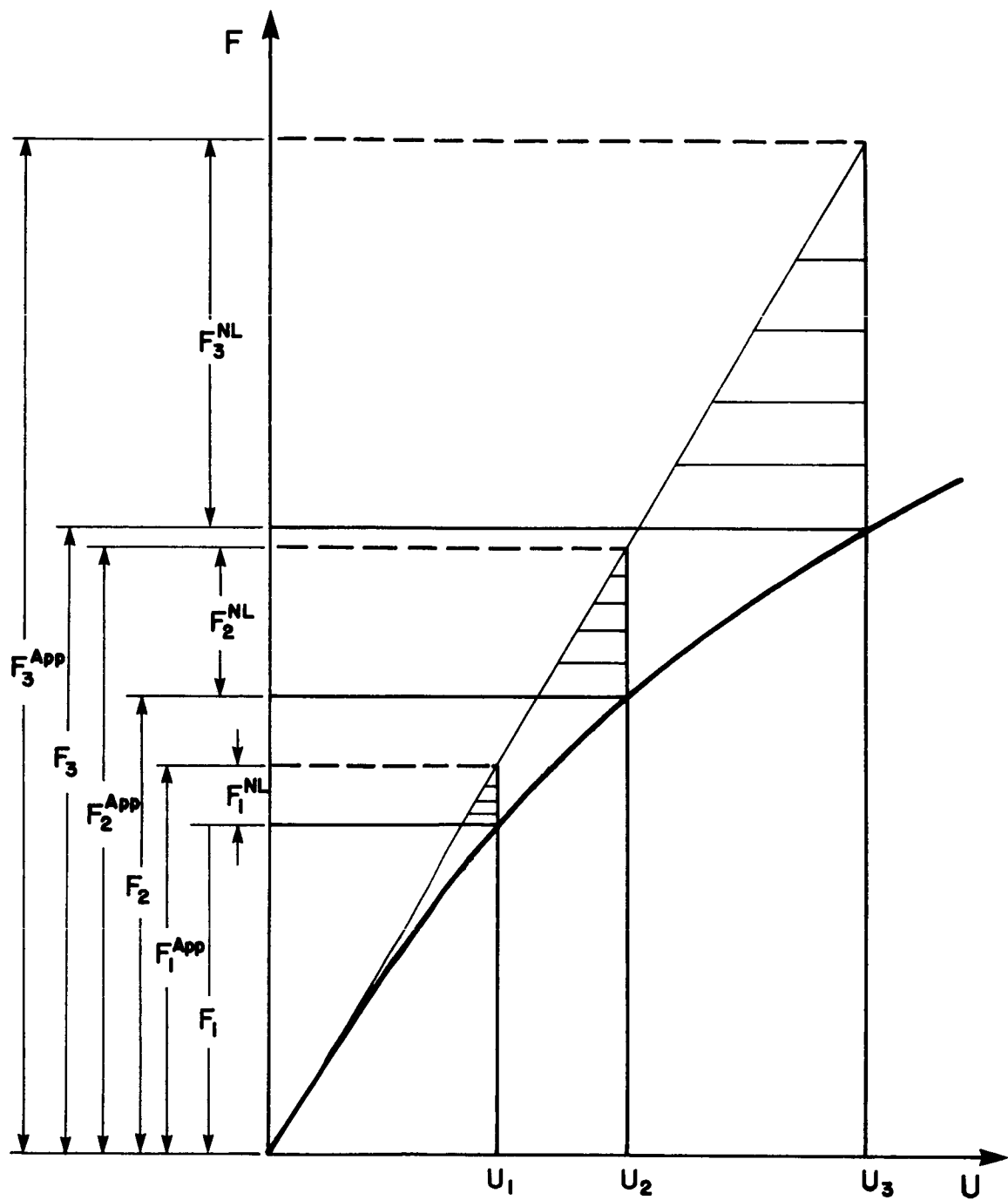
Figure 31. Force/Displacement Curve for Constant Strain Method
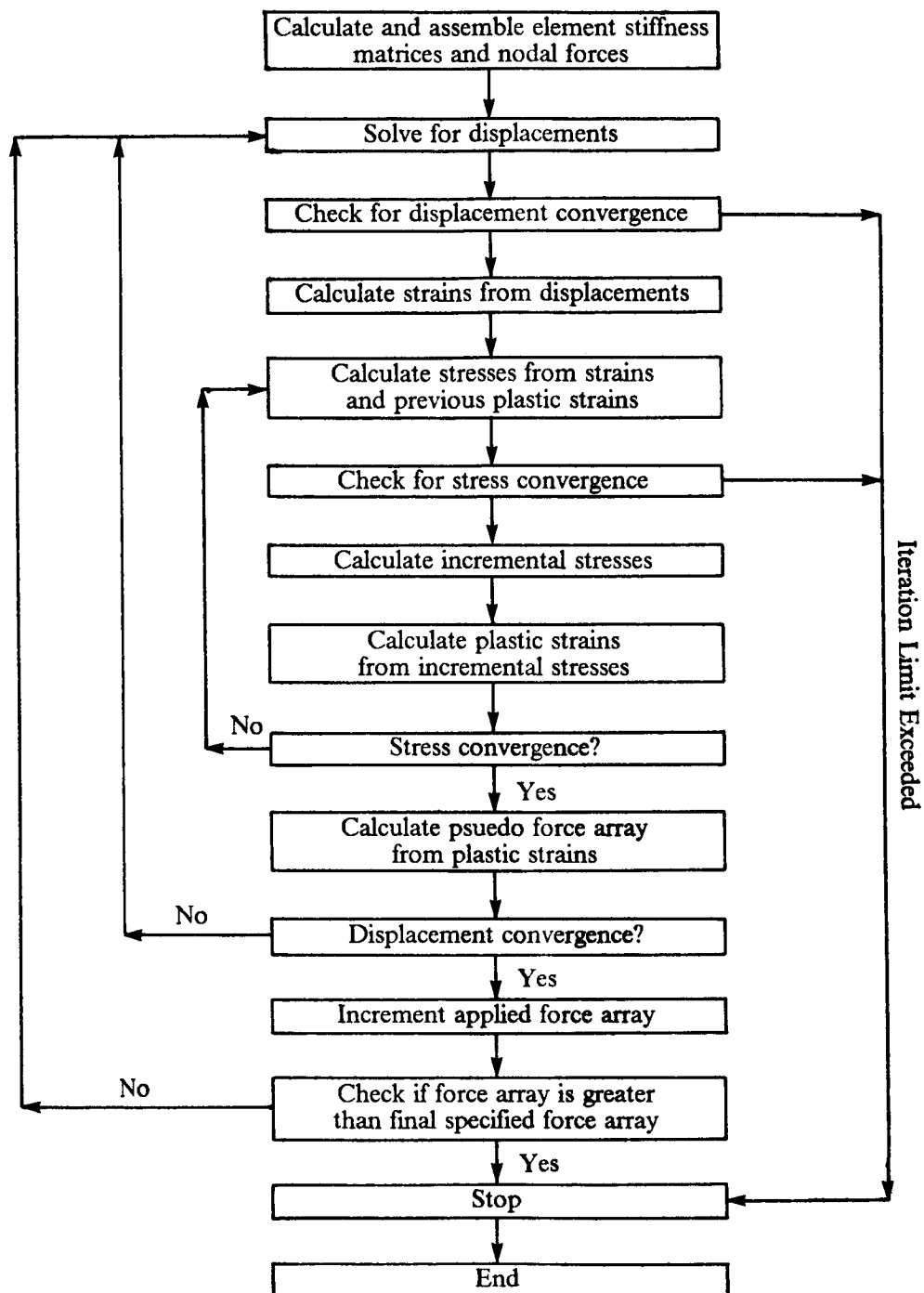
Figure 32. Flow Chart Showing Constant Strain Method

AMNISAP is a multipurpose program with options to run inversion symmetric or non- inversion symmetric analysis, and linear material or nonlinear material analysis. Within the nonlinear material option, the user may choose between two solution methods -- the constant stress method or the constant strain method. Finally, the program is written in Fortran 77 so that it is interchangeable with any computer facility having a Fortran 77 compiler.

4.0 Laminate Response

4.1 Introduction

This chapter presents an analysis of unnotched and notched angle-ply laminates loaded under uniaxial compression. In each analysis, analytical and experimental results are compared. Also, where appropriate, comparison is made between material linear and material non-linear predictions. The angle-ply laminates considered experimentally are: $[(\pm 10)_{12}]_s$, $[(\pm 20)_{12}]_s$, $[(\pm 30)_{12}]_s$, and $[(\pm 45)_{12}]_s$. Although these test laminates had 48 plies, they were modeled in the finite element analysis as having only 4 plies (i.e. $[\pm 10]_s$, $[\pm 20]_s$, $[\pm 30]_s$, and $[\pm 45]_s$) due to computer storage limitations. The analysis of unnotched laminates does not include edge effects and gives identical classical lamination theory results whether 48 plies or 4 plies are modeled. On the other hand, the analysis of laminates with holes does include edge effects around the hole boundary. These edge effects are dependent on the laminate stacking sequence. Since 48 ply laminates could not be investigated, it was decided to investigate four ply laminates which have the same alternating $\pm \varphi$ sequence as the 48 ply laminates. It is believed that the overall trends in the 4 ply laminates are similar to those in the 48 ply laminates. It is also important to note that the hole diameter is not the

same for all the notched laminates. Table 7 gives the dimensions of the laminates tested. The dimensions of the finite element models are identical to those in Table 7 except for the thickness dimension which was 0.01″ in all finite element models.

Note that the $[(\pm 10)_{12}]_s$ and $[(\pm 20)_{12}]_s$ laminates with 1/2″ diameter holes have a w/d (width to diameter) ratio of 5 while the other laminates have a w/d ratio of 10. The w/d ratio of 5 was used to investigate the influence of the width to diameter ratio on failure. In order to differentiate between the unnotched and notched laminates, they are referred to as $[\pm \varphi]_s$ and $[\pm (\varphi)_{12}]_s$, respectively.

4.2   Unloading Considerations

In the course of performing the finite element analysis, it was observed that the solution would converge quite rapidly for each load step up to a critical load level; however, at this critical load level, the solution would diverge rapidly. For some cases, this divergence phenomenon would occur before the load reached the experimentally observed failure load. Close investigation into this problem revealed that a component (or possibly many components) of stress was unloading at the critical load. Because the unloading causes a change in the sign of the slope (Figure 33) on the component's stress-strain diagram, the solution algorithm (either constant stress or constant strain) can not find the correct value of stress. The solution oscillates back and forth (with each oscillation growing larger) in an attempt to find the correct $\Delta\sigma_i$. Figure 33 shows this phenonomen schematically for the constant strain algorithm.

In Figure 33, the symbols σC_i and σ_i represent the stress level at the critical load and after the critical load step, respectively. The letter i represents the iteration number. At the critical load step, εC represents the strain from the initially applied load, and because the irreversible

Table 7. Test Specimen Dimensions

Layup	# of Specimens Tested	Length (in.)	Width (in.)	Thickness (in.)	Hole Diameter (in.)
Unnotched Laminates					
$[\pm 10]_s$	2	10.0	2.0	0.25	--
$[\pm 20]_s$	2	10.0	2.0	0.25	--
$[\pm 30]_s$	1	10.0	2.0	0.25	--
$[\pm 45]_s$	1	10.0	2.0	0.25	--
Notched Laminates					
$[(\pm 10)_{12}]_s$	2	10.0	2.5	0.25	0.25
$[(\pm 10)_{12}]_s$	2	10.0	2.5	0.25	0.50
$[(\pm 20)_{12}]_s$	2	10.0	2.5	0.25	0.25
$[(\pm 20)_{12}]_s$	2	10.0	2.5	0.25	0.50
$[(\pm 30)_{12}]_s$	1	10.0	5.0	0.25	0.50
$[(\pm 45)_{12}]_s$	1	10.0	5.0	0.25	0.50
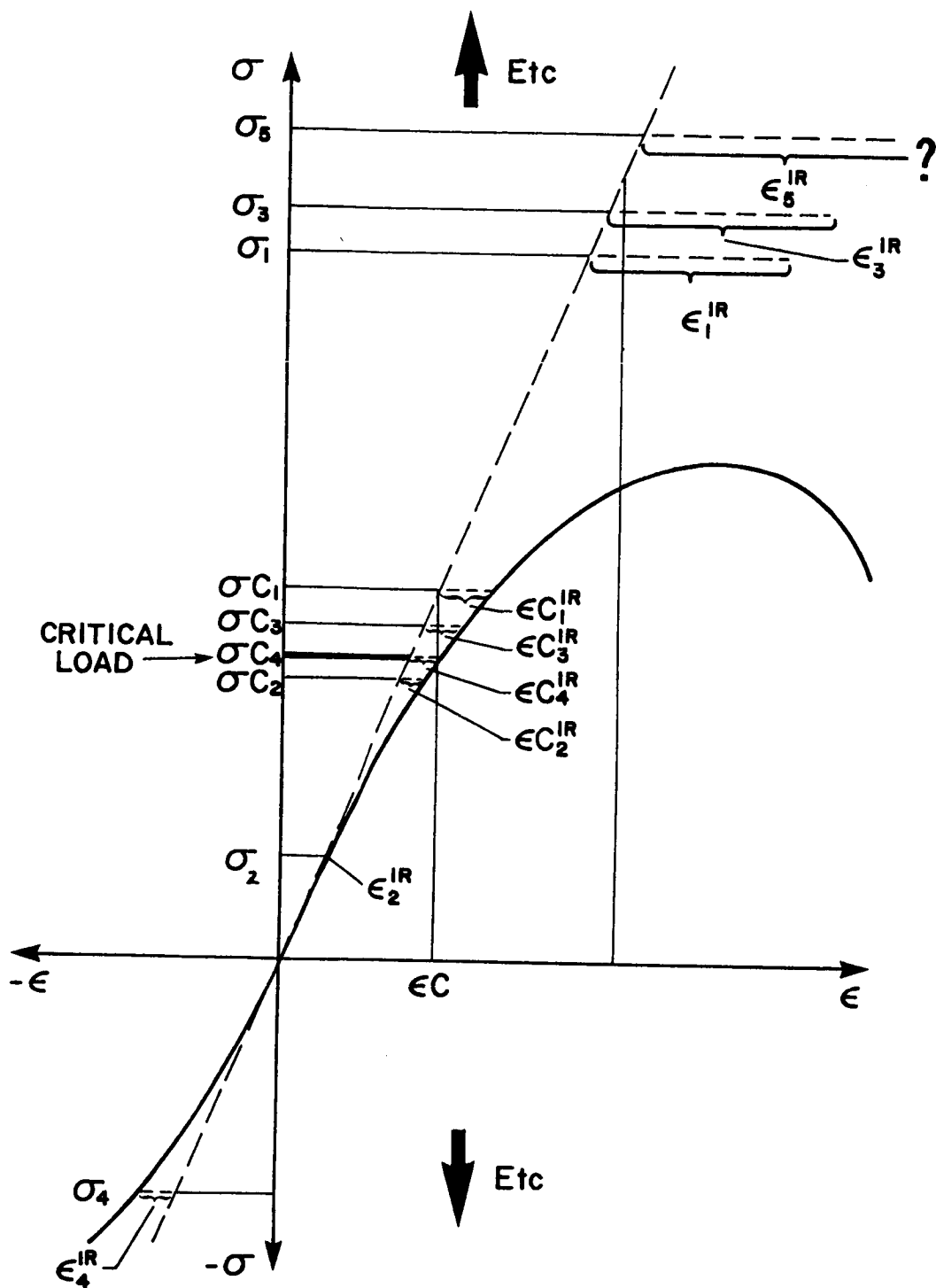
Figure 33. Oscillation About Inflection Point on Stress-Strain Diagram

strain has not yet been calculated, σC_1 corresponds to the linear elastic stress. The irreversible strain εC_1^{IR} is then calculated from σC_1 (3.29). Psuedo loads are calculated from εC_1^{IR} (3.30) and the process is repeated until a convergence criterion is satisfied at the fourth iteration. The stress σC_4 corresponds to the strain εC. At the following load step, the strain ε is calculated from the applied loads and psuedo loads. The stress σ_1 is calculated from the strain ε and εC_4^{IR} from the previous load step. The irreversible strain ε_1^{IR} is calculated from σ_1, but because the stress-strain curve slopes downward below stress level σ_1, the program calculates a large indeterminate value for ε_1^{IR} (imagine the curve continuing with no inflection point). At the second iteration, ε_1^{IR} is used to calculate σ_2. The irreversible strain ε_2^{IR} calculated from σ_2 is very small. At the third iteration, σ_3 is larger than σ_1 due to the small value of ε_2^{IR}. The irreversible strain ε_3^{IR} calculated from σ_3 is larger still than ε_1^{IR} and causes the stress σ_4 at the fourth iteration to be negative. When the stress becomes negative, divergence proceeds rapidly as the upwards and downwards arrows depict.

Although it is unknown whether this unloading phenomonen actually occurs in these laminates, the endochronic theory does predict it. Zinov'ev and Sarbaev [21] show a similar occurance for an unspecified fiberglass $[\pm 40]_s$ laminate loaded in uniaxial tension. Figure 5 in their paper shows the normal stress transverse to the fibers (σ_2) to be positive initially, but become negative approximately midway through the loading history. Because Zinov'ev and Sarbaev used a different formulation of the endochronic equations (i.e. they used multiple time scales whereas this study only uses a single time scale), it is highly unlikely that this phenomonen is an error in the formulation of the equations or in the finite element program. Rather, it appears that it is inherent to the endochronic theory. To prove or disprove whether the unloading is a real occurrence would require experimental verification.

Because the solution divergence phenomenon sometimes occurs before experimentally observed failure, a condition was imposed in the finite element program which allows the solution to progress past the critical load level. For the stress components which unload, the stress increments are set to zero ($\Delta\sigma_i = 0$) at the present load step and at all future load

steps. This essentially forces the components' stress-strain moduli to zero for the remainder of the loading history. In this manner, the strain components are calculated, but the stress components are artificially regulated. Of course, imposing this condition is equivalent to specifying an unknown, which hinders the solution's accuracy. However, this was found to be the most effective way to reach higher loading levels. In future sections, this condition is referred to as the zero-slope condition.

4.3 Experimental Results

Burns et al [1] performed experiments on the laminates listed in Table 7. The specimens were compression loaded quasi-statically in a rigid frame which provided clamped conditions at the loaded ends and simply supported conditions at the sides. Two specimens of each laminate configuration were tested except where noted in Table 7. Further detail of the experimental procedures is outlined in reference [1].

4.4 Finite Element Analysis

The material non-linear, three-dimensional finite element program AMNISAP was used to generate all the results. The elements used are 16 node, 3-D isoparametric displacement based elements. For further details of AMNISAP, refer to Chapter 3.

The finite element grid used to model the unnotched angle-ply laminates is an inversion symmetric 4 element mesh with one element through the thickness of each ply. This coarse mesh is not sensitive to edge effects and gives results identical to classical lamination theory.

The finite element grid used to model the notched angle-ply laminates with 1/2″ diameter holes is an inversion symmetric 744 element mesh; the 1/4″ diameter hole laminates were modeled with an inversion symmetric 792 element mesh. The meshes for the notched laminates have three elements through the thickness of each ply giving a total of six elements throughout the thickness of the laminates.

The ends of the laminates were loaded with a force distribution that gave each of the end nodes an approximately equal displacement. The end loading was modeled with end forces rather than end displacements so that it was not necessary to decompose the stiffness matrix for each iteration of the solution.

The load step size for each of the laminates was based upon the experimental failure loads. Twenty load steps were used as a compromise between accuracy and computational efficiency. The load step size for each laminate was determined by multiplying the experimental failure loads by approximately 1.2 and dividing by 20. The factor of 1.2 was used to allow the analyses to load past the experimental failure load if the solution proceeded for 20 load steps. An exception to this was used in analyzing the $[\pm 45]_s$ unnotched laminate. The results for this laminate exhibited more load step size sensitivity than the other laminates. In order to best match the experimental global stress-strain results, only 7 load steps were used. Table 8 shows the number of elements, number of nodal points, number of load steps, far field stress per load step, and the displacement based convergence criterion magnitude for each of the laminates analyzed.

The constant stress solution algorithm was used in all of the runs. This algorithm converged much faster than the constant strain algorithm. For laminates whose solution did not proceed to the experimentally observed failure load, the constant strain algorithm was used in an effort to advance the solution further. In all cases, no improvement was observed.

Table 8. Finite Element Parameters for Angle-Ply Laminates with and without Holes

Layup	Hole Size	# of Elements	# of Nodes	# of Load Steps	F.F.S. * per Load Step (psi)	Displacement Convergence Criterion
[± 10]$_s$	-	4	39	20	5760	0.001
[± 20]$_s$	-	4	39	20	2688	0.001
[± 30]$_s$	-	4	39	20	1920	0.001
[± 45]$_s$	-	4	39	7	6067	0.001
[(± 10)$_{12}$]$_s$	1/4″	792	3171	10	4608	0.001
[(± 20)$_{12}$]$_s$	1/4″	792	3171	13	2688	0.001
[(± 10)$_{12}$]$_s$	1/2″	744	2947	12	3840	0.001
[(± 20)$_{12}$]$_s$	1/2″	744	2947	15	2304	0.001
[(± 30)$_{12}$]$_s$	1/2″	744	2947	14	1920	0.001
[(± 45)$_{12}$]$_s$	1/2″	744	2947	13	1920	0.001

* F.F.S. - Far Field Stress

4.5 Unnotched Angle-Ply Laminates

4.5.1 Global Stress-Strain Response

4.5.1.1 Axial Response

Figure 34 shows comparisons of theory and experiment for the axial response of the four laminates considered. The experimental curves in Figure 34 are the same as those shown in Figure 18; however, the finite element results are given with smaller load steps in Figure 34. The curves are included in one figure for ease of comparison. As indicated in the figure, the comparison between theory and experiment is quite good. The response of the [± 10]$_s$, [± 20]$_s$, and [± 30]$_s$ laminates is nearly linear to failure whereas the [± 45]$_s$ laminate exhibits significant nonlinearity.

Comparison between theory and experiment is generally good; however, some interesting phenomena can be noted. Near the point of failure, the [± 10]$_s$ laminate exhibits more axial softening response than the [± 20]$_s$ laminate. This is due in part to the high compressive stress σ_1 in the [± 10]$_s$ laminate which causes some fiber direction softening. In addition, the [± 10]$_s$ laminate's response is more dependent upon the fiber direction response. The fiber direction softening response can be seen in Figure 2 of Chapter 2. Note that at equal stress levels, the [± 20]$_s$ laminate exhibits more axial softening response than the [± 10]$_s$ laminate (Figure 34). The [± 30]$_s$ laminate exhibits more nonlinear response than the [± 20]$_s$ laminate because of higher magnitudes of σ_6 (τ_{12}) and a greater dependence on the transverse and shear response. Due to an even greater dependency upon the transverse and shear response, the [± 45]$_s$ laminate shows significant axial softening.
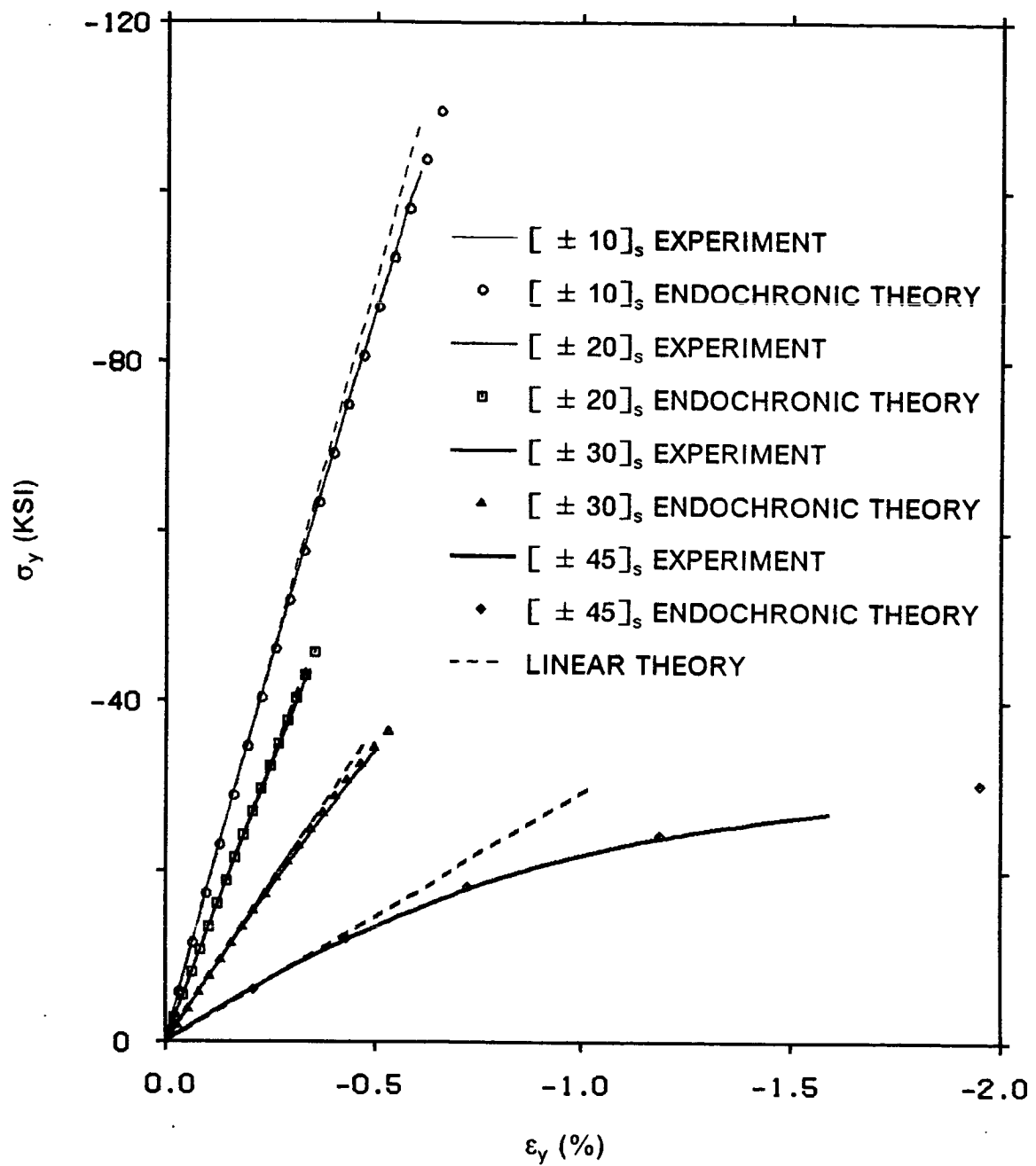
Figure 34. σ_y Versus ε_y for Unnotched Laminates -- AS4/3502 Graphite-Epoxy

4.5.1.2 Transverse Response

As can be seen in Figure 35, the agreement between theory and experiment for the transverse strain response of the four angle-ply laminates is generally good, but not quite as good as that for the axial response. In general, the predicted transverse strain response is stiffer than the experimental response for all the laminates. The predicted transverse strain response of the $[\pm 10]_s$ laminate falls between the linear elastic and experiment curves. The $[\pm 20]_s$ laminate's predicted transverse strain response follows the same trend as that of the $[\pm 10]_s$ laminate. The $[\pm 30]_s$ laminate's experimental transverse strain response shows significant softening. Unfortunately, the predicted response does not correlate as well with experiment, falling between the linear transverse strain curve and the experimental curve. Agreement between theory and experiment is very good for the $[\pm 45]_s$ laminate in which the most softening occurs. Considering the degree of softening, the correlation between the predicted transverse strain response and the experimental transverse strain response is excellent.

4.5.2 Response in Material Principal Coordinates

Examining the predicted stress-strain response in material principal coordinates reveals some interesting results. The fiber direction response (Figure 36) is intuitively predictable because ε_1^{IR} is only a function of σ_1 (2.11). Therefore, the degree of softening is directly related to the magnitude of σ_1. As Figure 36 shows, the magnitude of σ_1 is largest in the $[\pm 10]_s$ laminate and smallest in the $[\pm 45]_s$ laminate. Therefore, the $[\pm 10]_s$ laminate exhibits the greatest fiber direction softening and the $[\pm 45]_s$ laminate the least. Unlike the fiber direction response, the stress-strain response in the other principal material directions is not intuitively predictable. The non-linear strains in the transverse and shear directions may or may not be similar to the softening response in pure transverse loading or shear loading, respectively.

Figure 35. σ_y Versus ε_x for Unnotched Laminates -- AS4/3502 Graphite-Epoxy

(a) [± 10]ₛ **Unnotched Laminate**
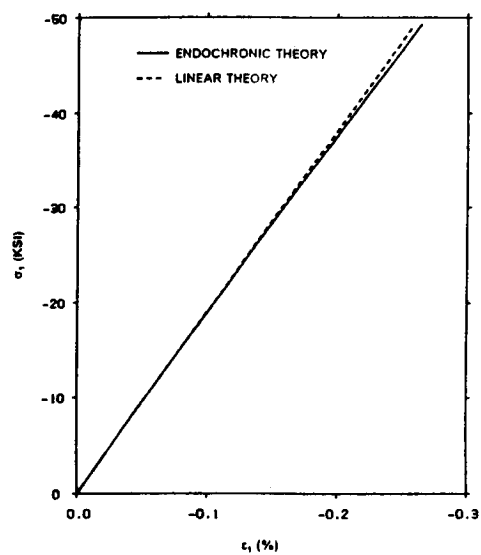
(b) [± 20]ₛ **Unnotched Laminate**
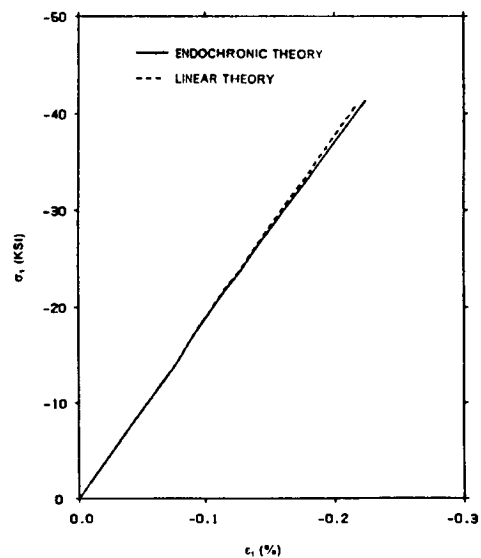
(c) [± 30]ₛ **Unnotched Laminate**

(d) [± 45]ₛ **Unnotched Laminate**

Figure 36. σ_1 Versus ε_1 for Unnotched Laminates -- AS4/3502 Graphite-Epoxy

The transverse direction response in these laminates can be compared to the transverse direction response under pure compression loading (see Figure 4 in Chapter 2) and to the linear elastic response (Figure 37). As shown in Figure 37, the $[\pm 10]_s$, $[\pm 20]_s$, and $[\pm 30]_s$ laminates show transverse direction stiffening response, and the $[\pm 45]_s$ laminate exhibits softening response. Note that σ_2 is positive in the laminates which show stiffening response ($[\pm 10]_s$, $[\pm 20]_s$, and $[\pm 30]_s$), but is negative in the laminate which shows softening response ($[\pm 45]_s$). This stiffening response may be due to the endochronic parameters' inability to model mixed principal coordinate stress states (σ_1 is negative in all the laminates); recall that the parameters were developed from uniaxial tests in which all stresses were of the same sign. Another possible explanation of this behavior is that the predicted stiffening response is real and exists within the laminates. However, without experimental results, it is difficult to prove or disprove this behavior. As a side note, it is possible that the endochronic parameters' inability to model mixed stress states caused the predicted global transverse strain response to be stiffer than experiment (Figure 35) for the $[\pm 10]_s$, $[\pm 20]_s$, and $[\pm 30]_s$ laminates. Recall that agreement was good for the $[\pm 45]_s$ laminate in which the principal stress states are of the same sign.

The predicted shear response in these laminates is compared to the pure shear loading response (Iosipescu test), off-axis loading response, and linear elastic response in Figure 38. All predicted curves show a softening response; however, the degree of softening differs among the laminates. The $[\pm 10]_s$ laminate exhibits more shear softening than both the 10° off-axis and Iosipescu tests. At a shear stress of 2.7 ksi, the predicted shear strain deviates -7.4% from linear strain, -5.1% from the 10° off-axis test strain, and -8.7% from the Iosipescu test strain. Both the 10° off-axis and Iosipescu tests show nearly linear response at the low shear stress level in the $[\pm 10]_s$ laminate (less than 3 ksi). The $[\pm 20]_s$ laminate exhibits less shear softening than the 15° off-axis test, but slightly more softening than the Iosipescu test. Actually, within the $[\pm 20]_s$ laminate, the predicted response is very nearly linear up to the maximum level of shear stress (4 ksi). At a shear stress of 3.7 ksi, the predicted shear
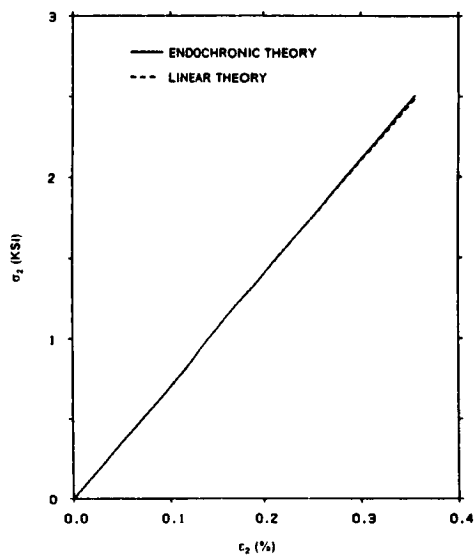
(a) [± 10]ₛ **Unnotched Laminate**
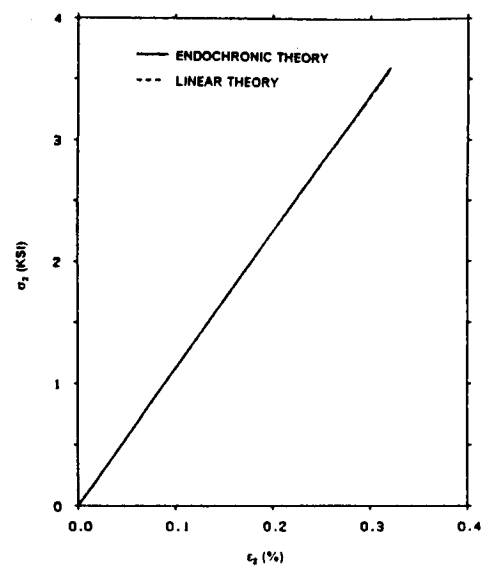
(b) [± 20]ₛ **Unnotched Laminate**
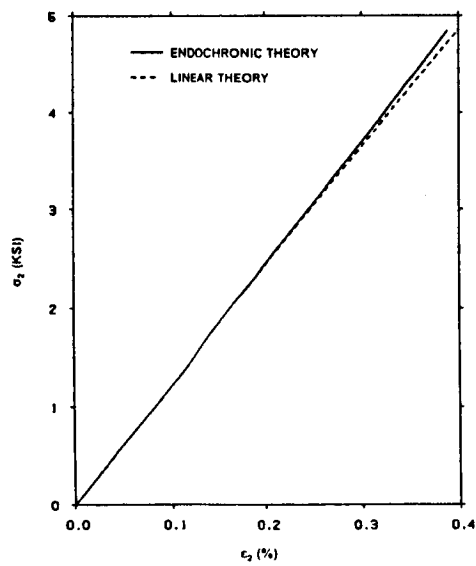
(c) [± 30]ₛ **Unnotched Laminate**
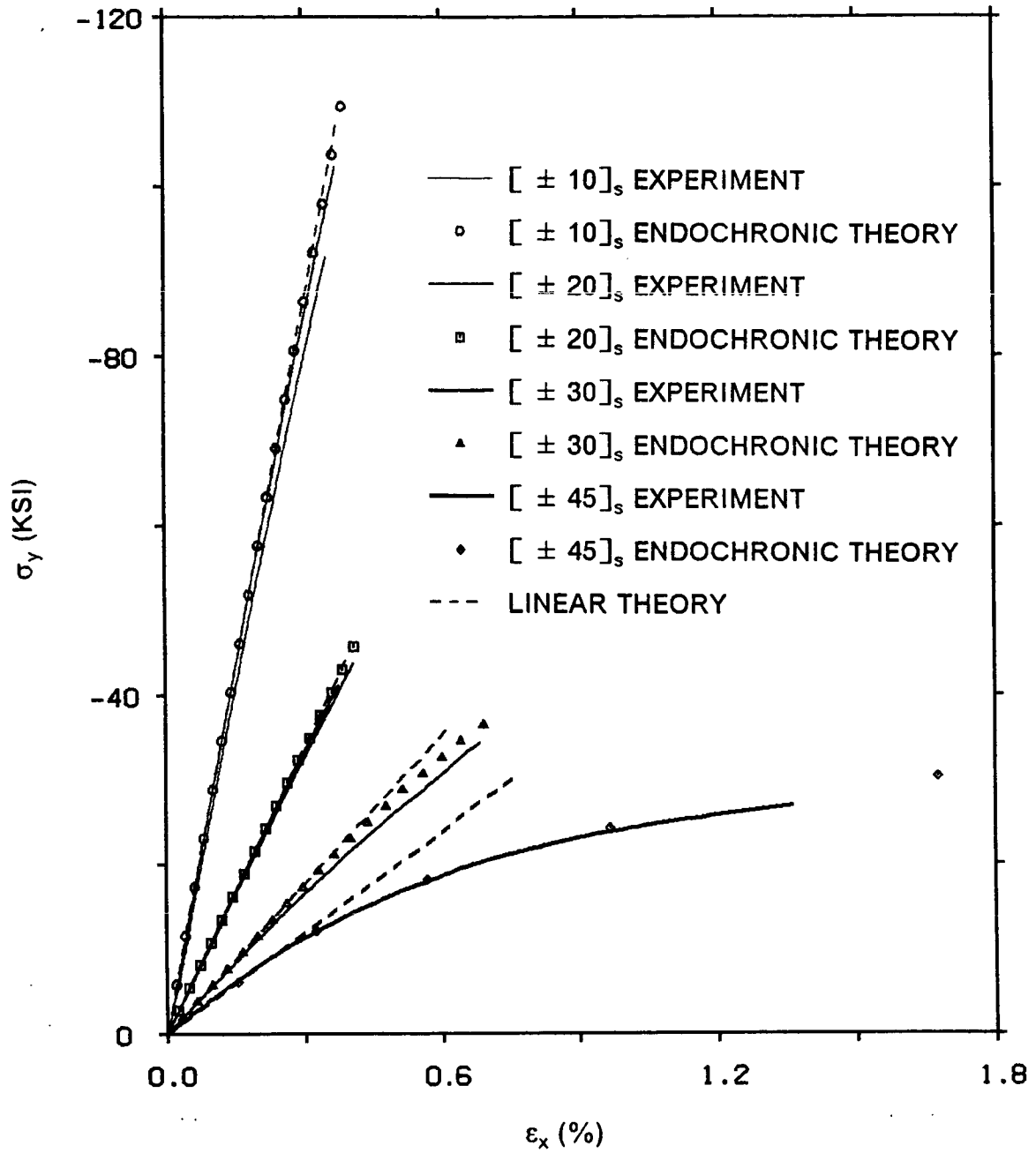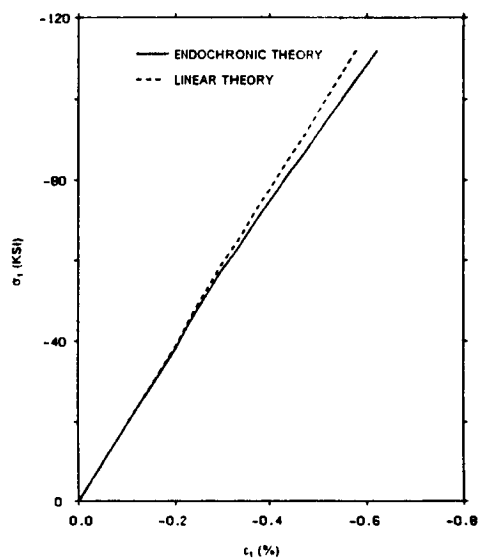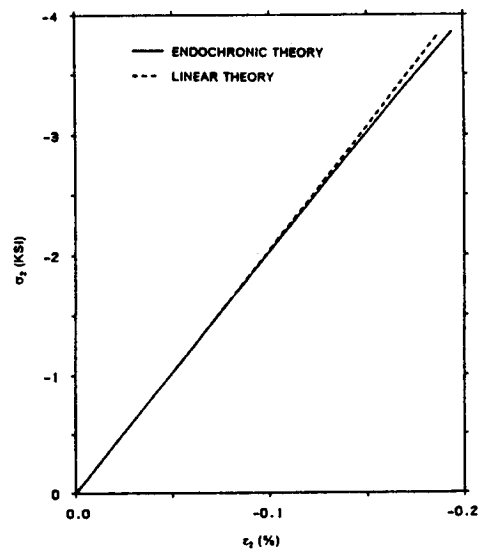
(d) [± 45]ₛ **Unnotched Laminate**

Figure 37. σ_2 Versus ε_2 for Unnotched Laminates -- AS4/3502 Graphite-Epoxy
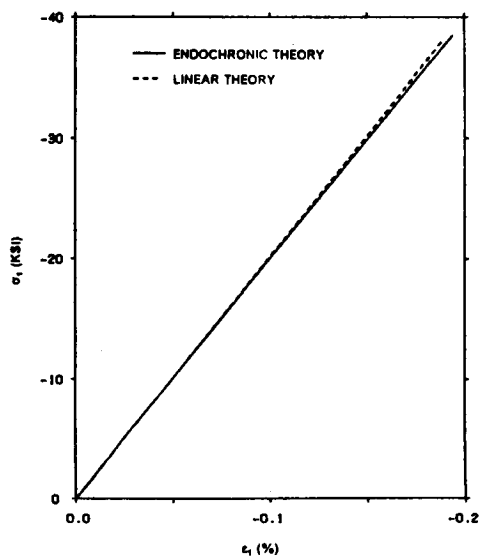
Laminate Response

strain deviates -2.1% from linear strain, 5.5% from the 15° off-axis test strain, and -2.1% from the Iosipescu test strain. The shear response in the [± 30]$_s$ laminate is softer than in the 30° off-axis test, but slightly stiffer than in the Iosipescu test. However, the difference between the Iosipescu test shear response and the predicted shear response is very small. At 7.4 ksi, the predicted shear strain deviates -11.4% from linear strain, 3.3% from the 30° off-axis test strain, and -3.0% from the Iosipescu test strain. The [± 45]$_s$ laminate shows more shear softening response than the Iosipescu test but not by a large degree. The 45° off-axis test does not load to a high enough stress level to make a useful comparison with predicted results. A useful feature of the [± 45]$_s$ laminate is that the shear response can be extracted. A plot of the shear response within the tested [± 45]$_s$ laminate is included in Figure 38. Comparison between the finite element prediction and the experimental curve reveals excellent agreement. At 12.5 ksi, the predicted shear strain deviates -36.4% from linear strain, -6.5% from the Iosipescu test strain, and only 4.4% from the [± 45]$_s$ laminate measured strain.

The previous comparison shows how dependent the predicted shear response is on the stress component ratios. This phenomenon is also obvious from the off-axis unidirectional tests. The ratios of the principal stress components greatly influence the shear stress-strain profile. However, as noted previously, unlike the off-axis unidirectional tests, the [± 10]$_s$, [± 20]$_s$, and [± 30]$_s$ laminates exhibit material principal stress components of opposite signs. Because the endochronic constants were not derived in this stress environment, the shear response for these laminates is questionable. It is encouraging, however, that within the [± 45]$_s$ laminate (which has principal stresses of the same sign), the experimental shear response and predicted shear response agree very well.
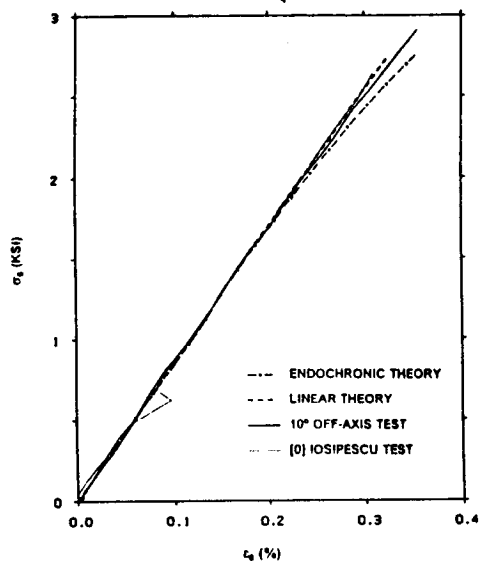
(a) $[\pm 10]_s$ **Unnotched Laminate**
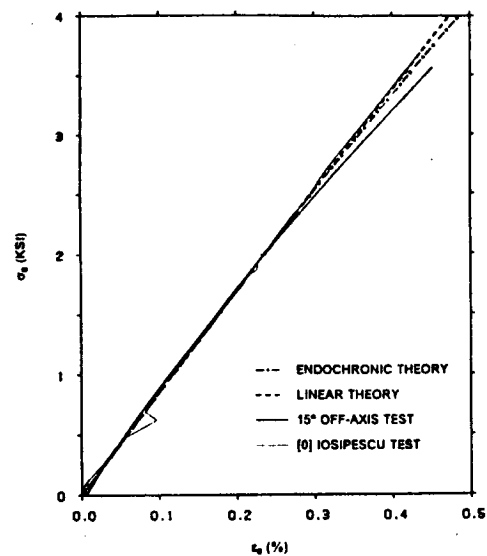
(b) $[\pm 20]_s$ **Unnotched Laminate**
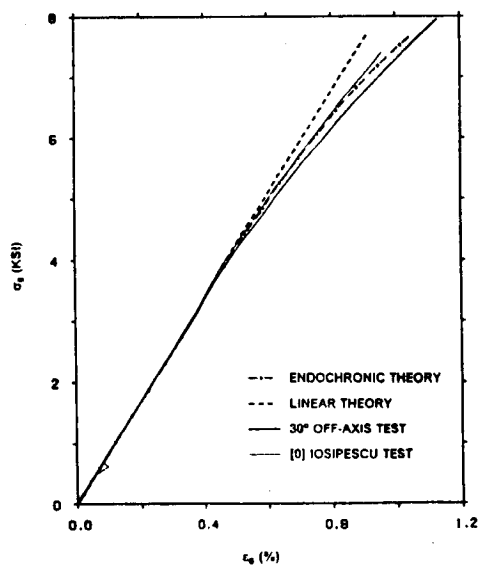
(c) $[\pm 30]_s$ **Unnotched Laminate**
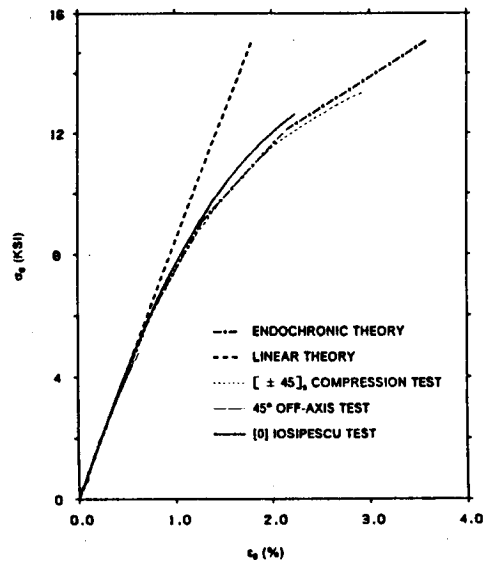
(d) $[\pm 45]_s$ **Unnotched Laminate**

Figure 38. σ_6 **Versus** ε_6 **for Unnotched Laminates - AS4/3502 Graphite-Epoxy**

4.6 Notched Angle-Ply Laminates

4.6.1 Far-Field Axial Response

As mentioned previously, the finite element analysis for laminates with holes did not load to the experimentally observed failure load in all cases. This was true of the $[(\pm 10)_{12}]_s$ and $[(\pm 20)_{12}]_s$ laminates with 1/4" diameter holes. However, as Figure 39 shows, far-field axial stress-strain correlation between theory and experiment for these laminates and for the $[(\pm 30)_{12}]_s$ and $[(\pm 45)_{12}]_s$ laminates is very good.

There are some interesting differences to note between the far-field axial response of the notched and unnotched laminates. Unlike the response of the unnotched laminates (Figure 34), the notched $[(\pm 20)_{12}]_s$ laminate (Figure 39) shows more axial softening response than the notched $[(\pm 10)_{12}]_s$ laminate. The cause for this difference is likely due to the stress concentration around the hole which causes non-linear strains at a lower load level. Unlike the unnotched $[\pm 30]_s$ laminate (Figure 34), the notched $[(\pm 30)_{12}]_s$ laminate with a 1/2" (Figure 39) hole shows very little axial softening response. In fact, the predicted results show slightly more softening response than the experimental results. The $[(\pm 30)_{12}]_s$ laminate's small degree of softening response is not expected and the cause is unknown. On the other hand, the $[(\pm 45)_{12}]_s$ laminates with 1/2" holes exhibit significant softening response. The predicted axial response of the $[(\pm 45)_{12}]_s$ laminate correlates extremely well with experimental results. Due to the degree of softening in this laminate, the excellent correlation is very encouraging.
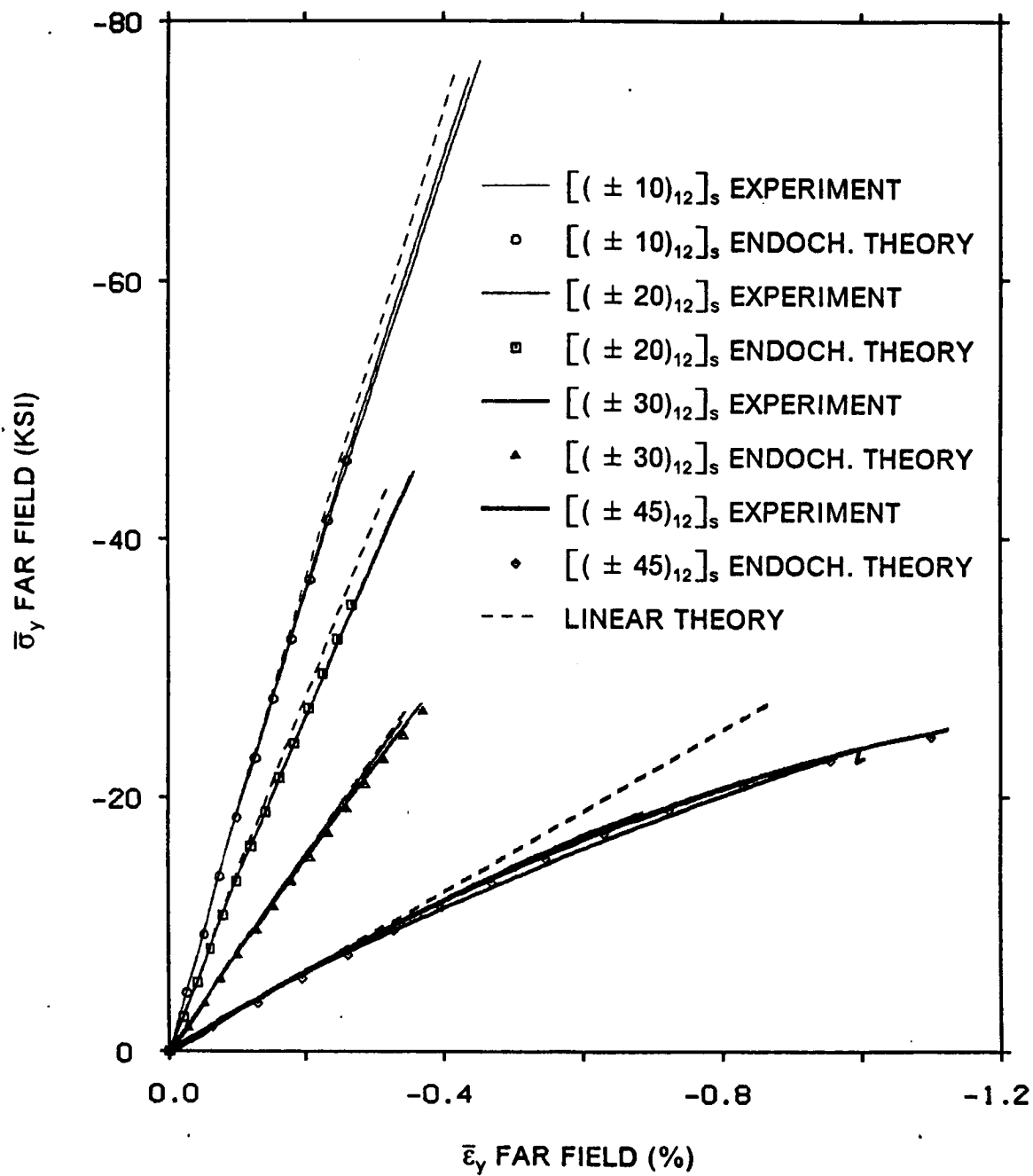
Figure 39. σ_y Versus ε_y for Notched Laminates with w/d Ratios of 10 -- AS4/3502 Graphite-Epoxy

4.6.2 Axial Strain Response Near The Hole

This section focuses on the axial strain at the outer surface of the laminates near the hole edge. All experiments were conducted with an axial strain gage located as near to the hole edge as possible. The location of the strain gage is illustrated in Figure 40.

In order to compare finite element results with experiment, the far field axial stress is plotted against the axial strain at $\theta = 0°$, $Z = 11H/12$ (the closest gauss plane to the free surface), and at various distances from the hole edge in Figure 41 through Figure 44. In order to compare 1/4″ hole laminates with 1/2″ hole laminates, the distance D from the hole edge is normalized with respect to the radius A.

The finite element stress-strain results agree satisfactorily with experiment between D/A = 0.17 and D/A = 0.36 for the $[(\pm 10)_{12}]_s$ (Figure 41) and $[(\pm 20)_{12}]_s$ (Figure 42) laminates. The strain calculated at the gauss point nearest the hole (D/A = 0.0048) is much larger than the experimentally measured value. At D/A = 0.17440, the predicted response (Figure 41 and Figure 42) correlates reasonably well with experiment; however, at this D/A, the stress-strain response is softer than the experimental response. The best correlation for both laminates appears to occur at 0.17 < D/A < 0.36.

The predicted results for the $[(\pm 20)_{12}]_s$ laminate (Figure 42) exhibit an interesting phenomonen in that the most non-linear stress-strain response occurs not at the gauss point closest to the hole edge, but at the next gauss point away (D/A = 0.02). In fact, the response at D/A = 0.0352 is also softer than the response at D/A = 0.0048. The $[(\pm 10)_{12}]_s$ laminate does not exhibit this behavior.

The predicted response of the $[(\pm 30)_{12}]_s$ laminate (Figure 43) correlates very well with experiment at the first three gauss points nearest the hole (D/A = 0.0044, D/A = 0.02, and D/A
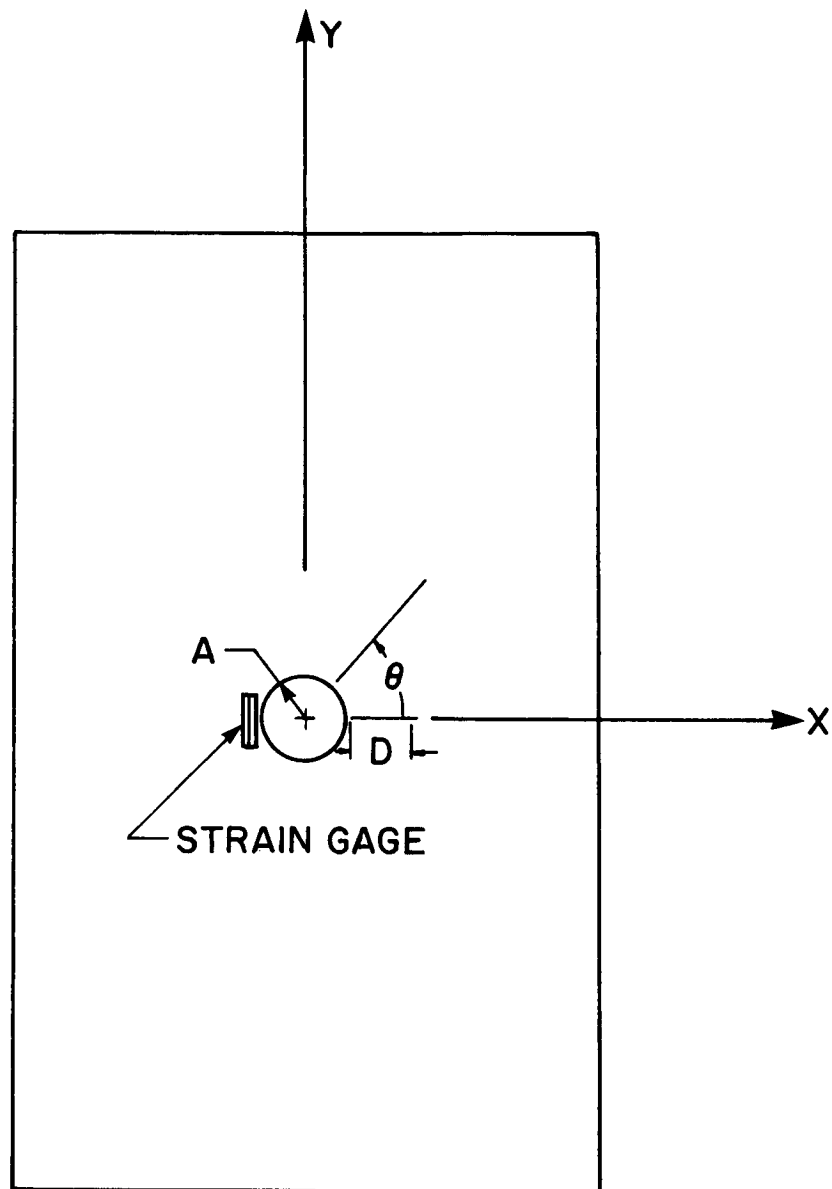
Figure 40. Near Hole Strain Gage Location
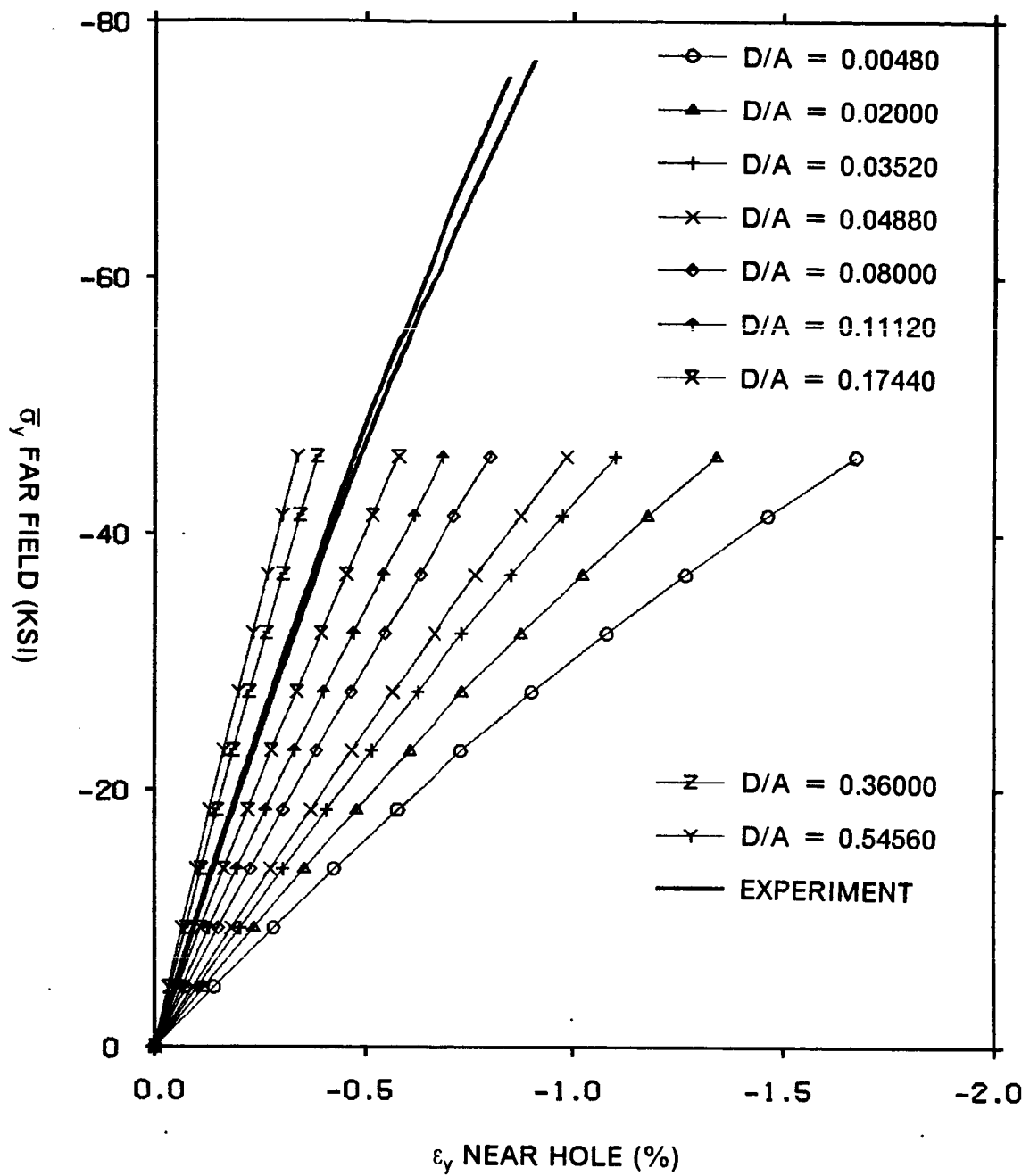
Figure 41. Far Field Axial Stress Versus Axial Strain on the Hole Edge for [± 10]ₛ Laminate with a 1/4″ Hole
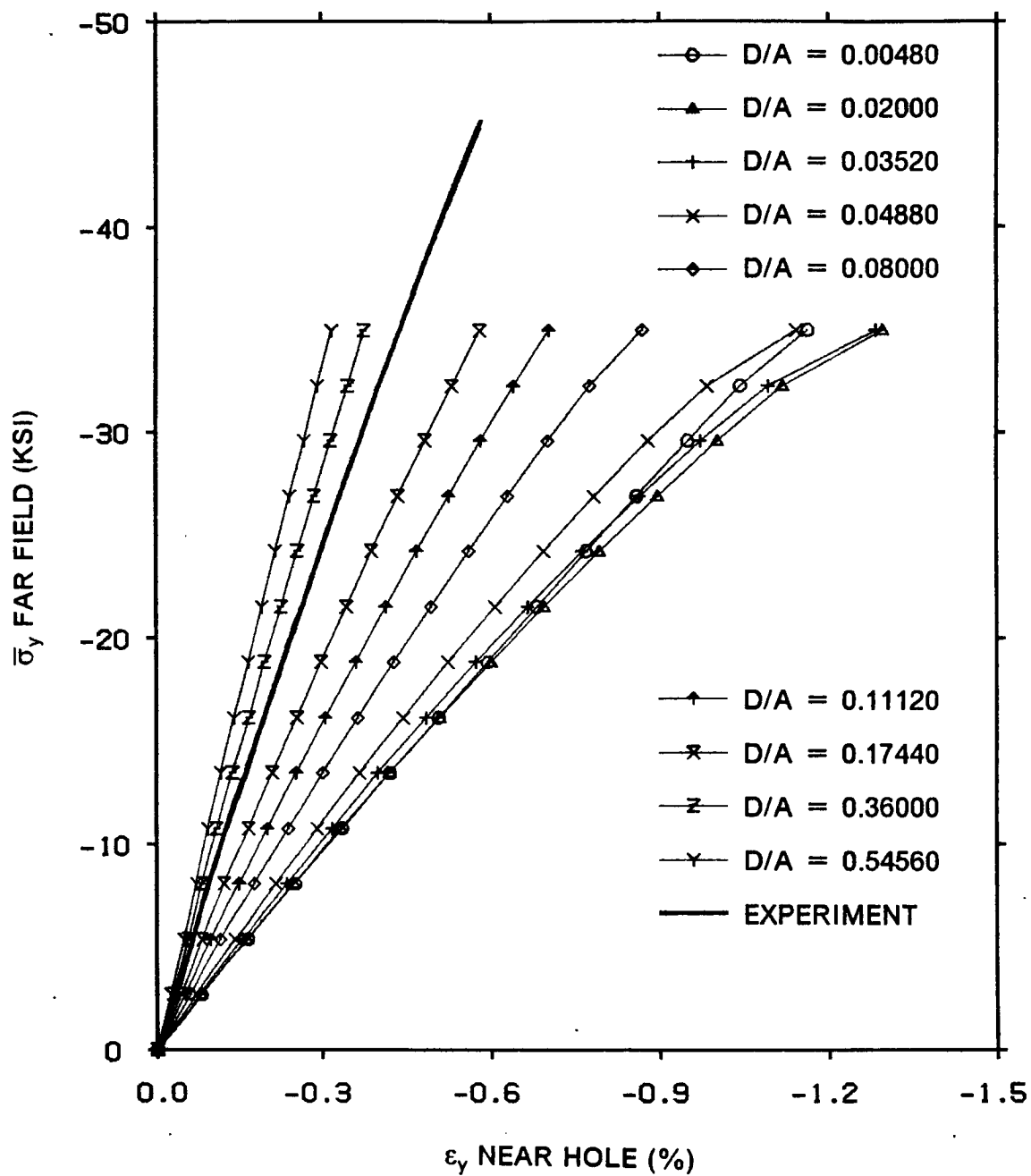
Figure 42. Far Field Axial Stress Versus Axial Strain on the Hole Edge for [± 20]ₛ Laminate with a 1/4″ Hole
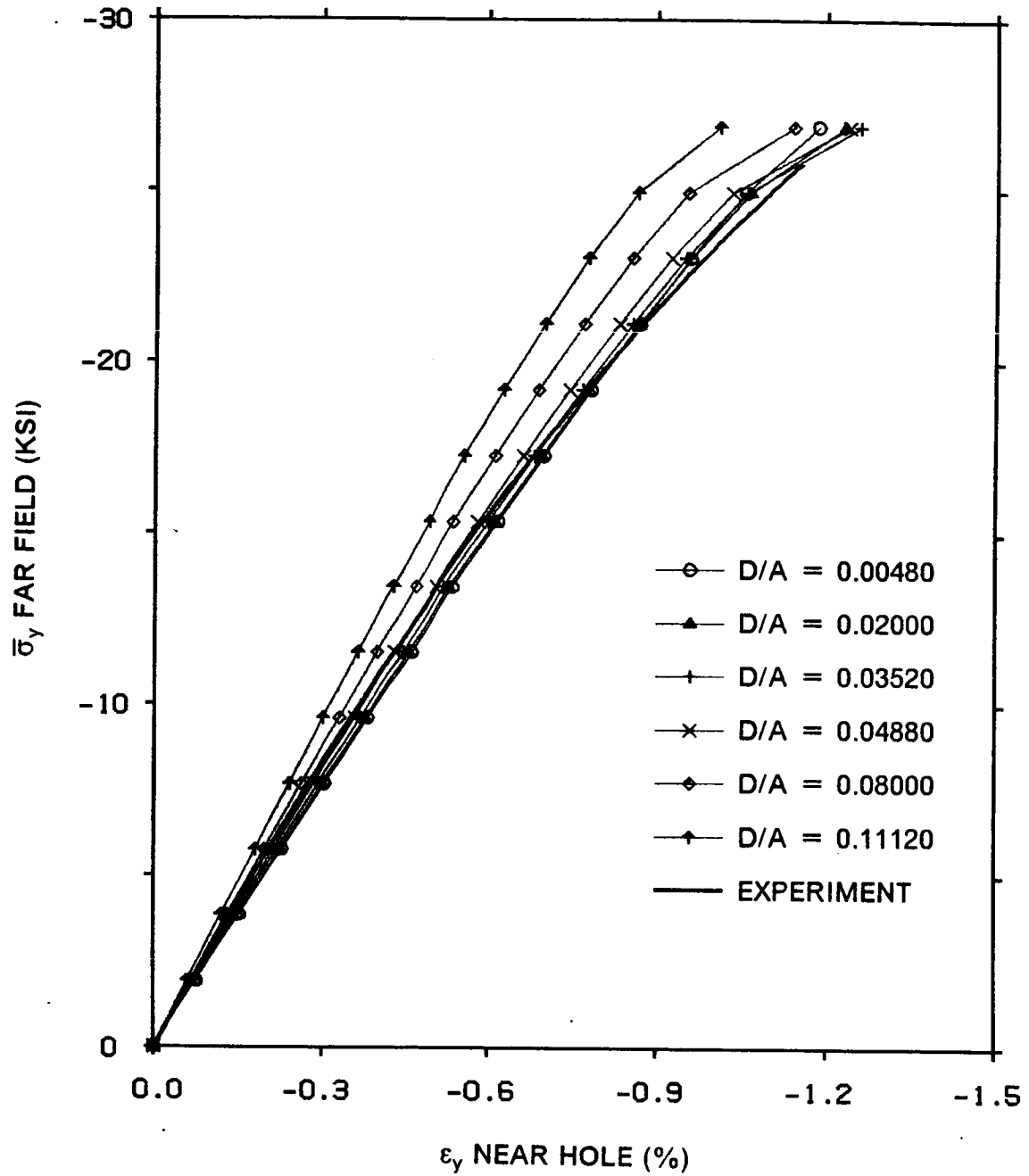
Figure 43. Far Field Axial Stress Versus Axial Strain on the Hole Edge for [± 30]ₛ Laminate with a 1/2″ Hole
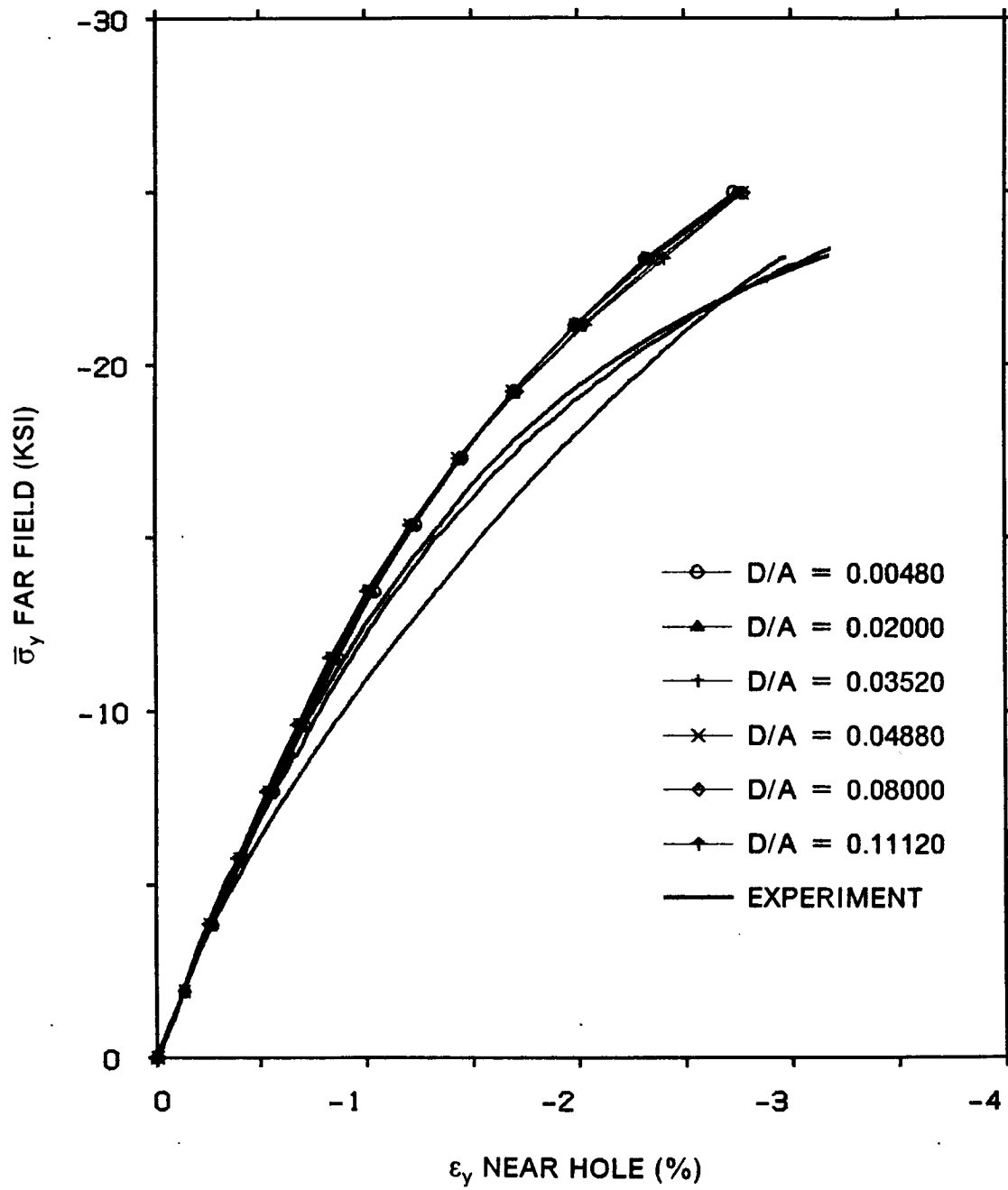
Figure 44. Far Field Axial Stress Versus Axial Strain on the Hole Edge for [± 45]ₛ Laminate with a 1/2″ Hole

= 0.0356). Of these three gauss points, the results at the third gauss point (D/A = 0.03520) appear to agree best with experiment. Similar to the predicted response in the $[(\pm 20)_{12}]_s$ laminate, the $[(\pm 30)_{12}]_s$ laminate's stress-strain response at D/A = 0.02 is slightly softer than the response at D/A = 0.0044, but this behavior is not as pronounced in the $[(\pm 30)_{12}]_s$ laminate. In fact, the curves from the nearest gauss point from the hole (D/A = 0.0044) to the furthest gauss point from the hole (D/A = 0.1108) all tend to be grouped closer than in the $[(\pm 20)_{12}]_s$ and $[(\pm 10)_{12}]_s$ laminates.

The response of the $[(\pm 45)_{12}]_s$ laminate (Figure 44) correlates reasonably well with experiment. Note that the predicted responses at all six gauss points (from D/A = 0.0044 to D/A = 0.1108) are nearly identical. The response at D/A = 0.02 and 0.0356 is softer than at D/A = 0.0044, but this behavior is nearly indistinguishable.

It appears from the above results that the laminates with larger layup angles φ show the non-linear region adjacent to the hole to extend further towards the free edge. The reason the predicted D/A values are larger in the 1/4" hole laminates than in the 1/2" hole laminates may be due to their smaller radius value A. At approximately the same distance from the hole edge, the D/A value of the 1/4" hole laminates is twice that of the 1/2" hole laminates.

4.6.3 Stress-Concentration Profile At $\theta = 0°$

This section examines stress concentration profiles along $\theta = 0°$ from the hole edge to a distance D/A = 0.6. Three stress components are examined -- σ_θ, $\tau_{\theta z}$, and σ_z. At the hole edge, due to free surface boundary conditions, these are the only nonzero stresses. Stress profiles from linear elastic predictions are compared with those from endochronic theory predictions in Figure 45 through Figure 51. The linear results were obtained from the first load step of the solution process, while the nonlinear results correspond to the last load step in the loading

history. All laminate stresses are normalized with respect to the absolute value of laminate's far field stress $|\bar{\sigma}_y|$ at the corresponding load step.

4.6.3.1 σ_θ Stress Concentration Profiles

Stress concentration profiles for σ_θ at the three gauss planes closest to the mid-plane $(Z=H/12, Z=H/4, Z=5H/12)$ are shown in Figure 45 through Figure 47 for the four notched laminates. At all three gauss planes, the $[(\pm 10)_{12}]_s$ laminate exhibits the highest σ_θ stress concentration and the $[(\pm 45)_{12}]_s$ laminate the lowest. Linear elastic analysis predicts a decrease in the peak σ_θ stress concentration as the layup angle φ increases from $10°$ to $45°$. The endochronic theory predicts a similar decrease in the peak σ_θ stress concentration as the layup angle φ increases from $10°$ to $45°$ at $Z=5H/12$, but at $Z=H/4$ and $Z=H/12$, it predicts the peak σ_θ stress concentration to be higher in the $[(\pm 30)_{12}]_s$ laminate than in the $[(\pm 20)_{12}]_s$ laminate. In the $[(\pm 10)_{12}]_s$ and $[(\pm 45)_{12}]_s$ laminates, as intuitively expected, linear elastic analysis predicts higher peak σ_θ stress concentrations than the endochronic theory. However, in the $[(\pm 20)_{12}]_s$ and $[(\pm 30)_{12}]_s$ laminates, linear elastic analysis predicts lower peak σ_θ stress concentrations than the endochronic theory, which is not intuitively expected. At the hole edge, the endochronic theory predicts significantly lower σ_θ stress concentrations than linear elastic analysis at all gauss planes within all of the laminates. Both analyses predict the peak σ_θ stress concentration to occur in the $[(\pm 10)_{12}]_s$ laminate at D/A = 0 and $Z=5H/12$. At this point, Figure 47 shows the linear elastic and endochronic theory σ_θ stress concentrations to be approximately -4.6 and -4.0, respectively. In contrast, the highest peak σ_θ stress concentration in the $[(\pm 45)_{12}]_s$ laminate occurs at D/A = 0.11120 and $Z=5H/12$ and has linear elastic and endochronic theory magnitudes of approximately -2.3 and -1.8, respectively. It is especially interesting to note the shape of the σ_θ profiles. With the exception of the $[(\pm 10)_{12}]_s$ laminate, at all gauss planes, the maximum stress concentration occurs not at the hole edge, but at a small distance inward. This phenomenon is especially pronounced in the
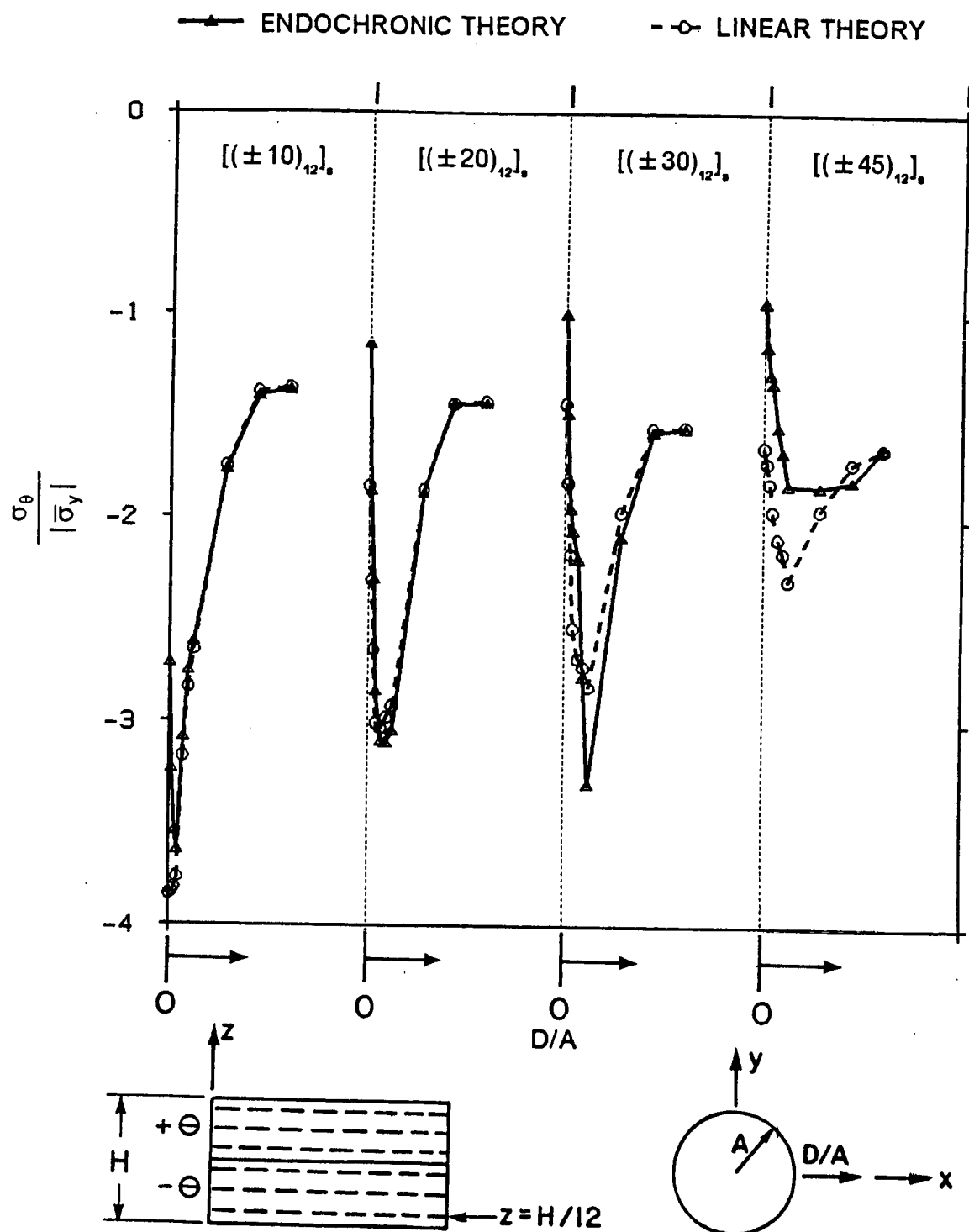
Figure 45. σ_θ Versus D/A for Notched Laminates with w/d Ratios of 10, Z = H/12
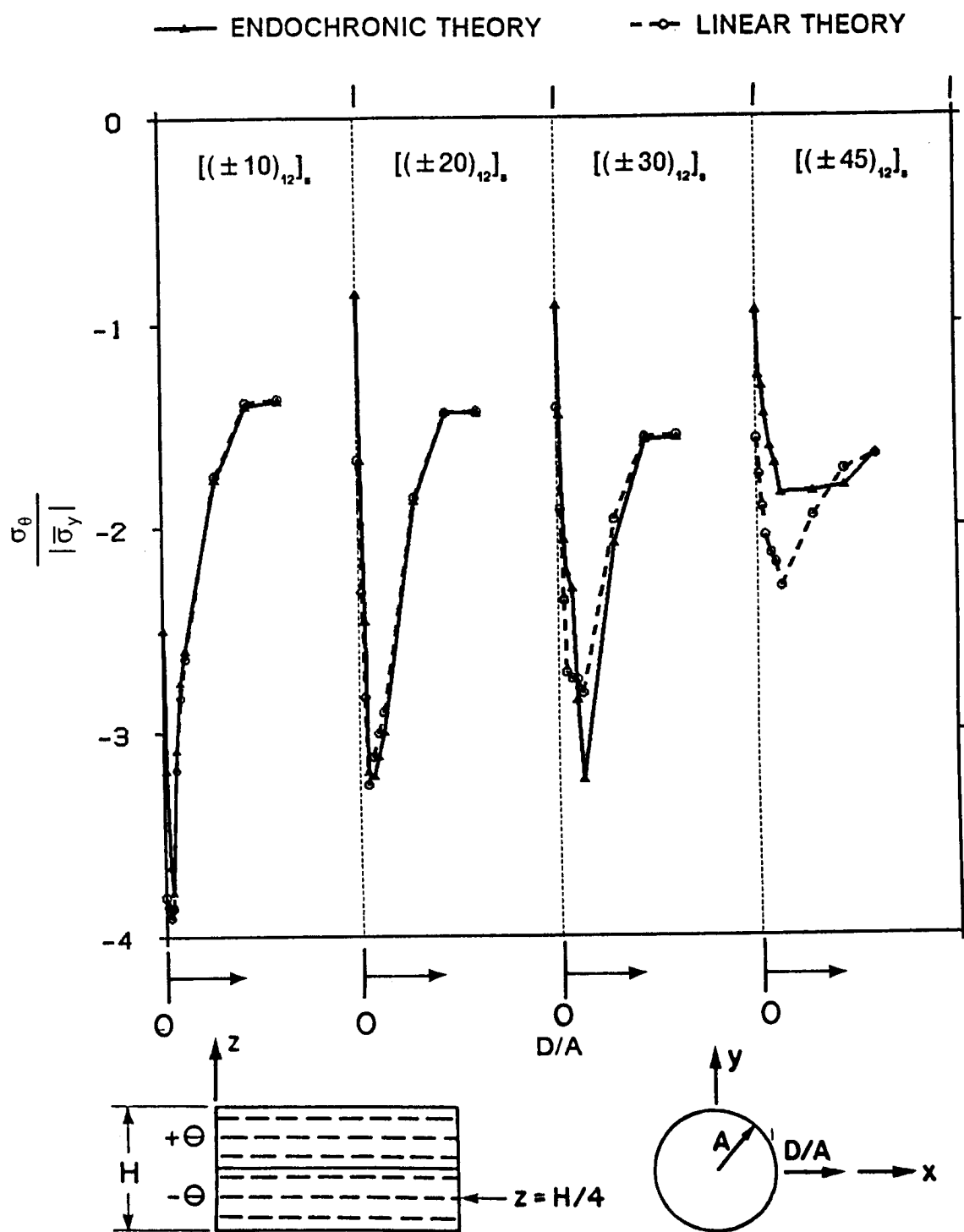
Figure 46. σ_θ Versus D/A for Notched Laminates with w/d Ratios o f 10, Z=H/4
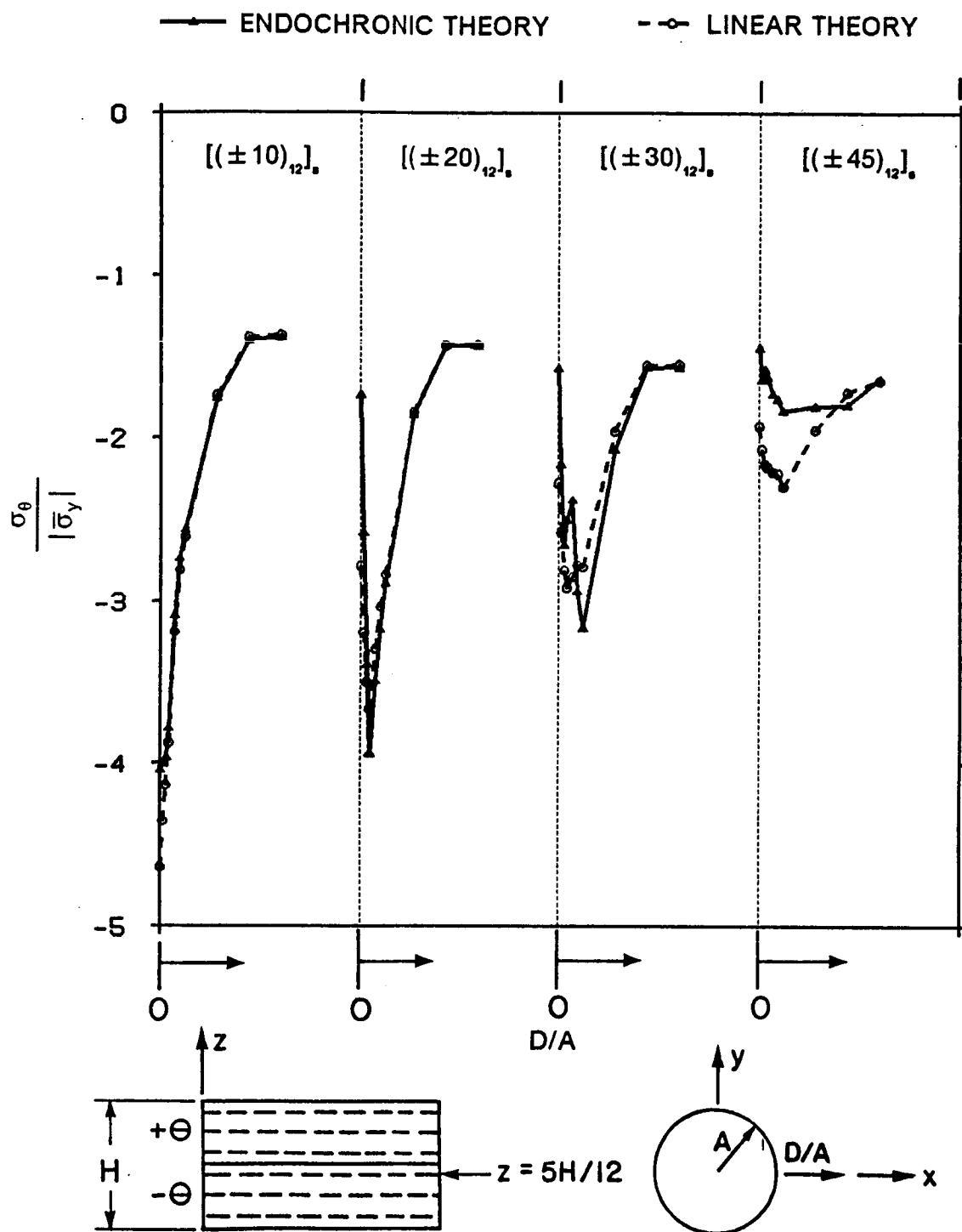
Figure 47. σ_θ Versus D/A for Notched Laminates with w/d Ratios of 10, Z=5H/12
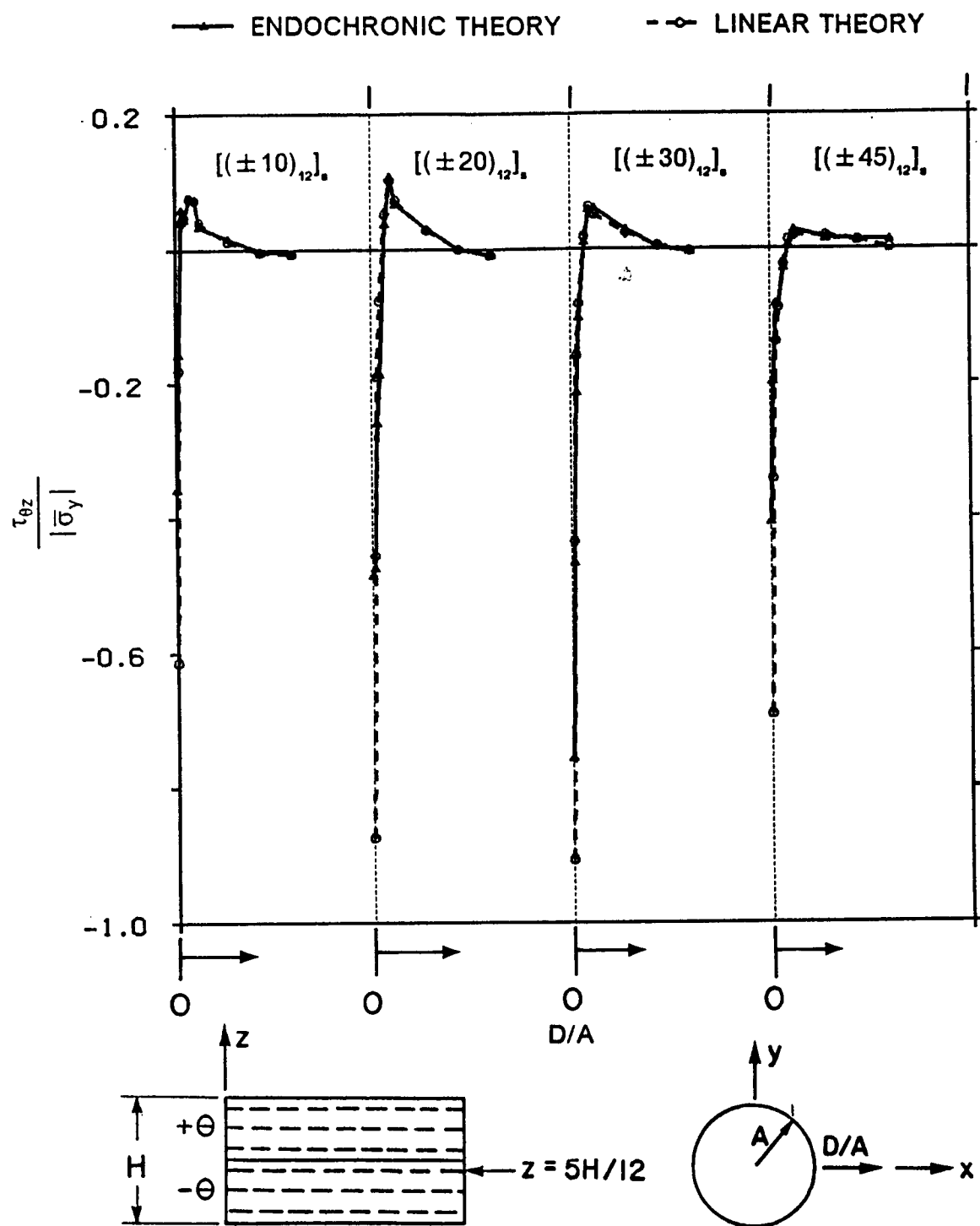
Figure 48. $\tau_{\theta z}$ Versus D/A for Notched Laminates with w/d Ratios of 10, Z=5H/12
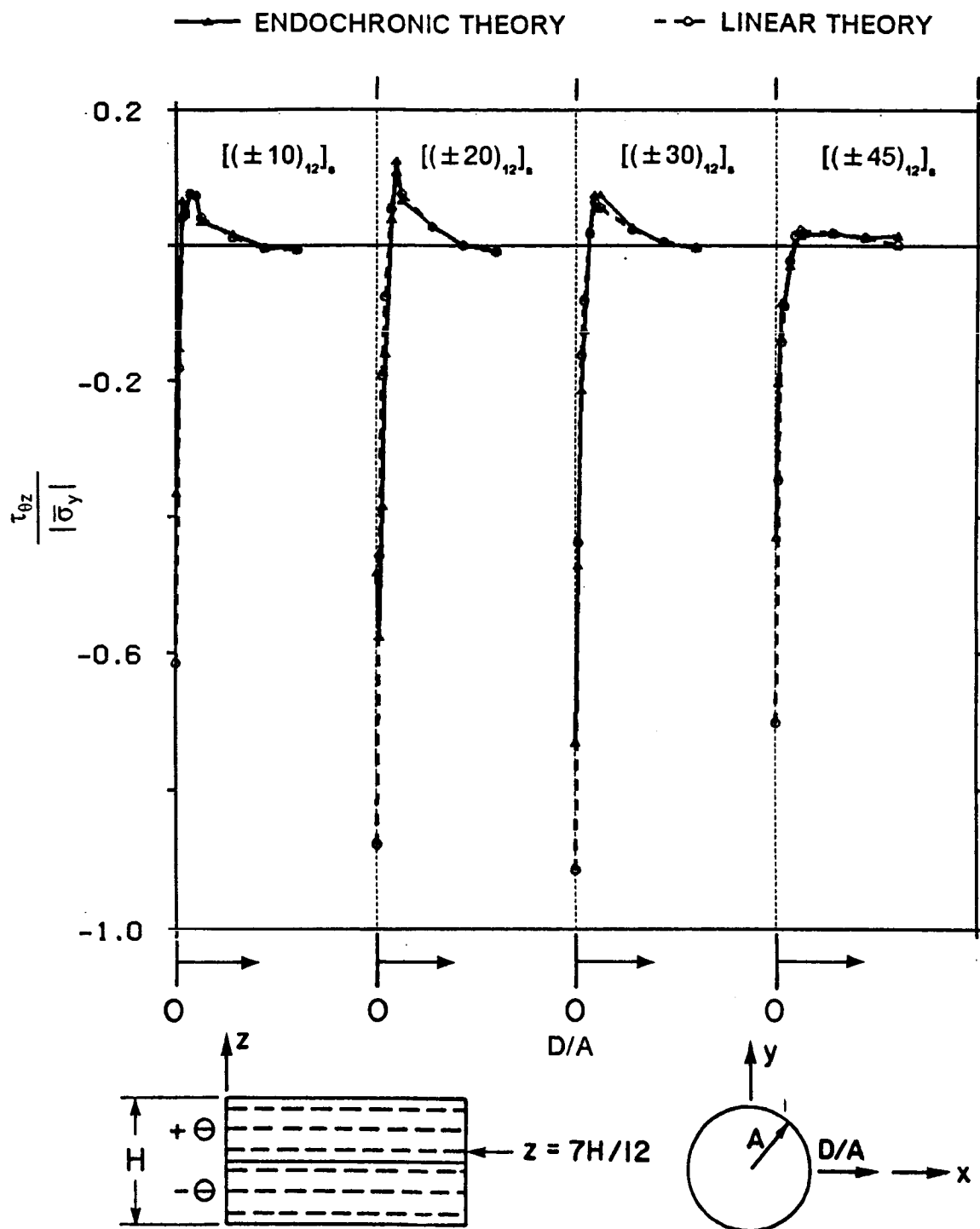
Figure 49. $\tau_{\theta z}$ Versus D/A for Notched Laminates with w/d Ratios of 10, Z=7H/12
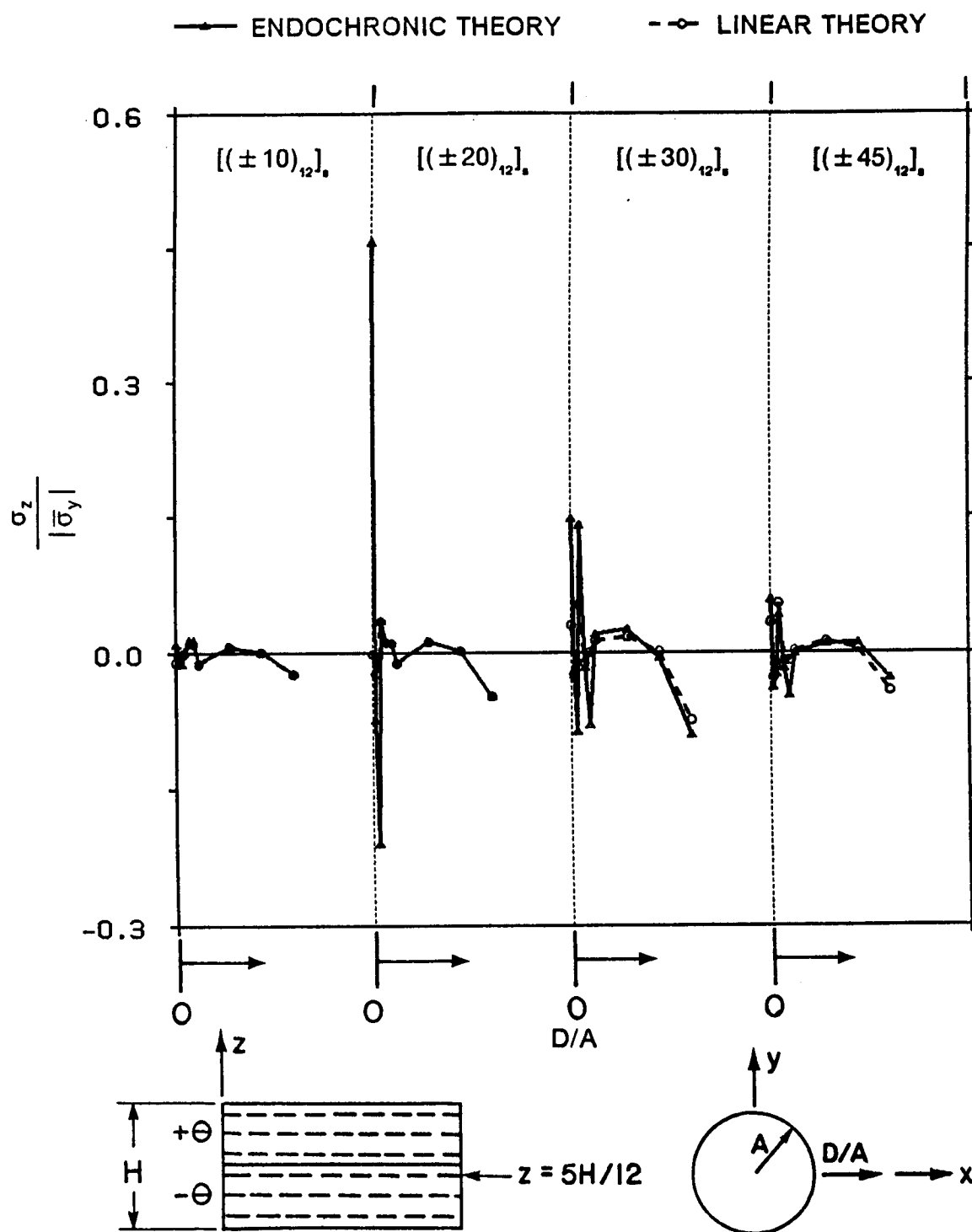
Figure 50. σ_z Versus D/A for Notched Laminates with w/d Ratios of 10, Z=5H/12
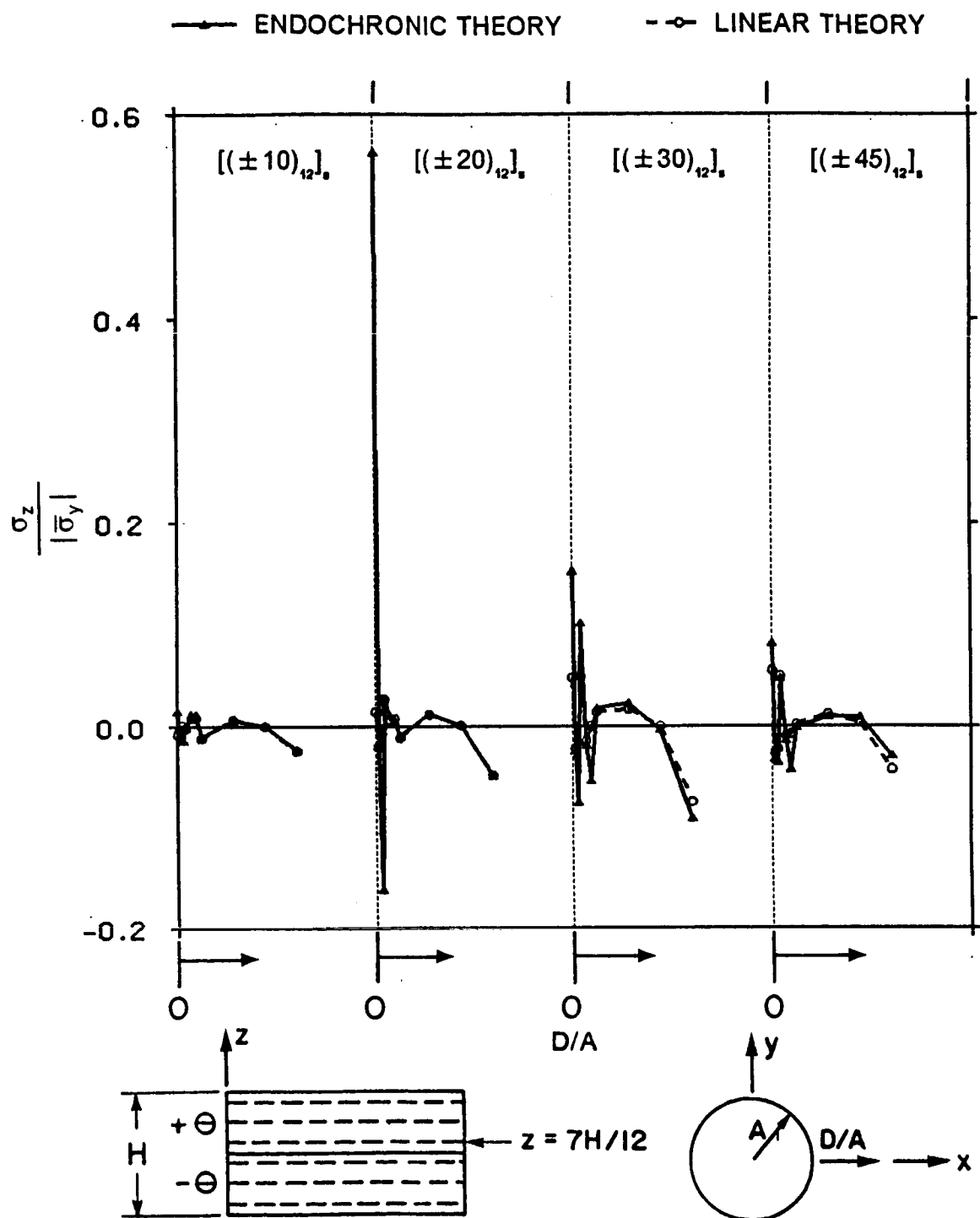
Figure 51. σ_z Versus D/A for Notched Laminates with w/d Ratios of 10, Z = 7H/12

endochronic theory results. Finally, note that at D/A = 0.6, all laminates at all three gauss planes exhibit approximately the same σ_θ stress concentration magnitude of -1.5. At larger D/A values, the σ_θ stress concentration approaches the value -1 because σ_θ approaches the magnitude of $\overline{\sigma}_y$.

4.6.3.2 $\tau_{\theta z}$ Stress Concentration Profiles

The interlaminar $\tau_{\theta z}$ shear stress concentration profiles at gauss planes directly below and above the ply interface (Z=5H/12, Z=7H/12) are shown in Figure 48 and Figure 49. These figures show the $[(\pm 30)_{12}]_s$ laminate to have the highest $\tau_{\theta z}$ stress concentration and the $[(\pm 10)_{12}]_s$ laminate the lowest. In all laminates, linear elastic analysis predicts significantly higher peak $\tau_{\theta z}$ stress concentrations than the endochronic theory. This is especially pronounced in the $[(\pm 20)_{12}]_s$ laminate. Other than this difference in peak magnitudes, the linear elastic and endochronic theory profiles are nearly identical. Note that the boundary layer in which $\tau_{\theta z}$ exists is very small; $\tau_{\theta z}$ is essentially zero for D/A $\geq$ 0.08 for all laminates.

4.6.3.3 σ_z Stress Concentration Profiles

The σ_z out-of-plane normal stress concentration profiles, at gauss planes directly below and above the ply interface, are shown in Figure 50 and Figure 51. These figures show that linear elastic and endochronic theory analysis predict nearly identical profiles at points away from the hole edge. However, near the hole edge, the profiles differ significantly, especially in the $[(\pm 20)_{12}]_s$ laminate. For the $[(\pm 20)_{12}]_s$ laminate, the endochronic theory predicts the σ_z stress concentration to be nearly 0.6 on the hole edge and at Z=7H/12 (Figure 51), compared to a linear elastic value of approximately zero. This high magnitude of σ_z may be the result of the zero-slope condition (see "Unloading Considerations" at the beginning of this chapter) imposed on another out-of-plane stress component. Note the oscillation about σ_z = 0 pre-

dicted by both analyses. Although the oscillation magnitudes predicted by the endochronic theory are larger than those of linear elastic analysis near the hole edge, both analyses show a similar pattern. These oscillations may or may not be real. Often times, displacement based finite element analysis gives stress oscillations in regions of large strain gradients.

4.6.4   Material Principal Coordinate Stress Profiles Around The Hole

This section examines profiles for all six principal stress components, at the hole edge, for $-90° \leq \theta \leq 90°$. As in the previous section, the stresses are normalized with the absolute value of far field stress $|\bar{\sigma}_y|$. In order to minimize the number of plots, the in-plane stress component profiles are examined at the mid-plane of the first ply ($Z = H/4$) and the out-of-plane stress component profiles are examined at the gauss plane directly below the ply interface ($Z = 5H/12$). These principal stress profiles can be seen in Figure 52 through Figure 57.

4.6.4.1   Axial Stress σ_1

Examination of the σ_1 profiles of the four angle-ply laminates (Figure 52) shows the linear and non-linear profiles to be very similar, except in the $[(\pm 45)_{12}]_s$ laminate. The $[(\pm 45)_{12}]_s$ laminate shows a difference between linear elastic and endochronic results, not so much in the shape of the curve, but in magnitude. The highest σ_1 stress concentration in the $[(\pm 45)_{12}]_s$ laminate is predicted at the same angle for both analyses, but has a value of -5.0 for linear results and a value of over -7.0 for non-linear results, a difference of 40%. The other laminates show relatively small differences in stress concentration. However, note that in both the $[(\pm 10)_{12}]_s$ and $[(\pm 45)_{12}]_s$ laminates, the endochronic theory predicts the largest peak stress concentration while in the $[(\pm 20)_{12}]_s$ and $[(\pm 30)_{12}]_s$ laminates, linear elastic analysis gives the largest peak stress concentration. As is intuitively expected for both linear

(a) $[(\pm 10)_{12}]_s$ Laminate - 1/4" Hole

(b) $[(\pm 20)_{12}]_s$ Laminate - 1/4" Hole

(c) $[(\pm 30)_{12}]_s$ Laminate - 1/2" Hole

(d) $[(\pm 45)_{12}]_s$ Laminate - 1/2" Hole

ENDOCHRONIC THEORY   LINEAR THEORY

Figure 52. σ_1 Versus θ for Notched Laminates with w/d Ratios of 10, Z = H/4

(a) $\left[(\pm 10)_{12}\right]_s$ **Laminate - 1/4" Hole**

(b) $\left[(\pm 20)_{12}\right]_s$ **Laminate - 1/4" Hole**

(c) $\left[(\pm 30)_{12}\right]_s$ **Laminate - 1/2" Hole**

(d) $\left[(\pm 45)_{12}\right]_s$ **Laminate - 1/2" Hole**

—▲— ENDOCHRONIC THEORY   – –◦– LINEAR THEORY

Figure 53. σ_2 **Versus** θ **for Notched Laminates with w/d Ratios of 10,** $Z = H/4$

Laminate Response

(a) $[(\pm 10)_{12}]_s$ Laminate - 1/4" Hole

(b) $[(\pm 20)_{12}]_s$ Laminate - 1/4" Hole

(c) $[(\pm 30)_{12}]_s$ Laminate - 1/2" Hole

(d) $[(\pm 45)_{12}]_s$ Laminate - 1/2" Hole

——— ENDOCHRONIC THEORY   – ❍ – LINEAR THEORY

Figure 54. σ_3 Versus θ for Notched Laminates with w/d Ratios of 10, Z=5H/12

(a) $[(\pm 10)_{12}]_s$ **Laminate - 1/4″ Hole**

(b) $[(\pm 20)_{12}]_s$ **Laminate - 1/4″ Hole**

(c) $[(\pm 30)_{12}]_s$ **Laminate - 1/2″ Hole**

(d) $[(\pm 45)_{12}]_s$ **Laminate - 1/2″ Hole**

——— ENDOCHRONIC THEORY   – ◦– LINEAR THEORY

Figure 55. σ_4 Versus θ for Notched Laminates with w/d Ratios of 10,   Z = 5H/12

(a) $\left[(\pm 10)_{12}\right]_s$ Laminate - 1/4″ Hole

(b) $\left[(\pm 20)_{12}\right]_s$ Laminate - 1/4″ Hole

(c) $\left[(\pm 30)_{12}\right]_s$ Laminate - 1/2″ Hole

(d) $\left[(\pm 45)_{12}\right]_s$ Laminate - 1/2″ Hole

━━ ENDOCHRONIC THEORY   ‒‒○‒ LINEAR THEORY

Figure 56. σ_s Versus θ for Notched Laminates with w/d Ratios of 10, Z=5H/12

(a) $[(\pm 10)_{12}]_s$ Laminate - 1/4" Hole

(b) $[(\pm 20)_{12}]_s$ Laminate - 1/4" Hole

(c) $[(\pm 30)_{12}]_s$ Laminate - 1/2" Hole

(d) $[(\pm 45)_{12}]_s$ Laminate - 1/2" Hole

ENDOCHRONIC THEORY   LINEAR THEORY

Figure 57. σ_s Versus θ for Notched Laminates with w/d Ratios of 10,   Z=H/4

elastic and endochronic theory results, the peak value of σ_1 occurs at approximately $-\varphi$ (the layup angle of each laminate).

4.6.4.2 Transverse Stress σ_2

Examination of the σ_2 profiles of the four laminates (Figure 53) shows the linear elastic and endochronic theory profiles to be very similar in the $[(\pm 10)_{12}]_s$ and $[(\pm 20)_{12}]_s$ laminates and relatively dissimilar in the $[(\pm 30)_{12}]_s$ and $[(\pm 45)_{12}]_s$ laminates. Note that the dissimilarities tend to occur in a very narrow range of θ angles. Also, the dissimilarities tend to be the most pronounced at the largest values of σ_2. The jaggedness in the linear elastic profiles is probably due to local stress oscillations at the gauss points which, as mentioned earlier, are common to displacement based finite element analysis in regions of high strain gradients. The jaggedness in the endochronic theory profiles is likely due to a combination of the aforementioned oscillations and to the zero-slope condition forced upon stress components if they start to unload in the analysis. Specifying the value of a specific stress component disrupts equilibrium and causes the other components to shift to re-establish equilibrium. The endochronic theory σ_2 stress concentration is generally lower than the linear elastic magnitude in all of the laminates except for the $[(\pm 30)_{12}]_s$ laminate. The $[(\pm 30)_{12}]_s$ laminate's profiles are very similar except in a region from $\theta \cong -30^\circ$ to $\theta \cong 20^\circ$. In this region, the endochronic theory stress concentration increases abruptly, likely caused by the aforementioned zero-slope imposition on a certain stress component and the need to re-establish equilibrium.

4.6.4.3 Interlaminar Normal Stress σ_3

The linear elastic and endochronic theory stress profiles for the σ_3 interlaminar stress (Figure 54) are very dissimilar for all the laminates except the $[(\pm 10)_{12}]_s$ laminate. In this

laminate, the endochronic theory stress magnitudes are slightly higher than the linear elastic magnitudes. Note the $[(\pm 10)_{12}]_s$ laminate's nearly anti-symmetric profile about $\theta = 0°$. The $[(\pm 20)_{12}]_s$ laminate's linear elastic and endochronic theory profiles agree reasonably well from $\theta = -90°$ to $\theta \cong -20°$ and from $\theta \cong 25°$ to $\theta = 90°$. However, between $\theta \cong -20°$ and $\theta \cong 25°$, the curves show a significant difference. This difference is mainly caused by a large jump in magnitude at $\theta \cong -5°$. Again, this jump is likely caused by the need to re-establish equilibrium due to a zero-slope imposition on another out-of-plane component. The $[(\pm 30)_{12}]_s$ and $[(\pm 45)_{12}]_s$ laminates' endochronic theory predicted σ_3 stress profiles exhibit radical jumps and show stress magnitudes much higher than the linear elastic profiles. Note that in all the laminates, except for the jumps in the endochronic theory profiles, the σ_3 stress concentration is relatively low, the absolute value not exceeding approximately 0.1.

4.6.4.4 Interlaminar Shear Stress σ_4

The linear elastic and endochronic theory stress concentration profiles for the σ_4 (τ_{23}) interlaminar shear stress (**Figure 55**) are similar in all of the laminates except for the $[(\pm 20)_{12}]_s$ laminate where the profiles show a significant difference in magnitude. In this laminate, the largest endochronic theory stress concentration is nearly 6 times greater than the largest linear stress concentration. The $[(\pm 10)_{12}]_s$ laminate shows the endochronic theory positive stress magnitude to be larger and the negative magnitude to be smaller than the linear elastic stress magnitude. The $[(\pm 30)_{12}]_s$ laminate's endochronic theory peak stress magnitude is larger than the linear elastic peak magnitude. In contrast, the $[(\pm 45)_{12}]_s$ laminate's endochronic theory predicted stress profile exhibits smaller magnitudes than linear elastic analysis. The largest predicted stress concentration occurs in the $[(\pm 45)_{12}]_s$ laminate at approximately -20°. Linear elastic analysis predicts a value of nearly -0.7 while endochronic theory analysis predicts a value near -0.5. The $[(\pm 30)_{12}]_s$ laminate exhibits magnitudes nearly as high. These large magnitudes of σ_4 stress concentration show

the potential for delamination. The magnitudes in the $[(\pm 20)_{12}]_s$ and $[(\pm 30)_{12}]_s$ laminates are not nearly as high.

4.6.4.5 Interlaminar Shear Stress σ_5

The linear elastic and endochronic theory σ_5 (τ_{13}) stress concentration profiles (Figure 56) agree reasonably well for all the laminates except the $[(\pm 20)_{12}]_s$ laminate (similar to the σ_4 profiles). This laminate shows odd behavior in that the endochronic theory stress concentration is opposite in sign to the linear elastic stress concentration, except in the region from $\theta \cong -25°$ to $\theta \cong 25°$. In this region, the profiles are of the same sign, but the endochronic theory stress magnitude is much larger than the linear elastic magnitude. In the $[(\pm 10)_{12}]_s$, $[(\pm 30)_{12}]_s$, and $[(\pm 45)_{12}]_s$ laminates, the endochronic theory stress magnitudes are generally lower than the linear elastic magnitudes. Again, the largest discrepancies occur near the stress concentration peaks.

4.6.4.6 Inplane Shear Stress σ_6

The σ_6 (τ_{12}) linear elastic and endochronic theory stress concentration profiles (Figure 57) are similar for all the laminates. In general, they show the endochronic theory stress magnitudes to be smaller than the linear elastic magnitudes. Differences are most pronounced at the profile peaks. Not only are the linear elastic and endochronic theory stress profiles similar, but the profiles for all laminates are very similar in shape, especially in the $[(\pm 10)_{12}]_s$, $[(\pm 20)_{12}]_s$, and $[(\pm 30)_{12}]_s$ laminates.

4.6.5 Cylindrical Coordinate Stress Profiles Around The Hole

This section examines cylindrical coordinate stress profiles at the hole edge from $-90° \leq \theta \leq 90°$. The in-plane normal stress, σ_θ, is plotted at the mid-plane of the first ply $(Z = H/4)$ in Figure 58, and the interlaminar shear stress, $\tau_{\theta z}$, is plotted at the gauss plane below the ply interface $(Z = 5H/12)$ in Figure 59.

4.6.5.1 Circumferential Stress σ_θ

Examination of the σ_θ stress profiles (Figure 58) around the hole shows the linear elastic and endochronic theory profiles to be very similar except in the $[(\pm 45)_{12}]_s$ laminate. The $[(\pm 45)_{12}]_s$ laminate shows the endochronic theory stress magnitude to be significantly higher from $\theta \cong 30°$ to $\theta \cong 50°$, while from $\theta \cong -25°$ to $\theta \cong 30°$, the linear elastic stress magnitude is higher. The $[(\pm 10)_{12}]_s$ laminate also shows the endochronic theory peak stress magnitude to be higher than the linear peak magnitude by a small amount. However, at all other values of θ, the endochronic theory stress magnitude is lower than that predicted by linear theory. In both the $[(\pm 20)_{12}]_s$ and $[(\pm 30)_{12}]_s$ laminates, the endochronic theory stress magnitude is lower than the linear elastic magnitude for all values of θ. Note how similar the σ_θ stress profiles are to the σ_1 profiles in the previous section. This most likely occurs because σ_1 is the largest stress component magnitude in all of the laminates and is the dominant term in the transformation from principal coordinates to cylindrical coordinates.

4.6.5.2 Interlaminar Shear Stress $\tau_{\theta z}$

The $\tau_{\theta z}$ stress profiles (Figure 59) show the maximum value of $\tau_{\theta z}$ to occur at $\theta \cong 0°$ for all of the laminates. In fact, all of the linear elastic stress profiles have very similar shapes. As φ
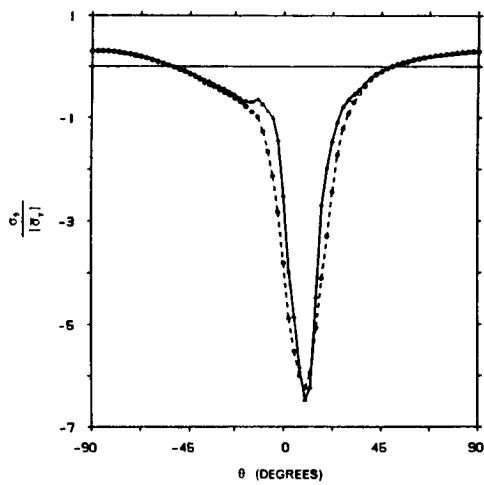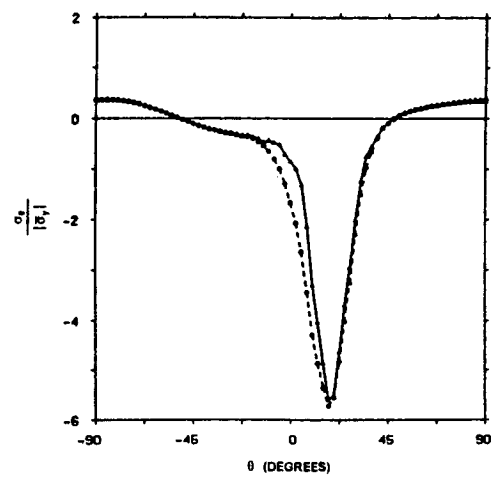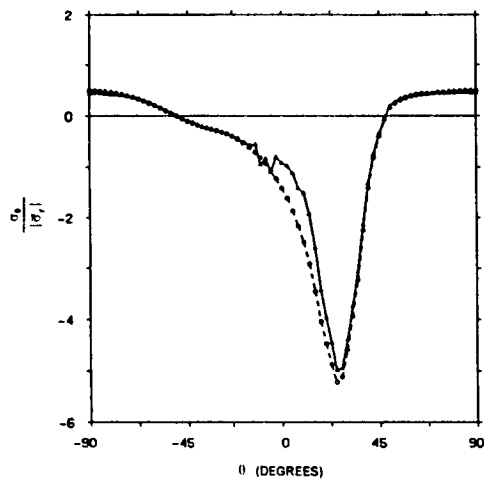
(a) $[(\pm 10)_{12}]_s$ Laminate - 1/4" Hole

(b) $[(\pm 20)_{12}]_s$ Laminate - 1/4" Hole

(c) $[(\pm 30)_{12}]_s$ Laminate - 1/2" Hole
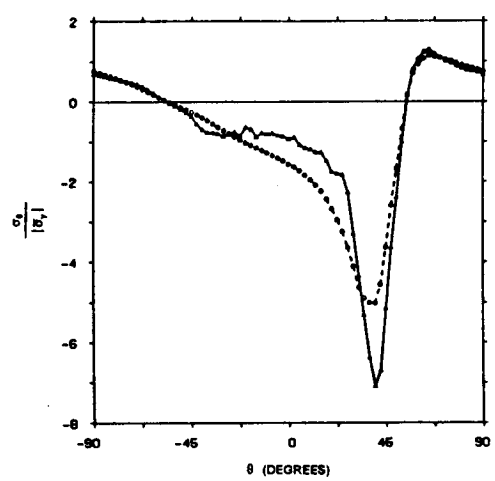
(d) $[(\pm 45)_{12}]_s$ Laminate - 1/2" Hole
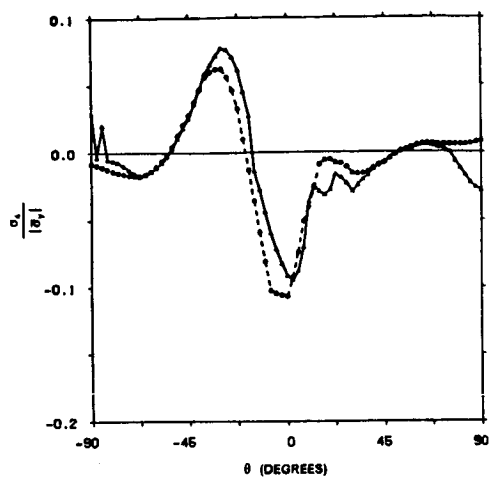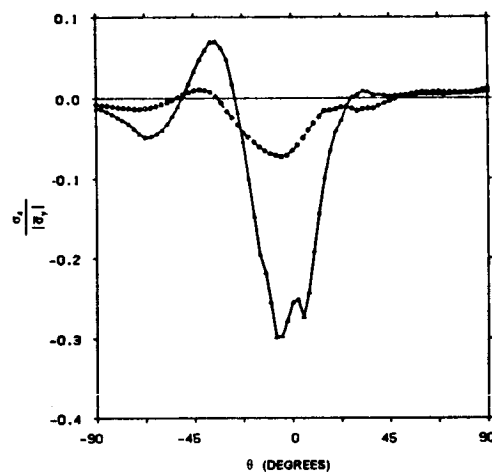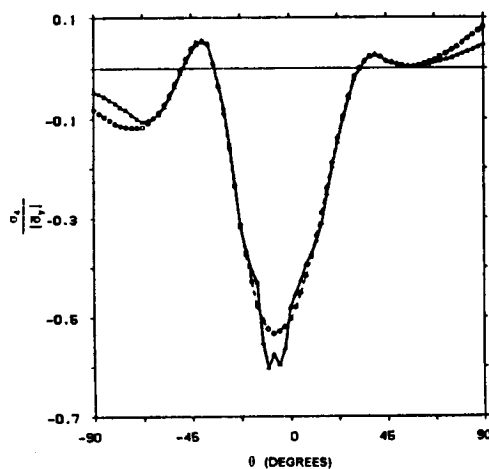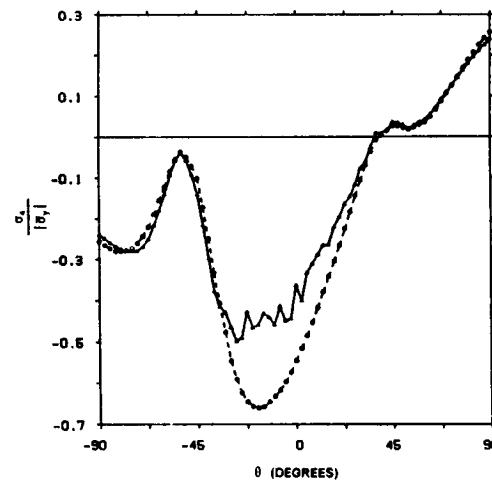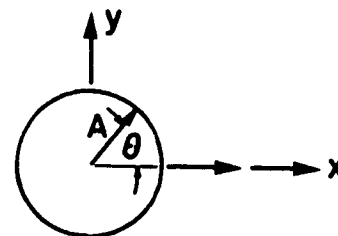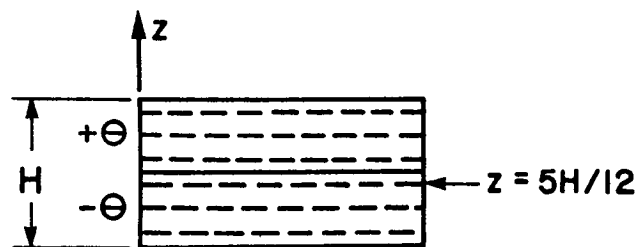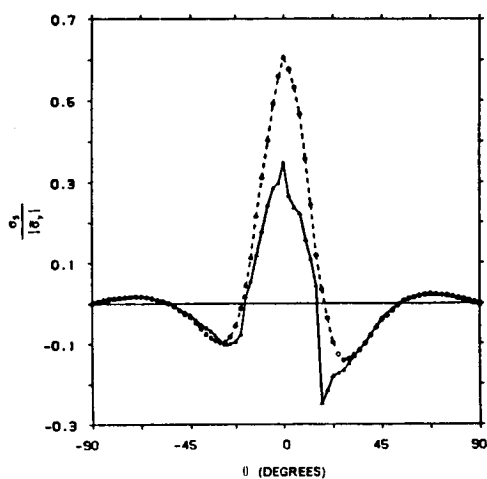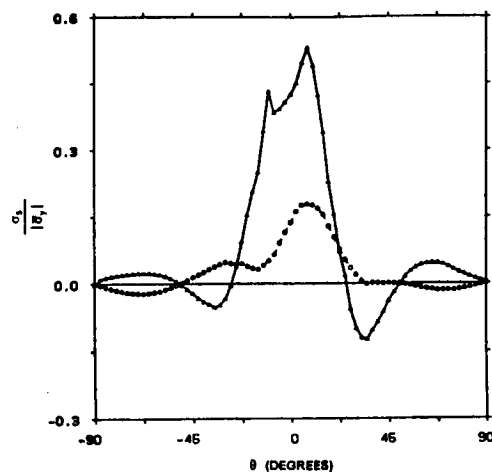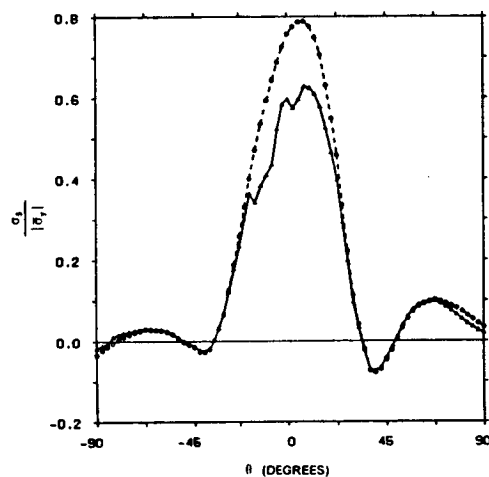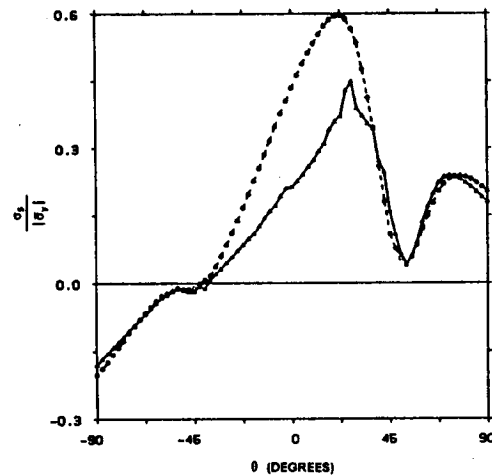
—•— ENDOCHRONIC THEORY   --○-- LINEAR THEORY
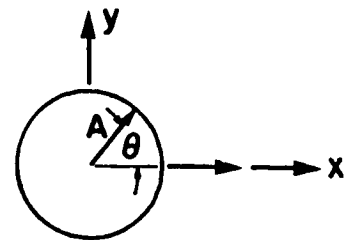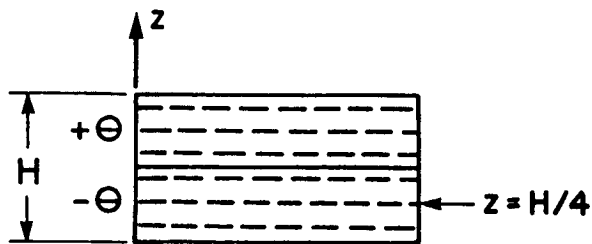
Figure 58. σ_θ Versus θ for Notched Laminates with w/d Ratios of 10, Z=H/4
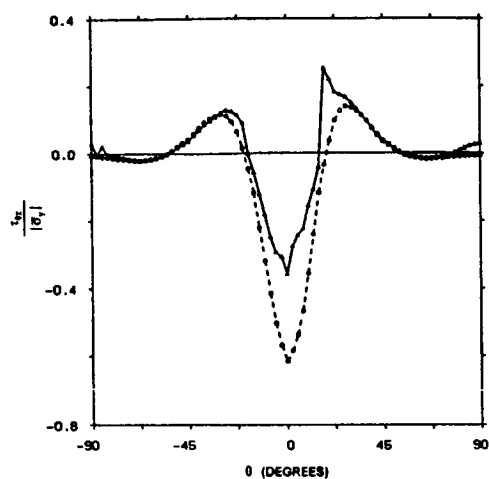
(a) $[(\pm 10)_{12}]_s$ Laminate - 1/4" Hole
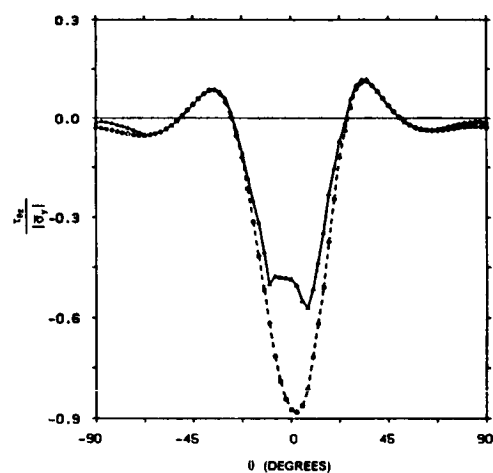
(b) $[(\pm 20)_{12}]_s$ Laminate - 1/4" Hole
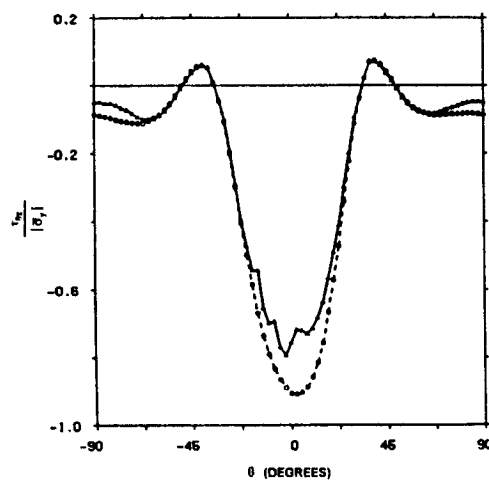
(c) $[(\pm 30)_{12}]_s$ Laminate - 1/2" Hole
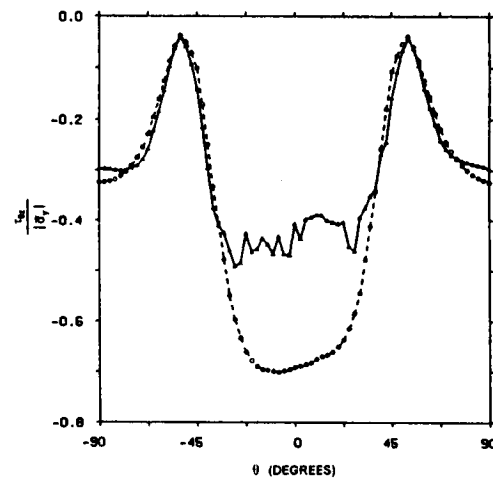
(d) $[(\pm 45)_{12}]_s$ Laminate - 1/2" Hole
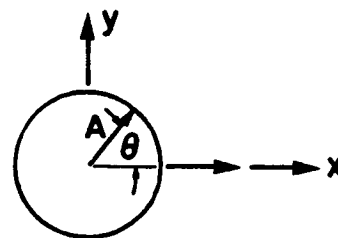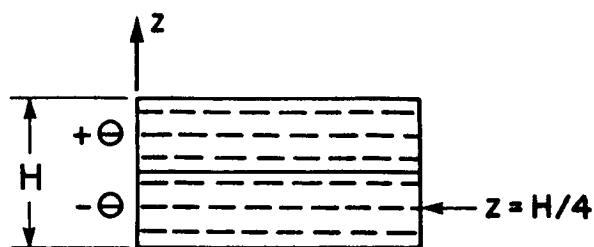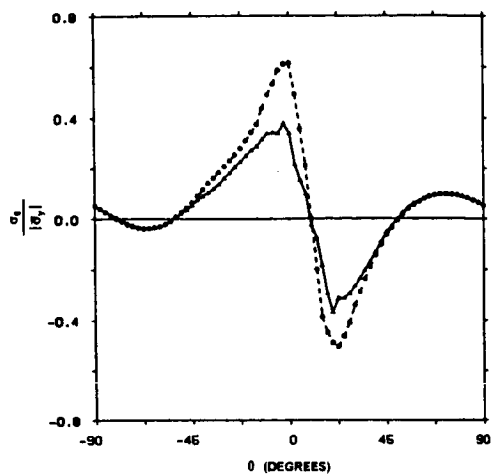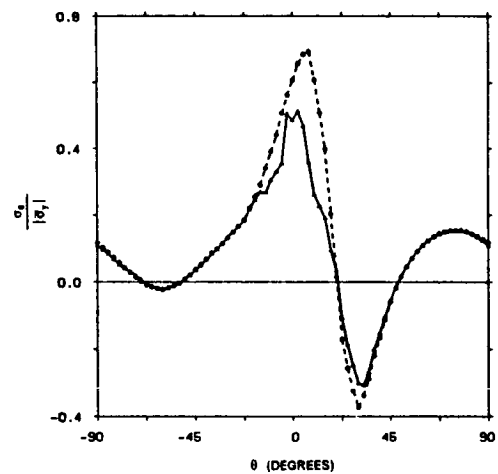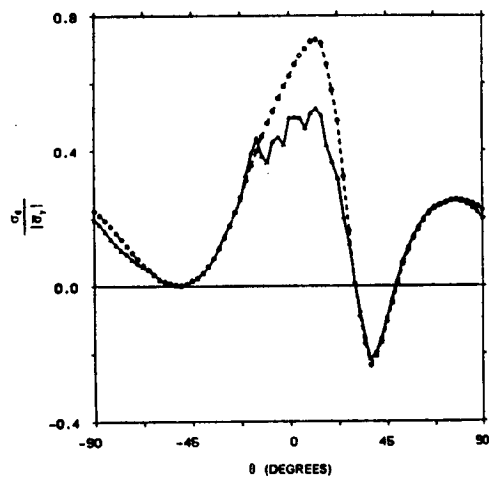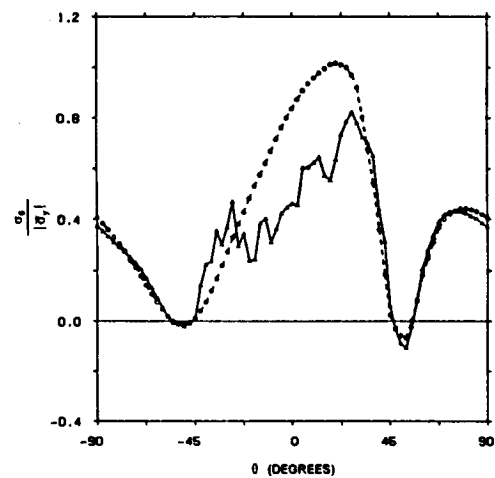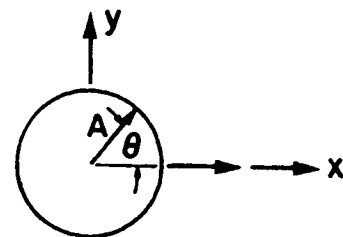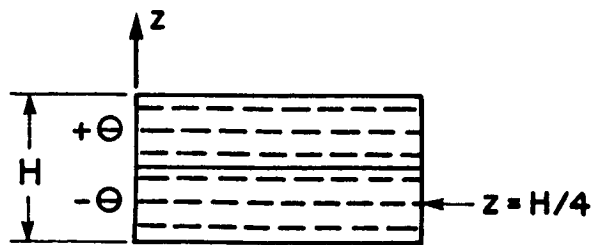
—▲— ENDOCHRONIC THEORY   — LINEAR THEORY
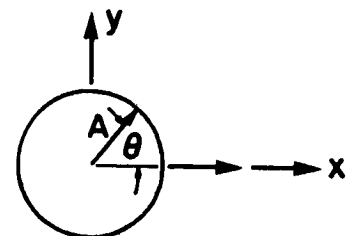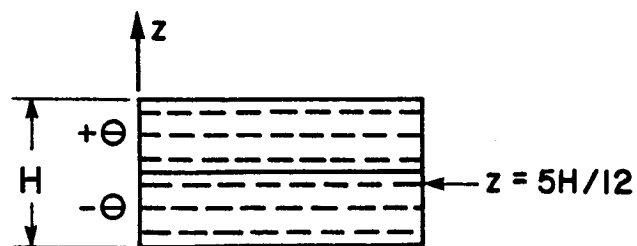
Figure 59. $\tau_{\theta z}$ Versus θ for Notched Laminates with w/d Ratios of 10, Z=5H/12

(the layup angle of the laminates) increases, the θ bandwidth of high $\tau_{\theta z}$ stresses around the hole widens. In fact, the $[(\pm 45)_{12}]_s$ laminate shows a nearly constant peak value of $\tau_{\theta z}$ from $\theta \cong -25°$ to $\theta \cong 25°$. On the other hand, the peak value of $\tau_{\theta z}$ occurs in a very limited region around $\theta = 0°$ in the $[(\pm 10)_{12}]_s$ laminate. The endochronic theory stress magnitudes are smaller than the linear elastic magnitudes for nearly all values of θ in all of the laminates. Only in the $[(\pm 10)_{12}]_s$ laminate is the endochronic theory stress magnitude larger than the linear elastic magnitude from $\theta \cong 15°$ to $\theta \cong 45°$. The reduction in the peak stress concentration due to endochronic theory analysis is as great as 30% in the $[(\pm 45)_{12}]_s$ laminate.

4.7 Summary

The overall stress-strain correlation between endochronic theory finite element analysis and experiment is very good. The endochronic theory was shown to predict axial and transverse response more accurately than linear elastic analysis in all of the laminates, especially for the $[\pm 45]_s$ and $[(\pm 45)_{12}]_s$ laminates. However, the predicted transverse response was not as good as the predicted axial response in the $[\pm 10]_s$, $[\pm 20]_s$, and $[\pm 30]_s$ unnotched laminates (where σ_1 and σ_2 are of opposite sign). A possible cause for the less accurate correlation in these laminates is that the endochronic parameters are unable to accurately model mixed stress states.

In spite of the generally good correlation, the endochronic theory finite element analysis is limited by numerical problems. The endochronic constitutive equations predict unloading of certain stress components in the angle-ply laminates at some point during their load history. This, coupled with the constant stress and constant strain algorithms which will not converge near unloading points, limits the utility of the finite element program AMNISAP. The unloading

problem is circumvented somewhat by the zero-slope condition. However, this is only a "patch-up" solution and results generated after unloading occurs are questionable.

The comparison between stresses from linear elastic and endochronic theory analyses reveals some interesting results. In general, the stress concentrations from endochronic theory analysis are smaller than those from linear elastic analysis. However, at various locations, the endochronic theory predicts stress magnitudes greater than linear elastic analysis. The endochronic theory stress profiles are generally more jagged than the linear elastic profiles, sometimes jumping to extreme magnitudes. An explanation for this unexpected phenomonen is that another stress component at the same location unloaded and the zero-slope condition was imposed. To re-establish equilibrium, the observed stress component shifted to a higher than expected value.

5.0 Failure

5.1 Introduction

In a previous analysis of compression loaded angle-ply laminates with central holes, Burns et al [1] found ultimate failure load predictions to be very conservative in comparison to experimental results. However, Burns et al prediction's of the mode and location of failure were quite good. In the present study, the main reason for using a nonlinear constitutive relationship was to asses the effect of nonlinear material response on the prediction of the failure load. It was reasoned that linear elastic analysis predicts stresses around the hole to be much higher than they are in real laminates. Inclusion of nonlinear material response in the analysis should result in more accurate (and lower) stress levels in the region of stress concentration around the hole.

Another possible explanation for the conservative predictions of failure using the finite element model is that the idealized model predicts a stress state near the hole which is much higher than the true stress state. This is because the finite element model treats the ply interface as being discrete -- the material properties change discontinuously across the

interface. Of course, this mathematical discontinuity is not present in actual laminates; therefore, the stresses predicted by the model may be significantly higher than those in real laminates [49].

This chapter presents a failure analysis of both unnotched and notched laminates based upon a nonlinear stress analysis and the tensor polynomial failure criterion. The stress results generated by AMNISAP were used in a post-processing program which employs the tensor polynomial failure criterion to predict the far field load, location (for laminates with holes), and mode of failure. The tensor polynomial was chosen as the failure criterion because it accounts for stress interaction, which may be especially important in the complex, three-dimensional stress field around the hole. Results of the failure analysis based upon linear and nonlinear material response are compared to experimental results.

Application of the tensor polynomial (a point-wise failure criterion) at points around the hole edge gives a prediction of the initial (first) failure event in the laminate. Often, this does not correspond to the ultimate load carrying capacity in real laminates. Damage, in the form of micro-cracks, usually forms in the highly stressed region of the hole edge prior to final fracture. One approach for the application of a point-wise failure criterion to notched laminates is to base failure on the stress state at a small distance d_0 from the edge of the hole. The distance d_0 from the hole edge has been called a characteristic distance[48], meaning that for a given material it does not change with the layup of the material. This chapter examines the tensor polynomial failure predictions at various radii around the hole to assess the correlation of theory and experiment.

The final objective of this chapter is to examine the effect of the w/d (width over hole diameter) ratio on failure. Results from linear elastic analysis are compared with those from inelastic analysis.

Failure

5.2 The Tensor Polynomial

The stress tensor polynomial can be written

$$F_i \sigma_i + F_{ij} \sigma_i \sigma_j \leq 1 \quad (i = 1,2,....,6)$$

where the stress components in material principal coordinates (σ_i) have been expressed in reduced notation. The F_i and F_{ij} are second order and fourth order strength tensors, respectively, determined from tests on unidirectional laminae. Determining the normal stress interaction constants F_{12}, F_{13}, and F_{23} requires difficult to perform biaxial tests. Fortunately, these constants have been previously shown to have little influence on the failure predictions. In this study, F_{12}, F_{13}, and F_{23} are set to zero. The required components of the strength tensors are determined as follows:

$$F_i = \frac{1}{\sigma_i^{uc}} + \frac{1}{\sigma_i^{ut}} \quad (i = 1,2,3)$$

$$F_{ii} = \frac{-1}{(\sigma_i^{uc})(\sigma_i^{ut})} \quad (i = 1,2,3, \text{no sum})$$

$$F_{ii} = \frac{1}{(\sigma_i^{ult})^2} \quad (i = 4,5,6, \text{no sum})$$

$$F_i = 0 \quad (i = 4,5,6)$$

$$F_{ij} = 0 \quad (i \neq j)$$

5.2.1 Strength Parameters for AS4/3502 Graphite-Epoxy

The AS4/3502 strength data used for failure prediction (Table 9) are the same as those used in Burns et al [1]. The constants σ_i^{uc} and σ_i^{ut} (i = 1,2,3) represent the principal material direction normal strengths in compression and tension, respectively. The constants σ_i^{ult} (i = 4,5,6) represent the principal material direction shear strengths. Since the time of Burns' work, improved test methods have shown the σ_5^{ult} and σ_6^{ult} shear strengths to be considerably higher than those used by Burns et al. The 1-2 plane [0] Iosipescu test used to determine endochronic constants in Chapter 2 (Figure 7) failed at a shear stress of 13.5 ksi; however, failure did not initiate in the shear region and the failure mode was transverse tension, not pure shear. Therefore, the true shear strength of AS4/3502 is believed to be higher than 13.5 ksi. Walrath and Adams [47] observed shear strengths of 15.5 ksi for AS4/3501-6 (a material very similar to AS4/3502) using the Iosipescu shear tests. Considering the above, the 1-2 and 1-3 plane shear strength (σ_6^{ult} and σ_5^{ult}, respectively) used in this study is 14 ksi. Both Burns et al value of 9.4 ksi and this new value of 14 ksi are considered in the failure analysis of notched and unnotched laminates and comparisons are made.

5.3 Unnotched Laminates

Failure analysis of the unnotched laminates presented few difficulties. Because the two-dimensional stress state (edge effects were not considered) is constant throughout the in-plane and thickness dimensions, ultimate fracture was assumed to occur when failure was first predicted by the tensor polynomial. Comparisons of failure based upon linear elastic stress analysis and nonlinear stress analysis are shown in Table 10 where the axial failure stress and failure strain are given as σ_y^{ult} and ε_y^{ult}, respectively.

Failure   161

Table 9. Lamina Strengths for AS4/3502 Graphite Epoxy

Strength Property	(ksi)
σ_1^{ut}	200.0
σ_1^{uc}	-122.0
σ_2^{ut}	7.0
σ_2^{uc}	-35.0
σ_3^{ut}	7.0
σ_3^{uc}	-35.0
σ_4^{ult}	8.0
σ_5^{ult}	9.4
σ_6^{ult}	9.4

As can be seen in Table 10, both linear theory and endochronic theory failure predictions for the unnotched angle-ply laminates were quite good. Since the tensor polynomial is based on stress, the endochronic theory and linear theory predictions of failure stress are nearly identical. However, the failure strains predicted by the two theories differ considerably -- the endochronic theory failure strains correlate with experiment significantly better than the linear theory failure strains.

As shown in Table 10, a shear strength of 9.4 ksi gives conservative failure predictions (both σ_y^{ult} and ε_y^{ult}) for all of the laminates, except the $[\pm 20]_s$ laminate. A shear strength of 14 ksi also gives conservative failure predictions except for the $[\pm 20]_s$ laminate and σ_y^{ult} of the $[\pm 45]_s$ laminate; however, the failure predictions are considerably more accurate (except for the $[\pm 20]_s$ laminate). Using the 14 ksi shear strength, the predicted σ_y^{ult} stresses and ε_y^{ult} strains are within 6% of experimental values for the $[\pm 10]_s$ and $[\pm 30]_s$ laminates. The endochronic theory predicted σ_y^{ult} and ε_y^{ult} are within 12% and 40% of experiment, respectively, for the $[\pm 45]_s$ laminate. The ε_y^{ult} strain is a significant improvement over that predicted using 9.4 ksi as the shear strength. The tested $[\pm 45]_s$ laminate did not fail at the stress and strain levels given in Table 10 -- the amount of axial deformation required to cause final fracture of this specimen was larger than the travel permitted by the loading frame. The σ_y^{ult} and ε_y^{ult} values presented are the maximum values attained during the test.

The reason for the $[\pm 20]_s$ laminate's poor correlation between theory and experiment is not understood. It is possible that the test specimens contained flaws which caused them to fail early. However, this is unlikely because both specimens failed at nearly identical loads. Another possibility is that the $[\pm 20]_s$ laminate failed due to interlaminar stresses which were not modeled in the stress analysis. If this is true, the $[\pm 20]_s$ laminate's failure mode is exclusive from the failure modes of the other angle-ply laminates since failure predictions are satisfactory for them.

Failure

Table 10. Comparison of Failure Predictions with Experiment for Unnotched Laminates

Laminate	$[\pm 10]_s$		$[\pm 20]_s$		$[\pm 30]_s$		$[\pm 45]_s$	
	σ_y^{ult} (ksi)	ε_y^{ult} (%)	σ_y^{ult} (ksi)	ε_y^{ult} (%)	σ_y^{ult} (ksi)	ε_y^{ult} (%)	σ_y^{ult} (ksi)	ε_y^{ult} (%)
$\sigma_5^{ult} = \sigma_6^{ult}$ = 9.4 ksi								
Linear Theory	-92.658	-0.5153	-48.503	-0.3679	-27.538	-0.3725	-19.058	-0.6531
Endochronic Theory	-92.880	-0.5461	-48.716	-0.3784	-27.363	-0.3808	-19.127	-0.7856
$\sigma_5^{ult} = \sigma_6^{ult}$ = 14 ksi								
Linear Theory	-95.504	-0.5310	-54.183	-0.4109	-34.594	-0.4680	-30.272	-1.0374
Endochronic Theory	-95.031	-0.5598	-53.626	-0.4184	-33.362	-0.4759	-30.205	-1.9361
Experiment*	-96.985	-0.5683	-42.490	-0.3306	-34.340	-0.5028	-26.760	-1.5910
Range	10.630 (ksi)	0.0668 (%)	2.540 (ksi)	0.0232 (%)	1 test	1 test	1 test	1 test

* Note:

Experimental values are averaged.

Range indicates the largest difference between experimental values.

5.4 Notched Laminates

Predicting the final fracture load of laminates containing notches is difficult because regions near the notch generally fail before the laminate as a whole fails. This local failure may or may not be observable. Micro-cracking is usually difficult to observe whereas shear crippling, fiber breakage and delamination are much easier to detect. The angle-ply laminates in this study displayed no signs of observable (x-ray) damage prior to ultimate failure (with the exception of the $[(\pm 45)_{12}]_s$ laminate with a 1/2″ hole). Another difficulty in predicting final fracture is obtaining an accurate stress state around the hole. As mentioned earlier, the finite element mesh models ply interfaces as being discrete. Therefore, the finite element analysis may give stresses that are too high.

Despite these difficulties, predicting the fracture load is only part of understanding the failure process of the notched angle-ply laminates. Predicting the mode of failure and the location at which failure initiates are important as well. Discussions of fracture, the mode, and the location of failure initiation are presented in the following two sections.

5.4.1   Fracture

Theory and experiment are compared for laminates with w/d ratios of 10 in Table 11, where σ_y^{ult} and ε_y^{ult} represent the far-field axial stress and strain at the fracture load. The fracture load is equivalent to the load at which the tensor polynomial predicts failure at the hole edge. As mentioned previously, because local failure at the hole edge does not necessarily correspond to fracture and because the finite element stresses may be too high, the theoretical σ_y^{ult} and ε_y^{ult} values in Table 11 are very conservative. A shear strength of 14 ksi gives slightly less conservative failure predictions than the 9.4 ksi shear strength; however, the improvement is

not as pronounced as with the unnotched laminates. The higher value of shear strength improves the $[(\pm 45)_{12}]_s$ laminates σ_y^{ult} stress most, bringing it to within approximately 50% of the experimental σ_y^{ult} stress.

Similar to the analysis of unnotched laminates, the linear theory and endochronic theory σ_y^{ult} stresses in Table 11 are nearly identical for all of the laminates. As mentioned previously, because the tensor polynomial is a stress based failure criterion and because the stresses are relatively proportional, this is expected. However, unlike the unnotched laminate analysis, the linear theory and endochronic theory ε_y^{ult} strains are also nearly identical. The reason the ε_y^{ult} strains are so similar is that at the low predicted values of σ_y^{ult}, the laminates have not been loaded significantly into their softening regions. If the theoretical σ_y^{ult} stresses were close to the experimental σ_y^{ult} stresses, the linear theory and endochronic theory ε_y^{ult} strains would differ significantly, the endochronic strains being the more accurate.

From Table 11, it appears that the problems of applying the tensor polynomial at the hole edge and finite element stresses that are possibly too high have caused the theoretical σ_y^{ult} failure stresses to be very conservative. Because of the low σ_y^{ult} stresses, the endochronic theory was not able to show an advantage over linear elastic analysis in predicting failure stresses σ_y^{ult} and failure strains ε_y^{ult}. The results from Chapter 4 clearly show that with more accurate values of σ_y^{ult} stresses, the endochronic theory would give more accurate predictions of ε_y^{ult} strains than linear theory.

5.4.2 Failure Mode and Location

The failure mode and location as predicted by linear and endochronic stress analyses agree quite well with experiment. Table 12 and Table 13 list the predicted location, fracture stress σ_y^{ult} and strain ε_y^{ult}, and the tensor polynomial terms at failure for the four angle-ply laminates

Laminate	$[(\pm 10)_{12}]_s$		$[(\pm 20)_{12}]_s$		$[(\pm 30)_{12}]_s$		$[(\pm 45)_{12}]_s$	
	σ_y^{ult} (ksi)	ε_y^{ult} (%)	σ_y^{ult} (ksi)	ε_y^{ult} (%)	σ_y^{ult} (ksi)	ε_y^{ult} (%)	σ_y^{ult} (ksi)	ε_y^{ult} (%)
$\sigma_5^{ult} = \sigma_6^{ult}$ = 9.4 ksi								
Linear Theory	-10.696	-0.0596	-7.956	-0.0605	-7.208	-0.0973	-7.952	-0.2722
Endochronic Theory	-10.640	-0.0592	-7.969	-0.0606	-7.222	-0.0975	-7.871	-0.2688
$\sigma_5^{ult} = \sigma_6^{ult}$ = 14 ksi								
Linear Theory	-14.603	-0.0812	-11.072	-0.0841	-9.570	-0.1292	-11.437	-0.3906
Endochronic Theory	-14.929	-0.0833	-11.223	-0.0855	-9.732	-0.1315	-12.195	-0.4239
Experiment*	-76.255	-0.4054	-45.010	-0.3550	-26.323	-0.3521	-25.227	-1.4387
Range	1.350 (ksi)	0.0161 (%)	0.420 (ksi)	0.0057 (%)	1.510 (ksi)	0.0289 (%)	4.28 (ksi)	0.3774 (%)

* Note:

   Experimental values are averaged.

   Range indicates the largest difference between experimental values.

using the two material models. Figure 60 through Figure 63 show the tensor polynomial profile around the hole edge for both linear and endochronic stress analyses. Note that the endochronic theory gives a profile nearly identical to the linear elastic profile. In the sections that follow, theory and experiment are compared.

5.4.2.1   10 ° Angle-Ply Laminate With A 1/4" Hole

The $[(\pm 10)_{12}]_s$ laminate failed in two modes, one a compressive failure across the horizontal axis of symmetry, and the other a fracture at 10 ° from the loading axis [1]. Both of these failures initiated at $\theta = 0°$. As shown in Table 12, both linear and endochronic theory analysis predict failure to occur at the first gauss plane above the ply interface (Z=7H/12) and at an angle of 0.0 ° from the x-axis. The largest term in the tensor polynomial is the out-of-plane shear term $F_{55}\tau_{13}^2$, which has a value of 0.51 for both types of analysis. This term, along with the relatively high in-plane shear term of $F_{66}\tau_{12}^2 = 0.21$ likely represents the shear crippling type failure observed in the test specimen. The compressive failure mode is harder to explain. The $F_1\sigma_1$ and $F_{11}\sigma_1^2$ terms are relatively small; however, the value of their sum is significant, being approximately 0.26. Both terms represent compressive failure, so their sum is the important value. Although this value is not as large as the $F_{55}\tau_{13}^2$ term, it is the next largest value and thus represents compressive failure as a second possible failure mode. Note that the linear elastic and endochronic theory tensor polynomial terms are nearly identical. Apparently, the stress states predicted at failure are very similar for both analyses. Using a shear strength of 14 ksi, Table 12 shows the endochronic prediction for failure location to be the same as the elastic prediction; however, the tensor polynomial terms are different from those using using a shear strength of 9.4 ksi. The compressive failure mode terms ($F_1\sigma_1$ and $F_{11}\sigma_1^2$) are higher, while the shear mode terms ($F_{55}\tau_{13}^2$ and $F_{66}\tau_{12}^2$) are lower. In fact, the sum of $F_1\sigma_1$ and $F_{11}\sigma_1^2$ is approximately equal to $F_{55}\tau_{13}^2$, both values being roughly 0.40. This is consistent with both failure

Table 12. **Tensor Polynomial Terms for Laminates with 1/4″ Holes**

$\sigma_5^{ult} = \sigma_6^{ult}$ $= 9.4$ ksi	$[(\pm 10)_{12}]_s$		$[(\pm 20)_{12}]_s$	
	Linear Theory	Endochronic Theory	Linear Theory	Endochronic Theory
Z	7H/12	7H/12	7H/12	7H/12
θ	0.0 °	0.0 °	-2.5 °	-2.5 °
σ_y^{ult}(psi)	-10,696	-10,640	-7,956	-7,969
ε_y^{ult}(%)	-.0596	-.0592	-.0605	-.0606
$F_1\sigma_1$	0.1583	0.1579	0.0801	0.0799
$F_{11}\sigma_1^2$	0.1005	0.1000	0.0257	0.0256
$F_2\sigma_2$	0.0008	0.0006	0.0362	0.0358
$F_{22}\sigma_2^2$	0.0000	0.0000	0.0004	0.0004
$F_3\sigma_3$	-0.0096	-0.0098	0.0178	0.0173
$F_{33}\sigma_3^2$	0.0000	0.0000	0.0001	0.0001
$F_{44}\tau_{23}^2$	0.0195	0.0197	0.0822	0.0819
$F_{55}\tau_{13}^2$	0.5174	0.5187	0.5582	0.5525
$F_{66}\tau_{12}^2$	0.2130	0.2111	0.1993	0.1965
$\sigma_5^{ult} = \sigma_6^{ult}$ $= 14$ ksi	Linear Theory	Endochronic Theory	Linear Theory	Endochronic Theory
Z	7H/12	7H/12	7H/12	7H/12
θ	0.0 °	0.0 °	-2.5 °	-2.5 °
σ_y^{ult}(psi)	-14,603	-14,929	-11,072	-11,223
ε_y^{ult}(%)	-.0812	-.0833	-.0841	-.0855
$F_1\sigma_1$	0.2173	0.2186	0.1113	0.1119
$F_{11}\sigma_1^2$	0.1893	0.1917	0.0497	0.0502
$F_2\sigma_2$	0.0012	0.0015	0.0503	0.0532
$F_{22}\sigma_2^2$	0.0000	0.0000	0.0008	0.0009
$F_3\sigma_3$	-0.0131	-0.0129	0.0247	0.0279
$F_{33}\sigma_3^2$	0.0001	0.0001	0.0002	0.0002
$F_{44}\tau_{23}^2$	0.0368	0.0380	0.1587	0.1614
$F_{55}\tau_{13}^2$	0.4027	0.3993	0.4453	0.4384
$F_{66}\tau_{12}^2$	0.1658	0.1604	0.1590	0.1529

Failure

Table 13. Tensor Polynomial Terms for Laminates with 1/2″ Holes

$\sigma_5^{ult} = \sigma_6^{ult}$ = 9.4 ksi	$[(\pm 30)_{12}]_s$		$[(\pm 45)_{12}]_s$	
	Linear Theory	Endochronic Theory	Linear Theory	Endochronic Theory
Z	7H/12	7H/12	5H/12	5H/12
θ	-5.0 °	-5.0 °	-17.5 °	-17.5 °
σ_y^{ult}(psi)	-7,208	-7,222	-7,952	-7,871
ε_y^{ult}(%)	-.0973	-.0975	-.2722	-.2688
$F_1\sigma_1$	0.0634	0.0631	0.0743	0.0741
$F_{11}\sigma_1^2$	0.0161	0.0160	0.0221	0.0220
$F_2\sigma_2$	0.0552	0.0557	-0.2451	-0.2414
$F_{22}\sigma_2^2$	0.0010	0.0010	0.0188	0.0182
$F_3\sigma_3$	0.0515	0.0516	0.0534	0.0570
$F_{33}\sigma_3^2$	0.0008	0.0008	0.0009	0.0010
$F_{44}\tau_{23}^2$	0.1494	0.1487	0.0906	0.0898
$F_{55}\tau_{13}^2$	0.4154	0.4114	0.2648	0.2670
$F_{66}\tau_{12}^2$	0.2472	0.2429	0.7202	0.7135
$\sigma_5^{ult} = \sigma_6^{ult}$ = 14 ksi	Linear Theory	Endochronic Theory	Linear Theory	Endochronic Theory
Z	7H/12	5H/12	7H/12	7H/12
θ	-5.0 °	-2.5 °	2.5 °	15.0 °
σ_y^{ult}(psi)	-9,570	-9,732	-11,437	-12,195
ε_y^{ult}(%)	-.1292	-.1315	-.3906	-.4239
$F_1\sigma_1$	0.0840	0.0663	0.0505	0.0265
$F_{11}\sigma_1^2$	0.0283	0.0176	0.0102	0.0028
$F_2\sigma_2$	0.0731	0.0516	-0.5591	-0.6354
$F_{22}\sigma_2^2$	0.0017	0.0008	0.0977	0.1262
$F_3\sigma_3$	0.0683	0.0608	0.0779	0.0785
$F_{33}\sigma_3^2$	0.0015	0.0012	0.0019	0.0019
$F_{44}\tau_{23}^2$	0.2623	0.3954	0.6390	0.9066
$F_{55}\tau_{13}^2$	0.3015	0.2470	0.1295	0.0551
$F_{66}\tau_{12}^2$	0.1794	0.1637	0.5524	0.4297
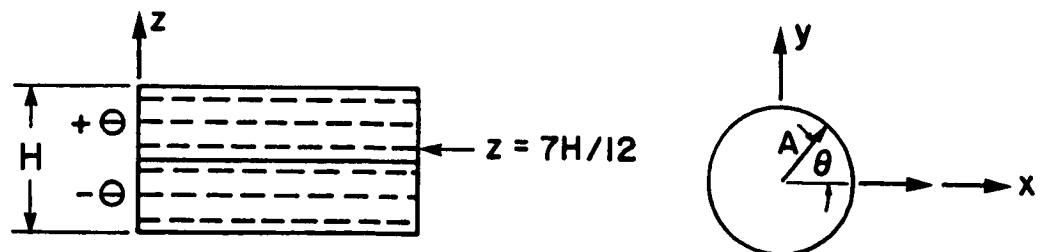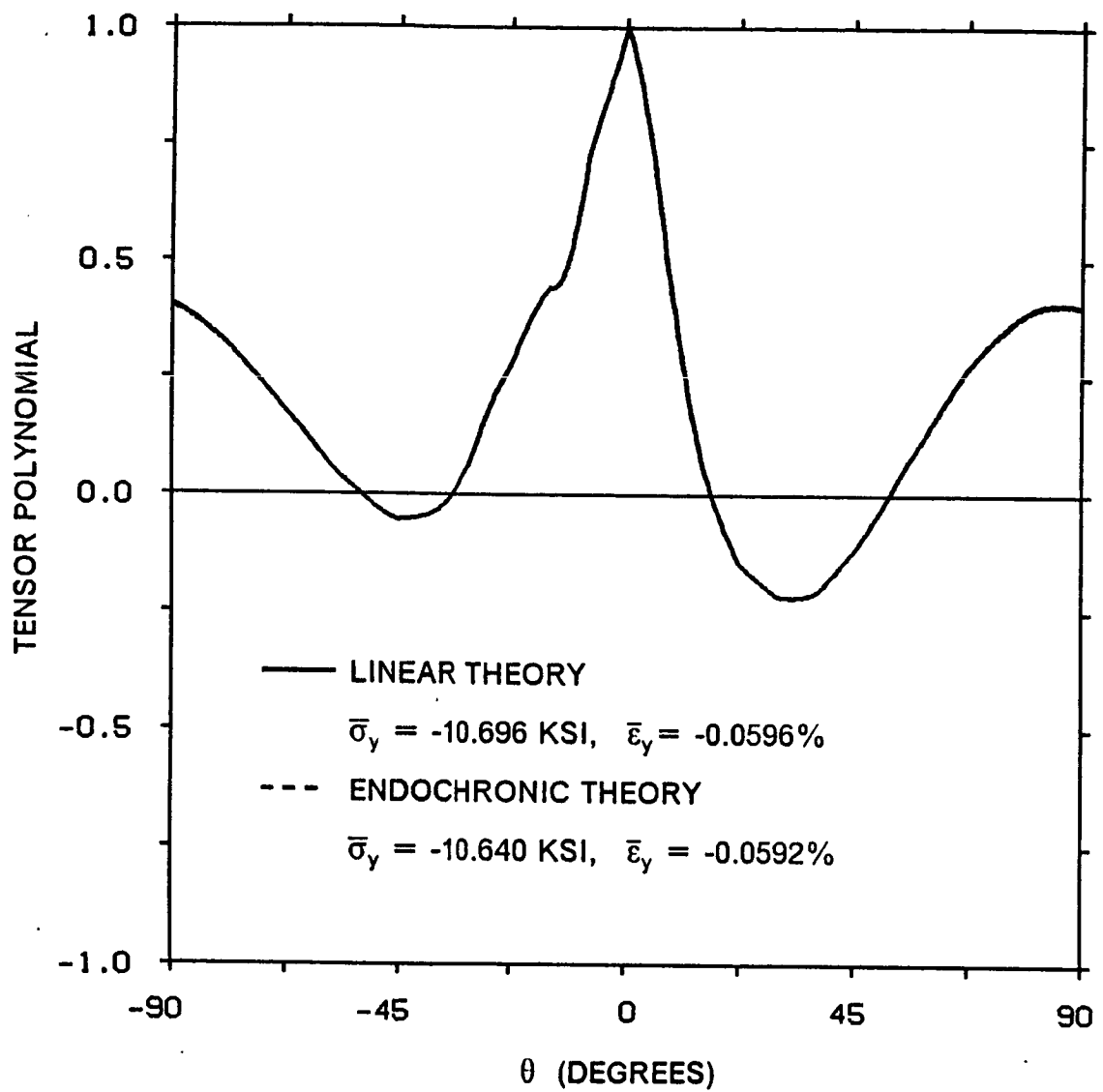
Figure 60. Tensor Polynomial Profile Around The Hole Edge -- $[(\pm 10)_{12}]_s$ Laminate With 1/4″ Hole, Z = 7H/12
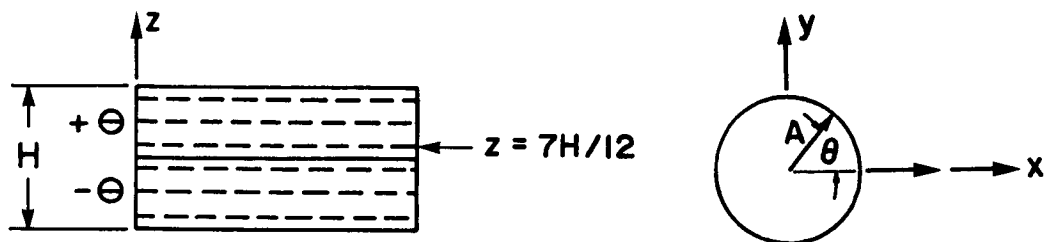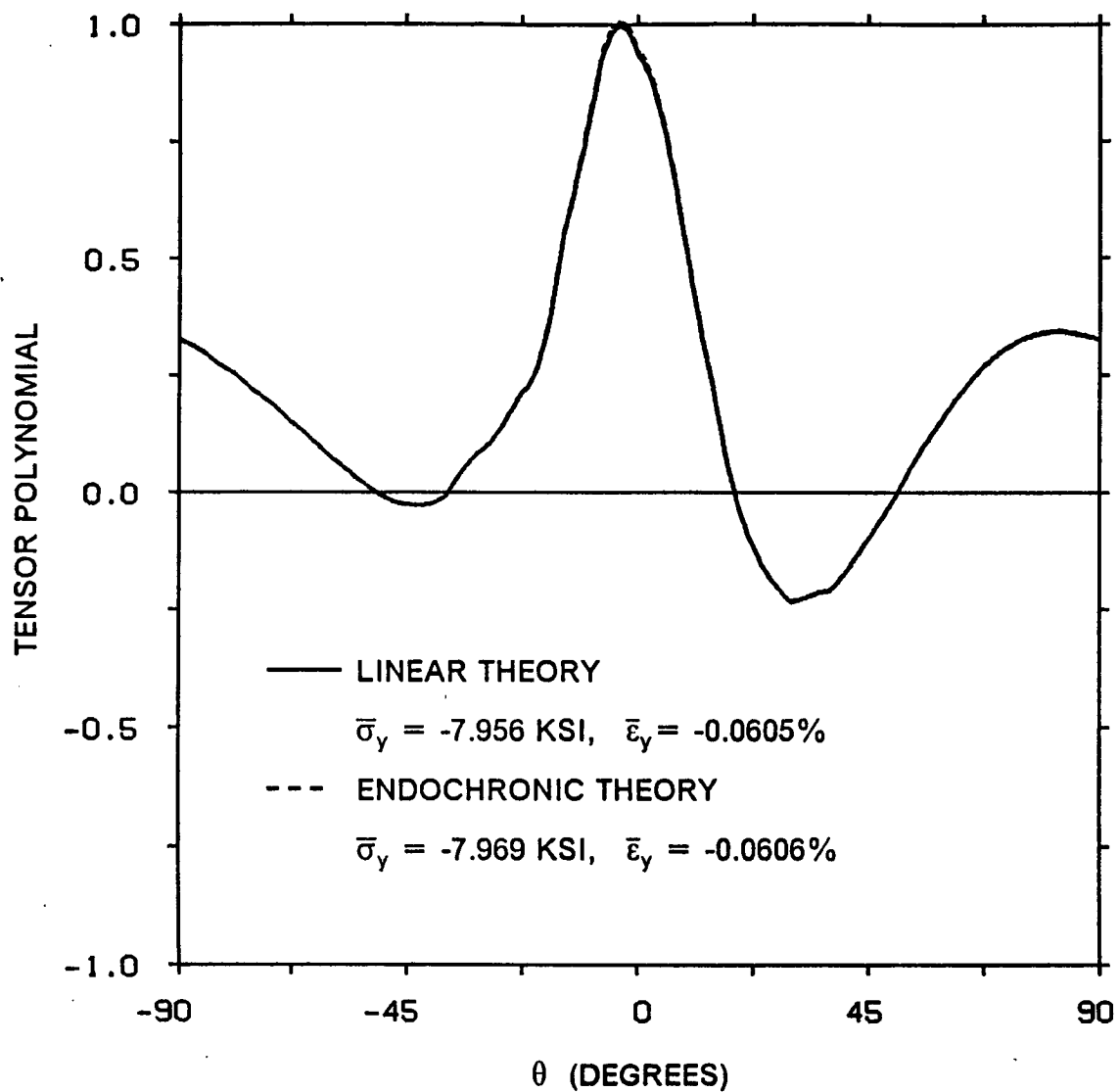
Figure 61. Tensor Polynomial Profile Around The Hole Edge -- [(±20)₁₂]ₛ Laminate With 1/4" Hole, Z = 7H/12
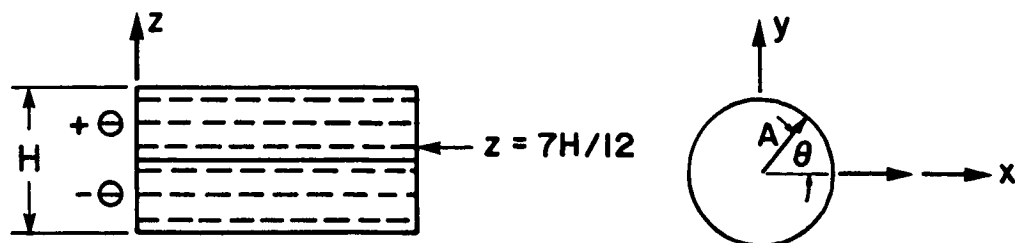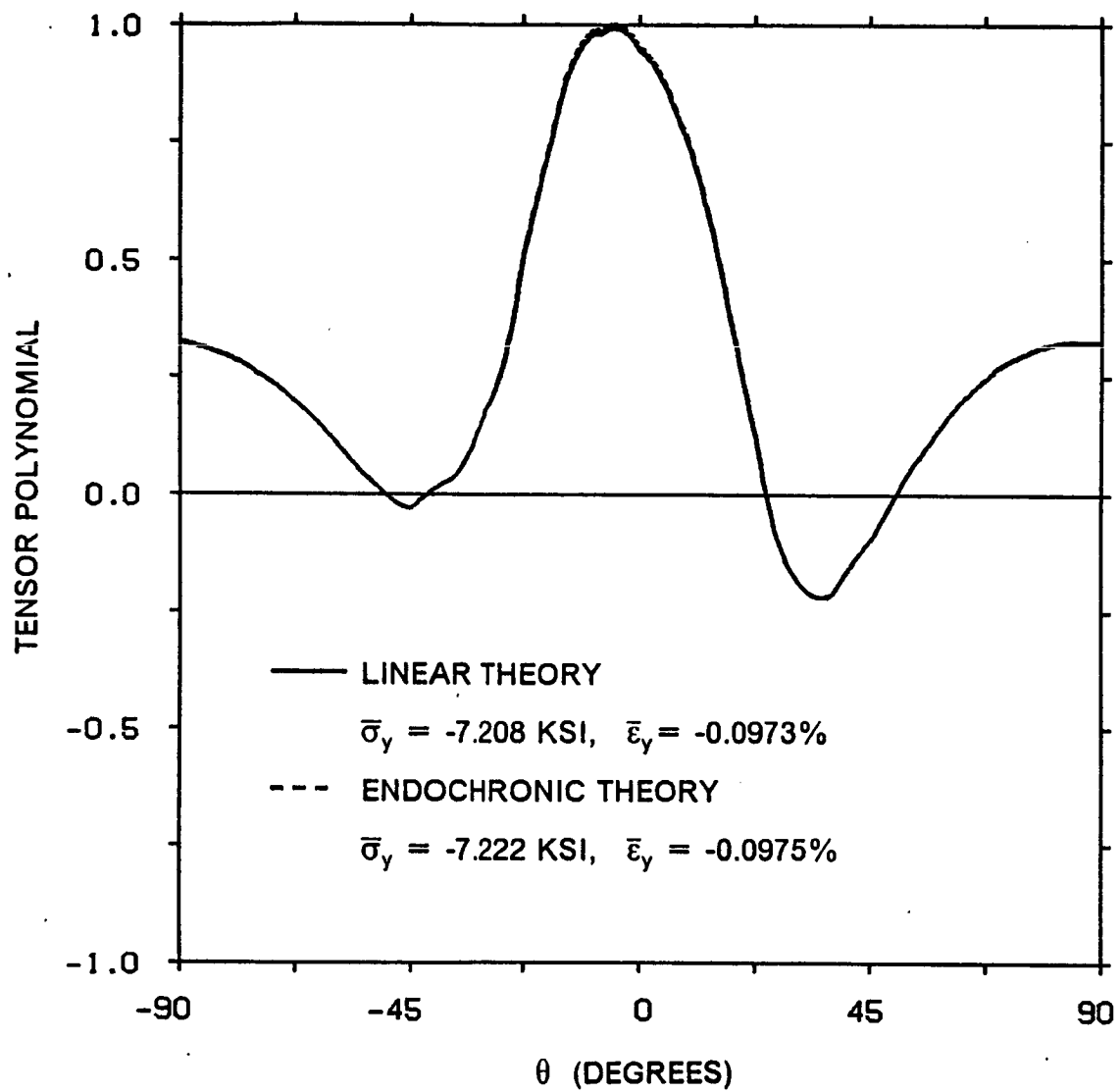
Figure 62. Tensor Polynomial Profile Around The Hole Edge -- [($\pm$30)$_{12}$]$_s$ Laminate With 1/2" Hole, Z = 7H/12
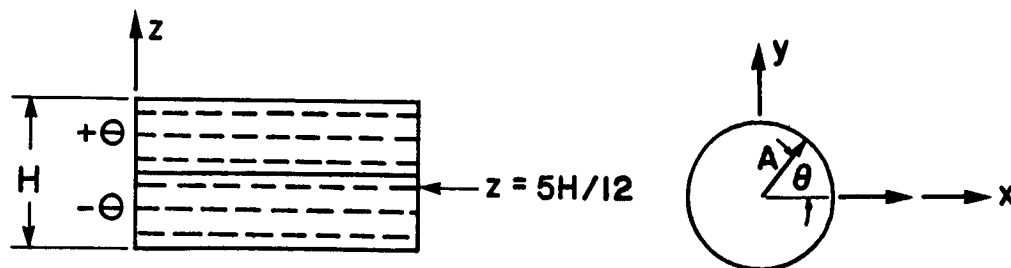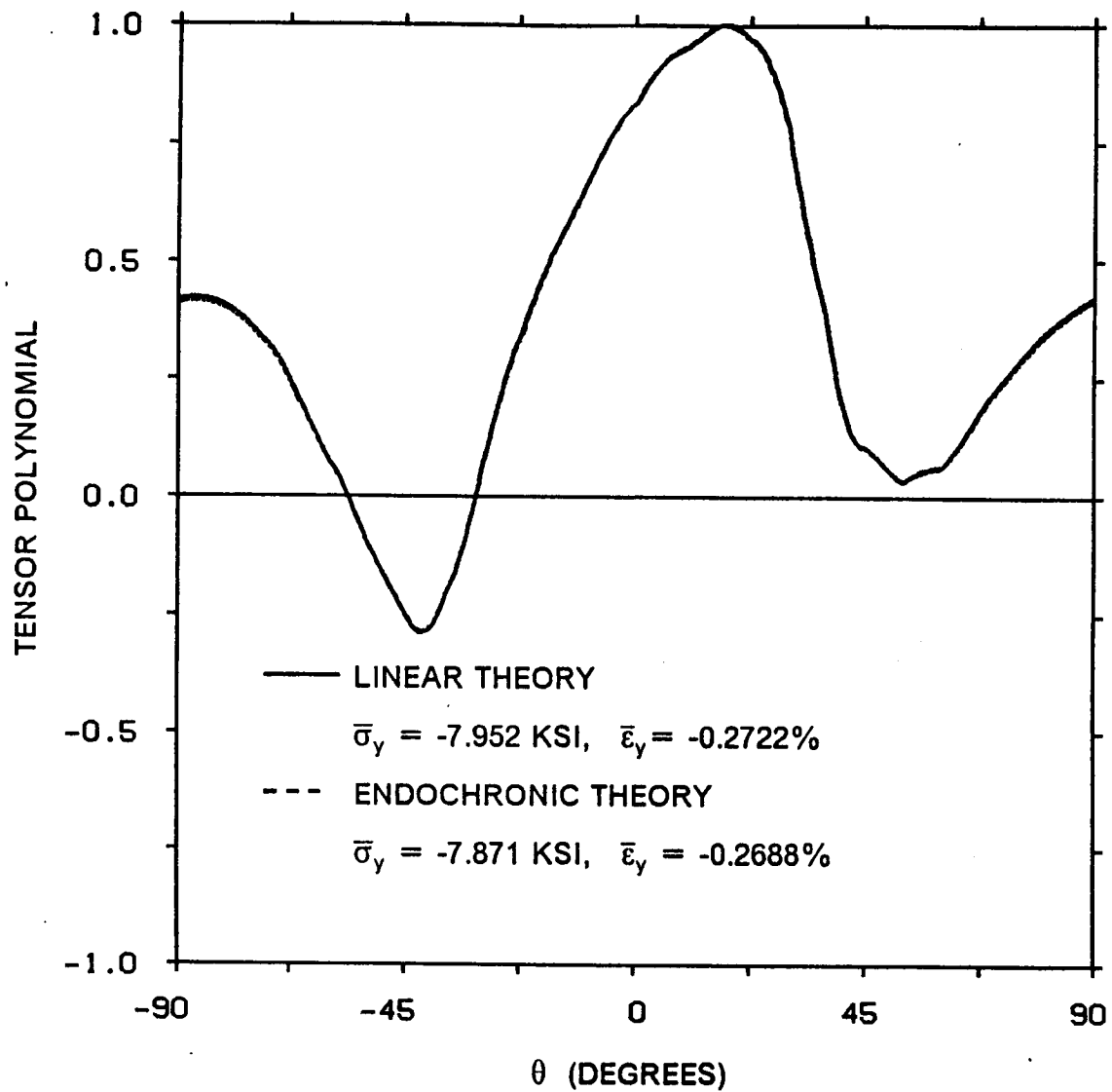
Figure 63. Tensor Polynomial Profile Around The Hole Edge -- [(±45)₁₂]ₛ Laminate With 1/2" Hole, Z = 5H/12

modes being present in the test specimen. This result also lends support for using the higher value of shear strength.

Figure 60 shows that not only are the linear elastic and endochronic theory stress states nearly identical at the point of failure, but around the profile of the hole as well. The endochronic theory results, represented by a dashed line, are nearly indistinguishable from the linear elastic results. The shape of the tensor polynomial profile is very interesting. The majority of the profile lies under the value of 0.5. At $\theta = 0°$, there is a very sharp peak where the tensor polynomial reaches 1.0. Note also that the profile is nearly symmetric about $\theta = 0°$. This is because of the relatively small fiber angle of 10 °. As the other figures show, the near symmetry about $\theta = 0°$ is less pronounced for larger fiber angles.

5.4.2.2   20 ° Angle-Ply Laminate With A 1/4″ Hole

The $[(\pm 20)_{12}]_s$ laminate failed due to a fracture at 20 ° from the loading axis [1]. Like the $[(\pm 10)_{12}]_s$ laminate, this fracture was parallel to the fiber direction in half of the plies and fractured fibers in the alternate plies. Failure initiated at $\theta = 0°$. Table 12 shows that both linear elastic and endochronic theory analysis predict failure to initiate in the first gauss plane above the ply interface $(Z=7H/12)$ and at $\theta = -2.5°$. The dominant tensor polynomial term is again the out-of-plane shear term $F_{55}\tau_{13}^2$ with a value of approximately 0.55. The next largest term is the in-plane shear component $F_{66}\tau_{12}^2$ with a value of approximately 0.20. Together, these two terms have a sum of 0.75, which represents a shear failure as being the dominant failure mode. Using a shear strength of 14 ksi, Table 12 shows a slight redistribution in the values of the tensor polynomial terms that lessens the dominant effect of the $F_{55}\tau_{13}^2$ and $F_{66}\tau_{12}^2$ terms and increases the values of the $F_1\sigma_1$, $F_{11}\sigma_1^2$, and $F_{44}\tau_{23}^2$ terms. However, the $F_{55}\tau_{13}^2$ term is still the largest term at a value of approximately 0.44. As with the $[(\pm 10)_{12}]_s$ laminate analysis, the tensor polynomial terms are nearly identical for both linear and endochronic theory analysis.

Figure 61 shows the tensor polynomial profile around the hole of the $[(\pm 20)_{12}]_s$ laminate to be nearly identical to the profile of the $[(\pm 10)_{12}]_s$ laminate. The peak value occurs at $\theta = -2.5°$ and the peak is not quite as sharp as in the $[(\pm 10)_{12}]_s$ laminate. Also, the near symmetry noted in Figure 60 is somewhat more skewed in Figure 61.

5.4.2.3   30 ° Angle-Ply Laminate With A 1/2" Hole

The $[(\pm 30)_{12}]_s$ laminate failed due to a fracture at 30 ° from the loading axis [1]. As in the $[(\pm 10)_{12}]_s$ and $[(\pm 20)_{12}]_s$ laminates, this fracture was parallel to the fiber direction in half of the plies and fractured fibers in the alternate plies. Failure appears to have initiated at $\theta \cong 0°$, although the failure band was fairly wide, thus it is difficult to pinpoint the exact location at which failure begins (see Figure 2.25 in Burns et al [1]). Using a shear strength of 9.4 ksi, Table 12 shows that both linear theory and endochronic theory analyses predict failure to initiate in the gauss plane above the ply interface and at $\theta = -5.0°$. This location is reasonably close to that observed in the test specimen. Like the $[(\pm 20)_{12}]_s$ laminate, the dominant tensor polynomial term is $F_{55}\tau_{13}^2$ with a value of 0.41. The second and third largest terms are $F_{66}\tau_{12}^2$ and $F_{44}\tau_{23}^2$, respectively. The sum of these shear terms is greater than 0.8, which shows that shear failure should be dominant. Note that all of the tensor polynomial terms agree quite well between linear elastic and endochronic theory analysis. Using a shear strength of 14 ksi, Table 13 shows a difference in the location of failure for the two types of analysis. Linear analysis predicts failure to occur at the same point $(Z=7H/12, \theta=-5.0°)$, whereas the endochronic theory predicts failure to occur at the gauss plane directly below the ply interface $(Z=5H/12)$ at an angle of $\theta = -2.5°$. The endochronic theory predicts the failure location more accurately than linear elastic analysis when the shear strength is set to 14 ksi. Note that the tensor polynomial terms differ fairly significantly between the two analyses and have shifted from the values using a shear strength of 9.4 ksi. Linear analysis still shows the $F_{55}\tau_{13}^2$ term to be dominant, but to a lessor degree. However, the endochronic theory shows

the $F_{44}\tau_{23}^2$ term to be dominant. In both analyses, the sum of the tensor polynomial shear terms using shear strengths of 14 ksi and 9.4 ksi are nearly the same; however, the individual terms are redistributed.

Figure 62 shows the tensor polynomial profile around the hole to be very similar to the profiles of the $[(\pm 10)_{12}]_s$ and $[(\pm 20)_{12}]_s$ laminates shown in Figure 60 and Figure 61, respectively. The peak has a much smoother profile and the bandwidth of points above 0.5 has increased. The near symmetry shape is still present, but more skewed.

5.4.2.4 45 ° Angle-Ply Laminate With A 1/2" Hole

Like the $[\pm 45]_s$ unnotched laminate, the $[(\pm 45)_{12}]_s$ laminates with 1/2" holes were not tested to failure due to the limited travel of the testing machine. However, these laminates did show damage in the form of bands of matrix damage, visible under ultrasonic C-scan, which formed at $\pm 45°$ to the loading axis [1]. It is nearly impossible to observe the precise location of failure initiation from the C-scan, although the damage bands seem to initiate at $\theta \cong \pm 15°$. Using a shear strength of 9.4 ksi, Table 13 shows both linear elastic and endochronic theory analysis to predict the failure location at the gauss plane directly below the ply interface (Z=5H/12) and at $\theta = 17.5°$, which agrees reasonably with experiment. The out-of-plane shear terms ($F_{44}\tau_{23}^2$ and $F_{55}\tau_{13}^2$) are much less dominant in this laminate. Instead, the in-plane shear term $F_{66}\tau_{12}^2$ dominants with a value of approximately 0.72. Part of the reason this value is so high is that the $F_2\sigma_2$ term is negative, which allows the other terms to be larger. Shear failure is the obvious failure mechanism predicted by both analyses. Again, the tensor polynomial terms are nearly identical for both analyses. Using a shear strength of 14 ksi, Table 13 shows a large discrepancy in the predicted location of failure between linear elastic and endochronic theory analysis. Both analyses predict failure to occur in the gauss plane directly above the ply interface (Z=7H/12). However, linear analysis predicts the angle of failure initiation to be 2.5° whereas endochronic theory analysis predicts $\theta = 15.0°$. The

Failure 177

endochronic analysis predicts the correct location more accurately than linear elastic analysis. Also, the tensor polynomial terms differ significantly between the two analyses. In both analyses, the dominant term has shifted from $F_{66}\tau_{12}^2$ to $F_{44}\tau_{23}^2$. However, this shift is most pronounced for the endochronic theory. Note also that the $F_2\sigma_2$ term using a shear strength of 14 ksi is almost three times larger than the $F_2\sigma_2$ term using a shear strength of 9.4 ksi.

The shape of the $[(\pm 45)_{12}]_s$ laminate's tensor polynomial profile is, again, very similar to the previously discussed laminates, as can be seen in Figure 63. The profile is anti-symmetric to the previous laminate's profiles because failure is predicted at Z=5H/12 instead of Z=7H/12. The bandwidth of points with magnitudes above 0.5 has increased, and the near symmetrical shape is much more skewed. As with the previously discussed laminates, the endochronic theory profile is nearly indistinguishable from the linear elastic profile.

5.4.3 Failure Away From The Hole Edge

Whitney and Nuismer [48] applied the characteristic distance theory by evaluating a given failure criterion at a set distance d_0 from the hole edge along the horizontal centerline of the specimen ($\theta = 0°$ here). Burns [1] also used this approach in his work and found the distance d_0 to be dependent on both hole diameter and laminate ply orientation. In other words, the distance d_0 was not found to be "characteristic".

Instead of examining the state of stress at various distances from the hole along $\theta = 0°$, this study applies the tensor polynomial at various radii (or distances from the hole edge) for $-90° \le \theta \le 90°$. Figure 64 and Figure 65 show the fracture stress σ_y^{ult} as a function of distance from the hole edge for the four notched laminates with a w/d ratio of 10. Figure 64 shows the profiles from linear elastic analysis and Figure 65 shows the endochronic theory

profiles. Table 14 lists the failure locations for the same four laminates as a function of distance from the hole edge.

Figure 64 and Figure 65 show the failure profiles from linear elastic analysis and endochronic theory analysis to be nearly the same. Note that the $[(\pm 30)_{12}]_s$ and $[(\pm 45)_{12}]_s$ laminates both have a local maximum at D/A = 0.0045. In other words, the predicted failure stress is lower at D/A = 0.02 than at 0.0045. In fact, for the $[(\pm 45)_{12}]_s$ laminate, this local maximum is the absolute maximum for the data shown. The $[(\pm 45)_{12}]_s$ laminate's profile appears to have nearly a 0 ° slope after the point D/A = 0.02. These figures show that very large D/A values are required to predict the experimentally measured strengths.

As D/A increases, the location of failure also changes as shown in Table 14. Both linear elastic and endochronic theory analysis predict the same failure location in all of the laminates except for the $[(\pm 45)_{12}]_s$ laminate. However, the discrepancy in this case is small and only occurs at D/A = 0.02 and D/A = 0.0355. Note that the through-the-thickness Z location varies widely, especially for the $[(\pm 10)_{12}]_s$ and $[(\pm 20)_{12}]_s$ laminates. The θ locations tend to vary less than the Z locations with the exception of the $[(\pm 10)_{12}]_s$ laminate, where it jumps to nearly 90° at D/A = 0.08. In examining this table, keep in mind that the through-the-thickness location Z and the angle θ are not entirely separate. A point located at a given θ and Z = 7H/12 has nearly the same stress state as a point located at $-\theta$ and Z = 5H/12. For example, in the $[(\pm 30)_{12}]_s$ laminate, failure is predicted to occur at D/A = 0.0045, Z = 7H/12 and $\theta = -3.75°$. At D/A = 0.02, failure is predicted at Z = 5H/12 and $\theta = 3.75°$. Although these points are different, the failure mechanism and mode are likely the same.
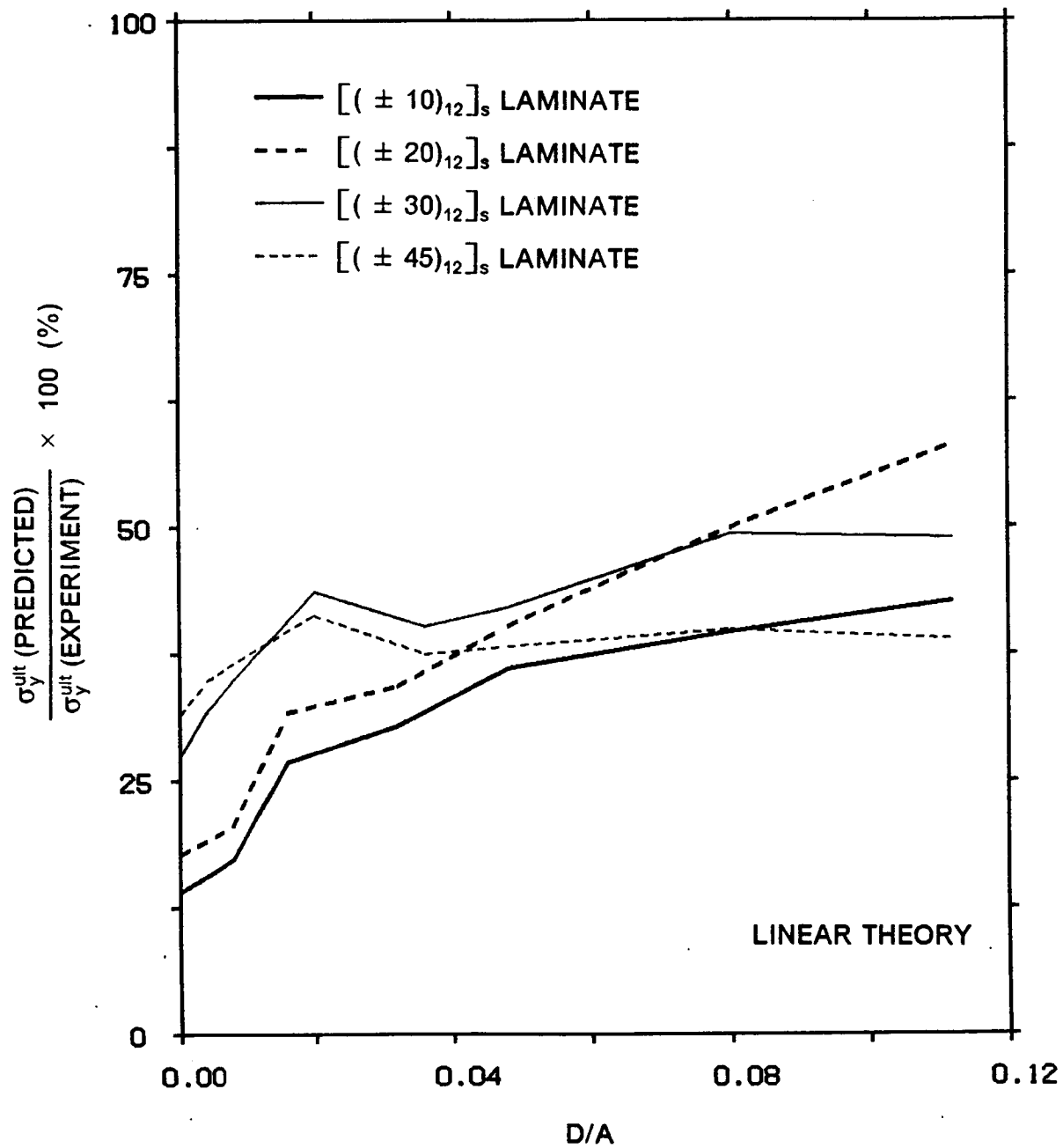
Figure 64. Predicted Failure Stress Versus Distance Away From Hole Edge Using Linear Analysis
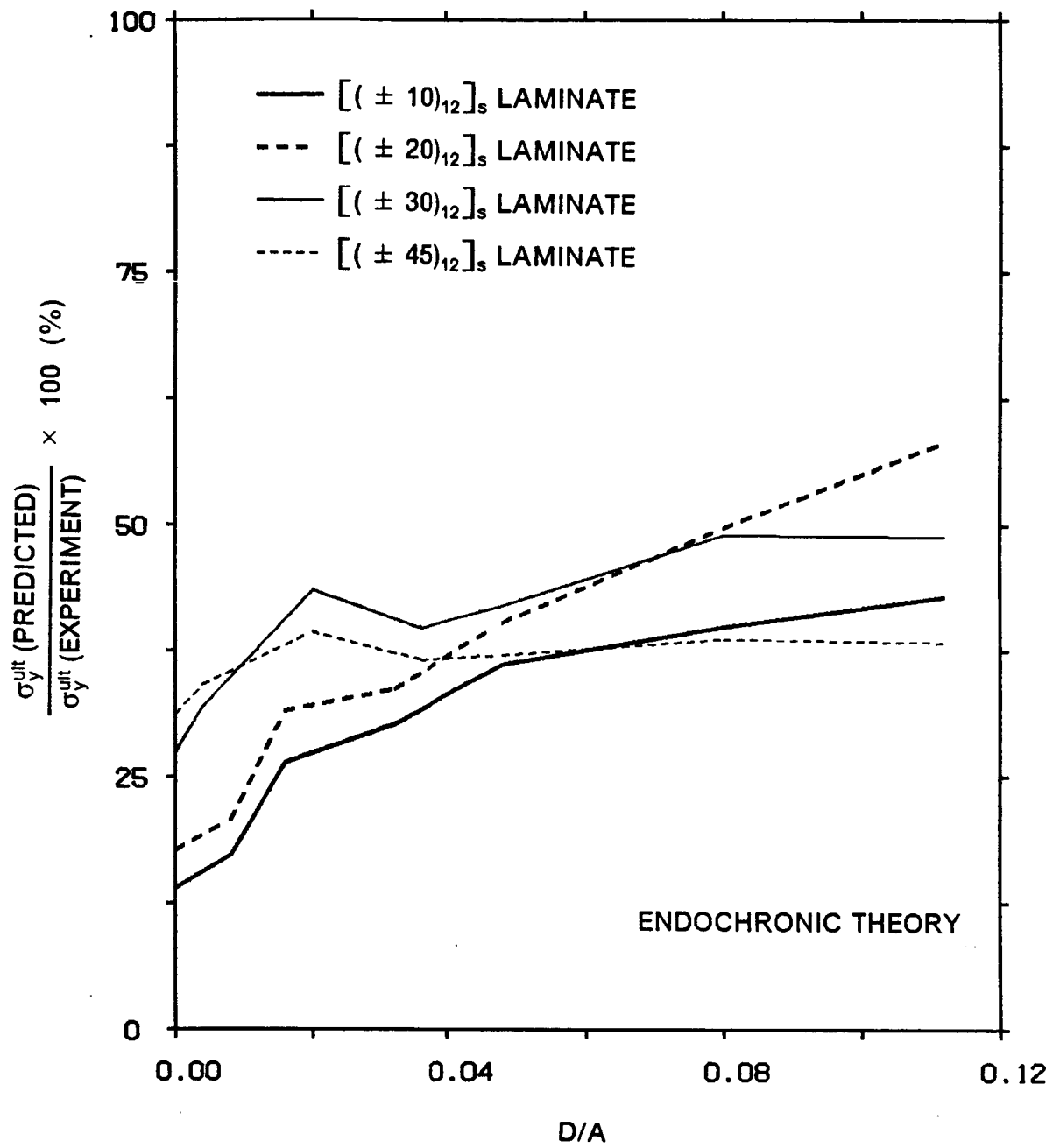
Figure 65. Predicted Failure Stress Versus Distance Away From Hole Edge Using Endochronic Theory Analysis

Failure

Table 14. Location of Failure at Various Distances from the Hole Edge

	$[(\pm 10)_{12}]_s$				$[(\pm 20)_{12}]_s$			
	Linear Theory		Endochronic Theory		Linear Theory		Endochronic Theory	
D/A	Z	θ	Z	θ	Z	θ	Z	θ
0.00000	7H/12	0.0	7H/12	0.0	7H/12	-2.5	7H/12	-2.5
0.00450	5H/12	-0.85	5H/12	-0.85	7H/12	-3.75	7H/12	-3.75
0.020000	H/12	-3.75	H/12	-3.75	5H/12	0.85	5H/12	0.85
0.03550	H/12	-8.35	H/12	-8.35	5H/12	0.85	5H/12	0.85
0.04900	7H/12	-18.75	7H/12	-18.75	5H/12	0.85	5H/12	0.85
0.08000	H/12	89.15	H/12	89.15	5H/12	0.85	5H/12	0.85
0.11100	H/12	89.15	H/12	89.15	11H/12	3.75	11H/12	3.75

	$[(\pm 30)_{12}]_s$				$[(\pm 45)_{12}]_s$			
	Linear Theory		Endochronic Theory		Linear Theory		Endochronic Theory	
D/A	Z	θ	Z	θ	Z	θ	Z	θ
0.00000	7H/12	-5.0	7H/12	-5.0	5H/12	17.5	5H/12	17.5
0.00450	7H/12	-3.75	7H/12	-3.75	5H/12	15.85	5H/12	15.85
0.020000	5H/12	3.75	5H/12	3.75	5H/12	14.15	5H/12	8.35
0.03550	5H/12	0.85	5H/12	0.85	5H/12	8.35	5H/12	3.75
0.04900	5H/12	0.85	5H/12	0.85	5H/12	3.75	5H/12	3.75
0.08000	5H/12	3.75	5H/12	3.75	5H/12	3.75	5H/12	3.75
0.11100	11H/12	-0.85	11H/12	-0.85	11H/12	-3.75	11H/12	-3.75

Failure

C-3

5.4.4 The Effect Of W/D On Failure

Thus far, this chapter has only examined failure in those laminates with w/d ratios of 10. However, $[(\pm 10)_{12}]_s$ and $[(\pm 20)_{12}]_s$ laminates with 1/2" holes and w/d ratios of 5 were also tested [1]. This section examines the effect this reduction in w/d has on both the experimental and predicted fracture stress, σ_y^{ult}, and strain, ε_y^{ult}.

If a hole in a plate caused no stress concentration, the reduction in strength due to a decrease in the ratio w/d would simply be equal to the reduction in cross-sectional area. However, in this study, the angle-ply laminates have in-plane and out-of-plane stress concentrations at both the hole edge and at the edge of the laminate. For the anisotropic plates of this study, the stress concentrations at the hole edge are dependent on the hole size as well. With this in mind, it is not surprising that the reduction in strength does not follow the reduction in cross-sectional area. Comparing the laminates with w/d ratios of 10 to those with w/d ratios of 5, there is only a 11.1% reduction in cross-sectional area. However, as Table 15 shows, experiments reveal a reduction in strength of approximately 18.5% and a reduction in ultimate failure strain of approximately 20% for both laminates. The finite element analyses do not predict the same strength reduction as experiment. Both linear theory and endochronic theory analysis predict approximately an 11% reduction in strength and ultimate failure strain for the $[(\pm 10)_{12}]_s$ laminates. For the $[(\pm 20)_{12}]_s$ laminates, linear elastic analysis predicts approximately a 9% reduction in strength and ultimate failure strain while the endochronic theory predicts approximately a 10% reduction. Therefore, the finite element results tend to follow the reduction in cross-sectional area of approximately 11%. Because the finite element results are extremely conservative in predicting the fracture load, it may not be realistic to expect them to agree with the experimental strength reduction.

Failure

Table 15. The Effect of w/d on Notched Laminate Failure

$[(\pm 10)_{12}]_s$		σ_y^{ult} (ksi)	ε_y^{ult}(%)	Z	θ
Experiment (Average)	w/d = 10	-76.255	-0.44485	--	0.0
	w/d = 5	-62.020	-0.35170	--	0.0
Linear Elastic	w/d = 10	-10.696	-0.05960	7H/12	0.0
	w/d = 5	-9.568	-0.05320	7H/12	0.0
Endochronic Theory	w/d = 10	-10.640	-0.05920	7H/12	0.0
	w/d = 5	-9.441	-0.05240	7H/12	0.0
$[(\pm 20)_{12}]_s$		σ_y^{ult} (ksi)	ε_y^{ult}(%)	Z	θ
Experiment (Average)	w/d = 10	-45.010	-0.35495	--	0.0
	w/d = 5	-36.675	-0.28365	--	0.0
Linear Elastic	w/d = 10	-7.956	-0.06050	7H/12	-2.5
	w/d = 5	-7.226	-0.05490	7H/12	-2.5
Endochronic Theory	w/d = 10	-7.969	-0.06060	7H/12	-2.5
	w/d = 5	-7.190	-0.05460	7H/12	-2.5

5.5 Summary

Failure predictions for the unnotched angle-ply laminates were very good whereas failure predictions for the notched laminates were very conservative. The predicted failure response of unnotched laminates correlated quite well with experiment using a shear strength of 9.4 ksi. However, a shear strength of 14 ksi yielded even better correlation for all laminates except the $[(\pm 20)_{12}]_s$ laminate whose failure prediction was non-conservative with the shear strength of 9.4 ksi. The endochronic theory predicted σ_y^{ult} stresses almost identical to those of linear analysis. However, the endochronic theory predicted ε_y^{ult} strains more accurately than linear analysis, especially for the $[(\pm 45)_{12}]_s$ laminate which exhibits the most ductility.

Using the tensor polynomial at the hole edge to predict the fracture load of notched laminates gave extremely conservative results. One reason for this is likely due to local failure in the region around the hole before ultimate failure occurs. Another is that the predicted stresses around the hole are too high due to the finite element model idealization of discrete ply interfaces.

The tensor polynomial predicted the correct location and mode of failure initiation for the notched laminates. However, changing the shear strength from 9.4 ksi to 14 ksi showed a difference in the predicted location of failure for some of the laminates. Almost all failures were predicted to be caused by τ_{13} or τ_{12} shear stresses or both of them combined. A shear failure mode agrees well with the observed failure mode of the test specimens.

Endochronic theory analysis gives a stress state nearly identical to that of linear analysis, for a given loading, in both the unnotched and notched laminates. Therefore, both analyses predicted σ_y^{ult} stresses to be nearly the same for all notched laminates. Unlike the unnotched laminates, the linear theory and endochronic theory analyses predicted nearly identical ε_y^{ult}

values as well, the reason being that none of the laminates were deformed significantly into their softening regions before failure was predicted.

In conclusion, the endochronic theory failure analysis of notched laminates correlated with experiment only slightly better than the linear analysis due to the limits of the point-wise failure criterion and the finite element model that were used. Chapter 4 showed nonlinear material behavior to be an important factor in analyzing notched angle-ply laminates. Therefore, without the limitations imposed by the point-wise failure criterion and the discrete ply interface finite element model, the endochronic theory would likely predict significantly more accurate failure stresses, σ_y^{ult}, and failure strains, ε_y^{ult}.

6.0 Conclusions

This study has analyzed the loading response and failure of unnotched and notched angle-ply laminates subjected to uniaxial compression. The analysis was performed using the three-dimensional material nonlinear finite element program AMNISAP, which utilizes the endochronic theory as a constitutive relationship. Analytical results were compared to experiment and, where appropriate, results from the endochronic theory were compared to results from linear theory. The conclusions of this study from the previous chapters are presented below.

6.1 The Endochronic Theory

The endochronic theory is a macroscopic constitutive theory that was used in this study to model AS4/3502 graphite-epoxy. The theory, originally developed by Valanis [11] [12] and modified to model transversly isotropic materials by Pindera and Herakovich [19] [20], is based on irreversible thermodynamics and uses the concept of internal variables. The transversely

isotropic theory was extended to three-dimensions in this study to facilitate the analysis of laminates with cutouts.

Like the 2-D equations, the 3-D endochronic equations are based on two fundamental laws of thermodynamics: 1) Conservation of Energy, and 2) The Dissipation (Clausius-Duhem) Inequality. The 3-D equations contain 18 constants (15 independent) which are unique to AS4/3502 graphite-epoxy. These constants can be separated into reversible constants and irreversible constants. The determination of the constants is described as follows:

1. The six reversible constants (five independent) were used in the expression for reversible strain and consist of the compliance matrix A_{ij}. Because the compliance matrix models the linear response of the material, it was determined from the initial response of various unidirectional lamina tests. Straight lines were least squares fit through the initial data of the lamina tests and the slopes of these lines were used to determine the A_{ij}

2. Twelve irreversible constants (10 independent) were used in the expression for irreversible strain; they are the S_{ij} matrix and the n_1, B_{11}, n_2, B_{22}^0, n_6, and B_{66}^0 parameters. These constants, which model the nonlinear response of the material, were also determined from various unidirectional lamina tests. The logarithm of a strain component was plotted against the logarithm of its corresponding stress component and a straight line was least squares fit through this data. The slope and strain axis intercept of these lines were used to determine the constants. Sixteen sets of the irreversible constants were determined; however, only five sets were considered in the analysis -- those whose S_{ij} matrix was positive-definite. These five sets were used to model off-axis lamina response and unnotched angle-ply laminate response. The parameter set which best represented the experimental lamina and laminate tests was chosen for use in this study.

6.2 The Finite Element Program AMNISAP

The three-dimensional material nonlinear finite element program AMNISAP utilizes the endochronic constitutive theory and constant stress and constant strain solution algorithms to solve the nonlinear system of equations. It also utilizes a symmetry relationship called inversion symmetry. In this study, the program was vectorized to run on NASA's Cyber 205 super computer. The important features of AMNISAP are outlined below.

1. The inversion symmetry utilized in AMNISAP consists of rotating a plate through 180° about the axis of symmetry. Defining an x_i coordinate system ($i = 1,2,3$), with the x_3 coordinate the axis of symmetry, a symmetry transformation changes the coordinates x_α ($\alpha = 1,2$) of each material point of the plate into $-x_\alpha$. The inversion symmetry analysis in this study resulted in considerable storage and run time savings over conventional half plate analysis.

2. The vectorizing utility VAST was used to vectorize the three subroutines COLSOL, ELKAY, and STRESS in AMNISAP because they were found to use the majority of CPU time. Based on a 20 element mesh, a total speed factor of 12 was realized by using vectorized inversion symmetry analysis over non-vectorized half plate analysis. Considerably higher speed factors were likely realized for the analysis of notched angle-ply laminates in this study.

3. The constant stress and constant strain solution algorithms used in AMNISAP are based on the concept of initial strain and are classified as step-iterative methods. They each utilize a psuedo load vector which contains all the nonlinear terms of the equations. Therefore, the global stiffness matrix is formed only once and remains constant throughout the analysis. Both algorithms were included in AMNISAP because one of them might

be better suited for a given problem. The user can choose the algorithm which best fits the problem at hand.

6.3   *Laminate Response*

The response of unnotched and notched angle-ply laminates subjected to uniaxial compressive loading was analyzed and compared to experiment. All theoretical results were obtained using AMNISAP. The highlights of this analysis are outlined below.

6.3.1   Unnotched Laminates

1.   The unnotched angle-ply laminates' axial and transverse response agreed very well with experiment. The agreement of theory and experiment for the [± 45]$_s$ laminate was especially good, considering this laminate's substantial softening response. Although the theoretical/experimental correlation for transverse response was good, it was not quite as good as that for axial response in the [± 10]$_s$, [± 20]$_s$, and [± 30]$_s$ laminates. A possible cause for the less accurate transverse response is that the endochronic equations used cannot accurately model mixed stress states (σ_1 and σ_2 are of opposite sign in the [± 10]$_s$, [± 20]$_s$, and [± 30]$_s$ laminates).

6.3.2 Notched Laminates

1. The endochronic equations were found to predict unloading of various stress components in the analysis of the notched laminates. At a critical load level, this unloading phenomenon prevented higher loading by causing the solution to diverge. A condition referred to in this study as the zero-slope condition was implemented in AMNISAP to allow loading past the critical load level. The zero-slope condition forces an unloading stress component's stress-strain modulus to zero for the remainder of the loading history.

2. Theoretical/experimental correlation of the notched angle-ply laminates' far field axial response was excellent. Due to the unloading phenomenon mentioned above, the $[(\pm 10)_{12}]_s$ and $[(\pm 20)_{12}]_s$ laminates did not reach the experimentally observed failure load.

3. The theoretically predicted axial strain response near the hole agreed well with experiment. However, the predicted response was dependent on the distance from the hole, especially in the $[(\pm 10)_{12}]_s$ and $[(\pm 20)_{12}]_s$ laminates. The D/A value (nondimensional distance from the hole) at which the $[(\pm 10)_{12}]_s$ and $[(\pm 20)_{12}]_s$ laminates best agreed with experiment was different from the D/A value for the $[(\pm 30)_{12}]_s$ and $[(\pm 45)_{12}]_s$ laminates. However, the $[(\pm 10)_{12}]_s$ and $[(\pm 20)_{12}]_s$ laminates had 1/4″ holes whereas the $[(\pm 30)_{12}]_s$ and $[(\pm 45)_{12}]_s$ laminates had 1/2″ holes, which may have influenced the placement of the strain gage on the test specimens.

4. The predicted σ_θ, $\tau_{\theta z}$, and σ_z stress concentration profiles were examined along $\theta = 0°$ from the hole edge to a distance D/A$=0.6$. The endochronic theory profiles differed significantly from the linear theory profiles, especially for the out-of-plane shear stress $\tau_{\theta z}$. The important features of the stress concentration profiles are given below:

- The $[(\pm 10)_{12}]_s$ laminate exhibited the highest σ_θ stress concentration value and the $[(\pm 45)_{12}]_s$ laminate the lowest value. At gauss planes near an interface ($Z = H/12$ and $Z = 5H/12$), the endochronic theory predicted a lower peak σ_θ stress concentration in the $[(\pm 10)_{12}]_s$ and $[(\pm 45)_{12}]_s$ laminates and a higher peak σ_θ stress concentration in the $[(\pm 20)_{12}]_s$ and $[(\pm 30)_{12}]_s$ laminates. Both analyses predicted the peak σ_θ stress concentration to occur at the hole edge for the $[(\pm 10)_{12}]_s$ laminate and at points a small distance away from the hole edge for the other laminates.

- The $[(\pm 30)_{12}]_s$ laminate exhibited the highest $\tau_{\theta z}$ stress concentration and the $[(\pm 10)_{12}]_s$ laminate the lowest. In all laminates, linear theory predicted significantly higher peak $\tau_{\theta z}$ stress concentrations than the endochronic theory. The peak $\tau_{\theta z}$ stress concentration occured at the hole edge.

- The σ_z concentration profiles oscillate between positive and negative values, although the magnitudes are very small. The endochronic theory profiles are very similar to the linear theory profiles except near the hole edge where the endochronic theory predicts much larger σ_z stress concentrations than linear theory.

5. The predicted stress profiles in material principle coordinates were examined at the hole edge, for $-90° \leq \theta \leq 90°$. The highlights of these profiles are listed below:

- The linear theory and endochronic theory σ_1 stress profiles are very similar for all laminates except the $[(\pm 45)_{12}]_s$ laminate where the endochronic theory predicts a 40% higher peak σ_1 stress concentration. The endochronic theory predicts higher peak σ_1 stress concentrations than the linear theory for the $[(\pm 10)_{12}]_s$, and $[(\pm 45)_{12}]_s$ laminates and lower than linear theory concentrations for the $[(\pm 20)_{12}]_s$ and $[(\pm 30)_{12}]_s$ laminates.

- The linear theory and endochronic theory σ_2 stress profiles are similar in the $[(\pm 10)_{12}]_s$ and $[(\pm 20)_{12}]_s$ laminates and relatively dissimilar in the $[(\pm 30)_{12}]_s$ and $[(\pm 45)_{12}]_s$ laminates. The endochronic theory σ_2 stress profiles are much more jagged than the linear theory profiles.

- The linear theory and endochronic theory σ_3 (σ_z) stress profiles differ significantly for all the laminates except the $[(\pm 10)_{12}]_s$ laminate. The endochronic theory σ_3 stress profiles exhibit radical jumps and show stress magnitudes much higher than the linear theory profiles.

- The linear theory and endochronic theory interlaminar shear stress σ_4 (τ_{23}) profiles are similar for all the laminates except the $[(\pm 20)_{12}]_s$ laminate where the profiles show a significant difference in magnitude.

- The linear theory and endochronic theory interlaminar shear stress σ_5 (τ_{13}) profiles agree reasonably well for all laminates except the $[(\pm 20)_{12}]_s$ laminate. The endochronic theory peak σ_5 stress concentrations are significantly lower than the linear theory concentrations in all laminates except the $[(\pm 20)_{12}]_s$ laminate.

- The linear theory and endochronic theory shear stress σ_6 (τ_{12}) profiles are similar for all the laminates. The endochronic theory σ_6 stress profiles are much more jagged than the smooth linear theory profiles. In all of the laminates, the peak σ_6 stress concentration is lowest for endochronic theory analysis.

6. Cylindrical coordinate σ_θ and $\tau_{\theta z}$ stress profiles were examined at the hole edge for $-90° \leq \theta \leq 90°$. The highlights of the σ_θ and $\tau_{\theta z}$ stress profiles are listed below.

- The σ_θ stress profiles are very similar to the σ_1 stress profiles and show the same trends.

- The $\tau_{\theta z}$ stress profiles show the maximum $\tau_{\theta z}$ stress to occur at $\theta \cong 0°$ for all laminates. The linear theory and endochronic theory $\tau_{\theta z}$ stress profiles are similar in shape, but differ in peak magnitude. In all laminates, the endochronic theory predicted lower peak $\tau_{\theta z}$ stress concentrations than the linear theory.

6.4 Failure

A failure analysis of the unnotched and notched angle-ply laminates was performed using the tensor polynomial failure criterion. The tensor polynomial was used to predict the fracture load and, for the notched laminates, the location and mode of failure. Failure away from the hole edge was examined by applying the tensor polynomial at radii greater than the hole radius for $-90° \leq \theta \leq 90°$. Finally, the effect of the ratio w/d on failure was investigated for the $[(\pm 10)_{12}]_s$ and $[(\pm 20)_{12}]_s$ laminates. The important feature of the failure analysis are outlined below.

1. Theoretical fracture load predictions agreed very well with experiment for all of the unnotched laminates except the $[\pm 20]_s$ laminate. For the $[\pm 20]_s$ laminate, theory gave non-conservative failure predictions. An in-plane shear strength value of 14 ksi gave better fracture load predictions than a shear strength value of 9.4 ksi. The endochronic theory predicted σ_y^{ult} stresses nearly the same as linear theory, but predicted ε_y^{ult} strains more accurately than linear theory.

2. Fracture load predictions for the notched laminates were very conservative. A shear strength value of 14 ksi gave better fracture load predictions than a shear strength value of 9.4 ksi; however, the fracture load predictions were still very conservative. The endochronic theory and linear theory σ_y^{ult} stresses were very similar. However, the

endochronic theory ε_y^{ult} strains did not correlate with experiment significantly better than the linear theory ε_y^{ult} strains because the conservative fracture loads did not allow the laminates to be deformed significantly into their softening regions.

3. The material nonlinear endochronic theory fracture predictions for the notched laminates did not correlate with experiment significantly better than the linear theory predictions. Therefore, the cause of the conservative fracture loads is likely due to finite element stresses near the hole edge that are too high and the application of the tensor polynomial at the hole edge. Laminates often exhibit local failure (micro-cracking) near notches before fracture; therefore, the tensor polynomial may actually be predicting local failure and not fracture.

4. Application of the tensor polynomial at the hole edge gave very accurate predictions of the locations and modes of failure. When a shear strength of 9.4 ksi was used, the endochronic theory gave failure modes and locations identical to those of the linear theory for all laminates. However, when a shear strength of 14 ksi was used, the endochronic theory and linear theory predicted different failure locations and different tensor polynomial terms for the $[(\pm 30)_{12}]_s$ and $[(\pm 45)_{12}]_s$ laminates. In the $[(\pm 30)_{12}]_s$ laminate, the endochronic theory predicted a different failure mode than the linear theory using a shear strength of 14 ksi.

5. Application of the tensor polynomial at various radii (or distances from the hole edge) for $-90° \le \theta \le 90°$ shows the lowest fracture loads to occur at the hole edge. The profiles of far field σ_y^{ult} stress versus the distance D/A do not converge at any D/A value; therefore, a characteristic distance does not seem to exist. As D/A increases, the predicted failure locations change in both θ and Z dimensions. The endochronic theory and linear theory predict identical failure locations as a function of D/A for all laminates except the $[(\pm 45)_{12}]_s$ laminate.

Conclusions

6. $[(\pm 10)_{12}]_s$ and $[(\pm 20)_{12}]_s$ laminates with w/d ratios of 10 and 5 were tested [1] and analyzed. For a decrease in w/d from 10 to 5, experiments revealed a reduction in strength of approximately 18.5% and a reduction in ultimate failure strain of approximately 20% for both laminates. Both linear theory and endochronic theory gave reductions in strength and ultimate failure strain approximately equal to the 11.1% reduction in cross-sectional area.

7.0 References

1   S. W. Burns, C. T. Herakovich and J. G. Williams, "Compressive Failure of Notched Angle-Ply Composite Laminates: Three-Dimensional Finite Element Analysis and Experiment," Masters Thesis, Virginia Polytechnic Institute and State University, VPI-E-85-22, 1985.

2   G. J. Dvorak and Y. A. Bahei-el-din, "Elastic-Plastic Behavior of Fibrous Composites," *J. Mech. Phys. Solids,* Vol. 27, pp.51-72.

3   J. Aboudi, "Elastoplasticity Theory For Composite Materials," *SM Archives,* Nov. 1986, pp.141-183.

4   H. T. Hahn and S. W. Tsai, "Nonlinear Elastic Behavior of Unidirectional Composite Laminae," *J. Composite Materials,* Vol. 7, Jan. 1973, pp. 102-118.

5   R. S. Sandhu, "Nonlinear Behavior of Unidirectional and Angle Ply Laminates," *J. Aircraft,* Vol. 13, No. 2

6   Z. Hashin, D. Bagchi and B. W. Rosen, "Nonlinear Behavior of Fiber Composite Laminates," NASA CR-2313, April 1974

7   G. J. Dvorak and M. S. M. Rao, "Axisymmetric Plasticity Theory of Fibrous Composites," *Int. J. Engr. Sci.,* Vol. 14, 1976, pp.361-373

8   J. Aboudi, "A continuum Theory for Fiber-Reinfoced Elastic-Viscoplastic Composites," *Int. J. Eng. Sci.* Vol. 20, 1982, pp. 605-621.

9   J. Aboudi, "Effective Behavior of Inelastic Fiber-Reinforced Composites," *Int. J. Eng. Sci.* Vol. 22, 1984.

10 J. Aboudi and Y. Benveniste, "Constitutive Relations for Fiber-Reinforced Inelastic Laminated Plates," *J. Applied Mechanics,* Vol. 51, March 1984, pp.107-113.

11 K. C. Valanis, "A Theory of Viscoplasticity Without A Yield Surface," Part I. General Theory, *Archives of Mechanics,* 1971, pp. 517-533.

12 K. C. Valanis, "A Theory of Viscoplasticity Without A Yield Surface," Part II. Application to Mechanical Behavior of Metals, *Archives of Mechanics,* 1971, pp. 535-551.

13 K. C. Valanis, "Observed Plastic Behavior of Metals vis-a-vis the Endochronic Theory of Plasticity," International Symposium on Plasticity, Proceedings, Warsaw 1972.

[14]   K. C. Valanis, "Effect of Prior Deformation of Cyclic Response of Metals," *J. Applied Mechanics,* Vol. 4, 1974, p.441

[15]   K. C. Valanis, "On the Foundations of the Endochronic Theory of Viscoplasticity," *Archives of Mechanics,* Vol. 27, 1975, pp.857-868.

[16]   K. C. Valanis, "Endochronic Theory with Proper Hysteresis Loop Closure Properties," Systems, Science and Software Report, SSS-R-80-4182.

[17]   K. C. Valanis and C. F. Lee, "Some Recent Developments of the Endochronic Theory with Applications," *Nuclear Engineering and Design,* Vol. 69, 1982, p. 327.

[18]   K. C. Valanis, "Fundamental Consequences of a New Intrinsic Time Measure. Plasticity as a Limit of the Endochronic Theory," *Archives of Mechanics,* Vol. 32, No. 2, 1980, pp. 171-191.

[19]   M. J. Pindera and C. T. Herakovich, "An Endochronic Theory for Transversely Isotropic Fibrous Composites," Ph.D. Dissertation, Virginia Polytechnic Institute and State University, VPI-E-81-27, August, 1981.

[20]   M. J. Pindera, and C. T. Herakovich, "An Endochronic Model for the Response of Unidirectional Composites Under Off-Axis Tensile Load," *Mechanics of Composite Materials: Recent Advances,* Z. Hashin and C. T. Herakovich, Eds., Pergamon Press, 1983, pp. 367-381.

[21]   P. A. Zinov'ev and B. S. Sarbaev, N. E. Bauman Moscow Technical Institution of Higher Learning. Translated from *Mekhanika Kompozitnykh Materialov,* No. 3, May-June 1985, pp. 423-430.

[22]   W. Lansing, W. R. Jensen, and W. Falby, "Matrix Analysis Methods for Inelastic Structures," Proceedings of the First Conference (26-28 Oct. 1965) on Matrix Methods in Structural Mechanics, Wright-Patterson Air Force Base, Ohio, Nov. 1966. Review of the Initial Strain Method and Application to the Flow Theory of Plasticity. Available from NTIS, Springfield, VA, AD 646 300.

[23]   J. L. Turner, R. W. Clough, H. C. Martin, and L. J. Topp, "Stiffness and Deflection Analysis of Complex Structures," *Journal of Aeronautical Science,* Vol. 23, No. 9, Sept. 1956, pp. 805-825.

[24]   A. Mendelson and S. S. Manson, "Practical Solution of Plastic Deformation Problems in the Elastic-Plastic Range," NASA TR R28, 1959.

[25]   R. H. Gallagher, J. Padlog, and P. P. Bijlaard, "Stress Analysis of Heated Complex Shapes," *ARS Journal,* May 1962, pp. 700-707.

[26]   J. Padlog, R. D. Huff, and G. F. Holloway, "The Unelastic Behavior of Structures Subjected to Cyclic, Thermal and Mechanical Stressing Conditions," Bell Aerosystems Company, Report WPADD TR 60-271, 1960.

[27]   G. Pope, "A Discrete Element Method for Analysis of Plane Elasitc-Plastic Stress Problems," Royal Aeronautical Establishment TR 65028, 1965.

[28]   J. L. Swedlow and W. H. Yang, "Stiffne s Analysis of Elastic-Plastic Plates," Graduate Aeronautical Laboratory, California Institute of Technology SM 65-10, 1965.

29 P. V. Marcal and I. P. King, "Elastic-Plastic Analysis of Two-Dimensional Stress Systems by the Finite Element Method," *Int. Journal of Mechanical Science,* Vol. 9, No. 3, 1967, pp. 143-155.

30 K. C. Valanis and J. Fan, "Endochronic Analysis of Cyclic Elastoplasitc Strain Fields in a Notched Plate," *J. Applied Mechanics,* Vol. 50, December 1983, pp. 789-794.

31 O. Watanabe and S. N. Atluri, "A New Endochronic Approach to Computational Elastoplasticity: Example of a Cyclically Loaded Cracked Plate," *J. Applied Mechanics,* Vol. 52, Dec. 1985, pp.857-864.

32 D. F. Adams and A. K. Miller, "Hygrothermal Microstresses in a Unidirectional Composite Exhibiting Inelastic Material Behavior," *J. Composite Materials,* Vol. 11, 1977, pp. 285-299.

33 D. F. Adams, "Inelastic Analysis of a Unidirectional Composite Subjected to Transverse Normal Loading," *J. Composite Materials,* Vol. 4, 1970, pp. 310-328.

34 R. L. Foye, "Theoretical Post-Yielding Behavior of Composite Laminates," Part I - Inelastic Micromechanics, *J. Composite Materials,* Vol. 7, 1973, pp. 178-193.

35 G. D. Renieri and C. T. Herakovich, "Nonlinear Analysis of Laminated Fibrous Composites," Ph.D. Dissertation, Virginia Polytechnic Institute and State University, VPI-E-76-10, June, 1976.

36 A. P. Nagarkar and C. T. Herakovich, "Nonlinear Temperature Dependent Failure Analysis of Finite Width Composite Laminates," Masters Thesis, Virginia Technic Institute and State University, VPI-E-79-36, Dec. 1979.

37 O. H. Griffin, Jr., M. P. Kamate, and C. T. Herakovich, "Three Dimensional Inelastic Finite Element Analysis of Laminated Composites," Ph.D. Dissertation, Virginia Polytechnic Institute and State University, VPI-E-80-28, Nov. 1980.

38 Y. A. Bahei-El-Din, "Plastic Analysis of Metal-Matrix Composite Laminates," Ph.D. Dissertation, Duke University, 1979.

38 G. J. Dvorak and Y. A. Bahei-El-Din, "Plasticity of Composite Laminates," Proc. Research Workshop on Mechanics of Composite Materials, Duke University, 1978, pp. 32-54.

40 Y. A. Bahei-El-Din and G. J. Dvorak, "Plastic Yielding at a Circular Hole in a Laminated FP-Al Plate," *Modern Developments in Composite Materials and Structures,* 1979, pp. 123-147.

41 Y. A. Bahei-El-Din, G. J. Dvorak and S. Utka, "Finite Element Analysis of Elastic-Plastic Fibrous Composite Structures," *Computers and Structures,* Vol. 13, June 1981, pp. 321-330.

42 H. S. Morgan and R. M. Jones, "Analysis of Nonlinear Stress-Strain Behavior of Laminated Fiber-Reinforced Composite Materials," Proc. 2nd International Conference on Composite Materials, Toronto, Canada, April 16-20, 1978. (A79-16981 05-24) Warrendal, Pa., Metallurgical Society of AIME, 1978, pp. 337-352.

43 R. S. Sandhu, G. P. Sendeckyj, and R. L. Gallo, "Modeling of the Failure Process in Notched Laminates," Mechanics of Composite Materials: Recent Advances; Proceedings of the Symposium, Blacksburg, VA, August 16-19, 1982 (A84-33376 15-24). New York and Oxford, Pergamon Press, 1983, pp. 179-189.

References 199

[44] S. Maksimovic, "Elasto-Plastic Analysis of Fibrous Composite Shells Using 'Semiloof' Finite Elements," Composites Structures 2; Proc. 2nd International Conference, Paisley, Scotland, Sept. 14-16, 1983 (A84-10426 01-24). London, Applied Science Publishers, 1983, pp. 155-163.

[45] A. K. Noor and R. A. Camin, "Symmetry Considerations for Anisotropic Shells," *Computer Methods In Applied Mechanics and Engineering,* Vol. 9, 1976, pp. 317-335.

[46] S. C. Desai and J. F. Abel, "Introduction to the Finite Element Method -- A Numerical Method For Engineering Analysis," Von Nostrand Reinhold Publishing Company, 1972, Chapter 7.

[47] D. E. Walrath, and D. F. Adams "Verification and Application of the Iosipescu Shear Test Method," UWME-DR-401-103-1, University of Wyoming, June, 1984.

[48] J. M. Whitney, and R. J. Nuismer, "Stress Fracture Criteria for Laminated Composites Containing Stress Concentrations" *J. Composite Materials,* Vol. 8, July 1974, pp. 253-265.

[49] C. T. Herakovich, D. Post, M. B. Buczek, and R. Czarnek, "Free Edge Strain Concentrations in Real Composite Laminates: Experimental-Theoretical Correlation," *J. Applied Mechanics,* Vol. 107, December 1985, pp. 787-793.

[50] J. L. Beuth, Private Communication. Experimental tests conducted during the summer of 1986 at VPI.

Appendix A. Data Reduction

For a given test, a straight line representing a "best fit" through the data is required. The data reduction in Chapter 2 uses a least squares fit to best approximate this straight line. A straight line is represented by the equation $y = mx + b$ where m is the slope and b is the y-intercept on a cartesian coordinate system. If x is designated to be the independent variable, then for a given x data point, there exists both a y data point (called y-observed or y_{obs}) and a y value corresponding to the equation $y = mx + b$ The difference between these values is represented by the equation $d = y_{obs} - mx + b$.

It is desired to minimize this difference over the entire range of data points, but since d may be a positive or negative quantity, the difference d cannot simply be summed over each point. The least squares method sums the square of the difference (function f below) over each point. This may be represented in functional form as

$$f(m,b) = \sum_{i=1}^{n} d_i^2 \tag{A.1}$$

where

$$d_i = y_i - mx_i - b$$

In order to minimize this function of the two variables m and b, the derivative of the function with respect to each variable is set equal to zero and the resulting two equations are solved simultaneously.

$$\frac{\partial f}{\partial m} = \frac{\partial f}{\partial b} = 0 \tag{A.2}$$

$$\frac{\partial f}{\partial m} = \sum_{i=1}^{n} 2(y_i - mx_i - b)x_i = 0$$

$$\frac{\partial f}{\partial b} = \sum_{i=1}^{n} -2(y_i - mx_i - b) = 0$$

Equations (A.2) may be expanded to yield:

$$m \sum_{i=1}^{n} x_i + bn = \sum_{i=1}^{n} y_i \qquad (A.3)$$

$$m \sum_{i=1}^{n} x_i^2 + b \sum_{i=1}^{n} x_i = \sum_{i=1}^{n} x_i y_i$$

In matrix form, equations (A.3) exhibit the form:

$$\begin{bmatrix} \sum_{i=1}^{n} x_i & n \\ \sum_{i=1}^{n} x_i^2 & \sum_{i=1}^{n} x_i \end{bmatrix} \begin{Bmatrix} m \\ b \end{Bmatrix} = \begin{Bmatrix} \sum_{i=1}^{n} y_i \\ \sum_{i=1}^{n} x_i y_i \end{Bmatrix} \qquad (A.4)$$

Equations (A.4) yield a "best fit" value for the slope m and the y-intercept b.

Appendix B. Tables of Endochronic Constants

The following Tables are referenced in Chapter 2 for determining the endochronic constants. They contain slopes and y-axis intercepts from various lamina tests.

Table B.1. Tables for Determining A_{11}, v_{12}, A_{22}, and A_{44}

(a) A_{11} Determined from 0° Uniaxial Compression Tests

Test #	Slope m (psi)	Y-intercept (psi)	A_{11}
1	19,509,667.9	13.17	5.12566E-08
2	19,500,513.2	-48.80	5.12807E-08
Average	19,505,090.5	-17.82	5.12687E-08

(b) v_{12} Determined from 0° Uniaxial Compression Tests

Test #	Slope m (psi)	Y-intercept (psi)	v_{12}
1	-0.3500225	-6.81225E-06	0.3500225
2	-0.3159658	-1.69590E-05	0.3159658
Average	-0.3329942	-1.18856E-05	0.3329942

(c) A_{22} Determined from 90° Uniaxial Tests

Test #	Slope m (psi)	Y-intercept (psi)	A_{22}
1	1,525,254.8	150.04	6.55628E-07
2	1,527,561.5	-55.12	6.54638E-07
Average	1,526,408.2	47.46	6.55133E-07

(d) A_{44} Determined from 2-3 Plane Iosipescu Tests

Test #	Slope m (psi)	Y-intercept (psi)	A_{44}
1	472,208.9	-31.94	2.11771E-06
2	445,017.1	51.94	2.24710E-06
Average	458,613.0	10.0	2.18049E-06

Table B.2. Tables for Determining A_{66}, B_{11}, n_1, n_2, and B^0_{22}

(a) A_{66} Determined from 1-2 Plane Iosipescu Tests and Off-Axis Tests

Iosipescu Tests	Slope m (psi)	Y-intercept (psi)	A_{66}
1	812,268.9	1.46	1.23112E-06
2	903,552.3	0.04	1.10674E-06
Off-Axis	Slope m (psi)	Y-intercept (psi)	A_{66}
10	839,663.2	0.00	1.19095E-06
15	887,303.5	0.00	1.12701E-06
30	789,924.2	0.00	1.26594E-06
45	836,014.9	-0.05	1.19615E-06
Average	844,787.2	0.48	1.18373E-06

(b) B_{11} and n_1 Determined from 0° Uniaxial Compression Tests

Test#	Slope m (psi)	Y-intercept (psi)	n_1	B_{11}
1	2.403743	-35.79	2.403743	2.85762E-16
2	2.492074	-36.89	2.492074	9.55283E-17
Average	2.447909	-36.34	2.447909	1.90645E-16

(c) n_2 Determined from 90° Uniaxial Compression Tests

Test #	Slope m (psi)	Y-intercept (psi)	n_2
1	2.84790	-35.62	1.8479
2	4.07145	-48.00	3.0714
Average	3.459675	-41.81	2.4597

(d) B^0_{22} Calculated Using n_2 from 90° Uniaxial Tests

Test #	Y-intercept	$B^0_{22} \times S^{1.22984}_{22}$
1	-41.9532	2.08449E-18
2	-41.7110	2.65574E-18
Average	-41.8321	2.37010E-18

Table B.3. Tables for Determining n_6 and S_{66}

(a) n_{6A} Determined from 1-2 Plane Iosipescu Tests and Off-Axis Tests Using the Average Value of A_{66}

Iosipescu Tests	Slope k_6	ln C_6	$n_{6A} = k_6 - 1$
1	3.84135	-41.29	2.84135
2	4.04939	-43.18	3.04939
Off-Axis Tests	Slope k_6	ln C_6	$n_{6A} = k_6 - 1$
10	2.99530	-33.08	1.99530
15	2.96310	-32.33	1.96310
30	3.73866	-39.83	2.73866
45	3.68246	-38.59	2.68246
Average	3.54504	-31.62	2.54504

(b) n_{6B} Determined from 1-2 Plane Iosipescu Tests and Off-Axis Tests Using Individual Values of A_{66}

Iosipescu Tests	Slope k_6	ln C_6	$n_{6B} = k_6 - 1$
1	3.84140	-41.14	2.84140
2	4.18540	-44.69	3.18540
Off-Axis Tests	Slope k_6	ln C_6	$n_{6B} = k_6 - 1$
10	2.99770	-33.08	1.99770
15	2.97490	-32.58	1.97490
30	3.61290	-38.47	2.61290
45	3.58900	-37.77	2.58900
Average	3.53355	-37.96	2.53355

(c) S_{66} Calculated Using n_{6A} for 1-2 Plane Iosipescu Tests

Test #	Y-intercept	S_{66}
1	-38.60	1.81042E-13
2	-38.40	2.12236E-13
Average	-38.50	1.96639E-13

Appendix C. Criterion For Positive Definiteness

Consider the following S_{ij} matrix:

$$\begin{bmatrix} S_{11} & S_{12} & S_{12} & 0 & 0 & 0 \\ S_{12} & S_{22} & S_{23} & 0 & 0 & 0 \\ S_{12} & S_{23} & S_{22} & 0 & 0 & 0 \\ 0 & 0 & 0 & S_{44} & 0 & 0 \\ 0 & 0 & 0 & 0 & S_{55} & 0 \\ 0 & 0 & 0 & 0 & 0 & S_{66} \end{bmatrix}$$ (B.1)

To be positive definite, the above matrix must meet the following criteria:

$$S_{11} > 0$$ (B.2)

$$\begin{vmatrix} S_{11} & S_{12} \\ S_{12} & S_{22} \end{vmatrix} > 0$$ (B.3)

$$\begin{vmatrix} S_{11} & S_{12} & S_{12} \\ S_{12} & S_{22} & S_{23} \\ S_{12} & S_{23} & S_{22} \end{vmatrix} > 0$$ (B.4)

Expanding equations (B.2) through (B.4) gives the following conditions:

1. $S_{11} > 0$

2. $S_{11}S_{22} - S_{12}^2 > 0$

3. $S_{11}(S_{22}^2 - S_{23}^2) + 2S_{12}^2(S_{23} - S_{22}) > 0$

Appendix D. Finite Element Implementation of

Inversion Symmetry

A finite element model is a set of N equations with N unknowns. The inversion symmetry conditions introduce M new equations, reducing the number of equations and unknowns to N - M. Applying the inversion symmetry condition to an anisotropic plate in the modeling stage reduces the geometry of the model from full to half. Any line passing through the center of symmetry which splits the plate into two half sections may be used. The symmetry line chosen for modeling the plate with a central hole of this study is the y-axis (Figure D.1).

A simple example is used here to show how a full finite element model is reduced to a half model. Consider an anisotropic plate under compression. A simple four element grid with 4 node elements represents the finite element model as shown in Figure D.1. For the sake of simplicity, assume that each node has only one degree of freedom, that in the y-direction.

The global set of equations is written

$$
\begin{bmatrix}
K_{11} & K_{12} & 0 & K_{14} & K_{15} & 0 & 0 & 0 & 0 \\
K_{12} & K_{22} & K_{23} & K_{24} & K_{25} & K_{26} & 0 & 0 & 0 \\
0 & K_{23} & K_{33} & 0 & K_{35} & K_{36} & 0 & 0 & 0 \\
K_{14} & K_{24} & 0 & K_{44} & K_{45} & 0 & K_{47} & K_{48} & 0 \\
K_{15} & K_{25} & K_{35} & K_{45} & K_{55} & K_{56} & K_{57} & K_{58} & K_{59} \\
0 & K_{26} & K_{36} & 0 & K_{56} & K_{66} & 0 & K_{68} & K_{69} \\
0 & 0 & 0 & K_{47} & K_{57} & 0 & K_{77} & K_{78} & 0 \\
0 & 0 & 0 & K_{48} & K_{58} & K_{68} & K_{78} & K_{88} & K_{89} \\
0 & 0 & 0 & 0 & K_{59} & K_{69} & 0 & K_{89} & K_{99}
\end{bmatrix}
\begin{Bmatrix}
V_1 \\ V_2 \\ V_3 \\ V_4 \\ V_5 \\ V_6 \\ V_7 \\ V_8 \\ V_9
\end{Bmatrix}
=
\begin{Bmatrix}
F_1 \\ F_2 \\ F_3 \\ 0 \\ 0 \\ 0 \\ -F_3 \\ -F_2 \\ -F_1
\end{Bmatrix}
\qquad (D.1)
$$

where V_i represent the unknown nodal displacements.

Applying the inversion symmetry relationship to the displacements, using the Y-axis as the line of symmetry,
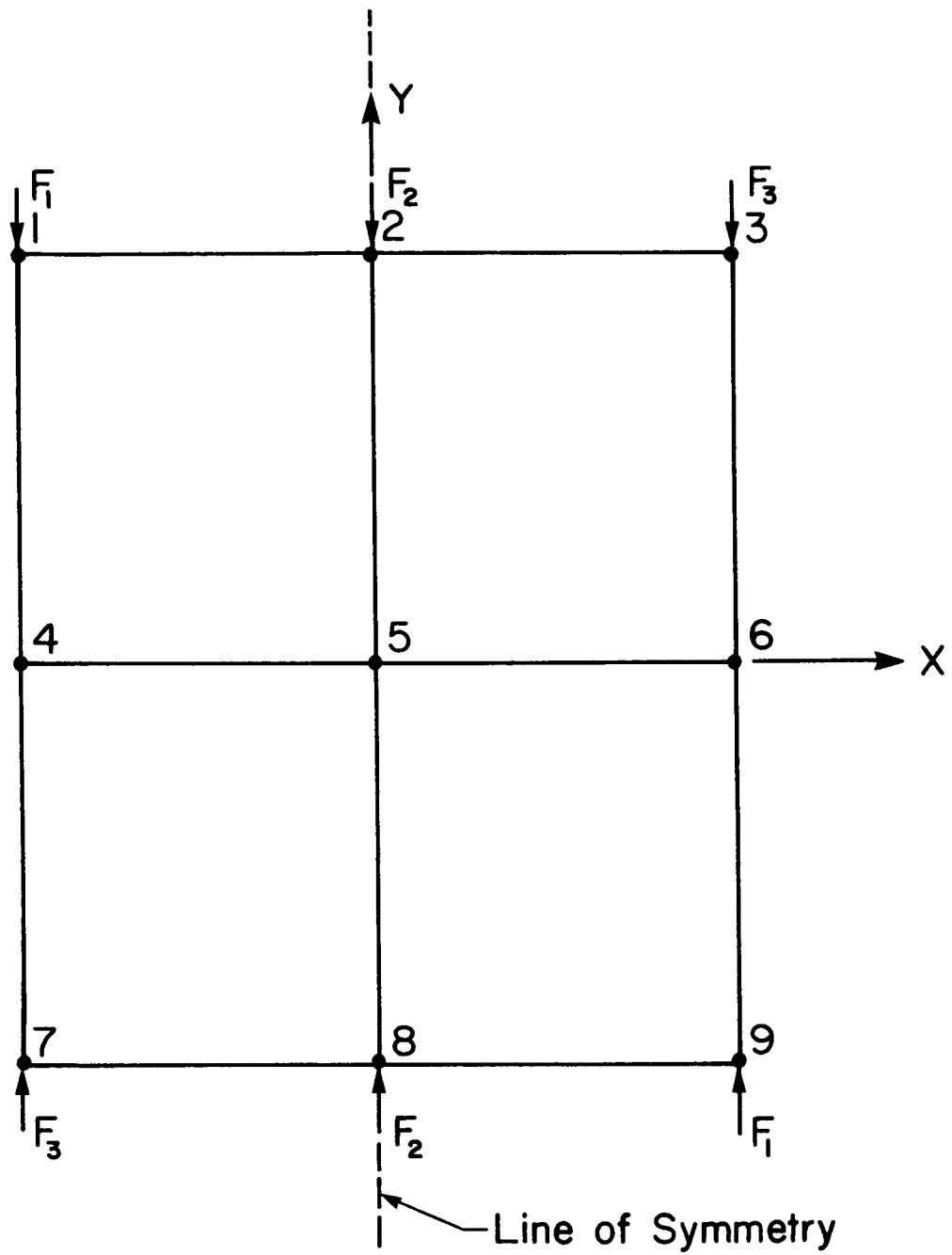
Figure D.1. Four Element Finite Element Grid with 4 Node Elements for Anisotropic Plate Under Compression Loading

$$V_7 = -V_3$$

$$V_4 = -V_6 \qquad\qquad (D.2)$$

$$V_1 = -V_9$$

$$V_8 = -V_2$$

Substituting equations (D.2) into (D.1) gives the following set of equations.

$$
\begin{bmatrix}
K_{11} & K_{12} & 0 & K_{14} & K_{15} & 0 & 0 & 0 & 0 \\
K_{12} & K_{22} & K_{23} & K_{24} & K_{25} & K_{26} & 0 & 0 & 0 \\
0 & K_{23} & K_{33} & 0 & K_{35} & K_{36} & 0 & 0 & 0 \\
K_{14} & K_{24} & 0 & K_{44} & K_{45} & 0 & K_{47} & K_{48} & 0 \\
K_{15} & K_{25} & K_{35} & K_{45} & K_{55} & K_{56} & K_{57} & K_{58} & K_{59} \\
0 & K_{26} & K_{36} & 0 & K_{56} & K_{66} & 0 & K_{68} & K_{69} \\
0 & 0 & 0 & K_{47} & K_{57} & 0 & K_{77} & K_{78} & 0 \\
0 & 0 & 0 & K_{48} & K_{58} & K_{68} & K_{78} & K_{88} & K_{89} \\
0 & 0 & 0 & 0 & K_{59} & K_{69} & 0 & K_{89} & K_{99}
\end{bmatrix}
\begin{Bmatrix}
-V_9 \\ V_2 \\ V_3 \\ -V_6 \\ V_5 \\ V_6 \\ -V_3 \\ -V_2 \\ V_9
\end{Bmatrix}
=
\begin{Bmatrix}
F_1 \\ F_2 \\ F_3 \\ 0 \\ 0 \\ 0 \\ -F_3 \\ -F_2 \\ -F_1
\end{Bmatrix}
\qquad (D.3)
$$

Equation set (D.3) has only five unknown displacements -- four of the unknown displacements were eliminated using inversion symmetry. Rearranging equation set (D.3) yields:

$$
\begin{bmatrix}
K_{11} & -K_{12} & 0 & K_{14} & -K_{15} & 0 & 0 & 0 & 0 \\
-K_{12} & K_{22} & K_{23} & -K_{24} & K_{25} & K_{26} & 0 & 0 & 0 \\
0 & K_{23} & K_{33} & 0 & K_{35} & K_{36} & 0 & 0 & 0 \\
K_{14} & -K_{24} & 0 & K_{44} & -K_{45} & 0 & K_{47} & K_{48} & 0 \\
-K_{15} & K_{25} & K_{35} & -K_{45} & K_{55} & K_{56} & -K_{57} & -K_{58} & K_{59} \\
0 & K_{26} & K_{36} & 0 & K_{56} & K_{66} & 0 & -K_{68} & K_{69} \\
0 & 0 & 0 & K_{47} & -K_{57} & 0 & K_{77} & K_{78} & 0 \\
0 & 0 & 0 & K_{48} & -K_{58} & -K_{68} & K_{78} & K_{88} & -K_{89} \\
0 & 0 & 0 & 0 & K_{59} & K_{69} & 0 & -K_{89} & K_{99}
\end{bmatrix}
\begin{Bmatrix}
V_9 \\ V_2 \\ V_3 \\ V_6 \\ V_5 \\ V_6 \\ V_3 \\ V_2 \\ V_9
\end{Bmatrix}
=
\begin{Bmatrix}
-F_1 \\ F_2 \\ F_3 \\ 0 \\ 0 \\ 0 \\ F_3 \\ F_2 \\ -F_1
\end{Bmatrix}
$$

Reducing equation set (D.4) to the five independent equations and unknowns yields:

$$
\begin{bmatrix}
(K_{22}+K_{88}) & (K_{23}+K_{78}) & (K_{25}-K_{58}) & (K_{26}+K_{48})-(K_{24}+K_{88}) & (-K_{12}+-K_{89}) \\
(K_{23}+K_{78}) & (K_{33}+K_{77}) & (K_{35}-K_{57}) & (K_{47}+K_{36}) & 0 \\
(K_{25}+K_{58}) & (K_{35}-K_{57}) & K_{55} & (K_{56}-K_{45}) & (K_{59}-K_{15}) \\
(K_{48}+K_{26})-(K_{24}+K_{69}) & (K_{47}+K_{36}) & (K_{56}-K_{45}) & (K_{44}+K_{66}) & (K_{14}+K_{69}) \\
(-K_{12}+-K_{89}) & 0 & (K_{59}-K_{15}) & (K_{14}+K_{69}) & (K_{11}+K_{99})
\end{bmatrix}
\begin{Bmatrix}
V_2 \\ V_3 \\ V_5 \\ V_6 \\ V_9
\end{Bmatrix}
=
\begin{Bmatrix}
2F_2 \\ 2F_3 \\ 0 \\ 0 \\ -2F_1
\end{Bmatrix}
\quad (D.5)
$$

Because the stiffness terms are inversion symmetric as well, equation set (D.5) may be simplified even further. Note that

$$K_{88} = K_{22} \quad K_{78} = K_{23}$$

$$K_{48} = K_{26} \quad K_{24} = K_{68}$$

$$K_{12} = K_{89} \quad K_{77} = K_{33}$$

$$K_{57} = K_{35} \quad K_{47} = K_{36} \tag{D.6}$$

$$K_{58} = K_{25} \quad K_{56} = K_{45}$$

$$K_{44} = K_{66} \quad K_{15} = K_{59}$$

$$K_{14} = K_{69} \quad K_{11} = K_{99}$$

Therefore,

$$
\begin{bmatrix}
2K_{22} & 2K_{23} & 0 & 2(K_{26} - K_{68}) & -2K_{89} \\
2K_{23} & 2K_{33} & 0 & 2K_{36} & 0 \\
0 & 0 & K_{55} & 0 & 0 \\
2(K_{26} - K_{68}) & 2K_{36} & 0 & 2K_{66} & 2K_{69} \\
-2K_{89} & 0 & 0 & 2K_{69} & 2K_{99}
\end{bmatrix}
\begin{Bmatrix}
V_2 \\ V_3 \\ V_5 \\ V_6 \\ V_9
\end{Bmatrix}
=
\begin{Bmatrix}
2F_2 \\ 2F_3 \\ 0 \\ 0 \\ -2F_1
\end{Bmatrix}
\tag{D.7}
$$

Equation set (D.7) include stiffness and displacement terms from elements 1 and 2 only. Of course, a 2 can be factored from equations 1,2,4, and 5 in equation set (D.7).

This simple example shows how a full plate finite element model may be reduced to that of a half plate model (Figure D.2). In the above example, the line of symmetry was taken as the Y-axis. Alternatively, the X-axis, a line through node points 3, 5, and 7, or a line through points 1, 5, and 9 could have been used as the line of symmetry.

Of course, in modeling the full plate with a half plate mesh, the finite element program must be modified internally and the input data modified appropriately. This is discussed next.
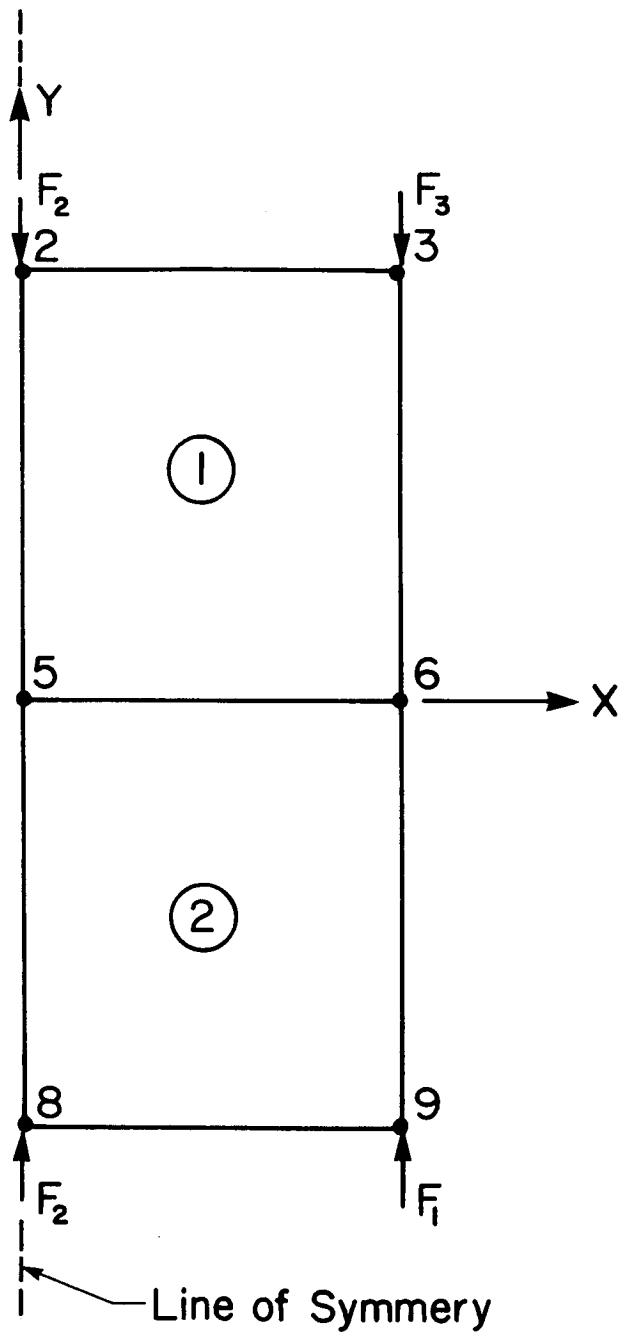
Figure D.2. Two Element Inversion Symmetry Finite Element Grid with 4 Node Elements for Anisotropic Plate Under Compression Loading

D.1 Finite Element Development

Independent and dependent nodes can be defined for the half plate mesh shown in Figure D.2. Those nodes associated with the independent degrees of freedom are called independent nodes. All other nodes are dependent nodes. In the plate in Figure D.2, node 8 (or node 2) is the only dependent node because its displacement is dependent upon the node 2 displacement (or the node 2 displacement is dependent upon the node 8 displacement).

In order to implement the inversion symmetry condition, the finite element program must know which nodes are independent and which nodes are dependent. This is done in the input data. Each node is labeled with an integer valued flag variable -- either a 0, 1, or -1. The variable 0 indicates that this node is independent. The variable 1 indicates that the node is independent, but has a dependent node which corresponds to it. The variable -1 indicates the node is dependent and corresponds to one of the nodes marked with a 1. The dependent nodes are matched to their appropriate independent nodes by their global coordinate relationship.

The program assigns each node to a global equation number. Dependent nodes are assigned to the same global equation number as their corresponding independent nodes. In the assembly procedure, the stiffness terms of the dependent nodes are added to the stiffness terms of the independent nodes. However, before the assembly of the global stiffness matrix, the elemental stiffness terms are modified in those elements which contain dependent nodes.

For elements with dependent nodes, the stiffness and load matrices are modified by transformations of the form

$$[\overline{K}] = [\Gamma]^T[K][\Gamma] \tag{D.8}$$

$$\{\overline{P}\} = [\Gamma]^T\{P\}$$

where [K] and {P} are the element stiffness and load matrices and [Γ] is the transformation matrix.

For element 2 in the mesh of Figure D.2, the elemental equations would appear as

$$
\begin{bmatrix}
K_{11}^2 & K_{12}^2 & K_{13}^2 & K_{14}^2 \\
K_{12}^2 & K_{22}^2 & K_{23}^2 & K_{24}^2 \\
K_{13}^2 & K_{23}^2 & K_{33}^2 & K_{34}^2 \\
K_{14}^2 & K_{24}^2 & K_{34}^2 & K_{44}^2
\end{bmatrix}
\begin{Bmatrix}
V_5 \\
V_6 \\
V_8 \\
V_9
\end{Bmatrix}
=
\begin{Bmatrix}
0 \\
0 \\
-F_2 \\
-F_1
\end{Bmatrix}
\tag{D.9}
$$

or

$$[K^2]\{V\} = \{P^2\}$$

The transformation matrix would look like

$$
[\Gamma] =
\begin{bmatrix}
1 & 0 & 0 & 0 \\
0 & 1 & 0 & 0 \\
0 & 0 & -1 & 0 \\
0 & 0 & 0 & 1
\end{bmatrix}
\tag{D.10}
$$

After the transformation, the transformed stiffness and load matrices would look like

$$[\overline{K}] = \begin{bmatrix} K_{11}^2 & K_{12}^2 & -K_{13}^2 & K_{14}^2 \\ K_{12}^2 & K_{22}^2 & -K_{23}^2 & K_{24}^2 \\ -K_{13}^2 & -K_{23}^2 & K_{33}^2 & -K_{34}^2 \\ K_{14}^2 & K_{24}^2 & -K_{34}^2 & K_{44}^2 \end{bmatrix}$$

(D.11)

$$\{\overline{P}\} = \begin{Bmatrix} 0 \\ 0 \\ F_2 \\ -F_1 \end{Bmatrix}$$

For element 1, the elemental equations would appear as:

$$\begin{bmatrix} K_{11}^1 & K_{12}^1 & K_{13}^1 & K_{14}^1 \\ K_{12}^1 & K_{22}^1 & K_{23}^1 & K_{24}^1 \\ K_{13}^1 & K_{23}^1 & K_{33}^1 & K_{34}^1 \\ K_{14}^1 & K_{24}^1 & K_{34}^1 & K_{44}^1 \end{bmatrix} \begin{Bmatrix} V_2 \\ V_3 \\ V_5 \\ V_6 \end{Bmatrix} = \begin{Bmatrix} F_2 \\ F_3 \\ 0 \\ 0 \end{Bmatrix}$$

(D.12)

or

$$[K^1]\{V\} = \{P^1\}$$

Assemblying the element stiffness and force matrices to form the global stiffness and force matrices yields

$$
\begin{bmatrix}
(K_{11}^1 + K_{33}^2) & K_{12}^1 & (K_{13}^1 - K_{13}^2) & (K_{14}^1 - K_{23}^2) & -K_{34}^2 \\
K_{12}^1 & K_{22}^1 & K_{23}^1 & K_{24}^1 & 0 \\
(K_{13}^1 - K_{13}^2) & K_{23}^1 & (K_{33}^1 + K_{11}^2) & (K_{34}^1 + K_{12}^2) & K_{14}^2 \\
(K_{14}^1 - K_{23}^2) & K_{24}^1 & (K_{34}^1 + K_{12}^2) & (K_{44}^1 + K_{22}^2) & K_{24}^2 \\
-K_{34}^2 & 0 & K_{14}^2 & K_{24}^2 & K_{44}^2
\end{bmatrix}
\begin{Bmatrix} V_2 \\ V_3 \\ V_5 \\ V_6 \\ V_9 \end{Bmatrix}
=
\begin{Bmatrix} F_2 \\ F_3 \\ 0 \\ 0 \\ -F_1 \end{Bmatrix}
\qquad \text{(D.13)}
$$

Transforming the elemental stiffness terms into global stiffness terms yields

$$
\begin{bmatrix}
K_{22} & K_{23} & 0 & (K_{26} - K_{68}) & -K_{89} \\
K_{23} & K_{33} & K_{35} & K_{36} & 0 \\
0 & K_{35} & K_{55} & K_{56} & K_{59} \\
(K_{26} - K_{68}) & K_{36} & K_{56} & K_{66} & K_{69} \\
-K_{89} & 0 & K_{59} & K_{69} & K_{99}
\end{bmatrix}
\begin{Bmatrix} V_2 \\ V_3 \\ V_5 \\ V_6 \\ V_9 \end{Bmatrix}
=
\begin{Bmatrix} F_2 \\ F_3 \\ 0 \\ 0 \\ -F_1 \end{Bmatrix}
\qquad \text{(D.14)}
$$

These global equations are identical to those of equation set (D.7) in the previous section.

F.0 Appendix E. Vectorization Examples

To compare scalar operations to vector operations, consider the following subroutine.

```
SUBROUTINE XT(N)
COMMON   A(100),B(100),C(100),D(100)
COMMON   X(100),Y(100)

DO 10 I=1,2
  X(I) = A(I)*B(I) + C(I)*D(I-1)
  Y(I) = ABS(X(I))
10   CONTINUE

RETURN
END
```

The sequence of scalar operations in this loop are as follows:

$D(1)*C(2)$ ---------------------- $Register_I$
$A(2)*B(2)$ ---------------------- $Register_J$
$Register_I + Register_J$ ---------- $Register_K$
$Register_K$ ---------------------------- $X(2)$
$ABS(Register_K)$ --------------------- $Y(2)$

$D(2)*C(3)$ ---------------------- $Register_I$
$A(3)*B(3)$ ---------------------- $Register_J$
$Register_I + Register_J$ ---------- $Register_K$
$Register_K$ ---------------------------- $X(3)$
$ABS(Register_K)$ --------------------- $Y(3)$

           *
           *
           *
           *

$D(N-1)*C(N)$ -------------------- $Register_I$
$A(N)*B(N)$ ---------------------- $Register_J$
$Register_I + Register_J$ ---------- $Register_K$
$Register_K$ ---------------------------- $X(N)$
$ABS(Register_K)$ --------------------- $Y(N)$

The Cyber 205 vector operation sequence is shown below:

$D(1)*C(2)$ -------------------- $TEMP_1(1)$
$D(2)*C(3)$ -------------------- $TEMP_1(2)$
         *

$$D(N-1)^*C(N) \text{ ----------- } TEMP_1(N-1)$$

$$A(2)^*B(2) \text{ -------------------- } TEMP_2(1)$$
$$A(3)^*B(3) \text{ ------------------- } TEMP_2(2)$$
$$*$$
$$*$$
$$A(N)^*B(N) \text{ ------------- } TEMP_2(N-1)$$

$$TEMP_1(1) + TEMP_2(1) \text{ --------- } X(2)$$
$$TEMP_1(2) + TEMP_2(2) \text{ --------- } X(3)$$
$$*$$
$$*$$
$$TEMP_1(N-1) + TEMP_2(N-1) \text{ --- } X(N)$$

$$ABS(X(2)) \text{ ------------------------ } Y(2)$$
$$ABS(X(3)) \text{ ------------------------ } Y(3)$$
$$*$$
$$*$$
$$ABS(X(N)) \text{ ------------------------ } Y(N)$$

As the example above shows, the vector processor performs its operations on vectors (or arrays) such as D(N-1)*C(N). It also may perform the above operations at the same time, referred to as parallel processing. Obviously, this processing is much speedier than the scalar processing.

However, not all do-loops can be vectorized. An array which is a function of previous values of itself may not be vectorized, as shown in the example below.

```
      SUBROUTINE XT(N)
      COMMON    A(100),B(100),C(100),D(100)
      COMMON    X(100),Y(100)

      DO 10 I=2,N
        X(I) = A(I)*B(I) + C(I)*X(I-1)
        Y(I) = ABS(X(I))
  10  CONTINUE

      RETURN
      END
```

Appendix E. Vectorization Examples

The above operation may only be computed one step at a time because the value of X(I) depends upon X(I-1). Vector processing would give erroneous results in this case. Cyber 205 vector processing restrictions are: (1) Arguments must be determinable prior to the operation, (2) Operands must be addressable under certain conventions, and (3) Array elements must be contiguous.

BIBLIOGRAPHIC DATA SHEET	1. Report No. CCMS-87-12, VPI-E-87-14	2.	3. Recipient's Accession No.

4. Title and Subtitle	5. Report Date
NONLINEAR ANALYSIS FOR THE RESPONSE AND FAILURE OF COMPRESSION-LOADED ANGLE-PLY LAMINATES WITH A HOLE	July 1987
	6.

7. Author(s) S. R. Mathison, C. T. Herakovich, M-J Pindera and M. J. Shuart	8. Performing Organization Rept. No. VPI-E-87-14

9. Performing Organization Name and Address	10. Project/Task/Work Unit No.
Virginia Polytechnic Institute and State University Engineering Science and Mechanics Dept Blacksburg, Virginia 24061	
	11. Contract/Grant No. NAG-1-343

12. Sponsoring Organization Name and Address	13. Type of Report & Period Covered
Structural Mechanics Branch National Aeronautics and Space Administration Langley Research Center Hampton, Virginia 23665	
	14.

15. Supplementary Notes

16. Abstracts

This study examines the effect of nonlinear material behavior on the response and failure of unnotched and notched angle-ply laminates under uniaxial compressive loading. A three dimensional finite element analysis incorporating the endochronic theory with an incremental/interative initial strain algorithm was used to model the AS4/3502 graphite epoxy material system. Computer efficiency was increased by using a 180° rotational symmetry relation, and by vectorizing the code to run on a super computer. Laminate response showed excellent agreement with experiment for both unnotched and notched angle-ply laminates. Predicted stresses in the region of the hole are presented to compare linear elastic analysis to the inelastic endochronic theory analysis. Failure analysis, using the quadratic tensor polynomial, for the unnotched and notched laminates predicted fracture loads that agreed well with experiment for the unnotched laminates, but were very conservative in comparison with experiment for the notched laminates.

17. Key Words and Document Analysis. 17a. Descriptors

composites, 3-D finite elements, inversion symmetry, nonlinear behavior, endochronic theory, compression, notched specimens, failure prediction

17b. Identifiers/Open-Ended Terms

17c. COSATI Field/Group

18. Availability Statement	19. Security Class (This Report) UNCLASSIFIED	21. No. of Pages 237
unlimited	20. Security Class (This Page) UNCLASSIFIED	22. Price